Structural and Optical Properties of WO_3 and its Gas Sensing Application

by

Malcolm Govender

Submitted in partial fulfillment of the requirements for the degree

Doctor of Philosophy

In the Faculty of Natural and Agricultural Sciences

University of Pretoria

Pretoria

October 2014

© University of Pretoria

Summary

The development of sensitive, selective, stable and suitable gas sensors for monitoring toxic gases in mineshafts and the environment in general, requires the basic understanding of the active sensing material. This dissertation focuses on the conductometric-type sensor which uses semiconducting metal oxides as the active sensing material. In particular, the focus was on tungsten trioxide semiconducting metal oxide, which amongst its “smart-material” capabilities, is known to exhibit several temperature-dependent phases viz. triclinic, monoclinic, orthorhombic and tetragonal WO_3. The phases influence the physical properties, which in turn influence the sensing capabilities towards certain toxic gases. To better understand the phase transitions and structural changes in this compound, these properties were investigated in light of the Landau-Lifshitz-Lyubarskii theory for second-order phase transitions. These structural changes are observed experimentally by Raman spectroscopy, and so the Raman-active modes for the corresponding Raman spectra of each phase are derived here. Reactive-sputtering with subsequent annealing was used here to synthesize triclinic-phase WO_3 film, and the film was characterized structurally, optically and electrically. The film was used to show the sensing of parts per million concentrations of nitrogen dioxide and ammonia at 30^{o}C and 100^{o}C, as well as the sensing of these gases simultaneously to show that pure triclinic WO_3 has better selectivity to NO_2. To speed up the recovery time of the film after exposure to the target gas, light was shone onto the film to remove any residual species on the surface. This dissertation is one of the first steps into an attempt to investigate the phases of WO_3 for the application of gas sensing.

© University of Pretoria

I, ……declare that the thesis/dissertation, which I hereby submit for the degree ……at the University of Pretoria, is my own work and has not previously been submitted by me for a degree at this or any other tertiary institution.

SIGNATURE: ……..
DATE: …….

© University of Pretoria

Acknowledgements

The author is grateful for the financial support from the DST/CSIR National Centre for Nanostructured Materials under project number HGER27S; for the travel grant from IBSA under project number HGER24X; for collaboration funding from the EU-FP7 grant.

The author is grateful for the facilities at the DST/CSIR National Centre for Nanostructured Materials under Prof. S. S. Ray.

The author is grateful for the facilities at the Department of Physics of the University of Pretoria under Prof. C. Theron.

Thanks to Dr. B. W. Mwakikunga for the opportunity to pursue this work at the CSIR and for the patience, helpfulness, discussion and providing excellent insight on the topic.

Thanks to Prof. H. W. Kunert for making the physics come alive and for all the fun and fruitful discussions throughout this work.

Thanks to Dr. A. G. J. Machatine for being an excellent teacher and always being available whenever I required assistance.

Thanks to Ms. A. Singh for the constant support, motivation and enthusiasm during this project.

Thanks to Dr. E. Manikandan and Prof. S. Umapathy and his team for assisting me with my work in India.

Thanks to Prof. S. Mathur and his group at the University of Cologne, and especially Dr. Y. Gönüllü for being so helpful in achieving certain aspects of this work.

Thanks to my parents for the love, support and prayers.

Thanks to my family and the Ramiahs for always believing in me.

Thanks to my friends and colleagues for being there for me throughout this project.

Finally and most importantly, I am eternally grateful to my Lord and Saviour for keeping me focused and in good health and for all the blessings.

© University of Pretoria

Table of Contents

© University of Pretoria

© University of Pretoria

List of Figures

© University of Pretoria

List of Tables

© University of Pretoria

List of Outputs by Candidate

Oral presentations

[1] Indaba 7 Conference-Insights from Structure, Skukuza, South Africa (2012), "Raman Scattering in Crystals determined by Clebsch-Gordan Coefficients".
[2] IISC, Bangalore, India (2013), "Review on Tungsten Trioxide WO_3".
[3] IBSA meeting, St. George's Hotel, Irene, South Africa (2013), "Synthesis, Characterization and Sensing Application of Tungsten Oxide Films".
[4] SAIP conference, University of Zululand, South Africa (2013), "Investigation of Phase Transitions in Tungsten Trioxide".
[5] SAIP conference, University of Zululand, South Africa (2013), "Synthesis, Characterisation and Gas-Sensing Application of Tungsten Trioxide".
[6] University of Cologne, Cologne, Germany (2013), "Selective Room-Temperature Sensing of NO_2 by WO_3 film/Graphene layer".
[7] NanoAfrica, Vaal University of Technology, Vanderbijlpark, South Africa (2014), "Synthesis, Characterisation and Gas Sensing of WO_3 film".
[8] SAIP conference, University of Johannesburg, South Africa (2014), "Towards Room-Temperature NO_2 sensing by Tungsten Trioxide film".

Poster presentations

[9] EMRS conference, Strasbourg, France (2013), "Characterization and Application of Tungsten Oxide grown by Laser Pyrolysis".
[10] SAIP conference, University of Pretoria, South Africa (2012), "Raman scattering tensors in tetragonal WO_3".
[11] MSSA conference, University of Cape Town, South Africa (2012), "Pt-contacts on single WO_3 nanorod by FIB-SEM".
[12] IEEE-Sensors Conference, Baltimore, United States of America (2013), "Operating Temperature Effect in WO_3 Films for Gas Sensing".
[13] EMRS conference, Lille, France (2014), "NH_3 gas sensing of amorphous WO_{3-x}".

Publications (available at end of thesis)

[14] H. W. Kunert, A. G. J. Machatine, P. Niyongabo, M. Govender, and B. W. Mwakikunga, Phys. Status Solidi C **9**(10-11), 1978-1980 (2012).
[15] H. W. Kunert, A. G. J. Machatine, P. Niyongabo, M. Govender, and B. W. Mwakikunga, Phys. Status Solidi C **9**(10-11), 1974-1977 (2012).
[16] M. Govender, D. E. Motaung, B. W. Mwakikunga, S. Umapathy, S. Sil, A. K. Prasad, A. G. J. Machatine, and H. W. Kunert, Sensors **2013** IEEE, 1-4 (2013).
[17] M. Govender, B. W. Mwakikunga, A. G. J. Machatine, and H. W. Kunert, Phys. Stat. Sol. (c) **11**, 349-354 (2014); and *Journal Back cover.*

© University of Pretoria

[18] H. W. Kunert, M. Govender, A. G. J. Machatine, B. W. Mwakikunga, and P. Niyongabo, Phys. Status Solidi A **211**(2), 435-439 (2014).
[19] M. Govender, B. W. Mwakikunga, S. Mathur, T. Singh, A. Kaouk, Y. Gönüllü, A. G. J. Machatine, and H. W. Kunert, Sensors **2014** IEEE, 1-4 (2014).

Submitted for Publication

[20] M. Govender, B. W. Mwakikunga, A. K. Prasad, S. Umapathy, S. Sil, A. G. J. Machatine, H. W. Kunert, S. Mathur, T. Singh, Y. Gönüllü, R. Müller, and E. Manikandan, Journal of Sensors and Sensor Systems (special issue) (2014).
[21] M. Govender, H. W. Kunert, A. G. J. Machatine, and B. W. Mwakikunga, Phys. Rev. B. (2014).

Other Publications

[22] L. Shikwambana, M. Govender, B. W. Mwakikunga, E. Sideras-Haddad, and A. Forbes, Advanced Materials Research **227**, 80-83 (2011).
[23] M. Govender, L. Shikwambana, B. W. Mwakikunga, E. Sideras-Haddad, R. M. Erasmus, and A. Forbes, Nanoscale Research Letters **6**(1), X1-8 (2011).
[24] G. F. Malgas, D. E. Motaung, G. H. Mhlongo, S. S. Nkosi, B. W. Mwakikunga, M. Govender, C. J. Arendse, and T. F. G. Muller, Thin Solid Films **555**, 100-106 (2014).

© University of Pretoria

CHAPTER 1

INTRODUCTION

1.1 The Need for Gas Sensors and Detectors

The presence of toxic gases in mines may be to blame for the growing number of fatalities of mineworkers, since most of these gases are not easily distinguishable by human senses [1]. Some of these mining-related diseases were reported by Kreuzer *et al.* [2]. This puts the mining industry under severe scrutiny, more especially in South Africa, as it is the driving force of the economy [3]. After mining processes such as blasting and drilling, there is a build-up of toxic gases which are also harmful to the environment, as shown in Fig. 1.1. Studies have shown that amongst the radon and silica dust found in mineshafts, CO_2, CO, H_2, CH_4 and NO_2 are common gases found at mining sites, and vary in concentrations between 0.03-390 ppm [4, 5].

Figure 1.1. The picture shows the pollution and gases emanating from a mine as a result of an underground mine explosion [1].

There are several types of sensors used by mineworkers, which include electrochemical gas detectors [6], infrared point sensors [7], ultrasonic gas detectors [8] and semiconductor sensors [9]. These sensors have drawbacks such as short-lifetime of 1-2 years for electrochemical gas detectors due to chemical contamination and corrosion; infrared point sensors are limited to only infrared-active gases; and ultrasonic gas detectors measure the leak rate of a gas but not the type and concentration of the gas. The disadvantage of semiconductor gas sensors when compared to infrared point sensors is the semiconductor

© University of Pretoria

sensor must be in direct contact with the gas. The semiconductor gas sensors can be miniaturized due to the advances in nanotechnology, and the nano-sized semiconductor sensing material are stable with a long-lifetime, and exhibits high sensitivity to parts per million concentration of toxic gas as a result of the large surface-to-volume ratio of nano-materials [10]. The semiconductor can also be made selective towards a certain gas by doping for example [11], which makes it versatile for sensing several of the common gases found at the mine sites. This motivates for the development of improved semiconductor based gas sensors than those commercially available to monitor the mine environment and thus improve safety procedures and better ventilation of mineshafts.

1.2 The Sensing Material of Semiconductor Gas Sensors

Semiconductor based gas sensors use mainly metal oxides (SMOs) as active sensing materials as it is easy, cost effective, easy up-scaling with controllability, robustness, lightweight, long lifetime, extensive sensitivity towards several gases, high resistance to harsh environments, high catalytic activity, and more specifically adaptability to standard microelectronic processing [12]. Some of the most researched *n*-type SMOs over the past three decades or so are TiO_2 SnO_2, ZnO, In_2O_3 and WO_3 while some of the most researched *p*-type SMOs are Cr_2O_3, NiO, Co_3O_4, Mn_3O_4 and Cu_xO [13, 14]. These SMOs have either direct or indirect wide band gaps in the range of 2-4 eV [15] depending on the crystal phase. The activation energy of the centres responsible for metal oxide conductivity are small for these SMOs, and the combination of wide band gap and small activation energy is necessary to avoid sensor operation in the region of self-conductance which is advantageous because the sensor will be less affected by surrounding temperatures. According to experimental data for SMO-based gas sensors, the optimum sensor operating temperature was found to be ~300^{o}C, which implies that the optimal band gap must be greater than 2.5 eV [16-19].

SnO_2 is the most researched SMO because it is sensitive to many gases, but this can be a disadvantage when it comes to selectivity, since an ideal sensor must have a balance between sensitivity, selectivity and stability [14]. WO_3 on the other hand was previously studied for its electro- and photochromic properties [15], but it was discovered that this material shows good sensitivity towards oxidizing gases even at low temperatures [15, 20]. Furthermore, WO_3 exhibits several temperature-dependent crystal phases [21], much more than the other SMOs, which can offer additional gas sensing benefits such as selectivity. Table 1.1 shows the various gases that the WO_3 phases can detect where the optimum operating temperature was between 200^{o}C-400^{o}C. The stable temperature referred to in Table 1.1 refers to the temperature range where that particular phase of WO_3 exists. However, it is possible to stabilize these phases with appropriate synthesis techniques at lower temperatures so that gas sensing can be carried out. These phases can be distinguished experimentally by neutron diffraction, x-ray diffraction, Raman spectroscopy and electron transport investigations.

WO_3 films are commonly used as the sensing layer due to the ease and availability of deposition techniques and for its robustness as a sensing material. Various deposition techniques to deposit films are available such as laser pyrolysis [22, 23], spray pyrolysis [24],

© University of Pretoria

screen-printing [25] chemical vapour deposition (CVD) [26] and physical vapour deposition (PVD) [27]. PVD gives excellent grain/crystallite size, porosity, surface roughness and crystallinity of high-quality for sensing applications [28].

Table 1.1. The various gases that the temperature-dependent phases of WO_3 can detect[a].

Structure	Symbol	Stable Temperature (^oC)	Space group[b]	Target gas
Tetragonal	α	>900	$D_{4h}^7,\ P4/nmm,\ 129$	H_2S[15, 29]
Orthorhombic	β	$320-720$	$D_{2h}^{16},\ Pnma,\ 62$	NO[15, 31]
Monoclinic	γ	$17-320$	$C_{2h}^5,\ P2_1/a,\ 14$	NO_2, O_3, H_2S, SO_2, NH_3, CO, CH_4, H_2[15, 29, 30]
Triclinic	δ	$-40-17$	$C_i^1,\ P\bar{1},\ 2$	NH_3, NO_2, acetone, alcohols[15]
Monoclinic	ε	<-40	$C_1,\ Pc,\ 1$	acetone[15]

[a]The selectivity towards the other common mine gases can possibly be achieved by doping a particular phase of WO_3.
[b]The *Space group* notation is in International and Schoenflies with the space group number from CDML tables [32].

1.3 Conductometric Gas Sensors

The SMO gas sensor falls under the conductometric class of sensors whose working principle is believed to be based on the gas interaction with the surface (adsorption-desorption) of a solid-state sensing material [15, 33-35]. When compared to other types of sensors such as ultrasonic, electrochemical, thermal conductive and infrared absorption on criteria of sensitivity, accuracy, selectivity, response time, stability, durability, maintenance, cost and suitability to portable instruments, conductometric gas sensors come out superior [36]. Fig. 1.2 shows a schematic of a conductometric gas sensor with a porous film as the active sensing material. The electrodes are placed on either side of the film forming a closed-circuit, and Fig. 1.2 also depicts how the energy profile of the film between the interface of the electrode and the grain boundaries of the sensing material contributes to the measured resistivity or conductivity. The concentration of the gas interacting in the surface reaction results in a proportional measured resistivity change by the closed circuit due to charge transfer between surface and gas [37]. The performance of the sensor can be characterised by: (1) the response R of the sensor which is the ratio of the difference in the resistivity of the film with the target gas ρ_{gas} and the resistivity in air ρ_0 divided by the resistivity in air ρ_0 given by

$$R = \left(\rho_{gas} - \rho_0\right)/\rho_0 , \qquad (1.1)$$

© University of Pretoria

(2) the sensitivity S of the sensor which is just the ratio of the resistivity of the film with the target gas ρ_{gas} divided by the resistivity in air ρ_0 given by

$$S = \rho_{gas} / \rho_0 \,, \tag{1.2}$$

(3) the response time of the sensor which is the time interval over which resistance of the sensor material attains about 90% of the final value when the sensor is exposed to full scale concentration of the gas, (4) the recovery time of the sensor which is the time interval over which sensor resistance reduces to 10% of the saturation value when the target gas is switched off and the sensor is placed in synthetic (or reference gas) air, and (5) the selectivity of the sensor which is the ratio of sensitivity towards interfering gas to the sensitivity towards the target gas. For a more complete and detailed analysis on sensor performance and efficiency, consult Mwakikunga *et al.* [38].

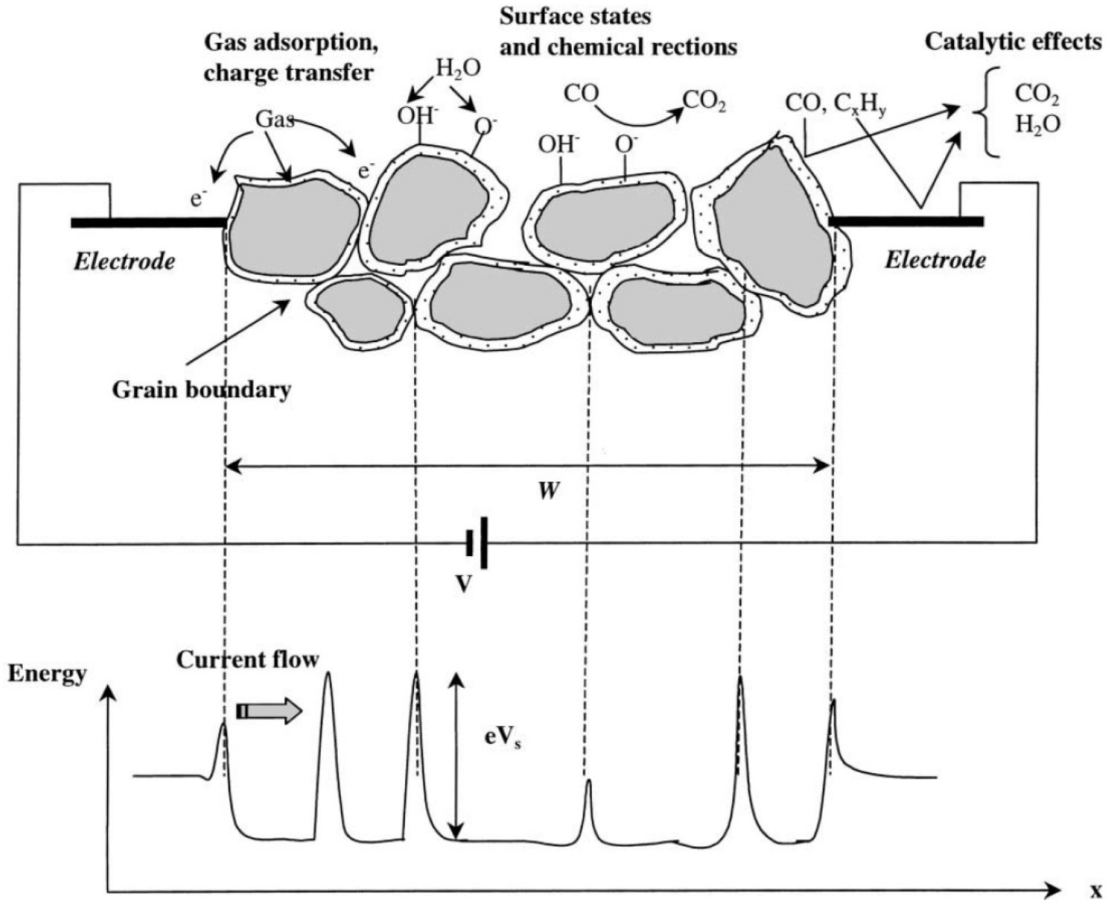

Figure 1.2. A schematic of a typical conductometric gas sensor set-up using a porous layer as the sensing material. The energy profile of the material between the electrodes is also shown here, as well as the surface reactions involving charge transfer and possible catalytic effects [37].

© University of Pretoria

1.3.1 The Conductometric Gas Sensor Mechanism

In the sensing mechanism of conductometric or resistive-type sensors, which are dependent on the concentration of ambient oxygen and sensor operating temperature, it is believed that ambient oxygen is first physisorbed by van der Waals forces on the sensing layer surface, and thereafter the oxygen becomes chemisorbed. The sensing mechanism is therefore microscopically restricted to the particle surface. The most-likely and experimentally determined ionosorbed species after chemisorption on the metal oxide surface concluded that the molecular O_2^- (<150°C) changes to atomic O^- (150-400°C) and adsorbed O^- and O^{2-} (400°C) [39, 40]. At higher temperatures (>600°C), the adsorbed species are directly incorporated into the lattice. The operating temperature also influences the reaction rate of all surface processes in the porous sensing layer and every analyte gas exhibits a specific temperature of maximum sensitivity which depends on its surface coverage and the conversion rate of ionosorbed oxygen [41]. We aim to keep the operating temperature as low as possible (<100°C) for the following reasons: (1) the production of room-temperature sensors is targeted as it consumes less power, (2) eliminate the possibility of inducing phase changes as will be discussed in Chapter 3, and so the operating temperature must be below the annealing temperature. So it can be concluded from this analysis that the molecular O_2^- species plays the major role in the gas sensing mechanism in this study.

The adsorption of oxygen onto the surface of WO_3 causes the oxygen to be electron acceptors and positioned just below the Fermi level E_F as depicted in Fig. 1.3. An electron-depleted region is formed at the surface of WO_3 when the adsorbed oxygen takes electrons from the conduction band E_C of WO_3 and the intrinsic oxygen vacancies [42, 43, 44]. The negative surface potential causes a corresponding enlargement of the positively-charged space charge layer Λ_{air}. According to the Weisz-limitation, the maximum surface coverage is about $10^{-3} - 10^{-2}\ cm^{-1}$ ions, which denotes the equilibrium between the Fermi level and the site energy [45]. According to the energy-band model, there is a band bending of the valence band E_V (not included in Fig. 1.3) and the conduction band E_C resulting from the negative surface potential [46]. The potential height of the surface potential barrier eV_{sur} is estimated to be about $0.5\text{-}1.0\,eV$ at the grain boundaries. The amount and the nature of ionosorbed oxygen influence the depth and the height of potential barrier of the surface and their associated charges [47]. The depth of the potential barrier corresponds to the Debye-length L_D which depends on the temperature for a particular donor concentration of WO_3 in this case.

The microstructure of the WO_3 bridging the electrodes in the sensor device greatly influences the sensing mechanism. In the WO_3 sensing layer, there are percolation paths created by grain-to-grain contacts which contributes to the electrical conductivity in the film. At the grain boundaries, Schottky-barriers are formed which are increased potential barriers which hinder the free electron flow within the film. These Schottky-barriers depends on the thermodynamic equilibrium of adsorption and desorption of the oxygen causing an increase

© University of Pretoria

in resistance. The Maxwell-Boltzmann distribution describes the number of electrons that may overcome the potential barrier and the conductance G of the sensing layer is expressed as $G \approx \exp\left(\frac{-eV_{sur}}{k_B T}\right)$ [48, 49].

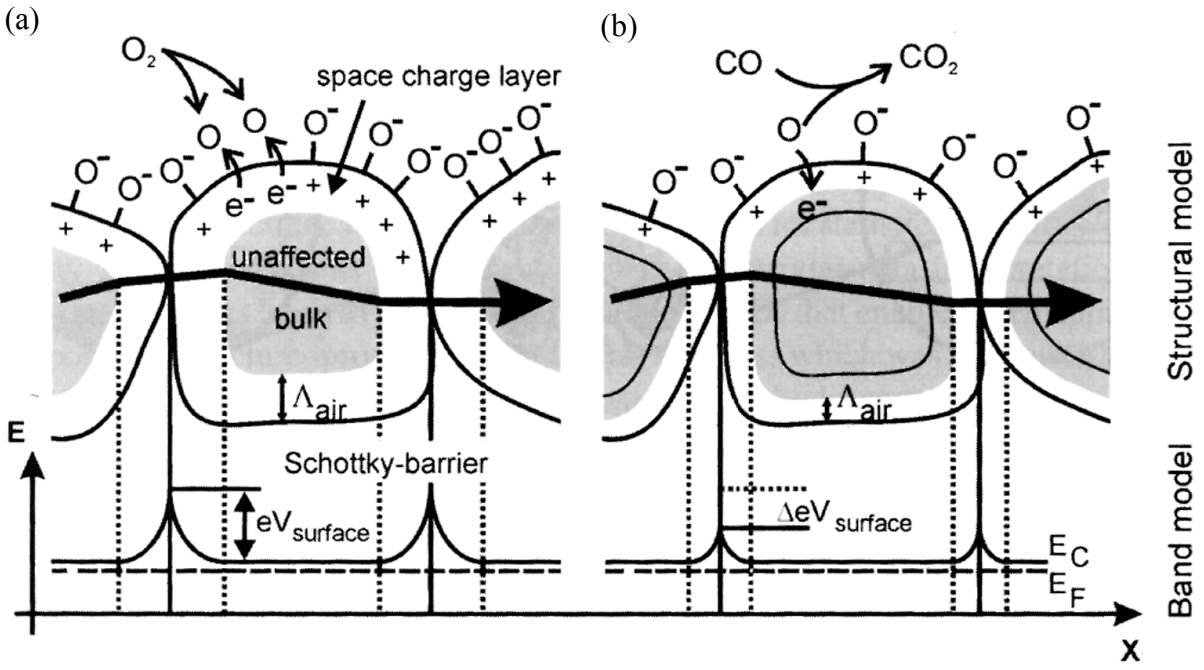

Figure 1.3. (a) The initial state of the sensing material when exposed to air and (b) the sensing material when exposed to CO target gas with the band model included at the bottom of the figure [46, 47].

In the case of reducing gases such as NH_3 and CO, there is a total oxidation of the gas. For instance, in the case of CO in Fig. 1.3 (b), carbonate groups result from the reaction with the ionosorbed oxygen species and then desorb as CO_2. Thus, the electrons that were localized are released back to the bulk of the metal oxide after desorption of the reacted target gas products. This implies that trace amounts of target gas significantly increases the electron density. On the contrary, for oxidizing gases such as NO_2 and O_2, there is direct chemisorption such that oxygen atoms are donated into the lattice. These oxygen atoms accept electrons from oxygen vacancies of the metal oxide and remove electrons from the bulk.

1.3.2 Classification and Sensor Properties of Oxidizing NO_2 and Reducing NH_3 gas

NO_2 gas is found at mines in small concentrations as was discussed in section 1.1, and WO_3 is known to be highly sensitive to this gas. A reducing nitrogen-containing gas in the form of NH_3 is considered to contrast with the sensing properties of the oxidizing gas.

© University of Pretoria

1.3.2.1 Oxidizing Gas: NO_2

Nitrous oxides (NO_x) are usually formed from combustion of fossil fuels and during the combustion reaction, there is a combining of nitrogen and oxygen. NO_2 is toxic upon inhalation and despite it being detectable by smell, a concentration as low as 4 ppm anaesthetises the nose. This gas can cause inflammation of the lungs and long term exposure may cause chronic bronchitis and emphysema [50, 51].

The interaction of *n*-type semiconductor oxides with NO_2 is accompanied by an increase in electrical resistivity because nitrogen dioxide is an electron acceptor [52]. The electron affinity of NO_2 molecule is 2.27 eV [53], which considerably exceeds the analogous value of the oxygen molecule (0.44 eV) [54]. This determines the possibility of detecting low concentrations of NO_2 in air and the presence of oxygen. According to FTIR and programmed desorption in temperature range 25-400^{o}C [55], there is a possibility of dissociation of NO_2 during interaction with the surface. The presence of NO in the thermal desorption products can serve as indirect evidence of the occurrence of the following reactions:

$$NO_{2(gas)} \leftrightarrow NO_{2(ads)}, \tag{1.3a}$$

$$NO_{2(ads)} + e^{-} \leftrightarrow NO^{-}_{2(ads)}, \tag{1.3b}$$

$$NO^{-}_{2(ads)} \leftrightarrow NO_{(gas)} + O^{-}_{(ads)}. \tag{1.3c}$$

The use of dopants that are able to transfer electron density to the oxygen belonging to the acceptor chemisorbed species through an increase in the degree of oxidation should accordingly enhance the sensing signal towards NO_2.

1.3.2.2 Reducing Gas: NH_3

Ammonia is used in fertilizers and is a source of nitrogen to living organisms. Ammonia gas is corrosive and hazardous with a characteristic pungent odour. High enough concentrations of ammonia have been found to be fatal to animals [56].

NH_3 molecules can be adsorbed on the oxide surface via the surface oxygen and the hydrogen of NH_3, leading to the oxidation of the NH_3. According to experimental data, enhancement of sensor response can be achieved by increasing the number of acidic adsorption sites. The main process that determines the sensor response of WO_3 to NH_3 is: [57]

$$2NH_{3(gas)} + \frac{3}{\beta} O^{-\alpha}_{\beta(ads)} \rightarrow N_{2(gas)} + 3H_2O + 3e^{-}. \tag{1.4}$$

© University of Pretoria

1.4 The Objectives

The objective is to construct a suitable gas sensor from WO_3, and this dissertation aims to achieve this by the following steps:

(1) Synthesise WO_3 films using PVD and characterize it to determine experimentally the structural, optical and electronic properties.
(2) Apply the pure synthesised WO_3 film to sense NO_2 and NH_3 gas to test its sensing performance.
(3) Use basic group theory to study the structural properties of WO_3 from the symmetries of the different crystal phases, to the type of the phase transition involved from one phase to the next as well as the possible phonons causing the phase transition. This information gives insights on the physical properties of WO_3 towards gas sensing.
(4) Use basic group theory to study the optical properties of WO_3 and determine the Raman-active modes of the crystal phases and relate it to the corresponding Raman spectra. This information helps to understand the of WO_3- NO_2/NH_3 interaction under Raman spectroscopic observation.

1.5 Layout of this dissertation

This dissertation is arranged as follows:

Chapter 2 introduces the fundamentals of Group Theory used in this work to study structural and optical properties of WO_3.
Chapter 3 focuses on the temperature-dependent phase transitions of WO_3 through the Landau, Lifshitz and Lyubarskii theory of second-order phase transitions, to gain an insight into the structural properties of WO_3.
Chapter 4 shows the determination of the theoretical Raman-active modes and relates the Brillouin zone to the Raman spectra of the WO_3 crystal structures.
Chapter 5 describes the synthesis technique of PVD utilized for the production of WO_3 films to be used as a sensing layer. The topography and thickness of the film is investigated with focused-ion beam scanning electron microscopy (FIBSEM) and transmission electron microscopy (TEM). The structural property of the crystalline film is characterized with x-ray diffraction (XRD) and the chemical composition is analysed with x-ray photoelectron spectroscopy (XPS) and energy-dispersive x-ray spectroscopy (EDX) mapping. Further structural and optical properties of the film are studied with Raman, photoluminescence (PL) and ultraviolet/visible (UV/Vis) spectroscopies. The electrical properties of the film are investigated by measuring the resistance of the film as a function of temperature.
Chapter 6 shows the sensing application of the synthesized WO_3 film and its performance.
Chapter 7 highlights the results of this work and gives perspective for the continuation towards the manufacture of gas sensors with WO_3.

© University of Pretoria

CHAPTER 2

Basic Group Theory

In this section, we provide the basic group theory required in the explanation of second-order phase transitions and the classification of particles and quasi-particles (electrons, holes, excitons, phonons, etc.) of WO_3. This section has been adapted from Hamermesh [58]. In the study of atomic systems or crystals with long translational symmetry, it is imperative to find the symmetry group G of the Hamiltonian $\boldsymbol{H}$, i.e. the set of transformations (symmetry operators) which leave the Hamiltonian invariant. The existence of a symmetry group raises the possibility of degeneracy associated to the dimensions of irreducible representations (irrps) and assignments (according to irrps of G). When the system possesses a well-established symmetry group of operators $\hat{g}$, then

$$g\boldsymbol{H}g^{-1} = \boldsymbol{H}\,,\ g\boldsymbol{H} = \boldsymbol{H}g = \boldsymbol{H}\,, \tag{2.1a}$$

and for

$$\boldsymbol{H}\phi_{\boldsymbol{n}} = E\left(g\phi_n\right) = E\phi_n'\,, \tag{2.1b}$$

$$g\phi_n = \phi_n' = \sum \phi_n D_{mn}\left(g\right). \tag{2.1c}$$

The above equations have the following meaning:

- The Hamiltonian $\boldsymbol{H}$ is invariant with respect to g.
- New eigenfunctions ϕ_n' are also the eigenfunctions of $\boldsymbol{H}$, but expressed as a linear combination of ϕ_n.
- The coefficients $D_{mn}\left(g\right)$ are matrix elements of representation D of group G to which operators g belong, i.e. $g \in G$.
- The number of ϕ_n determines the dimension of representation D and the degeneracy of states of energy E.
- The energy levels E are classified according to irrps of D of G.

2.1 Physical application of Group Theory

As an example, consider the Raman-active phonon modes shown in the Raman spectrum of some crystal in Fig. 2.1. These phonons are classified according to Γ_1 or Γ_2 or Γ_3 irrps of the space group symmetry of that crystal (see Chapter 4 for a more detailed analysis).

© University of Pretoria

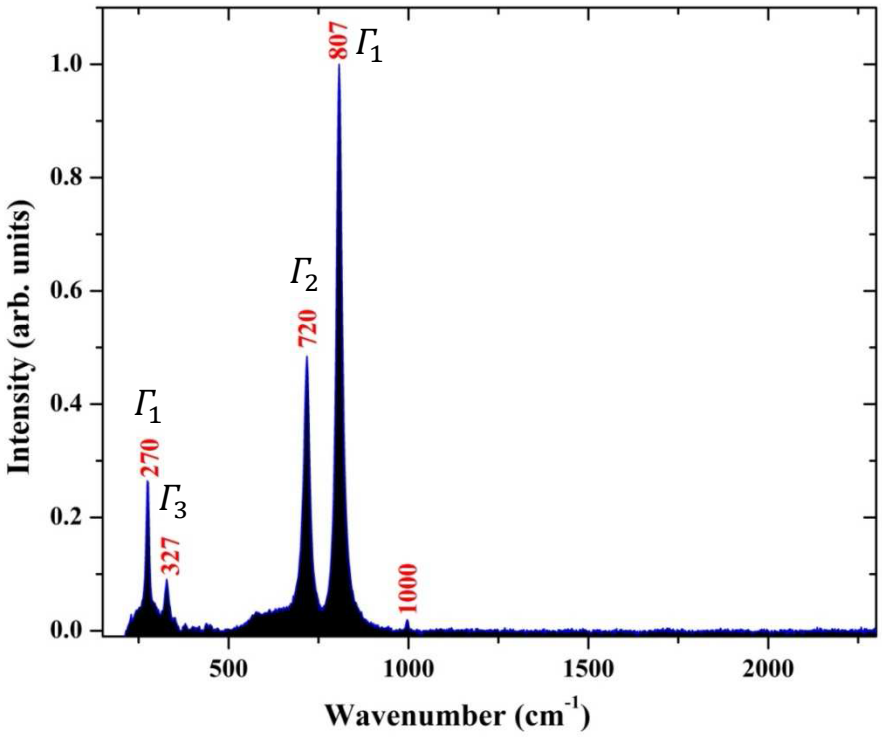

Figure 2.1. The Raman-active modes are assigned to Raman peaks which are classified according to the Γ-irrps of that crystal's space group (D_{2d}).

Now consider the hypothetical scheme of energy spectral terms (φ_n-basis functions of D) for point group D_{2d} shown in Fig. 2.2. The energy levels are classified according to Γ_{1-5} irrps.

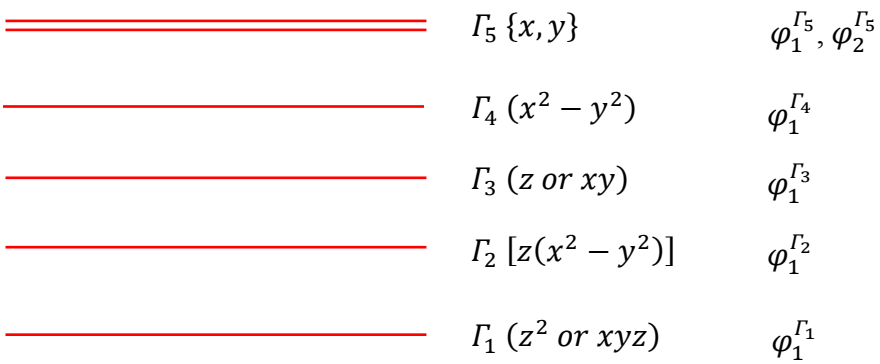

Figure 2.2. The energy level scheme for the D_{2d} symmetry group classified according to Γ-irrps.

2.2 The Kronecker Product

In physical applications such as optical selection rules, second-order phase transitions, Raman spectroscopy as well as interactions like spin-orbit and spin-spin, the need for Kronecker Products (KPs) arise. Any KP of the same two irrps can be decomposed onto a symmetrized and anti-symmetrized KP. Particularly, in the determination of Raman active modes, the KP of the vector representation (VR) is needed, because the Raman active irrps or modes are contained in the symmetrized squares of the KP. The VR for point group D_{2d} in

© University of Pretoria

Fig. 2.2 is $\Gamma_3(z)\oplus\Gamma_5(x,y)$ according to CDML tables [32]. So the KP of the VR of D_{2d} is $(\Gamma_3\oplus\Gamma_5)\otimes(\Gamma_3\oplus\Gamma_5)=(\Gamma_3\otimes\Gamma_3)\oplus 2(\Gamma_3\otimes\Gamma_5)\oplus(\Gamma_5\otimes\Gamma_5)$. The expression used to determine the symmetrized square KP of the VR for respective irrps σ is

$$\frac{1}{2}\sum_{g\in G}\left[\chi(g|\tau)^2+\chi^2(g|\tau)\right]_2\chi^{\sigma}(g|\tau), \tag{2.3a}$$

where $\chi^{\sigma}(g|\tau)$ represents the character or trace of the matrix of irrp σ under the symmetry operator g of the space group with factor group τ. For completeness, the expression used to determine the anti-symmetrized square KP of the VR is

$$\frac{1}{2}\sum_{g\in G}\left[\chi(g|\tau)^2-\chi^2(g|\tau)\right]_2\chi^{\sigma}(g|\tau). \tag{2.3b}$$

Applying Eq. (2.3a) to the KP of the VR of D_{2d}, the symmetrized square KP comes out to be $[\Gamma_1\oplus\Gamma_2\oplus\Gamma_3]_2$, and Eq. (2.3b) for the anti-symmetrized square KP comes out to be $\{\Gamma_4\}_2$. So the Raman active irrps of D_{2d} that may result in the peaks in the Raman spectrum are Γ_1, Γ_2 and Γ_3.

In the case of second-order phase transitions, the symmetrized cube KP is required according to Landau, Lifshitz and Lyubarskii theory [59]. The expression used to determine the symmetrized cube KP of the VR is

$$\sum_{g\in G}\left[\frac{1}{3}\chi(g|\tau)^3+\frac{1}{2}\chi(g|\tau)^2\chi(g|\tau)+\frac{1}{6}\chi^3(g|\tau)\right]_3\chi^{\Gamma_{1+}}(g|\tau), \tag{2.4a}$$

and again for completeness, the expression used to determine the anti-symmetrized cube KP of the VR is

$$\sum_{g\in G}\left[\frac{1}{3}\chi(g|\tau)^3-\frac{1}{2}\chi(g|\tau)^2\chi(g|\tau)-\frac{1}{6}\chi^3(g|\tau)\right]_3\chi^{\Gamma_{1+}}(g|\tau). \tag{2.4b}$$

In the forthcoming chapters, the KPs are used to determine the active-irrps in second-order phase transitions and Raman-active modes.

© University of Pretoria

CHAPTER 3

Phase Transitions in WO_3

Thermodynamical and statistical physics characterizes a first-order phase transition (F. Or. Ph. Tr.) by a discontinuous change in entropy at a fixed temperature which corresponds to a change in latent heat [59]. A second-order phase transition (S. Or. Ph. Tr.) is characterized by a continuous change in entropy which means there is no latent heat. The typical entropy change of the respective transitions is plotted in Fig. 3.1. These transitions can be investigated experimentally with differential scanning calorimetry, x-ray diffraction, neutron scattering and Raman spectroscopy amongst other techniques.

With respect to symmetry, there is a definite change at the transition temperature. In a discontinuous (first-order) transition, there are usually two distinct phases after phase transition which can co-exist together, example water and ice. However, we define a discontinuous phase transition as one where there is no relation between the symmetries of the two phases, such that there is sudden rearrangement of the crystal lattice. In a continuous (second-order) phase transition, there is a distinct symmetry before phase transition and another distinct symmetry after phase transition. However, the lower symmetry phase must form part of the higher symmetry phase. This is addressed in more detail with respect to WO_3 in section 3.1.3 below.

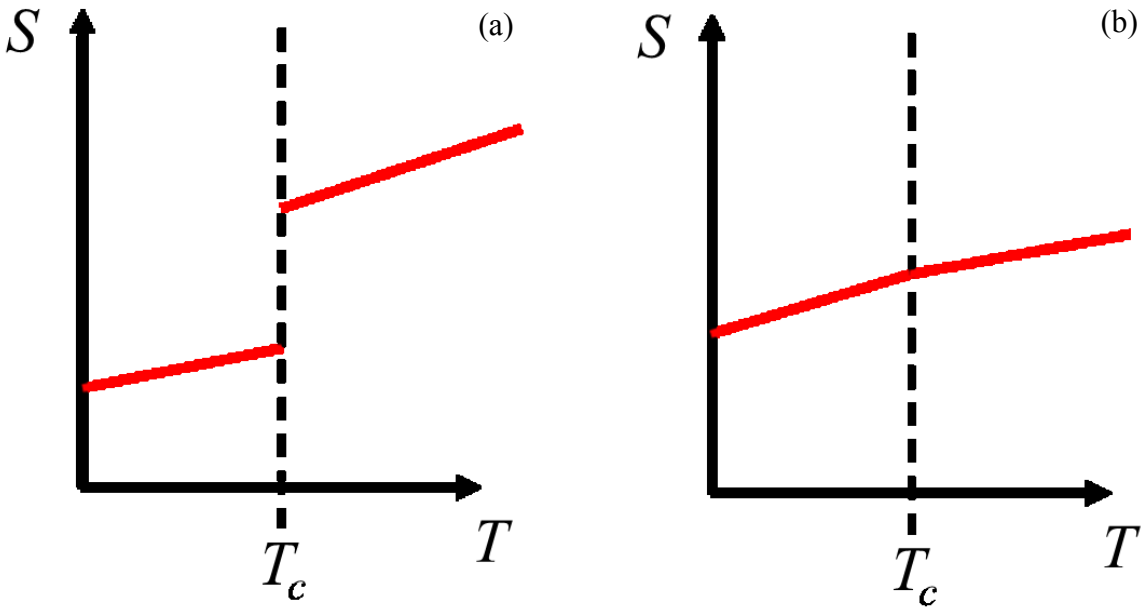

Figure 3.1. (a) First-order phase transition showing a discontinuity at the transition temperature T_c and (b) second-order phase transition showing continuity at the transition temperature T_c [60].

© University of Pretoria

3.1 Why does WO_3 undergo Phase Transitions?

Despite the simple stoichiometry of WO_3, it can take on a number of crystalline forms. WO_3 is most commonly described as distorted forms of cubic ReO_3 crystal structure, and the polymorphs of WO_3 are three-dimensional networks of corner-linked WO_6 octahedra [61]. The WO_3 compound falls under the cubic perovskite crystals (ABX_3) [62]. As the size of the *A*-cation decreases, the cubic perovskite crystal becomes increasingly unstable, and in the case of WO_3, the *A*-cation is completely missing as seen in Fig. 3.2. This leads to WO_3 having structural instability when pressure or thermal stress is applied to it. The WO_3 reacts to increasing temperature and pressure by becoming less tilted and distorted and can undergo cell-doubling transitions. The lower symmetry phases show high instability, which results in the cubic phase being extremely unstable to the point that it is not observed experimentally [63]. The symmetry breaking transitions in WO_3 is primarily due to the change in the metal-oxygen interaction, and not so much to the metal centre alone or oxygen-oxygen interactions. On the other hand, considering the band structure of WO_3, it is believed that since the conduction band of this compound is vacant, results in a W*d*-O*p* orbital hybridization which stabilizes the valence band in favour of the distorted structure over the cubic form [58, 59].

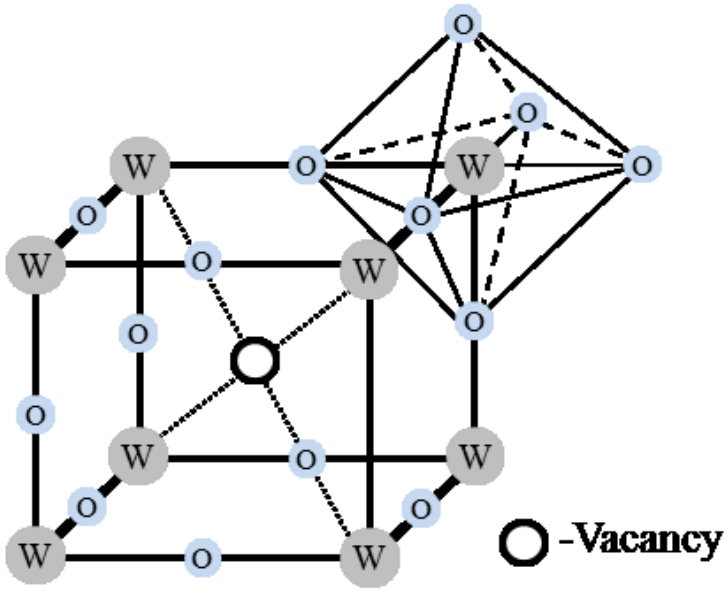

Figure 3.2. The unit cell of cubic WO_3 showing the relative positions of the W and O atoms as well as the missing *A*-cation in the centre of the perovskite structure. The WO_6 octahedron is shown in the top corner of the unit cell.

3.1.1 The Symmetries of the WO_3 crystal phases

It is important to realise that the morphology of the WO_3 directly influences the exact temperature or pressure at which the transition takes place. The phase transitions upon heating may not necessarily exhibit the same symmetry changes upon cooling. However, in most cases, after heating and cooling, the WO_3 always reverts back to its starting phase at room temperature. The symmetries found after phase transitions have been controversial with

© University of Pretoria

many authors arriving at different conclusions, and this discrepancy could be due to the improvement of synthesis and characterization techniques over the years. At temperatures below -40°C, it was found that WO_3 exhibits a monoclinic structure with space group symmetry Pc (C_1) [66]. As the temperature is increased up to 17°C, the structure becomes triclinic with space group symmetry $P\bar{1}$ (C_i^1) [20, 66, 67], but it is also observed that this phase is thermodynamically stable and is often observed as a metastable state at room temperature [68]. At temperatures up to 350°C, the phase changes to monoclinic symmetry again, but with space group symmetry $P2_1/n$ (C_{2h}^5) [67, 69, 70]. Increasing the temperature of the compound up to 720°C, causes the phase to change to an orthorhombic form. Early studies concluded that the space group of the orthorhombic phase is $Pmnb$ (D_{2h}^7) [20, 69], and more recent studies concluded that the orthorhombic space group symmetry is most likely $Pnma$ (D_{2h}^{16}) [70] or $Pbcn$ (D_{2h}^{14}) [67]. One study showed that between 750°C and 790°C, another monoclinic form existed with symmetry $P2_1/c$ (D_{2h}^2) [67]. Heating the WO_3 up to 830°C causes a transition to tetragonal form having space group $P4/ncc$ (D_{4h}^8) [67, 70, 71]. This phase was not observed in earlier studies probably due to lack of "sensitive" characterisation techniques. At temperatures above 930°C, all studies agreed that the highest symmetry phase after transitions is tetragonal symmetry belonging to space group $P4/nmm$ (D_{4h}^7) [20, 67, 69, 70, 71]. Another study suggested that the $P4/nmm$ transition to $Pnma$ occurs via space group $Cmca$ (D_{2h}^{18}) [70]. The existence of another tetragonal phase having symmetry $P\bar{4}2_1m$ (D_{2d}^3) was found by other studies [71, 72] to transition from $P4/nmm$.

3.1.2 The Structural changes involved in the Phase Transition of WO_3

The phase transition from triclinic to room-temperature monoclinic WO_3 phase is characterized by the tilt angle of the O octahedral with the interatomic distances and angles remaining almost unchanged [66]. This transition is supported by the very small changes of phonon frequencies at the phase transition point measured by Raman spectroscopy. Each tungsten atom has two short, two intermediate and two long bonds to oxygen, and the average W–O distances are essentially the same in both phases. The slightly higher density of triclinic WO_3 is attributed to better packing efficiency with its tilt system [68]. The BZ of the triclinic and room-temperature monoclinic phase is shown in Appendix A. The phase transition from room-temperature monoclinic to orthorhombic phase WO_3 is characterized by doubling of the *c*-axis [20]. This phase transition is believed to be driven by successive softening of the R_3 phonon mode [61], and another study proposed that this transition is tricritical ferro-elastic characterized by a soft mode at the Γ-point of the Brillouin zone (BZ) [70]. The BZ of the orthorhombic phase is shown in Appendix A. The transition from orthorhombic to tetragonal phase ($P4/nmm$) WO_3 is characterized by the phonon in the *X*-point of the tetragonal BZ. This *X*-point phonon is possibly responsible for the transition to lower symmetry phases [69], and this transition shows a decrease in volume and the *c*-axis [20]. Other studies concluded that the transition to the tetragonal phase is driven by successive softening of the M_3 phonon mode [61, 73]. The high symmetry points of the tetragonal BZ are shown in Fig. 3.3. The

© University of Pretoria

difference between the transition from the $P4/ncc$ and $P4/nmm$ structures is believed to be related to a tricritical non-ferroic transition characterized by a soft mode at the Z-point of the BZ, which induces antiphase rotations of the WO_6 octahedra about [001] [71]. The apparent phase transition from intermediate phase $Cmca$ to $P4/nmm$ proceeds via a soft mode at the Z-point of the BZ [70]. The phase transition from $Cmca$ to $Pnma$ occurs through a Y-point non-ferroic transition.

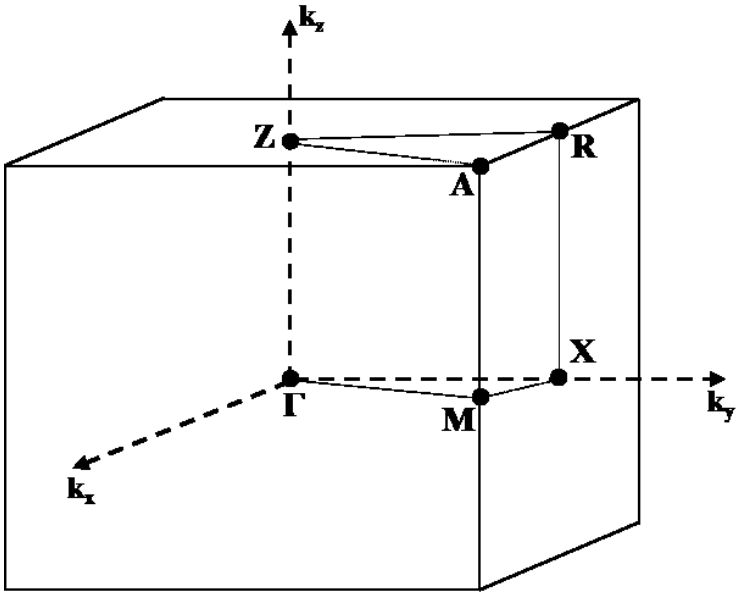

Figure 3.3. The Brillouin Zone of the tetragonal primitive cell and the relative positions of the high symmetry points $\mathbf{k}_\Gamma(0,0,0)$, $\mathbf{k}_Z\left(0,0,\frac{1}{2}\right)$, $\mathbf{k}_M\left(\frac{1}{2},\frac{1}{2},0\right)$, $\mathbf{k}_X\left(0,\frac{1}{2},0\right)$, $\mathbf{k}_R\left(0,\frac{1}{2},\frac{1}{2}\right)$ and $\mathbf{k}_A\left(\frac{1}{2},\frac{1}{2},\frac{1}{2}\right)$ where the lattice constant is the product with $\left(\frac{2\pi}{a_1},\frac{2\pi}{a_1},\frac{2\pi}{a_2}\right)$ and the high symmetry points [32]. NB. The Brillouin Zones of the lower symmetry phases are given in Appendix A.

3.1.3 The Continuous and Discontinuous Phase Transitions of WO_3

The transition from monoclinic (Pc) to triclinic WO_3 is discontinuous (first-order), and abrupt changes in directionality is observed experimentally [61]. The transition from triclinic to monoclinic ($P2_1/n$) phase is believed to be continuous [74]. The transition from room-temperature monoclinic phase to orthorhombic is classified as continuous (second-order) according to experiments [61, 66, 67]. However, the transition from orthorhombic $Pbcn$ to the new found $P2_1/c$ monoclinic phase is believed to be discontinuous, and from $P2_1/c$ to $P4/ncc$ is continuous [67]. The phase transition from orthorhombic to tetragonal is discontinuous (first-order) [61, 70, 75] according to the changes in lattice parameters and bond lengths. The transition from $Pnma$ to $P4/ncc$ is believed to be discontinuous [70], and from $P4/ncc$ to $P4/nmm$ is believed to be continuous [67]. The results obtained from literature for the symmetries of the several observed phases are summarized in Table 3.1. Here we use rigid group theoretical arguments in the framework of Landau-Lifshitz [59] and Lyubarskii [76] (LLL) theory of S. Or. Ph. Trs., which strictly resolves the symmetry of a crystal after transitions and predicts correctly the phonon modes involved in transitions. The

© University of Pretoria

assignment of phonon modes that are responsible for S. Or. Ph. Trs. are carried out here, to check the correlation with literature. The calculations are applied to the $P4/nmm$ (D_{4h}^{7}) space group because it is the highest observed symmetry of WO_3 by all the literature.

Table 3.1. Experimentally obtained structural information of WO_3 phases[a] [61, 66, 67, 70, 75].

Structure	Phase Symbol	Curie Temperature (°C)	Space group
Tetragonal	α	>900	D_{4h}^{7}, $P4/nmm$, 129
Tetragonal		$830-930$	D_{4h}^{8}, $P4/ncc$, 130
Tetragonal			D_{2d}^{3}, $P\bar{4}2_1m$, 113
Orthorhombic			D_{2h}^{18}, $Cmca$, 64
Monoclinic		$750-790$	D_{2h}^{2}, $P2_1/c$, 11
Orthorhombic	β	$320-720$	D_{2h}^{16}, $Pnma$, 62
Orthorhombic			D_{2h}^{14}, $Pbcn$, 60
Orthorhombic			D_{2h}^{7}, $Pmnb$, 53
Monoclinic	γ	$17-320$	C_{2h}^{5}, $P2_1/a$, 14
Triclinic	δ	$-40-17$	C_i^1, $P\bar{1}$, 2
Monoclinic	ε	<-40	C_1, Pc, 1

[a]The *Space group* notation is in International and Schoenflies with the space group number from CDML tables [32].

3.2 Theory of Second-Order Phase Transitions

The thermodynamical state of a crystal is characterised by the thermodynamical potential $\Phi = E - TS + pV$, where E is the energy, S is the entropy, p is the pressure and V is the volume. In the equilibrium state, the Φ must have a minimum value $\Phi(p,T,\rho)$.

The state of a crystal can be characterized by the density function $\rho(x,y,z)$, which describes the probability of finding a particle in a given volume $\rho(x,y,z)dv$ [76]. The density function can be determined from the minimum of the thermodynamic potential $\phi = \Phi(p,T,\rho)$ at equilibrium with the change of p and T.

At the equilibrium state (p_0,T_0), the density state function $\rho_0(x,y,z)$ corresponds to highest symmetry group G_0, and at the state (p,T), the density state $\rho(x,y,z)$ corresponds to the lower symmetry group G of the crystal. The density state can be written as

$$\rho(x,y,z) = \rho_0(x,y,z) + \delta\rho(x,y,z), \tag{3.1}$$

where $\delta\rho \to 0$ when $p,T \to p_0,T_0$. The $\delta\rho$ term denotes a small change of density ρ due to the transition, which is invariant with respect to $g \in G$ of a crystal. The $\delta\rho$ term can be

© University of Pretoria

expressed as a linear combination of the basis wave-functions ψ_i written as $\delta\rho = \sum_i c_i\psi_i$, and so $g\delta\rho \Rightarrow \sum \phi_m D_{mn}(g)$ following from equation (2.1c), and transforms according to the irreducible representations (irrps) of G after the S. Or. Ph. Tr. takes place. It is for this reason, according to the correspondence of irrps, that the low symmetry group G must be a subgroup of higher symmetry group G_0.

According to LLL-theory, the $\phi(p,T,\rho)$ can be expanded in a series of polynomials up to the fifth-order and can be expressed as

$$\phi = \phi_0 + \phi_2(c_i, p, T) + \phi_4(c_i, p, T). \tag{3.2}$$

Our aim is to find all possible symmetries of G after S. Or. Ph. Tr, i.e. the determination of active irrps or active phonon modes that may be responsible for the phase transitions in WO_3.

3.3 Selection of Active Irrps of D_{4h}^7 space group of WO_3

According to the LLL-theory, only active irrps can cause S. Or. Ph. Trs. The labelling used here for symmetry operators, irrps and Kronecker Products (KPs) follow from CDML tables [32]. Note that for the calculations, we start with the highest symmetry of WO_3 which is D_{4h}^7/T factor group with respect to translational group T, and find the subgroups and active irrps that may lead to S. Or. Ph. Trs. to the lower symmetry space groups of WO_3. There are several criteria that cause an irrp to be active, and these are outlined here:

1. The lower space symmetry group G after transition must necessarily be a space subgroup of higher initial space group G_0 before transition.

2. The irrps of G_0 must be real, and must satisfy the "reality test" written as

$$\frac{1}{|g|}\sum_{g\in k_1}\chi(g\,|\,\tau_g)^2 = \left.\begin{Bmatrix} 1 \\ 0 \\ -1 \end{Bmatrix}\right. \begin{matrix} \text{real} \\ \\ \text{non-real} \end{matrix}, \tag{3.3}$$

   where g is the order of the group, k_1 is the first wave-vector of G_0, and χ is the character of the irrp.

3. The anti-symmetrized square $\{D^l\}_2$ of an irreducible representation must not contain any component of the polar vector (x,y,z). $\{D^l\}_2$ can be determined by equation (2.3b).

© University of Pretoria

4. The symmetrized cube $\left[D^{\mu}\right]_3$ must not contain the identity irrp (usually denoted by Γ_1, Γ_{1+} or A_{1g} of G_0). $\left[D^{\mu}\right]_3$ can be determined from equation (2.4a).
5. D^{μ} must be compatible with the induced full representations (IFRs) of the small groups of G_0.

Following from criterion (1), the space subgroups of D_{4h}^7 are given in Table 3.2. The Brillouin zone of the D_{4h}^7 tetragonal primitive cell was illustrated in Fig. 3.3 to show the coordinates of Γ, Z, A, M, X and R high symmetry points. Applying the reality test on the irrps of $G^{\boldsymbol{k}_\Gamma}$, $G^{\boldsymbol{k}_M}$, $G^{\boldsymbol{k}_A}$, $G^{\boldsymbol{k}_Z}$, $G^{\boldsymbol{k}_X}$ and $G^{\boldsymbol{k}_R}$ according to criterion (2), it was found that all the irrps are real, and this determination can be found in Appendix C. The vector representation VR of D_{4h}^7 was found to be $\Gamma_{3-}(z)\oplus\Gamma_{5-}(x,y)$ according to Appendix B, and so $\left\{D^{\mu}\right\}_2$ must not contain one or both of these irrps. The decomposition of the KPs of $\left\{D^{\mu}\right\}_2$ according to criterion (3) is given in Appendix D, and it was found that the anti-symmetrized square of points X and R contained $\Gamma_{5-}(x,y)$, and so the irrps of these points are inactive. The decomposition of the KPs of $\left[D^{\mu}\right]_3$ according to criterion (4) is given in Appendix D, and it was found that the irrp Γ_{1+} is inactive. Therefore, these two points and their irrps are excluded in the participation of S. Or. Ph. Trs. Criterion (5) falls away because the points X and R are the small groups and have already been excluded. The active irrps responsible for the S. Or. Ph. Trs. to the space subgroups of D_{4h}^7 are summarized in Table 3.3, where the irrps of points Γ, Z, A and M are obtained from Appendix E.

From the set of invariant symmetry operators of the active irrps in Table 3.3, it is seen that eight do not form a space group and are therefore discarded from possible S. Or. Ph. Trs. Comparing the theoretical results from Table 3.3 to experimental observations in Table 3.1, only one S. Or. Ph. Tr. from D_{4h}^7 to D_{2d}^3 is observed. The active irrp that may cause this S. Or. Ph. Tr. is either Γ_{4-}, Z_{4-}, M_1 or A_1. Following from experimental analysis in literature, the most likely active irrp responsible for this transition is Z_{4-}. None of the other theoretical results were observed experimentally, and so no other S. Or. Ph. Tr. takes place from the D_{4h}^7 symmetry. The other S. Or. Ph. Trs. mentioned in Section 3.1.3, viz. $P2_1/n$ to $P\bar{1}$, $Pnma/Pbcn/Pmnb$ to $P2_1/n$ and $P4/ncc$ to $P4/nmm$, were verified by the LLL-theory. All these transitions did not satisfy the strict conditions of the LLL-theory because the observed symmetry after transition is not a space subgroup of the corresponding higher initial symmetry, and so we believe these transitions are of a higher-order.

© University of Pretoria

Table 3.2. The space subgroups G of initial space group D_{4h}^7/T [b]. The symmetry operators of the subgroups including non-primitive translations and their respective Brillouin zones belong to the set of symmetry operators of the D_{4h}^7 space group.

Highest symmetry space group of WO_3	**Space Subgroups of D_{4h}^7 and their symmetry operators**		
D_{4h}^7, $P4/nmm$, 129 E, 2.1, 3.1, 4, 13, 14.1, 15.1, 16, 25.1, 26, 27, 28.1, 37.1, 38, 39, 40.1	Tetraganol P		
	D_{2d}^5, $P\bar{4}m2$, 115 E, 4, 13, 16, 26, 27, 38, 39	D_{2d}^3, $P\bar{4}2_1m$, 113 E, 4, 13, 16, 26, 27, 38, 39	D_4^2, $P42_12$, 90 E, 2.1, 3.1, 4, 13, 14.1, 15.1, 16
	C_{4h}^3, $P4/n$, 85 E, 4, 14.1, 15.1, 25.1, 28.1, 38, 39	S_4^1, $P\bar{4}$, 81 E, 4, 38, 39	
	Tetraganol I		
	D_{2d}^9, $I\bar{4}m2$, 119 E, 4, 13, 16, 26, 27, 38, 39	S_4^2, $I\bar{4}$, 82 E, 4, 38, 39	
	Orthorhombic P		
	D_{2h}^{13}, $Pmmm$, 59 E, 2.1, 3.1, 4, 25.1, 26, 27, 28.1	C_{2v}^1, $Pmm2$, 25 E, 4, 26, 27	D_2^3, $P2_12_12$, 18 E, 2.1, 3.1 4
	Orthorhombic I	Orthorhombic F	Orthorhombic C
	C_{2v}^{20}, $Imm2$, 44 E, 4, 26, 27	C_{2v}^{18}, $Fmm2$, 42 E, 4, 26, 27	C_{2v}^{11}, $Cmm2$, 35 E, 4, 26, 27
	Monoclinic P		
	C_2^1, $P2$, 3 E, 4	C_1, Pc, 1 E	

[b] E represents the identity symmetry operator. $1 \rightarrow \left(\frac{1}{2}\frac{1}{2}0\right)$ is the non-primitive translation, for example, $2.1 \rightarrow 2\left|\frac{1}{2}\frac{1}{2}0\right.$. The notation in the table is in the form: International notation, Schoenflies notation, Space group number according to CDML tables [32]. See Appendix B for symmetry operators. It is clearly pointed out in the above table that the symmetry operators of the subgroups appear in the D_{4h}^7 space group.

© University of Pretoria

Table 3.3. The Irreducible Representations (irrps) of initial space group $G_0 = D_{4h}^7$ that may cause S. Or. Ph. Trs. by active modes of Γ, Z, A and M [c].

Highest symmetry space group of WO_3	**Active Irrps that may cause S. Or. Ph. Trs.**	**Space Subgroups of D_{4h}^7 and their symmetry operators**
D_{4h}^7, $P4/nmm$, 129 E, 2.1, 3.1, 4, 13, 14.1, 15.1, 16, 25.1, 26, 27, 28.1, 37.1, 38, 39, 40.1	$\xrightarrow{\Gamma_{2+},Z_{2+}}$	D_{2h}^{13}, $Pmmm$, 59 (E, 2.1, 3.1, 4,25.1, 26, 27, 28.1)
	$\xrightarrow{\Gamma_{3+},Z_{3+}}$	C_{4h}^3, $P4/n$, 85 (E, 4, 14.1, 15.1, 25.1, 28.1, 38, 39)
	$\xrightarrow{\Gamma_{4+},Z_{4+}}$	? (E, 4, 13, 16, 25.1, 28.1, 37.1, 40.1)
	$\xrightarrow{\Gamma_{5+},Z_{5+}}$	? (E, 16, 25.1, 40.1)
	$\xrightarrow{Z_{1+}}$	? (E, 2.1, 3.1, 4, 13, 14.1, 15.1, 16, 25.1, 26, 27, 28.1, 37.1, 38, 39, 40.1)
	$\xrightarrow{\Gamma_{1-},Z_{1-}}$	D_4^2, $P42_12$, 90 (E, 2.1, 3.1, 4, 13, 14.1, 15.1, 16)
	$\xrightarrow{\Gamma_{2-},Z_{2-}}$	? (E, 2.1, 3.1, 4, 37.1, 38, 39, 40.1)
	$\xrightarrow{\Gamma_{3-},Z_{3-}}$	? (E, 4, 14.1, 15.1, 26, 27, 37.1, 40.1)
	$\xrightarrow{\Gamma_{4-},Z_{4-}}$	D_{2d}^3, $P\bar{4}2_1m$, 113; D_{2d}^5, $P\bar{4}m2$, 115; D_{2d}^9, $I\bar{4}m2$, 119 (E, 4, 13, 16, 26, 27, 38, 39)
	$\xrightarrow{\Gamma_{5-},Z_{5-}}$	? (E, 13, 28.1, 40.1)
	$\xrightarrow{M_1,A_1}$	D_{2d}^3, $P\bar{4}2_1m$, 113; D_{2d}^5, $P\bar{4}m2$, 115; D_{2d}^9, $I\bar{4}m2$, 119 (E, 4, 13, 16, 26, 27, 38, 39)
	$\xrightarrow{M_2,A_2}$	C_{2v}^1, $Pmm2$, 25; C_{2v}^{11}, $Cmm2$, 35; C_{2v}^{18}, $Fmm2$, 42; C_{2v}^{20}, $Imm2$, 44 (E, 4, 26, 27)
	$\xrightarrow{M_3,A_3}$	? (E, 15.1, 26, 40.1)
	$\xrightarrow{M_4,A_4}$	? (E, 14.1, 26, 37.1)

[c]The irrps of D_{4h}^7 are tabulated in Appendix E. Column 1 in the above table lists the symmetry operators of D_{4h}^7 and Column 2 lists the irrps that may cause S. Or. Ph. Trs. to the respective space subgroups listed in column 3 with their respective symmetry operators. For example, $D_{4h}^7 \xrightarrow{\Gamma_{2+},Z_{2+}} D_{2h}^3$. The irrps can be verified from Table 3.4.

© University of Pretoria

Table 3.4. Irreducible representations of $G^{\boldsymbol{k}_\Gamma}$ for space group D_{4h}^7 at $\boldsymbol{k}_\Gamma = (0,0,0)\frac{2\pi}{a}$ *.

α-WO_3	E	$C_{2x}\mid\tau$	$C_{2y}\mid\tau$	C_{2z}	C_{2b}	$C_{4z}^{+}\mid\tau$	$C_{4z}^{-}\mid\tau$	C_{2a}	$I\mid\tau$	σ_x	σ_y	$\sigma_z\mid\tau$	$\sigma_{db}\mid\tau$	S_{4z}^{-}	S_{4z}^{+}	$\sigma_{da}\mid\tau$
$\{g/\tau\}$	**1**	**2.1**	**3.1**	**4**	**13**	**14.1**	**15.1**	**16**	**25.1**	**26**	**27**	**28.1**	**37.1**	**38**	**39**	**40.1**
Γ_{1+}	1	1	1	1	1	1	1	1	1	1	1	1	1	1	1	1
Γ_{2+}	1	1	1	1	-1	-1	-1	-1	1	1	1	1	-1	-1	-1	-1
Γ_{3+}	1	-1	-1	1	-1	1	1	-1	1	-1	-1	1	-1	1	1	-1
Γ_{4+}	1	-1	-1	1	1	-1	-1	1	1	-1	-1	1	1	-1	-1	1
Γ_{5+}	$\begin{bmatrix}1&0\\0&1\end{bmatrix}$	$\begin{bmatrix}1&0\\0&-1\end{bmatrix}$	$\begin{bmatrix}-1&0\\0&1\end{bmatrix}$	$\begin{bmatrix}-1&0\\0&-1\end{bmatrix}$	$\begin{bmatrix}0&-1\\-1&0\end{bmatrix}$	$\begin{bmatrix}0&-1\\1&0\end{bmatrix}$	$\begin{bmatrix}0&1\\-1&0\end{bmatrix}$	$\begin{bmatrix}0&1\\1&0\end{bmatrix}$	$\begin{bmatrix}1&0\\0&1\end{bmatrix}$	$\begin{bmatrix}1&0\\0&-1\end{bmatrix}$	$\begin{bmatrix}-1&0\\0&1\end{bmatrix}$	$\begin{bmatrix}-1&0\\0&-1\end{bmatrix}$	$\begin{bmatrix}0&-1\\-1&0\end{bmatrix}$	$\begin{bmatrix}0&-1\\1&0\end{bmatrix}$	$\begin{bmatrix}0&1\\-1&0\end{bmatrix}$	$\begin{bmatrix}0&1\\1&0\end{bmatrix}$
Γ_{1-}	1	1	1	1	1	1	1	1	-1	-1	-1	-1	-1	-1	-1	-1
Γ_{2-}	1	1	1	1	-1	-1	-1	-1	-1	-1	-1	-1	1	1	1	1
Γ_{3-}	1	-1	-1	1	-1	1	1	-1	-1	1	1	-1	1	-1	-1	1
Γ_{4-}	1	-1	-1	1	1	-1	-1	1	-1	1	1	-1	-1	1	1	-1
Γ_{5-}	$\begin{bmatrix}1&0\\0&1\end{bmatrix}$	$\begin{bmatrix}1&0\\0&-1\end{bmatrix}$	$\begin{bmatrix}-1&0\\0&1\end{bmatrix}$	$\begin{bmatrix}-1&0\\0&-1\end{bmatrix}$	$\begin{bmatrix}0&1\\1&0\end{bmatrix}$	$\begin{bmatrix}0&1\\-1&0\end{bmatrix}$	$\begin{bmatrix}0&-1\\1&0\end{bmatrix}$	$\begin{bmatrix}0&-1\\-1&0\end{bmatrix}$	$\begin{bmatrix}-1&0\\0&-1\end{bmatrix}$	$\begin{bmatrix}-1&0\\0&1\end{bmatrix}$	$\begin{bmatrix}1&0\\0&-1\end{bmatrix}$	$\begin{bmatrix}1&0\\0&1\end{bmatrix}$	$\begin{bmatrix}0&-1\\-1&0\end{bmatrix}$	$\begin{bmatrix}0&-1\\1&0\end{bmatrix}$	$\begin{bmatrix}0&1\\-1&0\end{bmatrix}$	$\begin{bmatrix}0&1\\1&0\end{bmatrix}$

*The symmetry operators that leave the wave functions unchanged have been obtained from the above table and were tabulated in Table 3.3. For example, consider irrp Γ_{2+}, with symmetry operators 1, 2.1, 3.1, 4, 25.1, 26, 27 and 28.1 of D_{4h}^7 that leave the basis $\varphi^{\Gamma_{2+}}$ unchanged of the density of states ($\rho = \rho_0 + \sum \psi_j D_{ji}$, where D_{ji} are matrix elements of D_{4h}^7, may cause S. Or. Ph. Trs. to the space subgroup containing this set of symmetry operators. In this way, one finds irrps responsible for transitions to the space subgroups after transitions. This method is purely group theoretical in terms of the subgroup chains method.

© University of Pretoria

CHAPTER 4

Raman Scattering Processes in WO_3

4.1 Raman Tensors

The general mechanism of Raman scattering (RS) is discussed here, followed by analysis of the experimentally obtained Raman spectra in terms of Raman-active modes (RAMs). In the study of elastic and inelastic scattering of light by quasi-particles in solids, it is useful to first introduce a scattering tensor which relates the Cartesian components (x, y, z) of the scattered radiation field to that of the incident field. This section has been adapted from Birman *et al* [77, 78]. If the unit polarization vector of the incident radiation is $\bar{e}_{i\beta}$ ($\beta = x, y, z$), and the unit polarization vector of the scattered radiation is $\bar{e}_{\rho\alpha}$ ($\alpha = x, y, z$) polarized in the α-direction, then we can relate the intensity of the scattered light by

$$I = C\left|e_{i\beta} P_{\alpha\beta} e_{\rho\alpha}\right|^2, \tag{4.1}$$

where $P_{\alpha\beta}$ is the scattering tensor (ST) and C is a coefficient that modulates the intensity. Depending upon the physical process under consideration, the ST can be further specified by giving the individual contributions from various sub-channels, each of which contributes to the total scattering and can be written as $C'\left|e_{\rho\alpha} P^{(1)}_{\alpha\beta} e_{i\beta}\right|^2$, $C''\left|e_{\rho\alpha} P^{(2)}_{\alpha\beta} e_{i\beta}\right|^2$, etc. The $P^{(1)}_{\alpha\beta}$ term represents the first-order (one-excitation) ST, and the $P^{(2)}_{\alpha\beta}$ term represents the second-order (two-excitation) ST and so on. The incident and scattered electric fields of the photon is given by

$$\bar{E}_j(r,t) = \bar{E}_{j0}\bar{e}_j \exp\left(i\bar{k}_j.\bar{r} - \omega_j t\right), \tag{4.2}$$

where $j = i, s$ represents the incident and scattered wave, respectively, $\bar{e}_j$ is the unit polarization vector which is transverse to $\bar{k}_j$ (the propagation vector), and ω_j is the photon frequency. The operator $P_{\alpha\beta}$ also depends on the ion position $\bar{R}$. The operator $P_{\alpha\beta}\left(\bar{R}\right)$ can be expanded in a Taylor series in the ion displacements from equilibrium $\bar{R} = \bar{R}_0 + \bar{u}$, where $\bar{u}$ is the displacement vector. Instead of the individual $\bar{u}$ for each ion, the normal coordinate Q^j_σ can be used, and so the Taylor series is

$$P_{\alpha\beta}\left(\bar{R}\right) = P^{(0)}_{\alpha\beta}\left(\bar{R}^o\right) + \sum_{j\sigma} P^{(1)}_{\alpha\beta}\left(\bar{R}^o, j\sigma\right) Q^j_\sigma + \sum_{jj'}\sum_{\sigma\sigma'} P^{(2)}_{\alpha\beta}\left(\bar{R}^o, j\sigma, j'\sigma'\right) Q^j_\sigma Q^{j'}_{\sigma'} + \ldots. \tag{4.3}$$

© University of Pretoria

which expresses several orders of STs.

We consider only the first-order ST $P^{(1)}_{\alpha\beta}$, and its transformation properties which is the most suitable for the study of the Raman spectra in this work ($C'\left|e_{\rho\alpha}P^{(1)}_{\alpha\beta}e_{i\beta}\right|^2$). It consists of two Cartesian vectors $\bar{e}_{\rho\alpha}$ and $\bar{e}_{i\beta}$ that transform as ordinary vector $\bar{r}$:

$$\hat{g}\begin{pmatrix}x\\y\\z\end{pmatrix}=\begin{pmatrix}\text{VR}\\\text{matrix}\end{pmatrix}\begin{pmatrix}x\\y\\z\end{pmatrix}=\begin{pmatrix}V_{xx}&V_{xy}&V_{xz}\\V_{yx}&V_{yy}&V_{yz}\\V_{zx}&V_{zy}&V_{zz}\end{pmatrix}\begin{pmatrix}x\\y\\z\end{pmatrix}. \tag{4.4}$$

The vector representation is readily obtainable from CDML tables and is given in Appendix B. Since $\bar{e}_{\rho\alpha}$ and $\bar{e}_{i\beta}$ transform according to the VR, their product (Eq. (4.4)) transforms according to the KP of the VR, $\text{VR}\otimes\text{VR}$. It follows from Eq. (4.1), that $\hat{g}I=I$ and $\hat{g}I=\hat{g}\left\{C\left|e_{\rho\alpha}P_{\alpha\beta}e_{i\beta}\right|^2\right\}$. Now $\hat{g}\bar{r}=\bar{r}'_{\mu}=\sum V_{\mu\gamma}\bar{r}_{\lambda}$ is the general form and so for $\bar{r}\to\bar{e}_{\rho\alpha},\bar{e}_{i\beta}$, $P_{\alpha\beta}\xrightarrow{\hat{g}}P'_{\alpha\beta}\sum_{\lambda\mu}V_{\alpha\lambda}V_{\beta\mu}P_{\lambda\mu}$ is obtained. Microscopic theory indicates that usually for ω_j (frequency of incident laser light) away from resonance, the ST for phonons is symmetric $P_{\alpha\beta}=P_{\beta\alpha}$, which can also be confirmed by Raman spectra. Therefore, $P_{\alpha\beta}$ should be written as

$$P_{\alpha\beta}=\sum_{\lambda\mu}\left(V_{\alpha\lambda}V_{\beta\mu}+V_{\alpha\mu}V_{\beta\lambda}\right). \tag{4.5}$$

Regarding the first-order term of the Taylor series in Eq. (4.3) written as $\sum_{j\sigma}P^{(1)}_{\alpha\beta}\left(\bar{R}^o,j\sigma\right)Q^j_{\sigma}$, we now consider the transformation property of normal coordinates Q^j_{σ} given by $\hat{g}Q^j_{\sigma}=Q^{j'}_{\sigma}=\sum_{\gamma}D^{(j)}(g)Q^j_{\gamma}$, which follows from Eq. (2.1c). The j indicates the irrp of G_0 (in this case D^7_{4h} and the Γ-irrps are listed in Appendix F). Consequently, the first-order RAMs (Γ's) are contained in the symmetrized square of the VR, ie $[\text{VR}]_2$.

4.2 Raman-Active Modes of the WO_3 Phases

For the D^7_{4h} symmetry of α-WO_3, the VR is $\Gamma_{3-}(z)\oplus\Gamma_{5-}(x,y)$. Therefore, $\text{VR}\otimes\text{VR}=[\text{VR}\otimes\text{VR}]+\{\text{VR}\otimes\text{VR}\}=[\text{VR}]_2+\{\text{VR}\}_2$, and so we have $(\Gamma_{3-}\oplus\Gamma_{5-})\otimes(\Gamma_{3-}\oplus\Gamma_{5-})=[(\Gamma_{3-}\oplus\Gamma_{5-})\otimes(\Gamma_{3-}\oplus\Gamma_{5-})]+\{(\Gamma_{3-}\oplus\Gamma_{5-})\otimes(\Gamma_{3-}\oplus\Gamma_{5-})\}=[\Gamma_{3-}\otimes\Gamma_{3-}\oplus\Gamma_{5-}\otimes\Gamma_{5-}\oplus2(\Gamma_{3-}\otimes\Gamma_{5-})]+\{\text{VR}\}_2$. Using Eq. (2.3a) to obtain the symmetrized squares of the VR, we get the symmetries of the RAMs which are $2\Gamma_{1+}$, Γ_{2+}, Γ_{4+} and $2\Gamma_{5+}$. Consequently, Raman bands must be assigned by these irrps for the spectrum of D^7_{4h} phase WO_3 (see Fig. 4. 2). The frequencies ω and intensities I of the RAMs can be readily obtained from the respective Raman spectra. In a

© University of Pretoria

similar way, the RAMs for the lower symmetry space groups can be found and these calculations are shown in Appendix F. The symmetries of the RAMs for orthorhombic phase β-WO_3 are $3\Gamma_{1+}$, Γ_{2+}, Γ_{3+} and Γ_{4+}. The symmetries of the RAMs for monoclinic phase γ-WO_3 are $4\Gamma_{1+}$ and $2\Gamma_{2+}$. The symmetries of the RAMs for triclinic phase δ-WO_3 are $6\Gamma_{1+}$. Table 4.1 shows the RAMs of the experimentally observed phases and the splitting of the modes from the high-symmetry to the low-symmetry that are seen the Raman spectra. Fig. 4.1 shows the Raman spectrum of C_i^1 phase WO_3 (synthesised in this work and will be discussed in Chapter 5), and Fig. 4.2 shows the pressure evolution of the WO_3 Raman spectrum from monoclinic to tetragonal phase WO_3; $C_{2h}^5 \rightarrow D_{2h}^{13} \rightarrow D_{4h}^7$.

Table 4.1. The Raman-active modes of the experimentally observed symmetry of WO_3, and the splitting of the modes as the symmetry is lowered [a].

D_{4h}^7	D_{2h}^{13}	C_{2h}^5	C_i^1
$\Gamma_{1+} \rightarrow$	Γ_{1+}	Γ_{1+}	
$\Gamma_{4+} \rightarrow$	Γ_{2+} $\rightarrow$		
Γ_{2+}		$\rightarrow$	
Γ_{5+}			Γ_{1+}
	Γ_{3+}	Γ_{2+}	
	Γ_{4+} $\rightarrow$		

[a]It is pointed out here that the Γ_{1+} of D_{4h}^7, D_{2h}^{13}, C_{2h}^5 and C_i^1 are all independent to its respective Brillouin zone, and are only related by compatibility of their irrps.

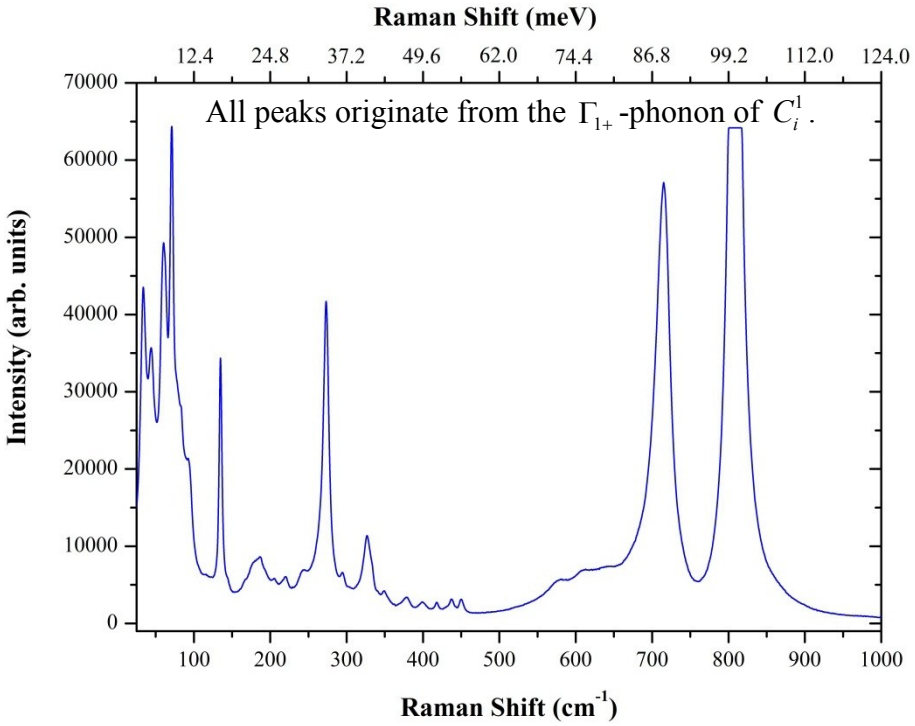

Figure 4.1. The Raman spectrum for triclinic phase WO_3 film for the wavenumber region 15-1000 cm^{-1} synthesized in this work.

© University of Pretoria

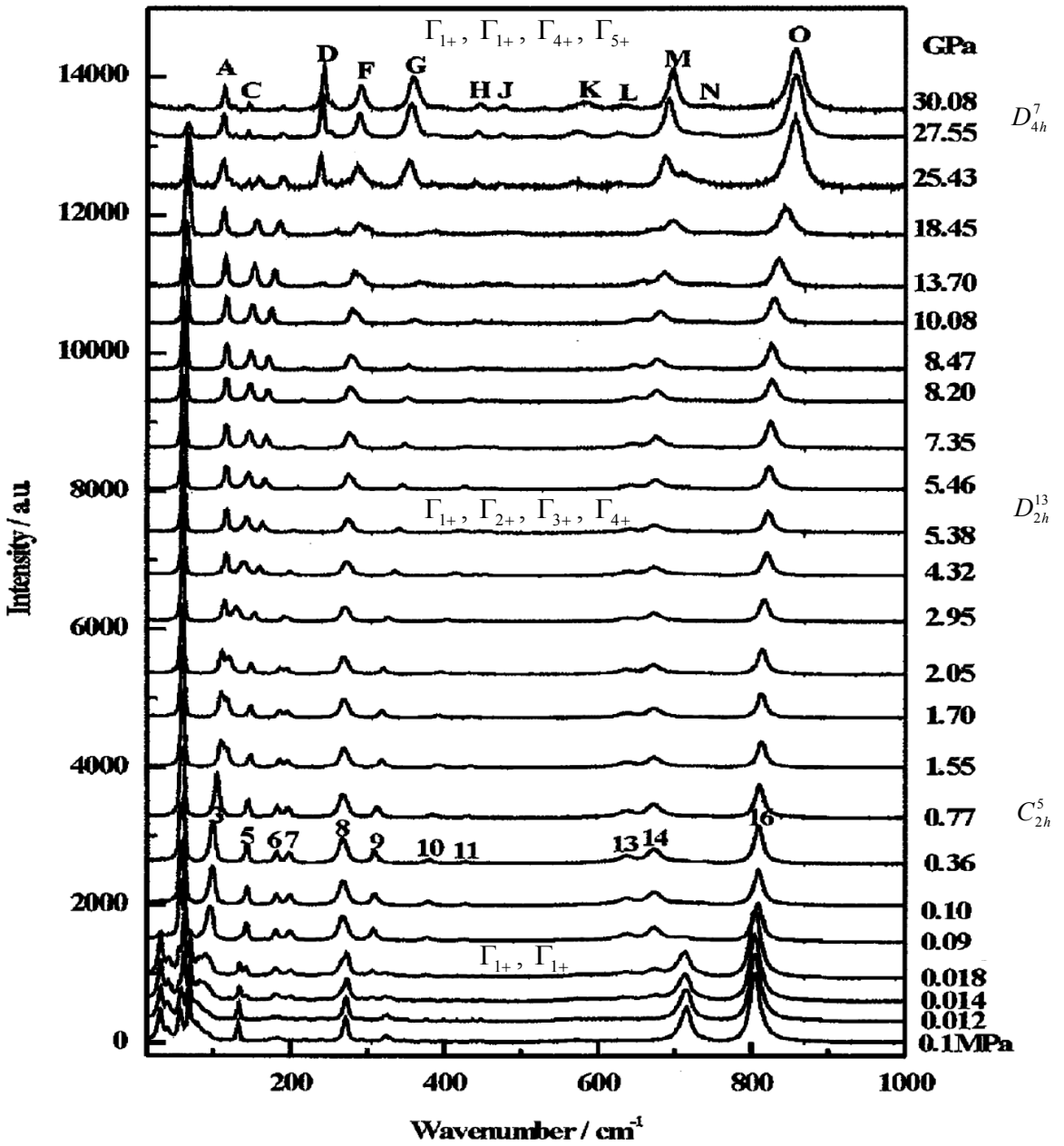

Figure 4.2. The Raman spectrum of WO_3 phases from monoclinic C^5_{2h} to tetragonal D^7_{4h} taken from Boulova *et al.* [79].

All BZs show the 800 cm^{-1} stretching vibration in the Raman spectra, and it is most likely that this vibration is caused by the Γ_{1+}-irrp of the respective BZs. The triclinic Γ_{1+} BZ is more tilted than the monoclinic C^5_{2h} BZ, and this difference is shown in the low-frequency vibrations (lattice modes) in the Raman spectra. The monoclinic BZ is shorter along the *z*-axis compared to the orthorhombic D^{13}_{2h} BZ, and this causes the elimination of one stretching vibration and the shifting of the bending modes. According to table 4.1, the two types of Raman-active phonons of the monoclinic BZ split into four Raman-active modes of the orthorhombic BZ, but this does not directly influence the number of Raman peaks seen. The orthorhombic BZ to the tetragonal D^7_{4h} BZ causes a lengthening along the *y*-axis, which causes the appearance of a stretching vibration and shifting of the bending modes [66-70].

© University of Pretoria

CHAPTER 5

Synthesis and Characterisation of WO_3

5.1 Synthesis of WO_3 films

Reactive-sputtering physical vapour deposition (PVD) was the chosen technique for the synthesis of WO_3 films. In reactive-sputtering, the atoms of the solid target precursor are physically removed and allowed to react with an appropriate gas. In this case, the target was solid pure tungsten (W), which was bombarded and allowed to react with oxygen (O_2) to give a WO_3 film. This process was carried out in the chamber of a PORTA 900 plasma unit from Plasma Electronics. The W-target is placed on a negative electrode which created an electric field in the chamber. A mixture of Ar/O_2 gas is flowed into the chamber at 500 sccm (Fig. 5.1 (a)) under vacuum, and the gas is ionised ($Ar^+/O_2^+/e^-$) at a high-power of 900 W (Fig. 5.1 (b)). The ionised gas is attracted toward the W-target due to the electric field, and bombards the target. This causes the W-atoms to become dislodged from the target and is transported towards the substrate. The atoms of W can react with O_2 during the transport stage in the plasma (Fig. 5.1 (c)) and at the substrate (Fig. 5.1 (d)). The substrate used here was an alumina (Al_2O_3) that had four Pt-contacts deposited on it (more information on this substrate is presented in Chapter 6), and a Pt-heater on the underside. The thickness of the deposited film is controlled by the deposition time, and here the deposition time was chosen to be 6 hours to give a continuous film.

5.1.1 Annealing of the as-synthesised film

The as-prepared sample was annealed in a furnace at 450^{o}C for 2 hours in air atmosphere. From Table 4.1, it is expected that the monoclinic phase exists at this temperature, and upon cooling, it is expected to be the stable phase at room-temperature. However, it is possible for the triclinic phase to exist at room-temperature as the metastable and thermodynamically favoured structure [68]. Increase in the annealing temperature shows improvement in crystal quality and a corresponding decrease in film resistance [80]. This is apparently due to the increase in oxygen vacancies and a corresponding decrease in oxygen atoms, and it is difficult for electrons to hop between oxygen vacancies [81]. Increase in the annealing temperature also causes an increase in surface roughness which increases sensitivity. However, the crystallite size increase decreases sensitivity. It was reported that film crystallization starts at an annealing temperature of 300^{o}C [82], and at 400^{o}C the films were crystalline with small grain sizes [83]. The higher annealing temperature also helps avoid drift in sensor response. Above 400^{o}C annealing temperature, there is structural rebuilding [84, 85] and the surface becomes smooth with large reconstructed domains.

© University of Pretoria

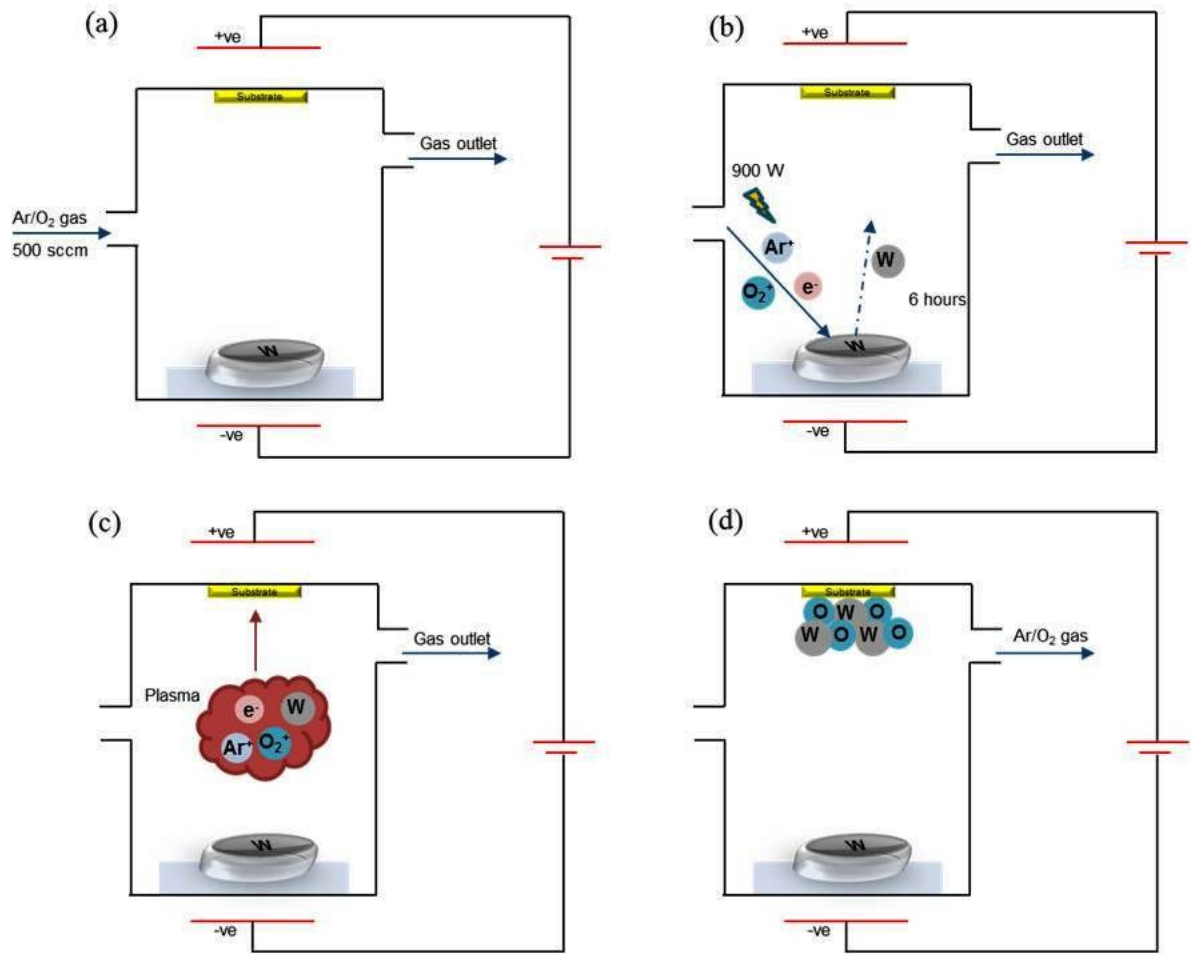

Figure 5.1. A simple schematic of the PVD process showing (a) the ionisation of the gases, (b) the attraction of the ionised gas towards the W-target due to the electric field causing W-atoms to be dislodged, (c) the generation of the reactive plasma and the reaction and transport of the atoms towards the substrate, and (d) the final synthesized WO_3 film sputtered onto the substrate.

5.2 Characterisation of the WO_3 films

The characterisation instruments used in this work are described here. SEM was carried out with a Carl Zeiss SMT Auriga™ Scanning Electron Microscope. The FIB system used was a Crossbeam® FIB Workstation with Gemini® FESEM Column and worked in tandem with the SEM system. TEM was carried out with a Jeol JEM-2100 LaB_6 Transmission Electron Microscope equipped with STEM, ED and EDX-mapping. XRD was carried out with a PANalytical X'Pert Pro X-ray Diffraction Unit with a CuK_α source outputting x-rays at a wavelength of 0.154 nm. XPS was carried out with Surface Science Instruments X-ray Photoelectron Spectroscopy chamber equipped with an ESCA M-probe high-resolution multi-channel hemispherical electron analyser with an AlK_α source outputting x-rays at 0.834 nm. Raman spectroscopy was carried out using a Horiba Jobin-Yvon T64000 Raman Spectrograph in the backscattering orientation with an argon-ion laser outputting a wavelength of 514.5 nm at a laser power of 150 mW. The Raman spectra were taken in the wavelength range 20-3000 cm^{-1}. UV/Vis spectrophotometry was carried out using a

© University of Pretoria

PerkinElmer Lambda 750S UV/Vis Spectrometer in the wavelength range 190-2500 nm. PL spectroscopy was carried out using a Horiba Jobin-Yvon iHR320 Imaging Spectrometer at an excitation wavelength of 290 nm. Resistance measurements were carried out on the film using a Keithley 2400 SourceMeter. The Keithley was connected to the four Pt-contacts on the alumina sensing substrate where the film was deposited on. The other side of the sensing substrate had a Pt-heating element which was supplied with power from an Elektro-Automatik PS-9000 power supply.

5.2.1 Topographical and Compositional techniques for investigation of the WO_3 films

5.2.1.1 Focused Ion Beam Scanning Electron Microscopy

The products from this technique show structures composed of micro-sized grains that are loosely packed together, similar to that observed and reported by Demiz *et al.* [86] using the same synthesis technique with similar parameters. The films are porous and provide more active sites for adsorption [87]. From the micrograph of the surface of the WO_3 film taken at a magnification of 10000 times shown in Fig. 5.2 (a), there are micrometric grains consisting of nano-metric crystallites. There was spaces of ~230 nm found between successive grains. The cracking on the surface show signs of residual stresses due to the annealing treatment since the substrate was not heated during deposition. The observed nano-metric crystallite could be a result of recrystallization since the temperature was well above 300°C. There is considerable amount of porosity throughout the film which could have led to the uniform cracking seen over the surface area shown in the micrographs taken at a 1000 and 2000 times magnification given in Appendix G1. With the use of XRD, an estimation of strain over the film can be determined.

From the cross-section of the WO_3 film shown in the micrograph in Fig. 5.2 (b) achieved with FIB-milling, reveals the film thickness average to be about 1.82±0.65 µm. Thin films are classified as less than 100 nm, so this film is regarded as thick. Even though the porous film is good for gas sensing, the thickness of the film reduces the surface-to-volume ratio which may decrease the sensitivity. It is also seen in this micrograph that the film moulds to the contours at the interface of the alumina substrate, so the thickness varies slightly over the film. The milling process revealed cracks as seen in Fig. 5.2 (b) in the film which result from the lattice mismatch between the substrate and film and possibly during the annealing process. It is observed that the cracking on the surface and the cracking in the bulk are not interconnected. The topmost layer of the micrograph is that of Pt which is deposited using FIB to keep the film intact during milling and cutting of the lamella. The Pt would have filled up the cracks in the bulk if the crack was continuous from the surface. The lamella is used for TEM and STEM analysis because it best preserves the film's integrity for a more intricate analysis. A micrograph of this lamella is given in Appendix G1, with a micrograph of the film cross-section taken in the Secondary Electron Mode of SEM to view the elemental contrast.

© University of Pretoria

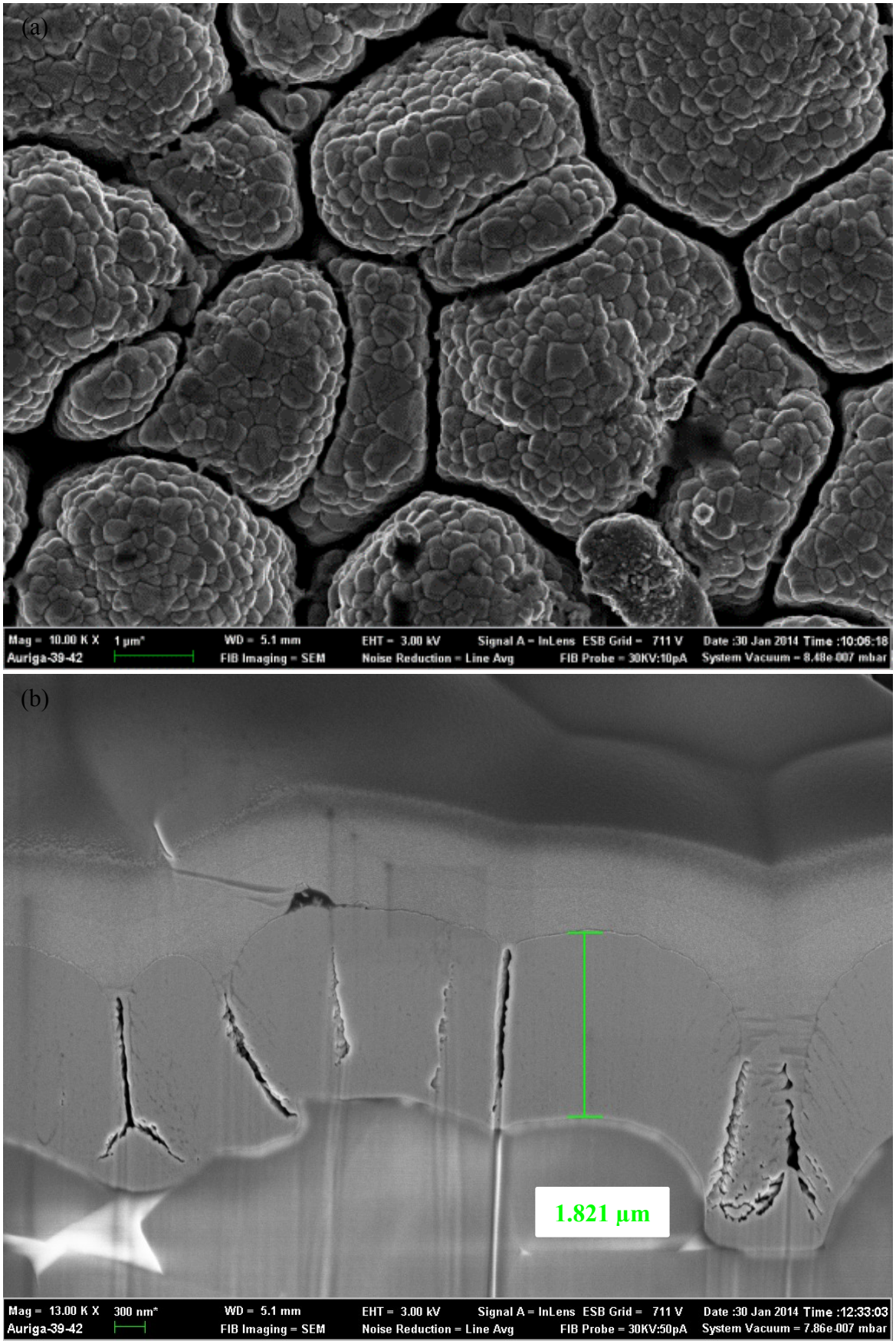

Figure 5.2. (a) A SEM micrograph taken at 10000 times magnification on the surface of the WO_3 film, and (b) a micrograph of the cross-section of the WO_3 film revealing its thickness and interface with the alumina substrate.

© University of Pretoria

5.2.1.2 Scanning Transmission Electron Microscopy

The lamella obtained from FIBSEM was analysed under STEM. A micrograph of the film taken by STEM at a magnification of 100000 times is shown in Fig. 5.3.1. (a). The corresponding EDX-mapping done over this area is shown to confirm the absence of any contaminants in the film. There is a clear distribution of tungsten and oxygen in the film and the topmost layer is confirmed to be Pt from the FIB deposition. It is clear that there is no Pt in the cracks of the bulk which confirms that the surface cracking and the cracking in the bulk are disjoined. From this micrograph, the thickness is approximately 1.213 µm which falls within the average thickness measured in FIBSEM.

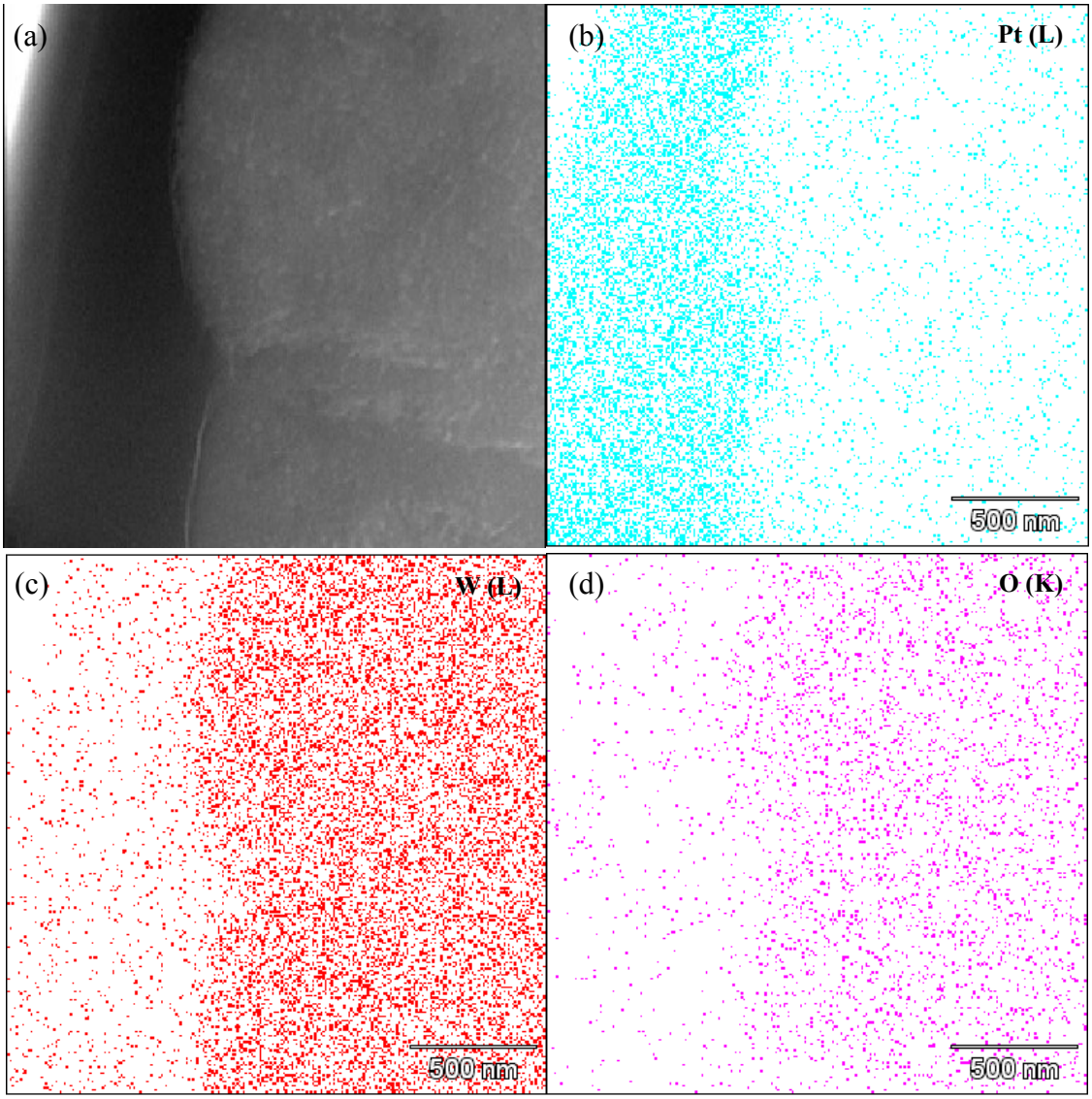

Figure 5.3.1. A STEM micrograph taken of the lamella of the WO_3 film. The EDX-mapping over the area gives an impression of the distribution of the elements in the film.

© University of Pretoria

The interplanar-spacing of the lattice can be measured at the edge of the lamella using TEM. The TEM micrograph presented in Fig. 5.3.2. (a) shows an interplanar-spacing of 0.369±0.011 nm. The SAED confirms a crystalline film and a single lattice. The other interplanar-measurements revealed interplanar-spacings of 0.385±0.12 nm and 0.375±0.011 nm, and these micrographs are given in Appendix G2. These values will be compared with the d_{hkl} from XRD to determine the amount of stress in the film and the corresponding Miller indices.

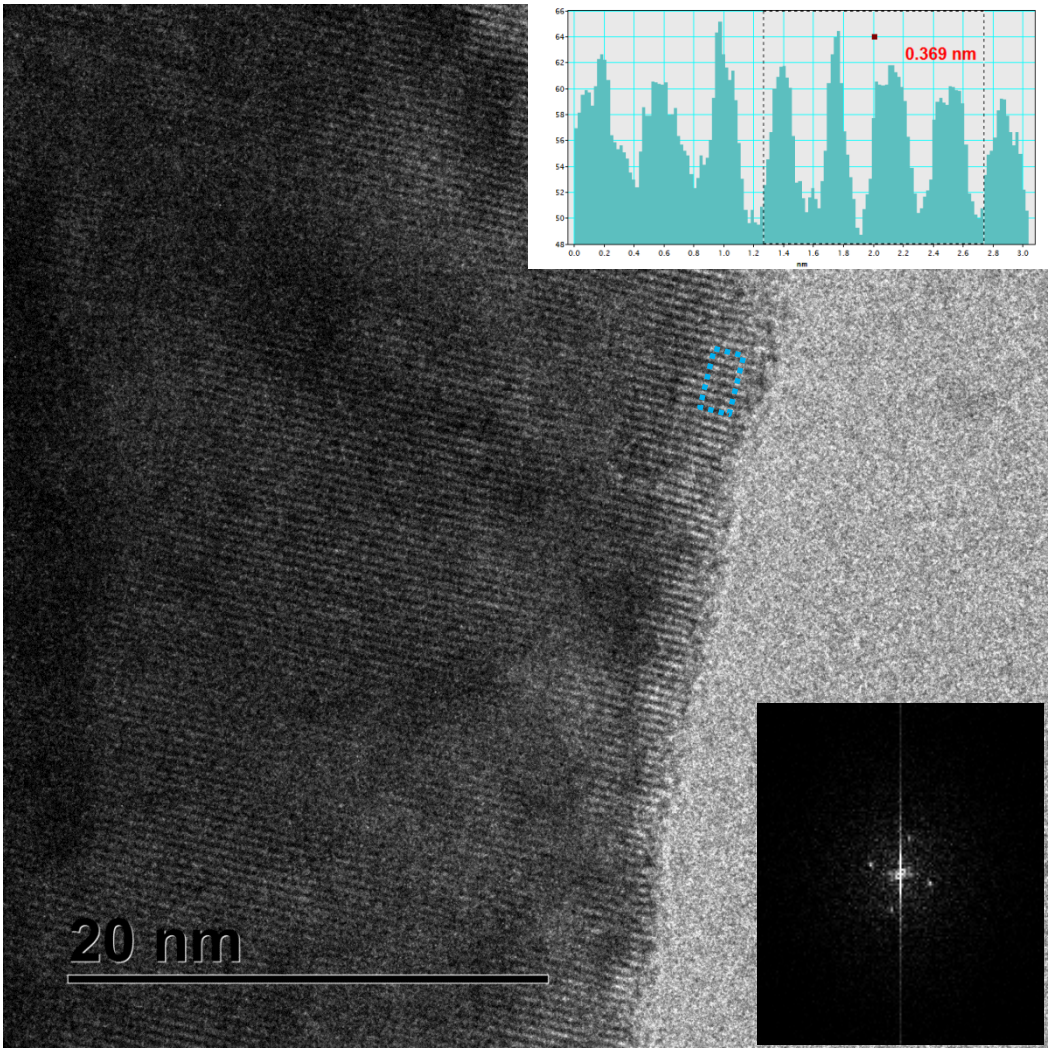

Figure 5.3.2. An HRTEM micrograph taken at 200000 times magnification on the lamella of the WO_3 film to measure the interplanar-spacing. The inset on the top of the figure shows the average interplanar-spacing while the inset at the bottom shows a selected area electron diffraction pattern of single lattice.

© University of Pretoria

5.2.1.3 X-ray Diffraction

The characteristic triplet peak centred at $2\theta = 23^{o}$ of WO_3 is observed in the diffractogram of the synthesized and annealed film as shown in Fig. 5.4. Comparing this diffractogram to the ICCD-database, the most probable crystal structure was found to be triclinic $P\bar{1}$ δ-phase WO_3 (PDF # 00-032-1395), and all peaks have been indexed accordingly. The preferred growth direction in the film is along the (020) plane. There is a slight down shift of the experimentally obtained diffraction angles when compared to the ICCD file, which implies there is uniform strain in the film. The XRD analysis confirmed the substrate to be $R\bar{3}c$-rhombohedral phase Al_2O_3 (PDF # 00-010-0173). This explains the cracking seen in the cross-section micrograph due to the lattice mismatch between the film and substrate. These strains most probably lead to the stabilization of the triclinic phase WO_3 at room temperature.

The Scherrer analysis estimates the crystallite size to be 0.67±0.05 nm, 0.69±0.04 nm and 0.40±0.06 nm from the (002), (002) and (200) diffraction peaks, respectively. This is consistent with the nano-metric crystallites in the SEM analysis. Comparing the d_{hkl} values from TEM to the ICCD file ($d_{002} = 0.384$ nm, $d_{020} = 0.376$ nm and $d_{200} = 0.365$ nm), the values are within error which signifies that the stress is not as high as anticipated. The XRD does conclude that the film is triclinic phase WO_3 and Raman spectroscopy will confirm the purity of this phase.

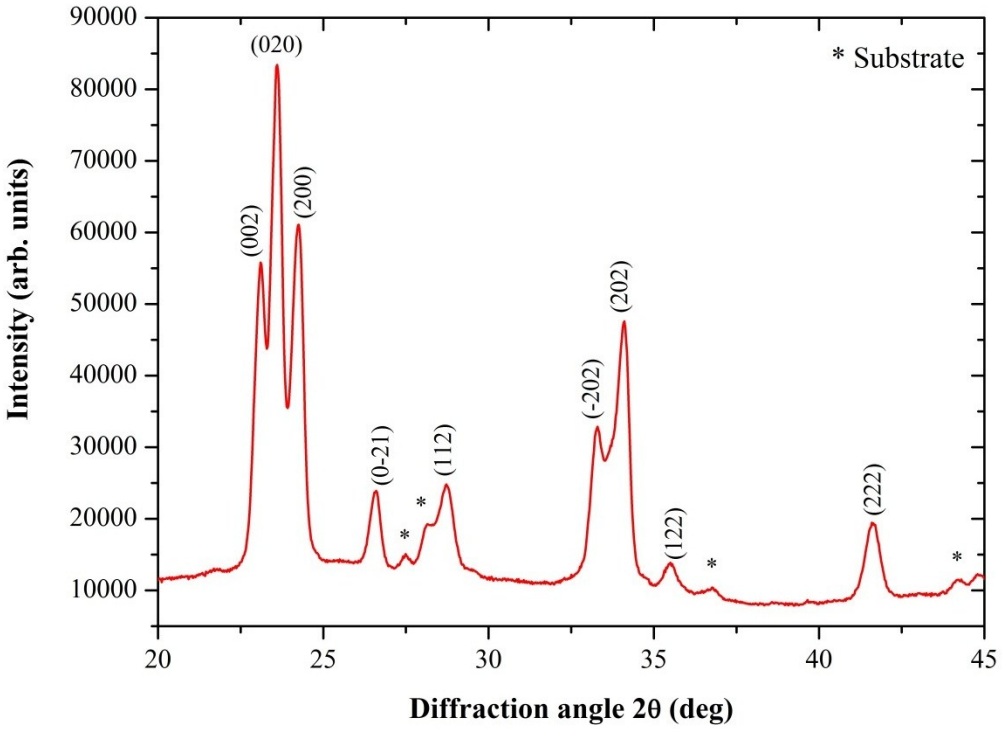

Figure 5.4. The XRD diffractogram of the annealed film that suggests the most probable phase of WO_3 is triclinic.

© University of Pretoria

5.2.1.4 X-ray Photoelectron Spectroscopy

The stoichiometry of the film is evaluated by XPS by analysing the chemical binding states of W. The peak for the W 4*f* shown in Fig. 5.5 (a) is deconvoluted to extract the relevant information. Two peaks were found centred at 35.7 eV and 37.7 eV which correspond to W $4f_{7/2}$ and W $4f_{5/2}$, respectively, corresponding to the W^{6+} state [88, 89]. Deconvoluting the O 1*s* peak in Fig. 5.5 (b), two peaks centred at 531.9 eV and 532.8 eV were found corresponding to oxygen in stoichiometric WO_3 and oxygen in adsorbed water on the surface, respectively. The oxygen of stoichiometric WO_3 forms 87% of the total oxygen content. The O/W ratio is 3±0.01, which indicates a stoichiometric WO_3 composition. A full XPS spectrum is given in Appendix G3 with its relevant peak assignments. As is common in this technique, a large carbon surface contamination was observed.

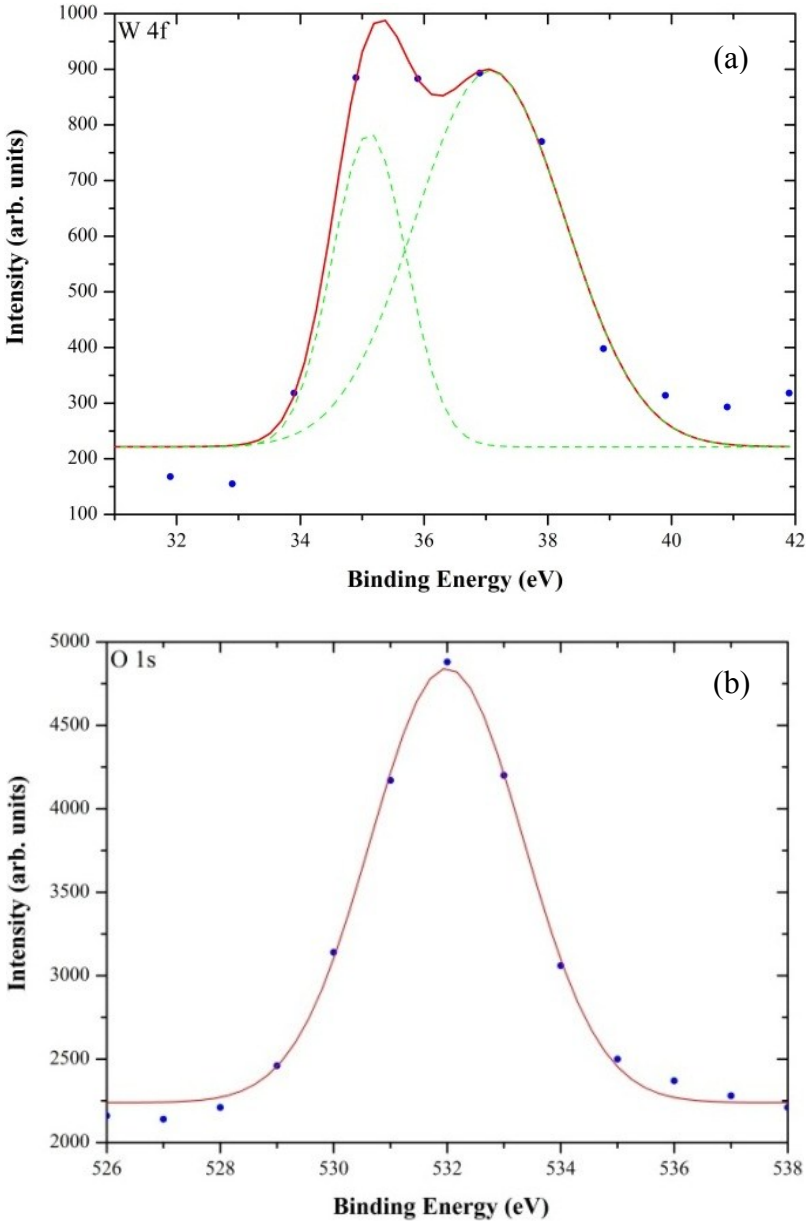

Figure 5.5. The XPS spectrum of the WO_3 thin film showing the peaks at the binding energy of (a) W 4*f* and (b) O 1*s*.

© University of Pretoria

5.2.2 Optical techniques for investigation of the WO_3 films

5.2.2.1 Raman Spectroscopy

The Raman spectrum of the annealed film is shown in Fig. 5.6. The region <200 cm^{-1} shows the lattice modes of WO_3 and can be used to identify the phase structure [90]. The region between 200-400 cm^{-1} arises from O–W–O deformation or bending modes and the region between 600-900 cm^{-1} arises from W–O stretching modes. It should be noted here that the room-temperature monoclinic phase and triclinic phase have a very similar structure and only differ by slight tilting of their O atoms about the W atom [82], as was discussed in Chapter 4. Therefore many of the vibrational properties and thus Raman peaks are similar for these two phases. The peaks in Fig. 5.6 at 135 cm^{-1}, 273 cm^{-1}, 714 cm^{-1} and 809 cm^{-1} are indicative of crystalline WO_3 network of monoclinic/triclinic phase [39]. The Raman peak at 44 cm^{-1} and the absence of the peak at 78 cm^{-1} confirms that the most probable phase of WO_3 must be triclinic [91, 92], which is in agreement with XRD. These Raman shifts are consistent with that found in bulk WO_3, which indicates that the film has small overall stress. Even though the monoclinic structure is most often found at room temperature, the triclinic structure is the thermodynamically favoured phase, and probably exists in a metastable state [68] as a consequence of the synthesis procedure. An extended wavenumber range of the Raman spectrum is given in Appendix G4 to confirm the absence of higher-order Raman modes.

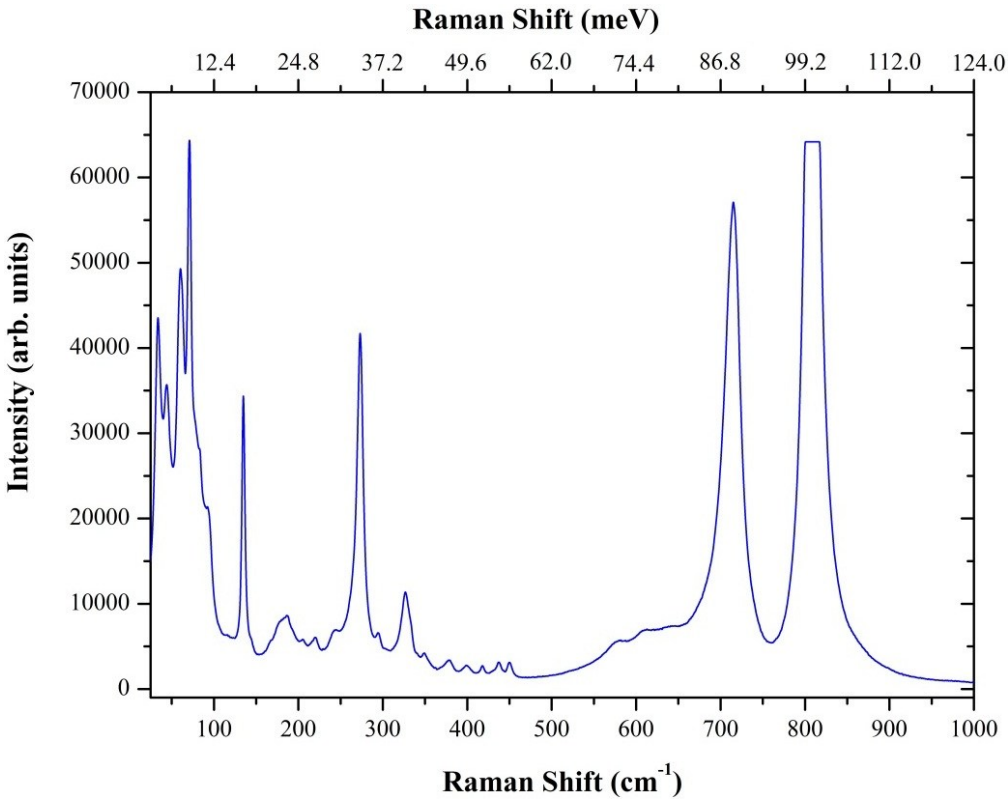

Figure 5.6. The Raman spectrum for the WO_3 film for the wavenumber region 25-1000 cm^{-1}.

© University of Pretoria

5.2.2.2 Ultraviolet/Visible Spectroscopy

WO_3 shows an average transparency in the spectral region due to a rough film and diffuse scattering. The transmission drops exponentially where the incident radiation is absorbed across the optical energy band gap E_g. The value of E_g can be estimated from the given UV/Vis spectrum in Fig. 5.7.1. The energy dependence of the absorption coefficient α (ratio of the absorbance of the film by the film thickness) for a semiconductor near the absorption edge is given by $(\alpha h\nu)^{1/r} = A(h\nu - E_g)$ [93], where A is the probability of a transition. A direct transition requires only that photons excite electrons, whereas indirect transitions require energy from the crystal lattice (phonons) [94]. The electron transitions obey well-defined selection rules, and so $r = 1/2$ for direct and allowed transitions, $r = 3/2$ for direct and forbidden transitions, $r = 2$ for indirect and allowed transitions and $r = 3$ for indirect and forbidden transitions. In indirect transitions, a phonon is either emitted or absorbed [95]. In WO_3, the E_g corresponds to electronic transitions from the top of the valence band (formed by filled O 2*p* orbitals) to the bottom of the conduction band (formed by empty W 5d orbitals) [96]. The non-linear region found at energies $< E_g$ is known as Urbach's tail, and is related to low-frequency acoustic modes. A plot of $(\alpha h\nu)^{1/r}$ vs $h\nu$ is linear at the band edge and the intercept of the line on the abscissa (at $(\alpha h\nu)^{1/r} = 0$) gives the optical absorption edge energy E_g. For WO_3 of the lower-symmetry phase, there is still a debate as to whether the band gap is direct or indirect. According to the band structure of triclinic phase WO_3, the maximum of the VB is either at high-symmetry point Γ or *Z* since their energies are almost the same, and the minima of the conduction band is at point Γ [88]. To clarify if the band gap is either direct or indirect, we can verify this experimentally by setting $r = 1/2$ and $r = 2$ for a film thickness of 1.82 µm and plot $(\alpha h\nu)^{1/r}$ vs $h\nu$ to check which plot shows a linear region. It was found that $r = 1/2$ showed the linear region as seen in Fig. 5.7.2, which means that the transition is direct and allowed from point Γ in the valence band to point Γ and in conduction band. The extrapolation of the linear part to the *x*-axis gives an estimated optical band gap of 3.19±0.1 eV, which is similar to that found in literature for triclinic phase WO_3 relative to the film thickness [97]. As the phase changes towards the more cubic form, the band gap decreases and the energy difference between the Γ-points decreases [88]. This decrease in band gap energy and the direct band gap is yet to be related to the gas sensing mechanism to explain the preferred gas or selectivity to WO_3 phase that was presented in Table 1.1.

© University of Pretoria

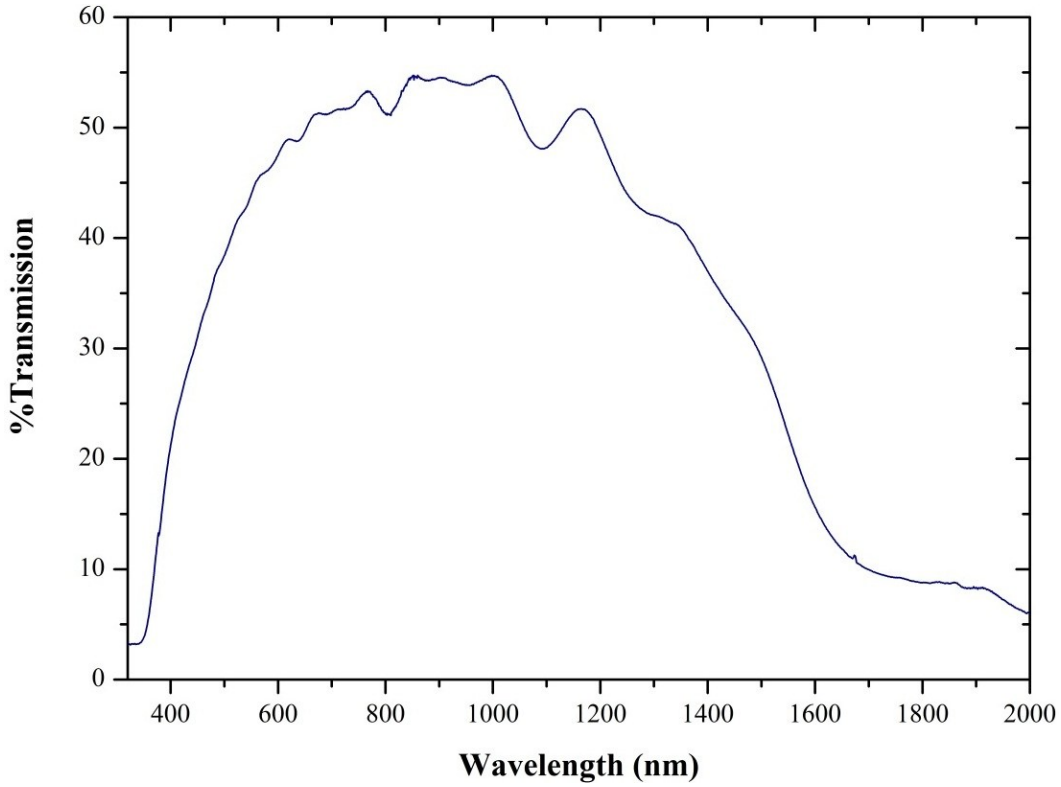

Figure 5.7.1. The UV/Vis spectrum of the WO_3 film showing typical coloration effect and an average transmission in the spectral region.

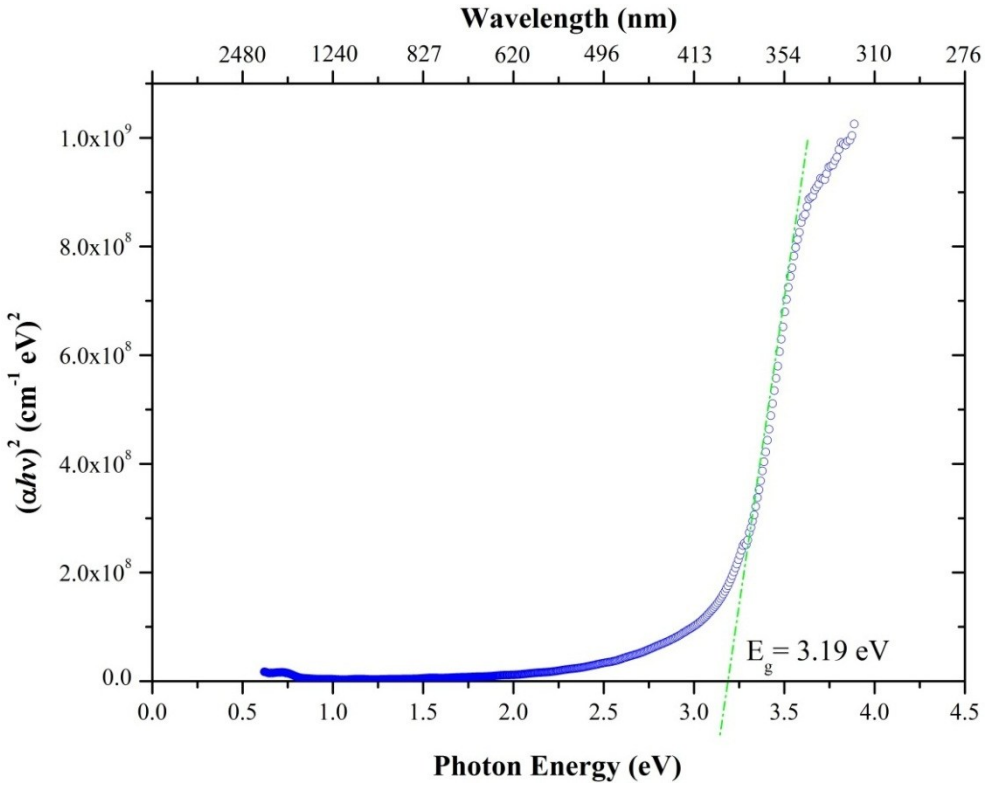

Figure 5.7.2. The plot of $(\alpha h\nu)^2$ vs $h\nu$ used to estimate the direct optical band gap of WO_3 film of thickness 1.82 µm. E_g was found to be 3.19±0.1 eV.

© University of Pretoria

5.2.2.3 Photoluminescence Spectroscopy

The PL spectrum of the WO_3 film is shown in Fig. 5.8 for an excitation wavelength of 290 nm. It is believed that the "smaller" ripple peaks in Fig. 5.8 at *a* (2.91 eV) and *b* (2.93 eV) are phonon replicas. Similarly, the peaks labelled *c* (3.00 eV), *d* (3.02 eV), *e* (3.04 eV) and *f* (3.06 eV) as well as *g* (3.12 eV) and *h* (3.14 eV) are also phonon replicas with all having an energy difference of 23 meV between respective peaks. This 23 meV corresponds to the Raman peak or phonon at 135 cm^{-1} in Fig. 5.6 above. The first broad peak centred at 2.92 eV is most likely due to oxygen vacancies or defects in the WO_3 lattice. These defects can trap an electron or hole to form a localized defect state, and when the electron of the defect state in the conduction band is excited to the hole in the valence band [98], the electron-hole (exciton) radiative recombination emission is viewed in the near UV region [99]. This peak is broad due to room-temperature measurement which increases the electron-phonon interaction, making it difficult to observe the exciton. The second broad peak centred at 3.12 eV which is very close to the estimated optical energy band gap E_g found in the previous section with UV/Vis spectroscopy which represents a band-band transition. This reiterates the point that the peak at 2.92 eV belongs to the exciton radiative recombination energy since this energy is known to be slightly less than E_g ($\Delta E = 0.2\,\text{eV}$). The slight difference in E_g between UV/Vis and PL spectroscopy could stem from the average film thickness used in the estimation in the previous section. The peak labelled *i* (3.21 eV) and the broad peak centred at 3.42 eV could be due to other crystal defects and impurities common in WO_3 [100]. The alumina substrate did not contribute to the PL spectrum. A full energy range of the PL spectrum is given in Appendix G5.

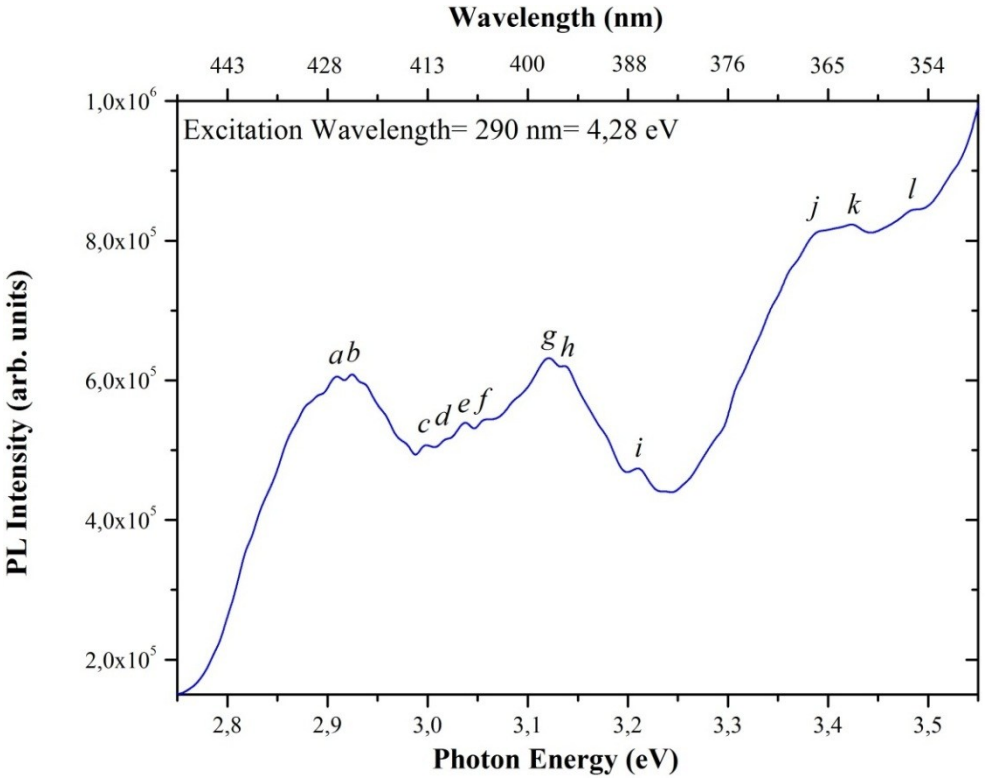

Figure 5.8. The room-temperature PL spectrum of the WO_3 film in the energy range 2.75-3.55 eV.

© University of Pretoria

5.2.3 Electrical technique for the investigation of the WO_3 films

5.2.3.1 Resistance as a function of Temperature

There are usually three contributions to the overall film resistance, ie., the bulk, the grain boundary and the electrode interface. The resistance of the film depends on the oxygen partial pressure, the thermal activation energy for the carrier generation, the diffusion, film thickness and grain size [101]. It is expected for this semiconductor that the resistance decreases exponentially as temperature increases according to the dependence expressed as $R = R_0 e^{\kappa/T}$ where κ is the thermal resistance coefficient. This relationship is shown in Appendix G6 for a plot of R vs T. From the Arrhenius equation for conductivity σ given by $\sigma = \sigma_0 \exp(E_a / k_B T)$, the activation energy of the film, which is the minimum amount of energy required to initiate a particular process can be estimated. Note, that the oxygen partial pressure was kept constant. The plot of $\ln(\sigma)$ vs $1000/T$ can be made as is shown in Fig. 5.9, and there are three gradients that can be extracted multiplied by Boltzmann's constant (8.617×10^{-5} eV K^{-1}). The activation energy E_a for the temperature regions 2.1-2.3 K^{-1}, 2.3-2.9 K^{-1} and 2.8-3.3 K^{-1} are 0.21±0.03 eV, 0.83±0.05 eV and 0.17±0.03 eV, respectively. These activation energies could correlate to the different adsorbed oxygen species on the surface due to temperature. It is known that oxygen can behave as an electron acceptor state which lies within the band gap of the oxide and located at the material surface [101].

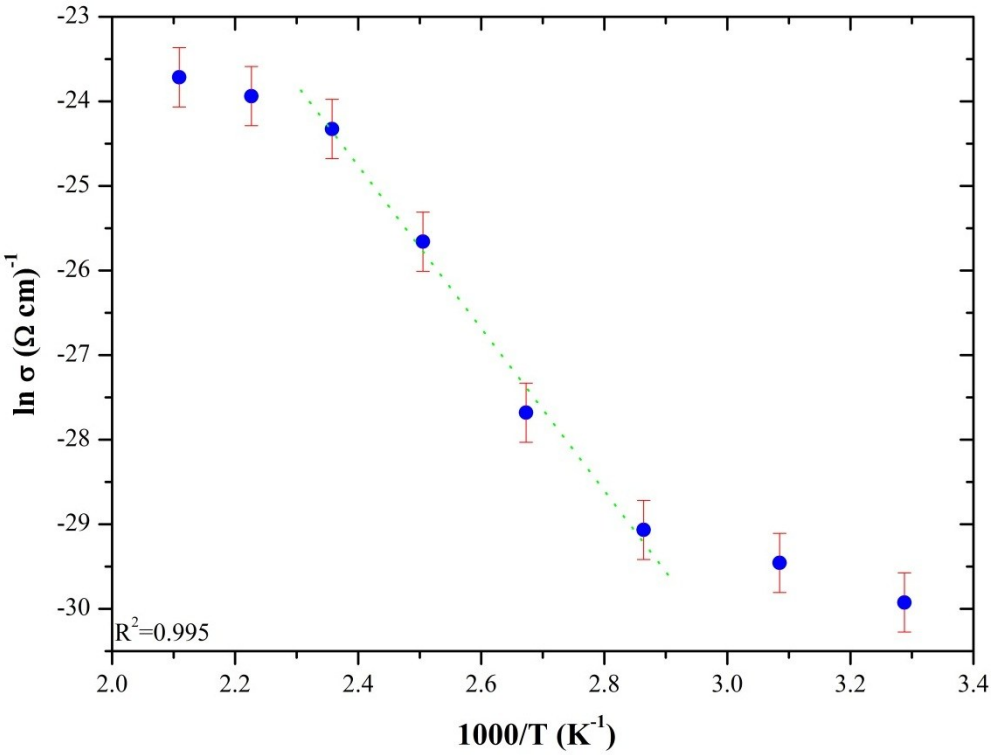

Figure 5.9. The Arrhenius plot of $\ln(\sigma)$ vs $1000/T$ used to calculate the activation energy of the WO_3 film.

© University of Pretoria

CHAPTER 6

Gas Sensing of WO_3

6.1 The Working Principle of WO_3 as a Gas Sensor

The working principle is addressed here for the unmodified WO_3 resistive gas sensor. The main parameters influencing sensor performance are the structural properties and the chemical composition of the WO_3 film. WO_3 is an *n*-type semiconductor in which charge transport results from mobile electrons, as opposed to *p*-type semiconductors such as CoO where holes are responsible for charge transport [102].

The active sensing element shown in Fig. 6.1 (a), consists of four Pt-electrodes (emulating a four-point probe) with a 1 mm spacing between electrodes on an alumina (Al_2O_3) substrate. The bottom of the substrate and electrodes were masked during deposition, and the WO_3 was deposited by the technique described in section 5.1. The as-deposited film appeared light yellow, and after the annealing step, the pale-yellow film which is indicative of WO_3 is visible on the substrate as seen in Fig. 6.1 (a). The measured area of the film was ($0.6\,\text{cm} \times 1.6\,\text{cm}$) 0.96 cm^2 and the volume of the film is thus 1.75×10^{-4} cm^3. On the reverse and underside of the substrate is the Pt-heating element shown in Fig. 6.1 (b) that could heat the sensor layer up to 400°C. The film is continuous over the four Pt-electrodes, which is used to measure the change in resistance/resistivity or sensor response. The measured resistivity includes the contributions from the bulk, the grain boundary and the electrode interface as was discussed in section 5.2.1.1. Fig. 6.1 (c) reveals the microstructure of the WO_3 sensing layer and is associated with a transducer function which depends on the ability of the film to transport electrons through grain boundaries and the Schottky barrier. The particle size and porosity play a pivotal role in the transducer function. The gas interaction with the surface of the WO_3 film represented in Fig. 6.1 (d) involves the corresponding receptor function which causes a change in the electrical resistance of each grain. The receptor function is the ability of the WO_3 surface to interact with the target gas, which is influenced by the surface properties such as oxygen vacancies. This change in electrical resistance on the molecular level can be transduced and measured macroscopically via the Pt-electrodes as the change in resistivity of the entire layer. It is more complete to present the sensing data of films in terms of resistivity ρ or conductivity σ which takes into account the width W and thickness t of the film, as well as the length L of the film (which is taken to be parallel to the electrodes). The resisitivity is given by

$$\rho = \frac{1}{\sigma} = \frac{RWt}{L} \text{ ohm cm}. \qquad (6.1)$$

© University of Pretoria

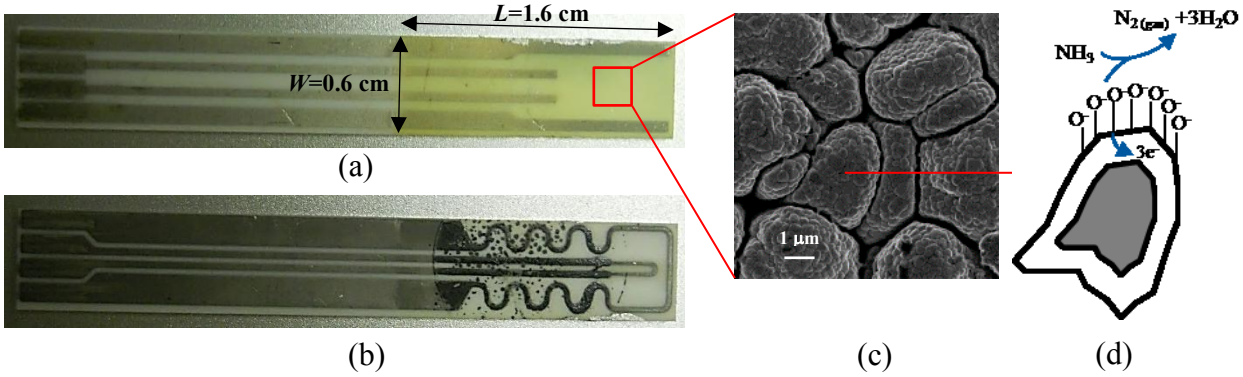

Figure 6.1. (a) The alumina substrate with the annealed WO_3 film on the four Pt-electrodes, (b) the underside of the substrate with the Pt-heater, (c) the SEM micrograph of the film showing the microstructure of the film and (d) the schematic of NH_3 target gas interaction with adsorbed oxygen on a grain of the film.

6.2. The WO_3 film Sensing Measurement towards NO_2 and NH_3 gas

In the gas-sensing set-up (see Appendix G7), the electrical measured input/output and the gas-flow meters are controlled, monitored and recorded with a LabView program. The sensing-substrate was placed inside a closed chamber, and the total volume of gas that was injected in via the inlet directly onto the WO_3 film was 200 sccm. The gas was evacuated via an exhaust outlet positioned behind the substrate in the closed chamber. The initial/maximum concentration of the NO_2 target gas was 20 ppm, and the initial concentration of the NH_3 target gas was 500 ppm. These gases were diluted with dry synthetic air to vary their concentrations for measurements, and the relative flow rates are given in Table 6.1. Synthetic dry air was also used to prepare the surface of WO_3 and clean the surface of target gas before another concentration of target gas was flowed in. It was not possible to achieve equal concentrations of target gases for comparisons due to the large difference in starting concentrations.

Table 6.1. The respective flow rates of the gases used to achieve the required concentrations and dilutions starting with 20 ppm NO_2 and 500 ppm NH_3.

NO_2 concentration (ppm)	NO_2 flow rate (sccm)	Air flow rate (sccm)		NH_3 concentration (ppm)	NH_3 flow rate (sccm)	Air flow rate (sccm)
5	50	150		125	50	150
10	100	100		250	100	100
15	150	50		375	150	50
20	200	0		500	200	0

6.2.1 The WO_3 film Sensing Performance towards NO_2 and NH_3 gas

Analysing the performance of the WO_3 film at an operating temperature of 30°C and 100°C towards NO_2 in Fig. 6.2.1 (a) and Fig. 6.2.2 (a), it can be seen that there is a better signal-to-noise ratio at 100°C. This could be due to an increase in electrons in the conduction band or Fermi level, or the higher temperature provided activation energy for the reaction at the

© University of Pretoria

surface, and these factors can decrease sensor signal drift. It could also be possible that more molecular O_2^- species are present at 100°C whose reaction with NO_2 has a better signal response.

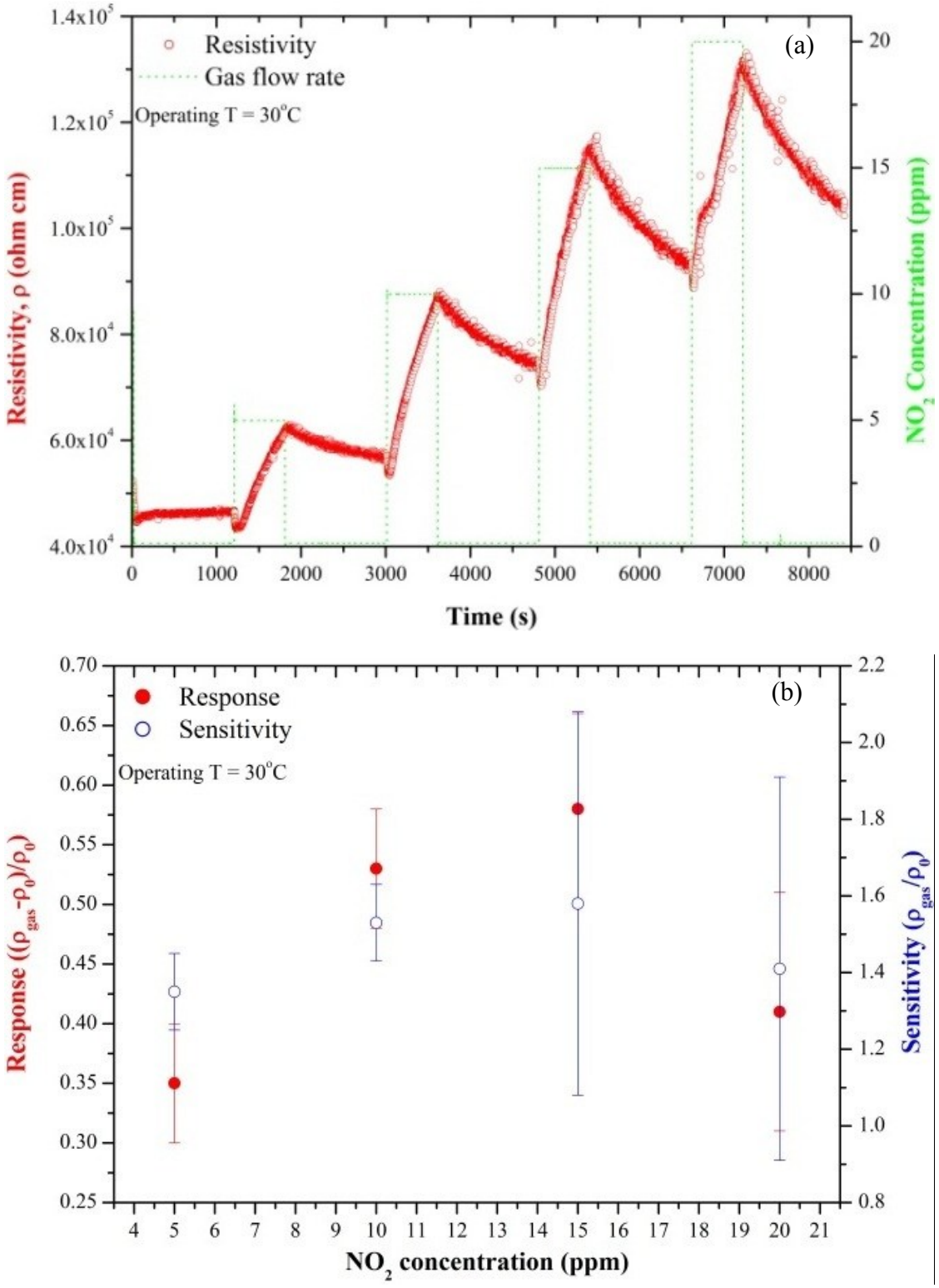

Figure 6.2.1. (a) The resistivity change of the WO_3 film as a function of NO_2 concentration at 30°C, and (b) the response and sensitivity of the WO_3 film as a function of NO_2 concentration at 30°C.

© University of Pretoria

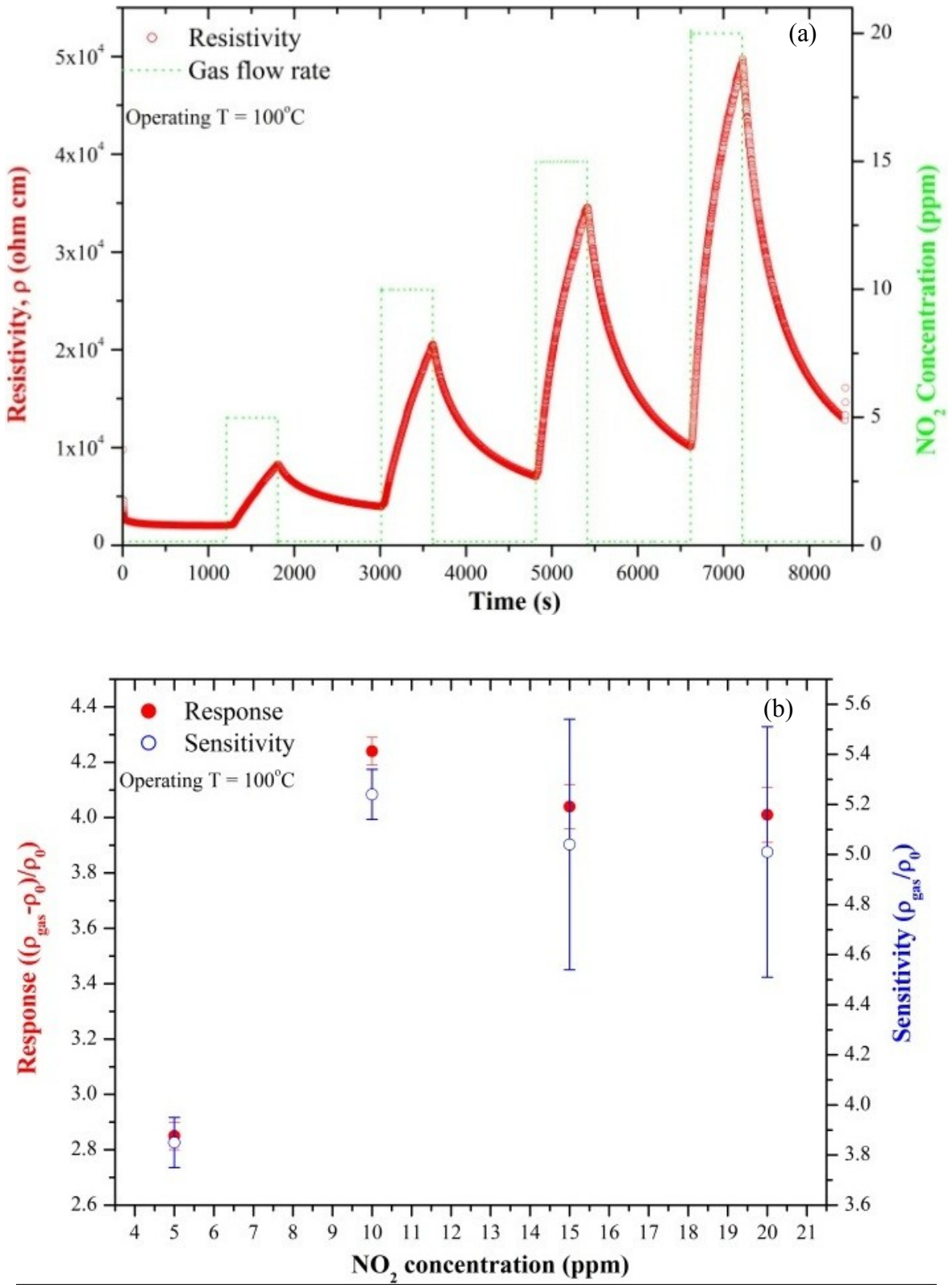

Figure 6.2.2. (a) The resistivity change of the WO_3 film as a function of NO_2 concentration at 100°C, and (b) the response and sensitivity of the WO_3 film as a function of NO_2 concentration at 100°C.

At 30°C, upon first exposure of NO_2 target gas, there is a drop in resistivity which implies an increase in the electron density in the film. According to XPS, there is 13% of surface oxygen, and the drop in resistivity could be due to NO_2 sweeping off physisorbed surface

© University of Pretoria

oxygen since it is assumed that there is probably less chemisorbed species due to lower energy. The removal of oxygen causes an increase of electrons in the film. Thereafter, the NO_2 attaches to the surface and removes electrons as stated in Eq. 1.3 (b). It can also be seen by the upward trend of the curve with respect to the baseline that the film does not saturate nor recover. More time was allowed for the film to reach saturation and the baseline, but the outcome was the same. The lack of saturation did not seem to be temperature-dependent because the slope of the curves for the different concentrations at both temperatures is similar. It is also unlikely that the gas molecules are being trapped in the porous film since the spaces between grains are large. This could mean that the triclinic WO_3 structure is responsible for the low reactivity and lack of saturation. The recovery time is improved at the higher temperature, which means more energy is required to dislodge the gas molecules from the film. The higher temperature drastically improves response and sensitivity, and this could mean that the increased energy allows electrons to overcome the potential barrier at the grain boundary and Schottky contacts. It could also mean that the molecular O_2^- species is increased at 100°C and correspondingly more electrons are moved out of the film which leads to higher sensitivity and response. The lack in linearity with target gas concentration is due to the film surface not being cleaned or recovered. Since the gas did not saturate the film, the response time and recovery time could not be calculated. However, it is pointed out here that the resistivity started to increase after ~80 s of NO_2 exposure at the 30°C operating temperature, and ~40 s of NO_2 exposure at the 100°C operating temperature, and so the higher temperature provided more energy to overcome potential barriers and activate a surface reaction. It can be concluded that a higher operating temperature improved performance of pure WO_3 film towards NO_2 gas as predicted by the sensing mechanism and literature. It should be noted here, that monoclinic phase exhibits higher sensitivity towards NO_2 when compared to our triclinic phase of similar structure and composition [30]. The main difference between the monoclinic and triclinic phase is a decrease in band gap, and thus the Fermi level. So this could imply that there is an optimum band gap of the material towards sensing a particular gas, and this needs to be incorporated into the sensing mechanism when addressing selectivity.

Even though the sensitivity increases with temperature, there is still a lack of saturation of the NO_2 gas. The film recovery from the adsorbed gas is not greatly improved by the increase in temperature as expected. This result is attributed to the surface coordination of the triclinic phase WO_3 film. From the analysis of the film surface in the previous chapter, it was found that the film was thick and consisting of micrometic grains composed of nanometric crystallites with uniform strain. PL spectrophotometry suggests the presence of oxygen vacancies on the surface. It is believed that the NO_2 adsorbs in the oxygen vacancies causing the extraction of electrons from the surface which is the measured signal observed. However, the transport properties of the thick film, the large grains with space barriers and the crystal orientation hinder the complete saturation of the film through the surface. The NO_2 that adsorbs in the oxygen vacancies bind strongly to the film, and are even chemisorbed or catalytically converted by the tungsten in the lattice, and this makes it difficult for the gas to be swept off and out of the surface.

© University of Pretoria

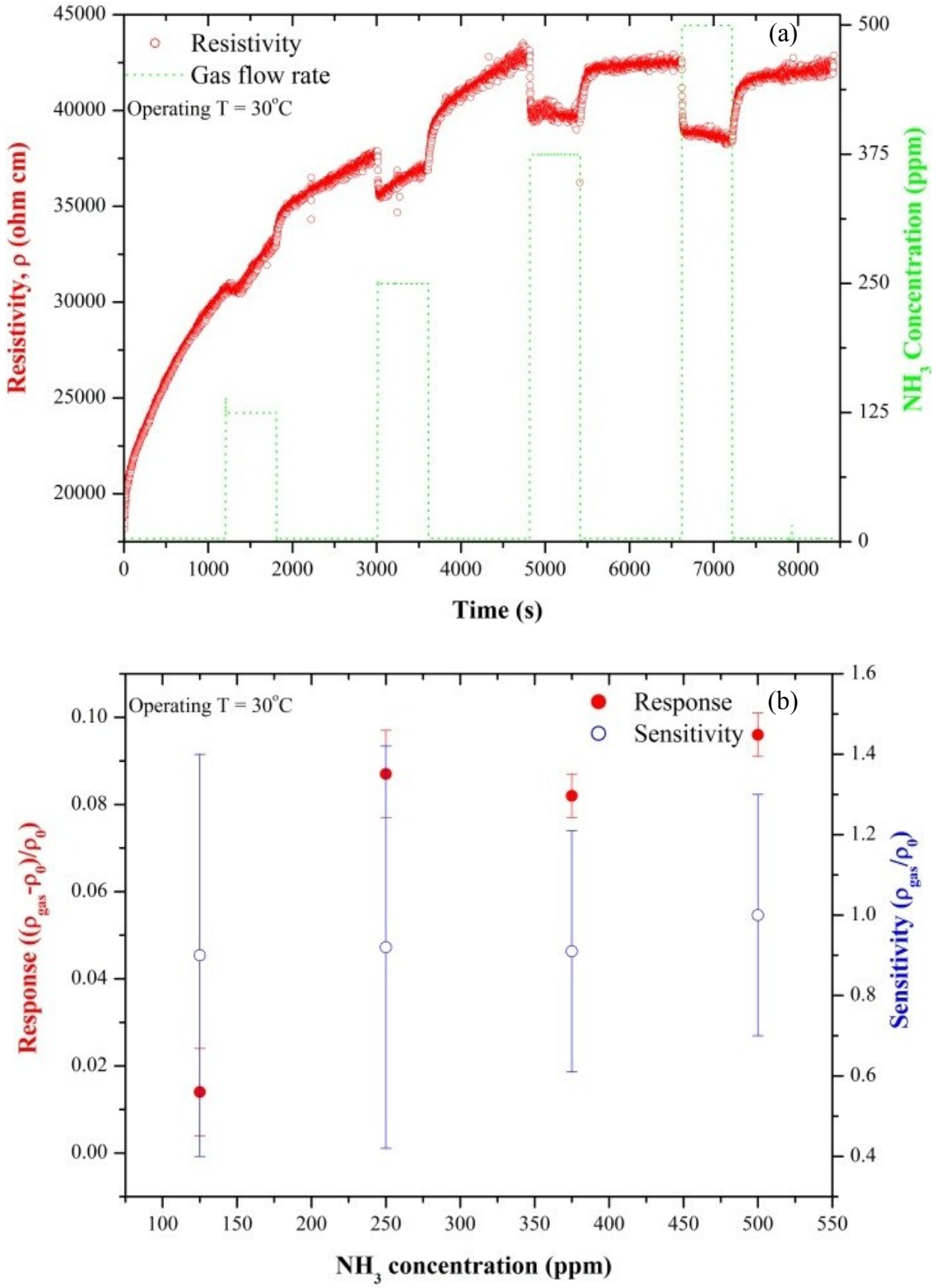

Figure 6.2.3. (a) The resistivity change of the WO_3 film as a function of NH_3 concentration at 30°C, and (b) the response and sensitivity of the WO_3 film as a function of NH_3 concentration at 30°C.

© University of Pretoria

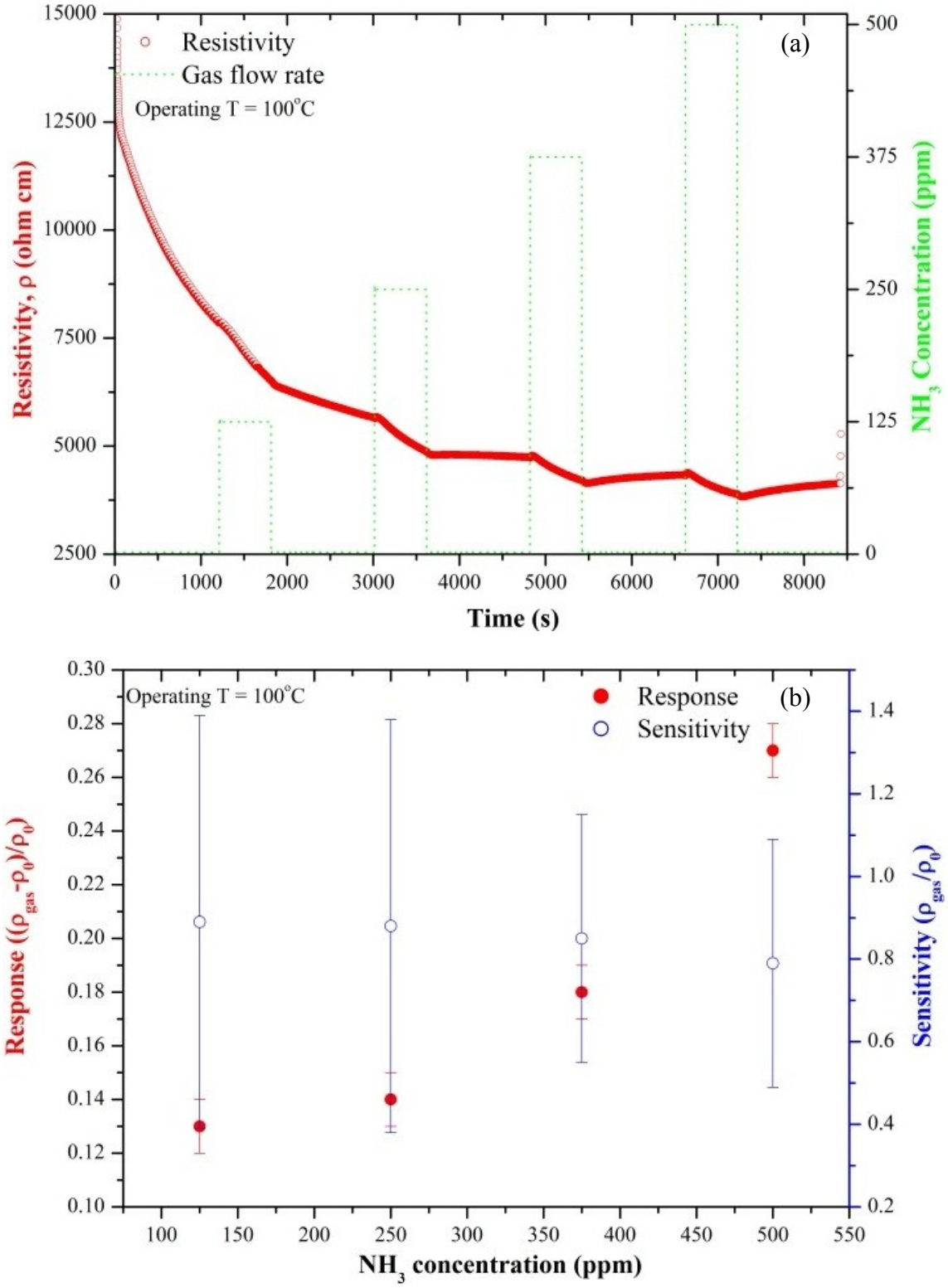

Figure 6.2.4. (a) The resistivity change of the WO_3 film as a function of NH_3 concentration at 100°C, and (b) the response and sensitivity of the WO_3 film as a function of NH_3 concentration at 100°C.

Analysing the performance of the WO_3 film at an operating temperature of 30°C and 100°C towards NH_3 in Fig. 6.2.3 (a) and Fig. 6.2.4 (a), it is again seen that there is a better signal-to-noise ratio at higher temperature. Thus, it is very likely that the higher temperature increases the electrons in Fermi level instead of providing activation energy for the reaction at the

© University of Pretoria

surface because the reactivity is lower at the higher temperature. It is unclear why the resistivity of the film showed a constant baseline increase at 30°C and decrease at 100°C. Even upon repetition of experiments with this reducing gas, the same trend was seen, and so it appears to be a result of the film's triclinic structure and composition. This was corrected for in the response and sensitivity estimations in Fig. 6.2.3 (b) and Fig. 6.2.4 (b). The film showed a higher reactivity to NH_3 at lower temperatures than at higher temperatures. This could confirm that there is more physisorbed oxygen species on the surface and a less negative surface potential at 30°C, and so the NH_3 readily donates its electrons into the surface, whereas the higher temperature causes more chemisorbed molecular O_2^- species and thus a more negative surface potential which would prefer not to take electrons from the reducing NH_3. Due to the low reactivity at higher temperatures, there is linearity in the response since the surface is clean. Again saturation and recovery of the film could not be reached even with NH_3 target gas, so it is pointed out here that the resistivity started to decrease after ~13 s of NH_3 exposure at the 30°C operating temperature, and ~80 s of NH_3 exposure at the 100°C operating temperature. This gives an idea of the surface species at the different temperatures and an insight into the sensing mechanism. Despite the NH_3 concentration being 25 times more than the NO_2 concentration, the sensitivity of the WO_3 film towards NO_2 is much higher. This confirms the discussion in section 1.2 that WO_3 has high sensitivity towards oxidizing gases even at low temperatures. However, it can be concluded here that the pure WO_3 of this particular triclinic phase, together with its composition and structure, is not ideal for sensing these particular gases and may show better performance to other target gases.

To test the cross-sensitivity and selectivity of the as- synthesized WO_3 film to these two gases, these gases where allowed to flow simultaneously onto the clean film surface with the concentration of NH_3 (100 ppm) being 10 times more than that of NO_2 (10 ppm). This result is shown in Fig. 6.4. At 30°C, the film sensitivity was 1.75 which increased from the pure NO_2 sensitivity of 1.53 which is probably a consequence of the surface being cleaned before the gases interacted with the surface. However, the presence of NO_2 at 30°C appeared to block the NH_3 from reacting with the surface. At 100°C, the sensitivity decreased from 5.24 to 2.48, which means the NO_2 reaction with the WO_3 film surface is competing with the reaction of the NH_3 with the surface. The selectivity was defined in section 1.3 as the ratio of sensitivity towards interfering gas to the sensitivity towards the target gas. The selectivity was found to be 0.65 and 0.19 for 30°C and 100°C, respectively, and so selectivity of this film is favoured at lower temperature.

To curb the set-back of recovery time and surface cleaning of the film, especially at lower temperatures, the use of light (ultraviolet+red+green+blue LEDs) was used to dislodge adsorbed NO_2 gas molecules from the film surface [103]. This is seen in Fig.6.5, where the recovery time was 15 min when light was used at 30°C as opposed to the film not recovering at all. The increase in energy and wavelength of the light breaks the bonds between the NO_2 gas and film surface. This might not fix the saturation of the film, but it should improve

© University of Pretoria

linearity with the concentration of gas even at room-temperature by cleaning the film surface of the target gas.

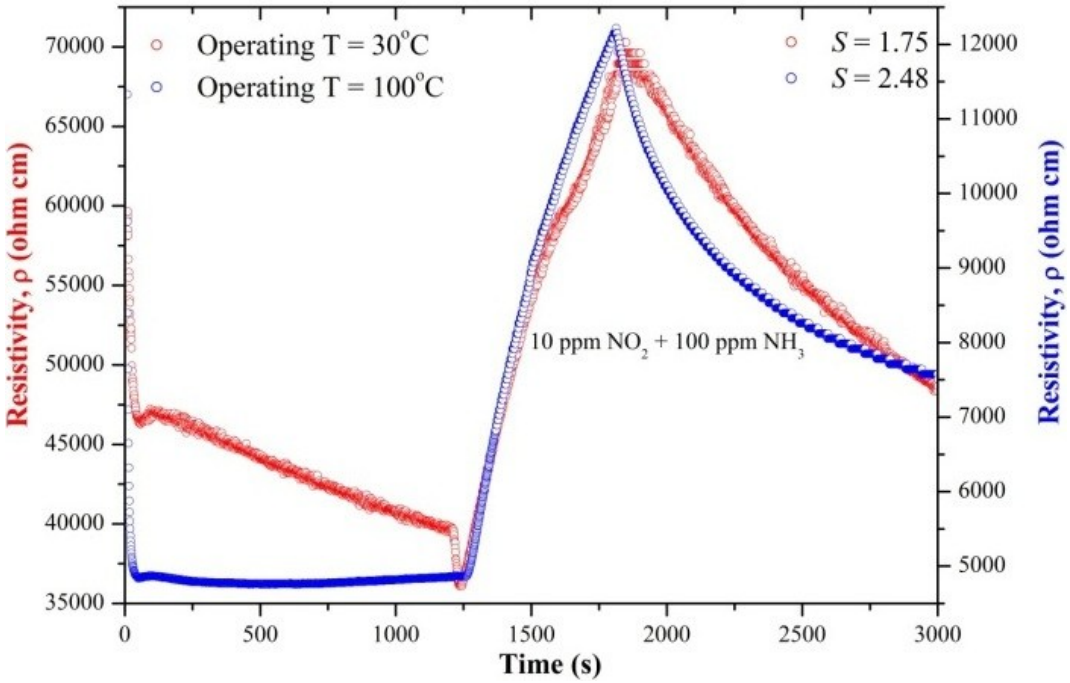

Figure 6.4. The resistivity change of the WO_3 film for simultaneously flowing 10 ppm NO_2 and 100 ppm NH_3 at 30°C and 100°C.

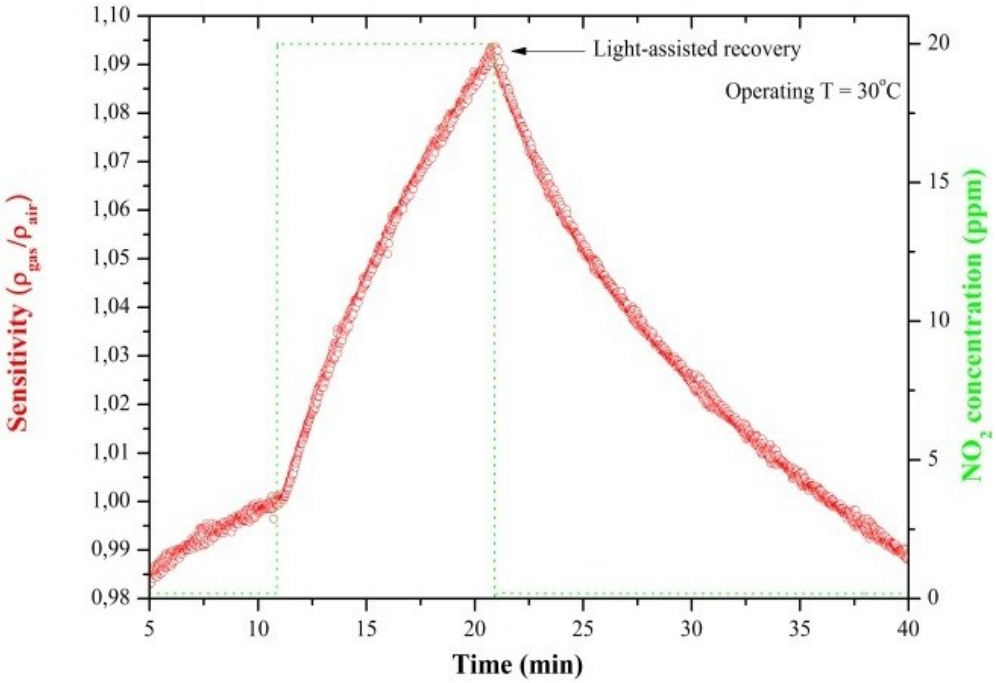

Figure 6.5. Light speeds up the recovery time of the WO_3 film by removing adsorbed NO_2 gas off the surface at 30°C.

© University of Pretoria

CHAPTER 7

Conclusion and Future Work

Amongst the various types of gas detectors and sensors used at mineshafts, the conductometric semiconductor senor offers the best gas sensing capabilities in that environment. However, there is a lot of speculation around the sensing mechanism of this type of sensor, and so more research is required to fully understand its operation. It was found in the literature that WO_3 offers very good sensing characteristics, and the several temperature-dependent phases of this compound can be used for selective gas sensing. These properties are directly due to the change in physical properties with the change in crystal structure. This leads to the study of the phase transitions involved in WO_3. It also appears that certain phases are more sensitive towards certain gases due to that phase's band gap. This provides hints into the selective sensing of the different phases of WO_3.

The topic of phase transitions, and more specifically S. Or. Ph. Trs. was approached by the LLL-theory using rigid group theoretical methods to determine the types of phase transitions and the phonon responsible for that transition. This determination has been addressed by other authors, but there were substantial differences in their conclusions. The calculations carried out here aimed to clear these discrepancies, as well as understand the structure and nature of WO_3. It was found that only one experimentally observed transition was second-order, and this was from $P4/nmm, D_{4h}^7$ to $P\bar{4}2_1m, D_{2d}^3$ via the Z_{4-} irrp or phonon. All the other transitions were either first-order or higher-order.

One of the simplest techniques used to distinguish the different phases in WO_3 is Raman spectroscopy, so a closer look was given to Raman scattering theory. The Raman-active modes of each phase of WO_3 were determined group theoretically and related to the respective Brillouin zone and Raman spectra. This gave a further insight into the crystal structure of WO_3. In future work, in-situ Raman spectroscopy can be carried out where the Raman spectra of the interaction with the target gas and WO_3 surface can be monitored to determine how the vibrational modes of the WO_3 are influenced by the target gas. This might give clues to the mechanism of conductometric sensing.

The technique used to synthesise WO_3 film sensing layer was reactive-sputtering followed by annealing of the as-synthesized film for 2 hours at 450^{o}C in air. This gave a uniform and stoichiometric porous film with thickness of 1.82 μm. The crystal phase was found to be triclinic $P\bar{1}$ δ-WO_3 from XRD and Raman spectroscopy. This phase is believed to be stabilized at room temperature by the stresses and strains in the film. The optical band gap was found to be 3.05 eV using UV/Vis spectroscopy and PL spectroscopy confirmed this result, and this value is similar to that found in literature for this phase. The activation energy

© University of Pretoria

of the film was found to be 0.83 eV which is a typical result for WO_3 films. This film was used for gas sensing and was much more sensitive to NO_2 gas than NH_3 gas, especially at 100^{o}C. This phase of WO_3 is not the best for sensing these gases since the target gas did not saturate the film, neither was it completely removed when only air was flowed on the film. The test for selectivity, where both gases were allowed to flow onto the film at the same time, revealed that the performance towards NO_2 sensing was better at 30^{o}C. To decrease the recovery time of the film at 30^{o}C, light was used to clean the surface of the WO_3 film from target gas. To better understand the sensing capabilities of this film, more target gases should be tested for sensing such as acetone and alcohols.

More attention needs to be given to the sensing mechanism of this type of gas sensors from an experimental perspective, because the available theory is very limited in explaining the observed results in its entirety. Thereafter, the film can be doped with noble metals to check how it influences sensitivity and selectivity at room-temperature. The next step will be to test these sensors for suitability, by subjecting the sensing material to similar conditions as that found at mineshafts. Thereafter, when all these issues have been addressed, the design and engineering of suitable sensors incorporating WO_3 that is sensitive, selective and stable can be produced on a large scale. This thesis unlocks the possibilities of using WO_3 and tailoring it for a specific application.

© University of Pretoria

Appendix A: Brillouin Zones of the lower symmetries of WO_3.

Orthorhombic Brillouin Zone for β-WO_3 $\left(D_{2h}^{13}\right)$

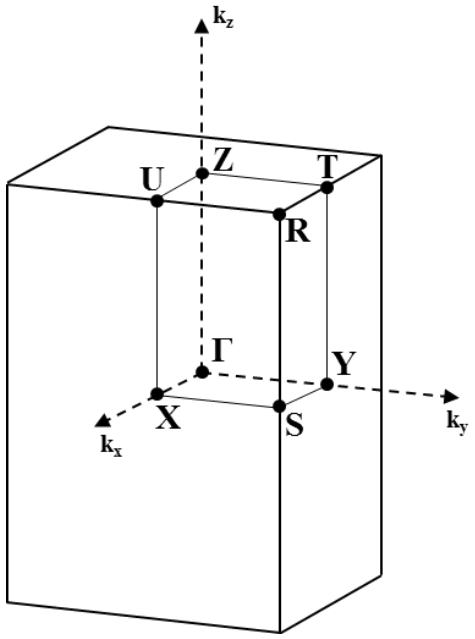

Figure A1. The Brillouin Zone of the orthorhombic primitive cell and the relative positions of the high symmetry points $\mathbf{k}_\Gamma(0,0,0)$, $\mathbf{k}_Z\left(0,0,\frac{1}{2}\right)$, $\mathbf{k}_U\left(\frac{1}{2},0,\frac{1}{2}\right)$, $\mathbf{k}_X\left(\frac{1}{2},0,0\right)$, $\mathbf{k}_T\left(0,\frac{1}{2},\frac{1}{2}\right)$, $\mathbf{k}_S\left(\frac{1}{2},\frac{1}{2},0\right)$ and $\mathbf{k}_Y\left(0,\frac{1}{2},0\right)$ where the lattice constant is the product with $\left(\frac{2\pi}{a_1},\frac{2\pi}{a_2},\frac{2\pi}{a_3}\right)$ and the high symmetry points [32].

Monoclinic Brillouin Zone for γ-WO_3 $\left(C_{2h}^{5}\right)$

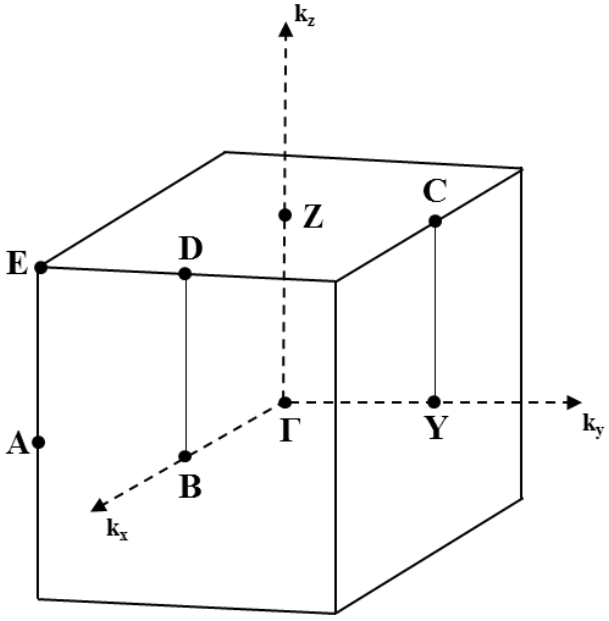

Figure A2. The Brillouin Zone of the monoclinic primitive cell and the relative positions of the high symmetry points $\mathbf{k}_\Gamma(0,0,0)$, $\mathbf{k}_Z\left(0,0,\frac{1}{2}\right)$, $\mathbf{k}_D\left(\frac{1}{2},0,\frac{1}{2}\right)$, $\mathbf{k}_B\left(\frac{1}{2},0,0\right)$, $\mathbf{k}_C\left(0,\frac{1}{2},\frac{1}{2}\right)$, $\mathbf{k}_Y\left(0,\frac{1}{2},0\right)$, $\mathbf{k}_A\left(\frac{1}{2},-\frac{1}{2},0\right)$ and $\mathbf{k}_E\left(\frac{1}{2},-\frac{1}{2},\frac{1}{2}\right)$ where the lattice constant is the product with $\left(\frac{2\pi}{a_1},\frac{2\pi}{a_2},\frac{2\pi}{a_3}\right)$ and the high symmetry points [32].

© University of Pretoria

Triclinic Brillouin Zone for δ-WO_3 $\left(P\bar{1}\right)$

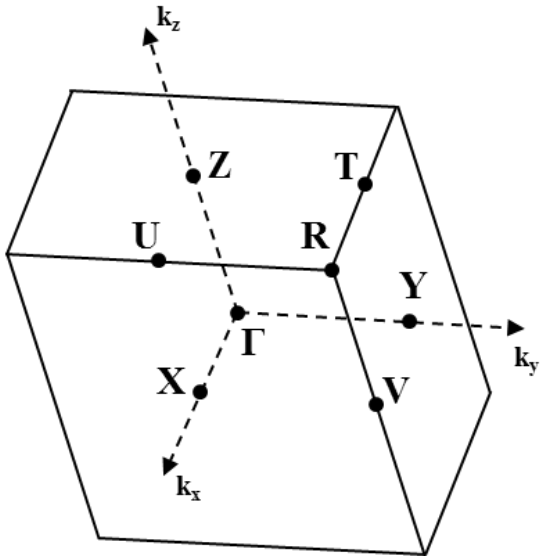

Figure A3. The Brillouin Zone of the triclinic primitive cell and the relative positions of the high symmetry points $\mathbf{k}_\Gamma(0,0,0)$, $\mathbf{k}_Z\left(0,0,\frac{1}{2}\right)$, $\mathbf{k}_T\left(0,\frac{1}{2},\frac{1}{2}\right)$, $\mathbf{k}_Y\left(0,\frac{1}{2},0\right)$, $\mathbf{k}_R\left(\frac{1}{2},\frac{1}{2},\frac{1}{2}\right)$, $\mathbf{k}_V\left(\frac{1}{2},\frac{1}{2},0\right)$, $\mathbf{k}_U\left(\frac{1}{2},0,\frac{1}{2}\right)$ and $\mathbf{k}_X\left(\frac{1}{2},0,0\right)$ where the lattice constant is the product with $\left(\frac{2\pi}{a_1},\frac{2\pi}{a_2},\frac{2\pi}{a_3}\right)$ and the high symmetry points [32].

© University of Pretoria

Appendix B: Symmetry operators of D_{4h}^7 space group.

Table B1. Vector representations of the D_{4h}^7 space group*.

1 E	(x,y,z)	$\left(\begin{array}{ccc} 1 & 0 & 0 \\ 0 & 1 & 0 \\ 0 & 0 & 1 \end{array}\right)$	25 I $(-x,-y,-z)$	$\left(\begin{array}{ccc} -1 & 0 & 0 \\ 0 & -1 & 0 \\ 0 & 0 & -1 \end{array}\right)$
2 C_{2x}	$(x,-y,-z)$	$\left(\begin{array}{ccc} 1 & 0 & 0 \\ 0 & -1 & 0 \\ 0 & 0 & -1 \end{array}\right)$	26 σ_x	$(-x,y,z)$	$\left(\begin{array}{ccc} -1 & 0 & 0 \\ 0 & 1 & 0 \\ 0 & 0 & 1 \end{array}\right)$
3 C_{2y}	$(-x,y,-z)$	$\left(\begin{array}{ccc} -1 & 0 & 0 \\ 0 & 1 & 0 \\ 0 & 0 & -1 \end{array}\right)$	27 σ_y	$(x,-y,z)$	$\left(\begin{array}{ccc} 1 & 0 & 0 \\ 0 & -1 & 0 \\ 0 & 0 & 1 \end{array}\right)$
4 C_{2z}	$(-x,-y,z)$	$\left(\begin{array}{ccc} -1 & 0 & 0 \\ 0 & -1 & 0 \\ 0 & 0 & 1 \end{array}\right)$	28 σ_z	$(x,y,-z)$	$\left(\begin{array}{ccc} 1 & 0 & 0 \\ 0 & 1 & 0 \\ 0 & 0 & -1 \end{array}\right)$
13 C_{2b}	$(-y,-x,-z)$	$\left(\begin{array}{ccc} 0 & -1 & 0 \\ -1 & 0 & 0 \\ 0 & 0 & -1 \end{array}\right)$	37 σ_{db}	(y,x,z)	$\left(\begin{array}{ccc} 0 & 1 & 0 \\ 1 & 0 & 0 \\ 0 & 0 & 1 \end{array}\right)$
14 C_{4z}^+	$(-y,x,z)$	$\left(\begin{array}{ccc} 0 & -1 & 0 \\ 1 & 0 & 0 \\ 0 & 0 & 1 \end{array}\right)$	38 S_{4z}^-	$(y,-x,-z)$	$\left(\begin{array}{ccc} 0 & 1 & 0 \\ -1 & 0 & 0 \\ 0 & 0 & -1 \end{array}\right)$
15 C_{4z}^-	$(y,-x,z)$	$\left(\begin{array}{ccc} 0 & 1 & 0 \\ -1 & 0 & 0 \\ 0 & 0 & 1 \end{array}\right)$	39 S_{4z}^+	$(-y,x,-z)$	$\left(\begin{array}{ccc} 0 & -1 & 0 \\ 1 & 0 & 0 \\ 0 & 0 & -1 \end{array}\right)$
16 C_{2a}	$(y,x,-z)$	$\left(\begin{array}{ccc} 0 & 1 & 0 \\ 1 & 0 & 0 \\ 0 & 0 & -1 \end{array}\right)$	40 σ_{da}	$(-y,-x,z)$	$\left(\begin{array}{ccc} 0 & -1 & 0 \\ -1 & 0 & 0 \\ 0 & 0 & 1 \end{array}\right)$

*The notation follows from CDML tables [32]. It is seen that the vector representation (VR) of D_{4h}^7 is reducible because it does not belong to the set of irrps of D_{4h}^7 (see Appendix E). The VR can be decomposed onto the $\Gamma_{3-}(z)$ and $\Gamma_{5-}(x,y)$ irrps. Following from criterion (3) of LLL-theory in chapter 3, the anti-symmetrized square $\{\ \}_2$ must not contain any component of the VR (x,y,z). In other words, $\{\ \}_2$ must not contain neither $\Gamma_{3-}(z)$ nor $\Gamma_{5-}(x,y)$.

© University of Pretoria

Appendix C: Reality test solutions of the high symmetry points of D_{4h}^7.

Table C1. The squares[+] of the symmetry operators $(g \mid \tau_g)^2$ of D_{4h}^7 for the Reality test following from equation (3.3).

$\{g/\tau\}$	E	$C_{2x} \mid \tau$	$C_{2y} \mid \tau$	C_{2z}	C_{2b}	$C_{4z}^{+} \mid \tau$	$C_{4z}^{-} \mid \tau$	C_{2a}	$I \mid \tau$	σ_x	σ_y	$\sigma_z \mid \tau$	$\sigma_{db} \mid \tau$	S_{4z}^{-}	S_{4z}^{+}	$\sigma_{da} \mid \tau$
	1	**2.1**	**3.1**	**4**	**13**	**14.1**	**15.1**	**16**	**25.1**	**26**	**27**	**28.1**	**37.1**	**38**	**39**	**40.1**
$(g \mid \tau_g)^2$	E	E	E	E	E	C_{2z}	C_{2z}	E	E	C_{2z}	C_{2z}	E	E	C_{2z}	C_{2z}	E
	1	**1**	**1**	**1**	**1**	**4**	**4**	**1**	**1**	**1**	**1**	**1**	**1**	**4**	**4**	**1**

[+]The squares of the symmetry operators and their non-primitive translations can be determined from

$$\begin{aligned}\{\phi_p \mid \boldsymbol{\tau}_p\}\{\phi_q \mid \boldsymbol{\tau}_q\} &= \{\phi_p\phi_q \mid \boldsymbol{\tau}_p + \phi_p\boldsymbol{\tau}_q\} \\ &= \{\varepsilon \mid \boldsymbol{\tau}_p + \phi_p\boldsymbol{\tau}_q - \boldsymbol{\tau}_{pq}\}\{\phi_{pq} \mid \boldsymbol{\tau}_{pq}\} \\ &= \{\varepsilon \mid \boldsymbol{t}_{pq}\}\{\phi_{pq} \mid \boldsymbol{\tau}_{pq}\} = \{\varepsilon \mid \boldsymbol{t}_{pq}\}\{\phi \mid \boldsymbol{\tau}_\phi\}\end{aligned},$$

where $\boldsymbol{t}_{pq} \equiv \boldsymbol{\tau}_p + \phi_p\boldsymbol{\tau}_q - \boldsymbol{\tau}_{pq} \equiv \boldsymbol{\tau}_p + \phi_p\boldsymbol{\tau}_q - \boldsymbol{\tau}_\phi$ and $\phi_p\phi_q \equiv \phi_{pq} \equiv \phi,\ \boldsymbol{\tau}_{pq} \equiv \boldsymbol{\tau}_\phi$.

As an example, consider $\left(14 \mid \frac{1}{2}\frac{1}{2}0\right)^2$. Using the above formula gives

$$\begin{aligned}\left\{14 \mid \tfrac{1}{2}\tfrac{1}{2}0\right\}\left\{14 \mid \tfrac{1}{2}\tfrac{1}{2}0\right\} &= \left\{14 \otimes 14 \mid \tfrac{1}{2}\tfrac{1}{2}0 \oplus 14\left(\tfrac{1}{2}\tfrac{1}{2}0\right)\right\} \\ &= \left\{\varepsilon \mid \tfrac{1}{2}\tfrac{1}{2}0 + \left(-\tfrac{1}{2}\tfrac{1}{2}0\right) - (000)\right\}\{4 \mid (000)\} \\ &= \{\varepsilon \mid (010)\}\{4 \mid (000)\}\end{aligned}$$

The resulting symmetry operator is 4. Now from $\varepsilon \mid (010)$, the phase can be calculated using $e^{i\frac{2\pi}{a}\mathbf{k}a}$. In this case, $\mathbf{k} = (010)$ which gives $e^{i2\pi} = 1$ and so $\left(14 \mid \frac{1}{2}\frac{1}{2}0\right)^2 = 4$. Now using Eq. (3.3a) for the symmetry operators squares in Table C1, it was found that all high symmetry points of one- and two-dimensional irrps comes out to be 1, meaning all irrps are real.

© University of Pretoria

Space group D_{4h}^7 at point Γ

$$\frac{1}{|g|}\sum_{g\in k_1}\chi\left(g\mid\tau_g\right)^2=\frac{1}{16}\sum_{g\in k_\Gamma}\chi\left(g\mid\tau_g\right)^2$$

$$\Gamma_{1+}=\Gamma_{2+}=\Gamma_{3+}=\Gamma_{4+}=\Gamma_{5+}=\Gamma_{1-}=\Gamma_{2-}=\Gamma_{3-}=\Gamma_{4-}=\Gamma_{5-}=1$$

Space group D_{4h}^7 at point M

$$\frac{1}{16}\sum_{g\in k_M}\chi\left(g\mid\tau_g\right)^2$$

$$M_1=M_2=M_3=M_4=1$$

Space group D_{4h}^7 at point A

$$\frac{1}{16}\sum_{g\in k_A}\chi\left(g\mid\tau_g\right)^2$$

$$A_1=A_2=A_3=A_4=1$$

Space group D_{4h}^7 at point Z

$$\frac{1}{16}\sum_{g\in k_Z}\chi\left(g\mid\tau_g\right)^2$$

$$Z_{1+}=Z_{2+}=Z_{3+}=Z_{4+}=Z_{5+}=Z_{1-}=Z_{2-}=Z_{3-}=Z_{4-}=Z_{5-}=1$$

Space group D_{4h}^7 at point X

$$\frac{1}{16}\sum_{g\in k_X}\chi\left(g\mid\tau_g\right)^2$$

$$X_1=X_2=1$$

Space group D_{4h}^7 at point R

$$\frac{1}{16}\sum_{g\in k_R}\chi\left(g\mid\tau_g\right)^2$$

$$R_1=R_2=1$$

Following from criterion (2) in section 3.3, it can be seen above that all high-symmetry points are real.

© University of Pretoria

Appendix D: The symmetrized and anti-symmetrized squares $\{\ \}_2$ and cubes $[\ ]_3$ of D_{4h}^7

Squares

$$\Gamma_{1+}\times\Gamma_{1+}=\Gamma_{2+}\times\Gamma_{2+}=\Gamma_{3+}\times\Gamma_{3+}=\Gamma_{4+}\times\Gamma_{4+}=\Gamma_{1-}\times\Gamma_{1-}=\Gamma_{2-}\times\Gamma_{2-}=\Gamma_{3-}\times\Gamma_{3-}=\Gamma_{4-}\times\Gamma_{4-}=[\Gamma_{1+}]+\{\ \}$$
$$\Gamma_{5+}\otimes\Gamma_{5+}=\Gamma_{5-}\otimes\Gamma_{5-}=[\Gamma_{1+}\oplus\Gamma_{2+}\oplus\Gamma_{4+}]\oplus\{\Gamma_{3+}\}$$

$$M_1\otimes M_1=M_2\otimes M_2=[\Gamma_{1+}\oplus\Gamma_{4+}\oplus\Gamma_{4-}]\oplus\{\Gamma_{1-}\}$$
$$M_3\otimes M_3=M_4\otimes M_4=[\Gamma_{1+}\oplus\Gamma_{4+}\oplus\Gamma_{3-}]\oplus\{\Gamma_{2-}\}$$

$$X_1\otimes X_1=X_2\otimes X_2=[\Gamma_{1+}\oplus\Gamma_{2+}\oplus\Gamma_{5+}\oplus\Gamma_{3-}\oplus\Gamma_{4-}]\oplus\{\Gamma_{5-}\}\oplus[M_2\oplus M_3]\oplus\{M_1\oplus M_4\}$$

$$A_1\otimes A_1=A_2\otimes A_2=[\Gamma_{1+}\oplus\Gamma_{4+}\oplus\Gamma_{4-}]\oplus\{\Gamma_{1-}\}$$
$$A_3\otimes A_3=A_4\otimes A_4=[\Gamma_{1+}\oplus\Gamma_{4+}\oplus\Gamma_{3-}]\oplus\{\Gamma_{2-}\}$$

$$R_1\otimes R_1=R_2\otimes R_2=[\Gamma_{1+}\oplus\Gamma_{2+}\oplus\Gamma_{5+}\oplus\Gamma_{3-}\oplus\Gamma_{4-}]\oplus\{\Gamma_{5-}\}\oplus[M_2\oplus M_3]\oplus\{M_1\oplus M_4\}$$

$$Z_{1+}\times Z_{1+}=Z_{2+}\times Z_{2+}=Z_{3+}\times Z_{3+}=Z_{4+}\times Z_{4+}=Z_{1-}\times Z_{1-}=Z_{2-}\times Z_{2-}=Z_{3-}\times Z_{3-}=Z_{4-}\times Z_{4-}=[\Gamma_{1+}]+\{\ \}$$
$$Z_{5+}\otimes Z_{5+}=Z_{5-}\otimes Z_{5-}=[\Gamma_{1+}\oplus\Gamma_{2+}\oplus\Gamma_{4+}]\oplus\{\Gamma_{3+}\}$$

From the above results, it follows that all irrps satisfy criterion (3) in section 3.3 accept X_1, X_2, R_1 and R_2. For example, $\{M_1\}_2$ contains Γ_{1-} which is not part of the polar coordinates and therefore satisfies the criterion, but $\{X_1\}_2$ contains Γ_{5-} which is part of the polar coordinates and therefore does not satisfy the criterion.

Cubes

$$\Gamma_{1+}\times\Gamma_{1+}\times\Gamma_{1+}=[\Gamma_{1+}]+\{\ \},\quad \Gamma_{2+}\times\Gamma_{2+}\times\Gamma_{2+}=[\Gamma_{2+}]+\{\ \},\quad \Gamma_{3+}\times\Gamma_{3+}\times\Gamma_{3+}=[\Gamma_{3+}]+\{\ \},$$
$$\Gamma_{4+}\times\Gamma_{4+}\times\Gamma_{4+}=[\Gamma_{4+}]+\{\ \},\quad \Gamma_{1-}\times\Gamma_{1-}\times\Gamma_{1-}=[\Gamma_{1-}]+\{\ \},\quad \Gamma_{2-}\times\Gamma_{2-}\times\Gamma_{2-}=[\Gamma_{2-}]+\{\ \},$$
$$\Gamma_{3-}\times\Gamma_{3-}\times\Gamma_{3-}=[\Gamma_{3-}]+\{\ \},\quad \Gamma_{4-}\times\Gamma_{4-}\times\Gamma_{4-}=[\Gamma_{4-}]+\{\ \},\quad \Gamma_{5+}\otimes\Gamma_{5+}\otimes\Gamma_{5+}=[2\Gamma_{5+}]\oplus\{\ \},$$
$$\Gamma_{5-}\otimes\Gamma_{5-}\otimes\Gamma_{5-}=[2\Gamma_{5-}]\oplus\{\ \}.$$

$$M_1\otimes M_1\otimes M_1=[2M_1]\oplus\{\ \},\ M_2\otimes M_2\otimes M_2=[2M_2]\oplus\{\ \},\ M_3\otimes M_3\otimes M_3=[2M_3]\oplus\{\ \}$$
$$,\ M_4\otimes M_4\otimes M_4=[2M_4]\oplus\{\ \}.$$

$$X_1\otimes X_1\otimes X_1=[2X_1]\oplus\{\ \}\oplus[2X_1\oplus X_2]\oplus\{X_2\},$$
$$X_2\otimes X_2\otimes X_2=[2X_2]\oplus\{\ \}\oplus[X_1\oplus 2X_2]\oplus\{X_1\}.$$

© University of Pretoria

$$A_1 \otimes A_1 \otimes A_1 = [2A_1] \oplus \{\}, \qquad A_2 \otimes A_2 \otimes A_2 = [2A_2] \oplus \{\}, \qquad A_3 \otimes A_3 \otimes A_3 = [2A_3] \oplus \{\},$$
$$A_4 \otimes A_4 \otimes A_4 = [2A_4] \oplus \{\}.$$
$$R_1 \otimes R_1 \otimes R_1 = [2R_1] \oplus \{\} \oplus [2R_1 \oplus R_2] \oplus \{R_2\},$$
$$R_2 \otimes R_2 \otimes R_2 = [2R_2] \oplus \{\} \oplus [R_1 \oplus 2R_2] \oplus \{R_1\}$$

$$Z_{1+} \times Z_{1+} \times Z_{1+} = [Z_{1+}] + \{\}, \qquad Z_{2+} \times Z_{2+} \times Z_{2+} = [Z_{2+}] + \{\}, \qquad Z_{3+} \times Z_{3+} \times Z_{3+} = [Z_{3+}] + \{\},$$
$$Z_{4+} \times Z_{4+} \times Z_{4+} = [Z_{4+}] + \{\}, \qquad Z_{1-} \times Z_{1-} \times Z_{1-} = [Z_{1-}] + \{\}, \qquad Z_{2-} \times Z_{2-} \times Z_{2-} = [Z_{2-}] + \{\},$$
$$Z_{3-} \times Z_{3-} \times Z_{3-} = [Z_{3-}] + \{\}, \quad Z_{4-} \times Z_{4-} \times Z_{4-} = [Z_{4-}] + \{\}, \quad Z_{5+} \otimes Z_{5+} \otimes Z_{5+} = [2Z_{5+}] \oplus \{\},$$
$$Z_{5-} \otimes Z_{5-} \otimes Z_{5-} = [2Z_{5-}] \oplus \{\}.$$

From the above results, it follows that only irrps of the point Γ can be considered in criterion (4) in section 3.3 because no other high symmetry point can contain the identity irrp Γ_{1+} due to wave vector selection rules. It is thus seen from above that only Γ_{1+} does not satisfy the criterion.

© University of Pretoria

Appendix E: The Irreducible Representations (Irrps) of the High Symmetry points of D_{4h}^{7}.

Table E1a. Irreducible representations of G^{k_Γ} for space group D_{4h}^{7} at $\boldsymbol{k}_\Gamma = (0,0,0)\frac{2\pi}{a}$ *.

α-WO_3	E	$C_{2x}\mid\tau$	$C_{2y}\mid\tau$	C_{2z}	C_{2b}	$C_{4z}^{+}\mid\tau$	$C_{4z}^{-}\mid\tau$	C_{2a}	$I\mid\tau$	σ_x	σ_y	$\sigma_z\mid\tau$	$\sigma_{db}\mid\tau$	S_{4z}^{-}	S_{4z}^{+}	$\sigma_{da}\mid\tau$
$\{g/\tau\}$	**1**	**2.1**	**3.1**	**4**	**13**	**14.1**	**15.1**	**16**	**25.1**	**26**	**27**	**28.1**	**37.1**	**38**	**39**	**40.1**
Γ_{1+}	1	1	1	1	1	1	1	1	1	1	1	1	1	1	1	1
Γ_{2+}	1	1	1	1	-1	-1	-1	-1	1	1	1	1	-1	-1	-1	-1
Γ_{3+}	1	-1	-1	1	-1	1	1	-1	1	-1	-1	1	-1	1	1	-1
Γ_{4+}	1	-1	-1	1	1	-1	-1	1	1	-1	-1	1	1	-1	-1	1
Γ_{5+}	$\begin{bmatrix}1&0\\0&1\end{bmatrix}$	$\begin{bmatrix}1&0\\0&-1\end{bmatrix}$	$\begin{bmatrix}-1&0\\0&1\end{bmatrix}$	$\begin{bmatrix}-1&0\\0&-1\end{bmatrix}$	$\begin{bmatrix}0&-1\\-1&0\end{bmatrix}$	$\begin{bmatrix}0&-1\\1&0\end{bmatrix}$	$\begin{bmatrix}0&1\\-1&0\end{bmatrix}$	$\begin{bmatrix}0&1\\1&0\end{bmatrix}$	$\begin{bmatrix}1&0\\0&1\end{bmatrix}$	$\begin{bmatrix}1&0\\0&-1\end{bmatrix}$	$\begin{bmatrix}-1&0\\0&1\end{bmatrix}$	$\begin{bmatrix}-1&0\\0&-1\end{bmatrix}$	$\begin{bmatrix}0&-1\\-1&0\end{bmatrix}$	$\begin{bmatrix}0&-1\\1&0\end{bmatrix}$	$\begin{bmatrix}0&1\\-1&0\end{bmatrix}$	$\begin{bmatrix}0&1\\1&0\end{bmatrix}$
Γ_{1-}	1	1	1	1	1	1	1	1	-1	-1	-1	-1	-1	-1	-1	-1
Γ_{2-}	1	1	1	1	-1	-1	-1	-1	-1	-1	-1	-1	1	1	1	1
Γ_{3-}	1	-1	-1	1	-1	1	1	-1	-1	1	1	-1	1	-1	-1	1
Γ_{4-}	1	-1	-1	1	1	-1	-1	1	-1	1	1	-1	-1	1	1	-1
Γ_{5-}	$\begin{bmatrix}1&0\\0&1\end{bmatrix}$	$\begin{bmatrix}1&0\\0&-1\end{bmatrix}$	$\begin{bmatrix}-1&0\\0&1\end{bmatrix}$	$\begin{bmatrix}-1&0\\0&-1\end{bmatrix}$	$\begin{bmatrix}0&1\\1&0\end{bmatrix}$	$\begin{bmatrix}0&1\\-1&0\end{bmatrix}$	$\begin{bmatrix}0&-1\\1&0\end{bmatrix}$	$\begin{bmatrix}0&-1\\-1&0\end{bmatrix}$	$\begin{bmatrix}-1&0\\0&-1\end{bmatrix}$	$\begin{bmatrix}-1&0\\0&1\end{bmatrix}$	$\begin{bmatrix}1&0\\0&-1\end{bmatrix}$	$\begin{bmatrix}1&0\\0&1\end{bmatrix}$	$\begin{bmatrix}0&-1\\-1&0\end{bmatrix}$	$\begin{bmatrix}0&-1\\1&0\end{bmatrix}$	$\begin{bmatrix}0&1\\-1&0\end{bmatrix}$	$\begin{bmatrix}0&1\\1&0\end{bmatrix}$

*The symmetry operators that leave the wave functions unchanged have been obtained from the above table and were tabulated in Table 3.3. For example, consider irrp Γ_{2+}, with symmetry operators 1, 2.1, 3.1, 4, 25.1, 26, 27 and 28.1 of D_{4h}^{7} that leave the basis $\varphi^{\Gamma_{2+}}$ unchanged, may cause S. Or. Ph. Trs. to the space subgroup containing this set of symmetry operators. In this way, one finds irrps responsible for transitions to the space subgroups after transitions. This method is purely group theoretical in terms of sub group chains method.

Table E1b. Generating relations for the two-dimensional irrps of tetragonal phase α-WO_3 (D_{4h}^{7}) for the $\Gamma_{5\pm}$-irrp presented above in Table E1a.

Augmenters: $4(-x,-y,z)$; $2.1(1/2+x,1/2-y,-z)$; $26(-x,y,z)$; $40.1(1/2-y,1/2-x,z)$. Generating relations: $4\times2.1=3.1$, $4\times26=27$, $2.1\times26=25.1$, $40.1\times2.1=38$, $2.1\times40.1=39$, $26\times40.1=15.1$, $40.1\times26=14.1$, $3.1\times26=28.1$, $2.1\times14.1=13$, $14.1\times2.1=16$, where the generators are 4 GEN, 2.1 GEN, 26 GEN and 40.1 GEN.

$\Gamma_{5+}: -E;4;4;2,$

$\Gamma_{5-}: -E;4;-4;2.$

© University of Pretoria

Table E2a. Irreducible representations of G^{k_Z} for space group D_{4h}^7 at $\left(\boldsymbol{k}_Z = 0,0,\frac{1}{2}\right)\frac{2\pi}{a}$ **.

α-WO_3	E	$C_{2x}\mid\tau$	$C_{2y}\mid\tau$	C_{2z}	C_{2b}	$C_{4z}^{+}\mid\tau$	$C_{4z}^{-}\mid\tau$	C_{2a}	$I\mid\tau$	σ_x	σ_y	$\sigma_z\mid\tau$	$\sigma_{db}\mid\tau$	S_{4z}^{-}	S_{4z}^{+}	$\sigma_{da}\mid\tau$
$\{g/\tau\}$	**1**	**2.1**	**3.1**	**4**	**13**	**14.1**	**15.1**	**16**	**25.1**	**26**	**27**	**28.1**	**37.1**	**38**	**39**	**40.1**
Z_{1+}	1	1	1	1	1	1	1	1	1	1	1	1	1	1	1	1
Z_{2+}	1	1	1	1	-1	-1	-1	-1	1	1	1	1	-1	-1	-1	-1
Z_{3+}	1	-1	-1	1	-1	1	1	-1	1	-1	-1	1	-1	1	1	-1
Z_{4+}	1	-1	-1	1	1	-1	-1	1	1	-1	-1	1	1	-1	-1	1
Z_{5+}	$\begin{bmatrix}1&0\\0&1\end{bmatrix}$	$\begin{bmatrix}1&0\\0&-1\end{bmatrix}$	$\begin{bmatrix}-1&0\\0&1\end{bmatrix}$	$\begin{bmatrix}-1&0\\0&-1\end{bmatrix}$	$\begin{bmatrix}0&-1\\-1&0\end{bmatrix}$	$\begin{bmatrix}0&-1\\1&0\end{bmatrix}$	$\begin{bmatrix}0&1\\-1&0\end{bmatrix}$	$\begin{bmatrix}0&1\\1&0\end{bmatrix}$	$\begin{bmatrix}1&0\\0&1\end{bmatrix}$	$\begin{bmatrix}1&0\\0&-1\end{bmatrix}$	$\begin{bmatrix}-1&0\\0&1\end{bmatrix}$	$\begin{bmatrix}-1&0\\0&-1\end{bmatrix}$	$\begin{bmatrix}0&-1\\-1&0\end{bmatrix}$	$\begin{bmatrix}0&-1\\1&0\end{bmatrix}$	$\begin{bmatrix}0&1\\-1&0\end{bmatrix}$	$\begin{bmatrix}0&1\\1&0\end{bmatrix}$
Z_{1-}	1	1	1	1	1	1	1	1	-1	-1	-1	-1	-1	-1	-1	-1
Z_{2-}	1	1	1	1	-1	-1	-1	-1	-1	-1	-1	-1	1	1	1	1
Z_{3-}	1	-1	-1	1	-1	1	1	-1	-1	1	1	-1	1	-1	-1	1
Z_{4-}	1	-1	-1	1	1	-1	-1	1	-1	1	1	-1	-1	1	1	-1
Z_{5-}	$\begin{bmatrix}1&0\\0&1\end{bmatrix}$	$\begin{bmatrix}1&0\\0&-1\end{bmatrix}$	$\begin{bmatrix}-1&0\\0&1\end{bmatrix}$	$\begin{bmatrix}-1&0\\0&-1\end{bmatrix}$	$\begin{bmatrix}0&1\\1&0\end{bmatrix}$	$\begin{bmatrix}0&1\\-1&0\end{bmatrix}$	$\begin{bmatrix}0&-1\\1&0\end{bmatrix}$	$\begin{bmatrix}0&-1\\-1&0\end{bmatrix}$	$\begin{bmatrix}-1&0\\0&-1\end{bmatrix}$	$\begin{bmatrix}-1&0\\0&1\end{bmatrix}$	$\begin{bmatrix}1&0\\0&-1\end{bmatrix}$	$\begin{bmatrix}1&0\\0&1\end{bmatrix}$	$\begin{bmatrix}0&-1\\-1&0\end{bmatrix}$	$\begin{bmatrix}0&-1\\1&0\end{bmatrix}$	$\begin{bmatrix}0&1\\-1&0\end{bmatrix}$	$\begin{bmatrix}0&1\\1&0\end{bmatrix}$

**The symmetry operators that leave the wave functions unchanged have been obtained from the above table and were tabulated in Table 3.3. For example, consider irrp Z_{3+}, with invariant symmetry operators 1, 4, 14.1, 15.1, 25.1, 28.1, 38 and 39 of D_{4h}^7 that leave the basis $\varphi^{Z_{3+}}$, may cause S. Or. Ph. Trs. to the space subgroup containing this set of symmetry operators.

Table E2b. Generating relations for the two-dimensional irrps of tetragonal phase α-WO_3 (D_{4h}^7) for the $Z_{5\pm}$-irrp presented above in Table E2a.

Augmenters: $4(-x,-y,z)$; $2.1(1/2+x,1/2-y,-z)$; $26(-x,y,z)$; $40.1(1/2-y,1/2-x,z)$. Generating relations: $4\times2.1=3.1$, $4\times26=27$, $2.1\times26=25.1$, $40.1\times2.1=38$, $2.1\times40.1=39$, $26\times40.1=15.1$, $40.1\times26=14.1$, $3.1\times26=28.1$, $2.1\times14.1=13$, $14.1\times2.1=16$, where the generators are 4 GEN, 2.1 GEN, 26 GEN and 40.1 GEN.

$Z_{5+}: -E;4;4;2,$

$Z_{5-}: -E;4;-4;2.$

© University of Pretoria

Table E3a. Irreducible representations of G^{k_M} for space group D_{4h}^7 at $\boldsymbol{k}_M = \left(\frac{1}{2},\frac{1}{2},0\right)\frac{2\pi}{a}$ ***.

α-WO_3	E	$C_{2x}\mid\tau$	$C_{2y}\mid\tau$	C_{2z}	C_{2b}	$C_{4z}^{+}\mid\tau$	$C_{4z}^{-}\mid\tau$	C_{2a}	$I\mid\tau$	σ_x	σ_y	$\sigma_z\mid\tau$	$\sigma_{db}\mid\tau$	S_{4z}^{-}	S_{4z}^{+}	$\sigma_{da}\mid\tau$
$\{g/\tau\}$	**1**	**2.1**	**3.1**	**4**	**13**	**14.1**	**15.1**	**16**	**25.1**	**26**	**27**	**28.1**	**37.1**	**38**	**39**	**40.1**
M_1	$\begin{bmatrix}1&0\\0&1\end{bmatrix}$	$\begin{bmatrix}i&0\\0&-i\end{bmatrix}$	$\begin{bmatrix}i&0\\0&-i\end{bmatrix}$	$\begin{bmatrix}1&0\\0&1\end{bmatrix}$	$\begin{bmatrix}1&0\\0&1\end{bmatrix}$	$\begin{bmatrix}-i&0\\0&i\end{bmatrix}$	$\begin{bmatrix}-i&0\\0&i\end{bmatrix}$	$\begin{bmatrix}1&0\\0&1\end{bmatrix}$	$\begin{bmatrix}0&-i\\i&0\end{bmatrix}$	$\begin{bmatrix}0&1\\1&0\end{bmatrix}$	$\begin{bmatrix}0&1\\1&0\end{bmatrix}$	$\begin{bmatrix}0&-i\\i&0\end{bmatrix}$	$\begin{bmatrix}0&-i\\i&0\end{bmatrix}$	$\begin{bmatrix}0&1\\1&0\end{bmatrix}$	$\begin{bmatrix}0&1\\1&0\end{bmatrix}$	$\begin{bmatrix}0&-i\\i&0\end{bmatrix}$
M_2	$\begin{bmatrix}1&0\\0&1\end{bmatrix}$	$\begin{bmatrix}i&0\\0&-i\end{bmatrix}$	$\begin{bmatrix}i&0\\0&-i\end{bmatrix}$	$\begin{bmatrix}1&0\\0&1\end{bmatrix}$	$\begin{bmatrix}-1&0\\0&-1\end{bmatrix}$	$\begin{bmatrix}i&0\\0&-i\end{bmatrix}$	$\begin{bmatrix}i&0\\0&-i\end{bmatrix}$	$\begin{bmatrix}-1&0\\0&-1\end{bmatrix}$	$\begin{bmatrix}0&i\\-i&0\end{bmatrix}$	$\begin{bmatrix}0&1\\1&0\end{bmatrix}$	$\begin{bmatrix}0&1\\1&0\end{bmatrix}$	$\begin{bmatrix}i&0\\0&-i\end{bmatrix}$	$\begin{bmatrix}0&i\\-i&0\end{bmatrix}$	$\begin{bmatrix}0&-1\\-1&0\end{bmatrix}$	$\begin{bmatrix}0&-1\\-1&0\end{bmatrix}$	$\begin{bmatrix}0&i\\-i&0\end{bmatrix}$
M_3	$\begin{bmatrix}1&0\\0&1\end{bmatrix}$	$\begin{bmatrix}i&0\\0&-i\end{bmatrix}$	$\begin{bmatrix}-i&0\\0&i\end{bmatrix}$	$\begin{bmatrix}-1&0\\0&-1\end{bmatrix}$	$\begin{bmatrix}0&i\\-i&0\end{bmatrix}$	$\begin{bmatrix}0&-1\\-1&0\end{bmatrix}$	$\begin{bmatrix}0&1\\1&0\end{bmatrix}$	$\begin{bmatrix}0&-i\\i&0\end{bmatrix}$	$\begin{bmatrix}0&i\\-i&0\end{bmatrix}$	$\begin{bmatrix}0&1\\1&0\end{bmatrix}$	$\begin{bmatrix}0&-1\\-1&0\end{bmatrix}$	$\begin{bmatrix}0&i\\-i&0\end{bmatrix}$	$\begin{bmatrix}-1&0\\0&-1\end{bmatrix}$	$\begin{bmatrix}-i&0\\0&i\end{bmatrix}$	$\begin{bmatrix}i&0\\0&-i\end{bmatrix}$	$\begin{bmatrix}1&0\\0&1\end{bmatrix}$
M_4	$\begin{bmatrix}1&0\\0&1\end{bmatrix}$	$\begin{bmatrix}i&0\\0&-i\end{bmatrix}$	$\begin{bmatrix}-i&0\\0&i\end{bmatrix}$	$\begin{bmatrix}-1&0\\0&-1\end{bmatrix}$	$\begin{bmatrix}0&-i\\i&0\end{bmatrix}$	$\begin{bmatrix}0&1\\1&0\end{bmatrix}$	$\begin{bmatrix}0&-1\\-1&0\end{bmatrix}$	$\begin{bmatrix}0&i\\-i&0\end{bmatrix}$	$\begin{bmatrix}0&i\\-i&0\end{bmatrix}$	$\begin{bmatrix}0&1\\1&0\end{bmatrix}$	$\begin{bmatrix}0&-1\\-1&0\end{bmatrix}$	$\begin{bmatrix}0&i\\-i&0\end{bmatrix}$	$\begin{bmatrix}1&0\\0&1\end{bmatrix}$	$\begin{bmatrix}i&0\\0&-i\end{bmatrix}$	$\begin{bmatrix}-i&0\\0&i\end{bmatrix}$	$\begin{bmatrix}-1&0\\0&-1\end{bmatrix}$

***Analysing the 2×2 matrix of the M_1 irrp for example, the symmetry operators 1, 4, 15, 16, 26, 27, 38 and 39 will not change the basis of $M_1\left(\varphi_1^{M_1},\varphi_2^{M_1}\right)$, may cause S. Or. Ph. Trs. to the space subgroup containing this set of symmetry operators. Take $27\begin{pmatrix}\varphi_1^{M_1}\\\varphi_2^{M_1}\end{pmatrix}=\begin{pmatrix}0&1\\1&0\end{pmatrix}\begin{pmatrix}\varphi_1^{M_1}\\\varphi_2^{M_1}\end{pmatrix}\Rightarrow\left(\varphi_2^{M_1}+\varphi_1^{M_1}\right)$, it can be seen that symmetry operator 27 leaves the basis invariant.

Table E3c. Generating relations for the two-dimensional irrps of tetragonal phase α-WO_3 (D_{4h}^7) at the point M

.Augmenters: $4(-x,-y,z);2.1(1/2+x,1/2-y,-z);26(-x,y,z);40.1(1/2-y,1/2-x,z)$. Generating relations: $26\times26=E$, $4\times2.1=3.1$, $40.1\times26=15.1$, $15.1\times4=14.1$, $14.1\times2.1=13$, $26\times4=27$, $26\times3.1=28.1$, $15.1\times2.1=16$, $4\times40.1=37.1$, $26\times13=38$, $27\times13=39$, $2.1\times26=25.1$, where generators are 4 GEN, 2.1 GEN, 26 GEN and 40.1 GEN.

$M_1: E;4i;2;3,$

$M_2: E;4i;2;-3,$

$M_3: -E;4i;2;E,$

$M_4: -E;4i;2;-E.$

© University of Pretoria

Table E4a. Irreducible representations of G^{k_A} for space group D_{4h}^7 at $k_A=\left(\frac{1}{2},\frac{1}{2},\frac{1}{2}\right)\frac{2\pi}{a}$ ****.

α-WO_3	E	$C_{2x}\mid\tau$	$C_{2y}\mid\tau$	C_{2z}	C_{2b}	$C_{4z}^{+}\mid\tau$	$C_{4z}^{-}\mid\tau$	C_{2a}	$I\mid\tau$	σ_x	σ_y	$\sigma_z\mid\tau$	$\sigma_{db}\mid\tau$	S_{4z}^{-}	S_{4z}^{+}	$\sigma_{da}\mid\tau$
$\{g/\tau\}$	**1**	**2.1**	**3.1**	**4**	**13**	**14.1**	**15.1**	**16**	**25.1**	**26**	**27**	**28.1**	**37.1**	**38**	**39**	**40.1**
A_1	$\begin{bmatrix}1&0\\0&1\end{bmatrix}$	$\begin{bmatrix}i&0\\0&-i\end{bmatrix}$	$\begin{bmatrix}i&0\\0&-i\end{bmatrix}$	$\begin{bmatrix}1&0\\0&1\end{bmatrix}$	$\begin{bmatrix}1&0\\0&1\end{bmatrix}$	$\begin{bmatrix}-i&0\\0&i\end{bmatrix}$	$\begin{bmatrix}-i&0\\0&i\end{bmatrix}$	$\begin{bmatrix}1&0\\0&1\end{bmatrix}$	$\begin{bmatrix}0&-i\\i&0\end{bmatrix}$	$\begin{bmatrix}0&1\\1&0\end{bmatrix}$	$\begin{bmatrix}0&1\\1&0\end{bmatrix}$	$\begin{bmatrix}0&-i\\i&0\end{bmatrix}$	$\begin{bmatrix}0&-i\\i&0\end{bmatrix}$	$\begin{bmatrix}0&1\\1&0\end{bmatrix}$	$\begin{bmatrix}0&1\\1&0\end{bmatrix}$	$\begin{bmatrix}0&-i\\i&0\end{bmatrix}$
A_2	$\begin{bmatrix}1&0\\0&1\end{bmatrix}$	$\begin{bmatrix}i&0\\0&-i\end{bmatrix}$	$\begin{bmatrix}i&0\\0&-i\end{bmatrix}$	$\begin{bmatrix}1&0\\0&1\end{bmatrix}$	$\begin{bmatrix}-1&0\\0&-1\end{bmatrix}$	$\begin{bmatrix}i&0\\0&-i\end{bmatrix}$	$\begin{bmatrix}i&0\\0&-i\end{bmatrix}$	$\begin{bmatrix}-1&0\\0&-1\end{bmatrix}$	$\begin{bmatrix}0&i\\-i&0\end{bmatrix}$	$\begin{bmatrix}0&1\\1&0\end{bmatrix}$	$\begin{bmatrix}0&1\\1&0\end{bmatrix}$	$\begin{bmatrix}i&0\\0&-i\end{bmatrix}$	$\begin{bmatrix}0&i\\-i&0\end{bmatrix}$	$\begin{bmatrix}0&-1\\-1&0\end{bmatrix}$	$\begin{bmatrix}0&-1\\-1&0\end{bmatrix}$	$\begin{bmatrix}0&i\\-i&0\end{bmatrix}$
A_3	$\begin{bmatrix}1&0\\0&1\end{bmatrix}$	$\begin{bmatrix}i&0\\0&-i\end{bmatrix}$	$\begin{bmatrix}-i&0\\0&i\end{bmatrix}$	$\begin{bmatrix}-1&0\\0&-1\end{bmatrix}$	$\begin{bmatrix}0&i\\-i&0\end{bmatrix}$	$\begin{bmatrix}0&-1\\-1&0\end{bmatrix}$	$\begin{bmatrix}0&1\\1&0\end{bmatrix}$	$\begin{bmatrix}0&-i\\i&0\end{bmatrix}$	$\begin{bmatrix}0&i\\-i&0\end{bmatrix}$	$\begin{bmatrix}0&1\\1&0\end{bmatrix}$	$\begin{bmatrix}0&-1\\-1&0\end{bmatrix}$	$\begin{bmatrix}0&i\\-i&0\end{bmatrix}$	$\begin{bmatrix}-1&0\\0&-1\end{bmatrix}$	$\begin{bmatrix}-i&0\\0&i\end{bmatrix}$	$\begin{bmatrix}i&0\\0&-i\end{bmatrix}$	$\begin{bmatrix}1&0\\0&1\end{bmatrix}$
A_4	$\begin{bmatrix}1&0\\0&1\end{bmatrix}$	$\begin{bmatrix}i&0\\0&-i\end{bmatrix}$	$\begin{bmatrix}-i&0\\0&i\end{bmatrix}$	$\begin{bmatrix}-1&0\\0&-1\end{bmatrix}$	$\begin{bmatrix}0&-i\\i&0\end{bmatrix}$	$\begin{bmatrix}0&1\\1&0\end{bmatrix}$	$\begin{bmatrix}0&-1\\-1&0\end{bmatrix}$	$\begin{bmatrix}0&i\\-i&0\end{bmatrix}$	$\begin{bmatrix}0&i\\-i&0\end{bmatrix}$	$\begin{bmatrix}0&1\\1&0\end{bmatrix}$	$\begin{bmatrix}0&-1\\-1&0\end{bmatrix}$	$\begin{bmatrix}0&i\\-i&0\end{bmatrix}$	$\begin{bmatrix}1&0\\0&1\end{bmatrix}$	$\begin{bmatrix}i&0\\0&-i\end{bmatrix}$	$\begin{bmatrix}-i&0\\0&i\end{bmatrix}$	$\begin{bmatrix}-1&0\\0&-1\end{bmatrix}$

**** Analysing the 2×2 matrix of the A_2 irrp for example, the symmetry operators 1, 4, 26 and 27 will not change the basis of $A_2\left(\varphi_1^{A_2},\varphi_2^{A_2}\right)$, may cause S. Or. Ph. Trs. to the space subgroup containing this set of symmetry operators.

Table E4b. Generating relations for the two-dimensional irrps of tetragonal phase α-WO_3 (D_{4h}^7) at the A-point $k_A=\left(\frac{1}{2},\frac{1}{2},\frac{1}{2}\right)\frac{2\pi}{a}$.

Augmenters: $4(-x,-y,z);2.1(1/2+x,1/2-y,-z);26(-x,y,z);40.1(1/2-y,1/2-x,z)$. Generating relations: $26\times26=E$, $4\times2.1=3.1$, $40.1\times26=15.1$, $15.1\times4=14.1$, $14.1\times2.1=13$, $26\times4=27$, $26\times3.1=28.1$, $15.1\times2.1=16$, $4\times40.1=37.1$, $26\times13=38$, $27\times13=39$, $2.1\times26=25.1$, where generators are 4 GEN, 2.1 GEN, 26 GEN and 40.1 GEN.

$A_1: E;4i;2;3$,

$A_2: E;4i;2;-3$,

$A_3: -E;4i;2;E$,

$A_4: -E;4i;2;-E$.

© University of Pretoria

Appendix F: Raman-Scattering modes for WO_3 phases.

F1: The Raman-Active Modes of the lower symmetries of WO_3

Orthorhombic phase β-WO_3 $\left(D_{2h}^{13}\right)$

The β-WO_3 is observed experimentally at temperatures between 700-900°C. The VR of the $Pnma$ group is

$$VR = B_{1u}\left(\Gamma_{2-}(z)\right) \oplus B_{2u}\left(\Gamma_{3-}(x)\right) \oplus B_{3u}\left(\Gamma_{4-}(y)\right),$$

and the SSQ is given by

$$\left[VR \otimes VR\right]_2 = 3A_g\left(\Gamma_{1+}\right) \oplus B_{1g}\left(\Gamma_{2+}\right) \oplus B_{2g}\left(\Gamma_{3+}\right) \oplus B_{3g}\left(\Gamma_{4+}\right).$$

Monoclinic phase γ-WO_3 $\left(C_{2h}^{5}\right)$

The γ-WO_3 is observed experimentally between room temperature and 330°C. The VR of the $P2_1/a$ group is

$$VR = A_u\left(\Gamma_{1-}(z)\right) \oplus B_u\left(\Gamma_{2-}(x,y)\right),$$

and the SSQ is given by

$$\left[VR \otimes VR\right]_2 = 4A_g\left(\Gamma_{1+}\right) \oplus 2B_g\left(\Gamma_{2+}\right).$$

Triclinic phase δ-WO_3 $\left(P\bar{1}\right)$

The δ-WO_3 is observed experimentally between -40°C and room temperature. The VR of the C_i^1 group is

$$VR = A_u\left(\Gamma_{1-}(x,y,z)\right),$$

and the SSQ is given by

$$\left[VR \otimes VR\right]_2 = 6A_g\left(\Gamma_{1+}\right).$$

© University of Pretoria

F2: The Irreducible Representations (Irrps) of the Γ-points of the Space groups of the different phases of WO_3.

Table F1a. Irreducible representations of G^{k_Γ} for space group D_{4h}^{7} at $\boldsymbol{k}_\Gamma = (0,0,0)\frac{2\pi}{a}$.

α-WO_3	E	$C_{2x}\mid\tau$	$C_{2y}\mid\tau$	C_{2z}	C_{2b}	$C_{4z}^{+}\mid\tau$	$C_{4z}^{-}\mid\tau$	C_{2a}	$I\mid\tau$	σ_x	σ_y	$\sigma_z\mid\tau$	$\sigma_{db}\mid\tau$	S_{4z}^{-}	S_{4z}^{+}	$\sigma_{da}\mid\tau$
$\{g/\tau\}$	**1**	**2.1**	**3.1**	**4**	**13**	**14.1**	**15.1**	**16**	**25.1**	**26**	**27**	**28.1**	**37.1**	**38**	**39**	**40.1**
Γ_{1+}	1	1	1	1	1	1	1	1	1	1	1	1	1	1	1	1
Γ_{2+}	1	1	1	1	-1	-1	-1	-1	1	1	1	1	-1	-1	-1	-1
Γ_{3+}	1	-1	-1	1	-1	1	1	-1	1	-1	-1	1	-1	1	1	-1
Γ_{4+}	1	-1	-1	1	1	-1	-1	1	1	-1	-1	1	1	-1	-1	1
Γ_{5+}	$\begin{bmatrix}1&0\\0&1\end{bmatrix}$	$\begin{bmatrix}1&0\\0&-1\end{bmatrix}$	$\begin{bmatrix}-1&0\\0&1\end{bmatrix}$	$\begin{bmatrix}-1&0\\0&-1\end{bmatrix}$	$\begin{bmatrix}0&-1\\-1&0\end{bmatrix}$	$\begin{bmatrix}0&-1\\1&0\end{bmatrix}$	$\begin{bmatrix}0&1\\-1&0\end{bmatrix}$	$\begin{bmatrix}0&1\\1&0\end{bmatrix}$	$\begin{bmatrix}1&0\\0&1\end{bmatrix}$	$\begin{bmatrix}1&0\\0&-1\end{bmatrix}$	$\begin{bmatrix}-1&0\\0&1\end{bmatrix}$	$\begin{bmatrix}-1&0\\0&-1\end{bmatrix}$	$\begin{bmatrix}0&-1\\-1&0\end{bmatrix}$	$\begin{bmatrix}0&-1\\1&0\end{bmatrix}$	$\begin{bmatrix}0&1\\-1&0\end{bmatrix}$	$\begin{bmatrix}0&1\\1&0\end{bmatrix}$
Γ_{1-}	1	1	1	1	1	1	1	1	-1	-1	-1	-1	-1	-1	-1	-1
Γ_{2-}	1	1	1	1	-1	-1	-1	-1	-1	-1	-1	-1	1	1	1	1
$\Gamma_{3-}(z)$	1	-1	-1	1	-1	1	1	-1	-1	1	1	-1	1	-1	-1	1
Γ_{4-}	1	-1	-1	1	1	-1	-1	1	-1	1	1	-1	-1	1	1	-1
$\Gamma_{5-}(x,y)$	$\begin{bmatrix}1&0\\0&1\end{bmatrix}$	$\begin{bmatrix}1&0\\0&-1\end{bmatrix}$	$\begin{bmatrix}-1&0\\0&1\end{bmatrix}$	$\begin{bmatrix}-1&0\\0&-1\end{bmatrix}$	$\begin{bmatrix}0&1\\1&0\end{bmatrix}$	$\begin{bmatrix}0&1\\-1&0\end{bmatrix}$	$\begin{bmatrix}0&-1\\1&0\end{bmatrix}$	$\begin{bmatrix}0&-1\\-1&0\end{bmatrix}$	$\begin{bmatrix}-1&0\\0&-1\end{bmatrix}$	$\begin{bmatrix}-1&0\\0&1\end{bmatrix}$	$\begin{bmatrix}1&0\\0&-1\end{bmatrix}$	$\begin{bmatrix}1&0\\0&1\end{bmatrix}$	$\begin{bmatrix}0&-1\\-1&0\end{bmatrix}$	$\begin{bmatrix}0&-1\\1&0\end{bmatrix}$	$\begin{bmatrix}0&1\\-1&0\end{bmatrix}$	$\begin{bmatrix}0&1\\1&0\end{bmatrix}$

Table F2a. Irreducible representations of G^{k_Γ} for space group D_{2h}^{13} at $\boldsymbol{k}_\Gamma = (0,0,0)\frac{2\pi}{a}$ *.

α-WO_3	E	$C_{2x}\mid\tau$	$C_{2y}\mid\tau$	C_{2z}	$I\mid\tau$	σ_x	σ_y	$\sigma_z\mid\tau$
$\{g/\tau\}$	**1**	**2.1**	**3.1**	**4**	**25.1**	**26**	**27**	**28.1**
Γ_{1+}	1	1	1	1	1	1	1	1
Γ_{2+}	1	-1	-1	1	1	-1	-1	1
Γ_{3+}	1	1	-1	-1	1	1	-1	-1
Γ_{4+}	1	-1	1	-1	1	-1	1	-1
$\Gamma_{1-}(z)$	1	1	1	1	-1	-1	-1	-1
$\Gamma_{2-}(x)$	1	-1	-1	1	-1	1	1	-1
$\Gamma_{3-}(y)$	1	1	-1	-1	-1	-1	1	1
Γ_{4-}	1	-1	1	-1	-1	1	-1	1

*Comparing the irrp of Γ_{1+} of D_{2h}^{13} for symmetry operators 1, 2.1, 3.1, 4, 25.1, 26, 27 and 28.1 to the irrp of Γ_{1+} of D_{4h}^{7}, there is a direct correspondence and therefore compatibility.

© University of Pretoria

Table F3a. Irreducible representations of G^{k_Γ} for space group C_{2h}^5 at $\boldsymbol{k}_\Gamma = (0,0,0)\frac{2\pi}{a}$ **.

α-WO_3	E	C_{2z}	$I \mid \tau$	$\sigma_z \mid \tau$
$\{g/\tau\}$	**1**	**4**	**25.1**	**28.1**
Γ_{1+}	1	1	1	1
Γ_{2+}	1	-1	1	-1
$\Gamma_{1-}(z)$	1	1	-1	-1
$\Gamma_{2-}(x,y)$	1	-1	-1	1

*Comparing the irrp of Γ_{2+} of C_{2h}^5 for symmetry operators 1, 4, 25.1 and 28.1 to the irrp of Γ_{3+} and Γ_{4+} of D_{2h}^{13}, there is a direct correspondence and therefore compatibility. This means the Γ_{2+} of C_{2h}^5 splits into Γ_{3+} and Γ_{4+} of D_{2h}^{13} as the symmetry changes.

Table F4a. Irreducible representations of G^{k_Γ} for space group C_i^1 at $\boldsymbol{k}_\Gamma = (0,0,0)\frac{2\pi}{a}$.

α-WO_3	E	$I \mid \tau$
$\{g/\tau\}$	**1**	**25**
Γ_{1+}	1	1
$\Gamma_{1-}(x,y,z)$	1	-1

© University of Pretoria

Appendix G: Characterisation Results.

G1. FIBSEM

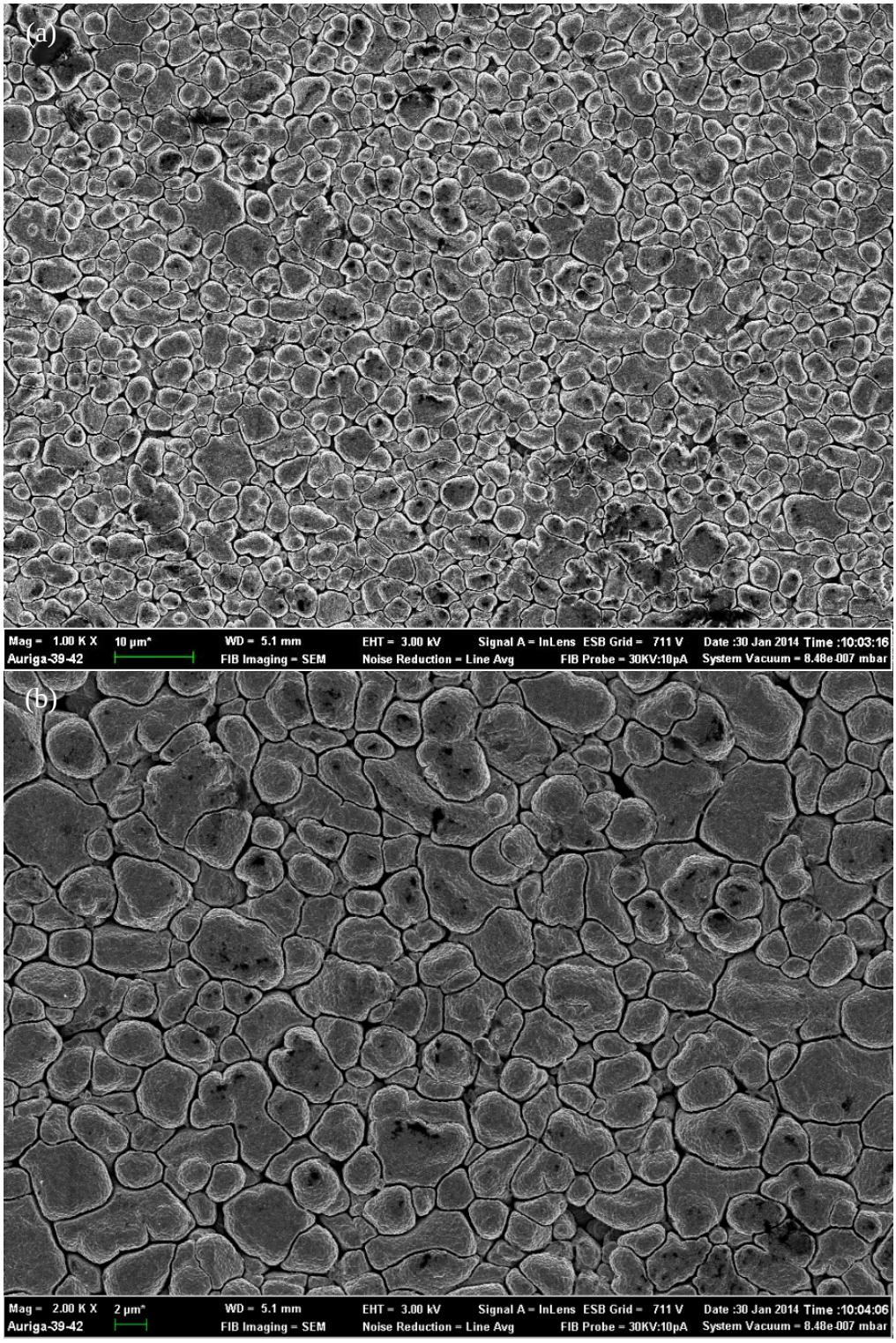

Figure G1.1. (a) A SEM micrograph taken at 1000 times magnification on the surface of the WO_3 film, and (b) SEM micrograph taken at 2000 times magnification on the surface of the WO_3 film showing the grain size distribution and tight-packing of the annealed film.

© University of Pretoria

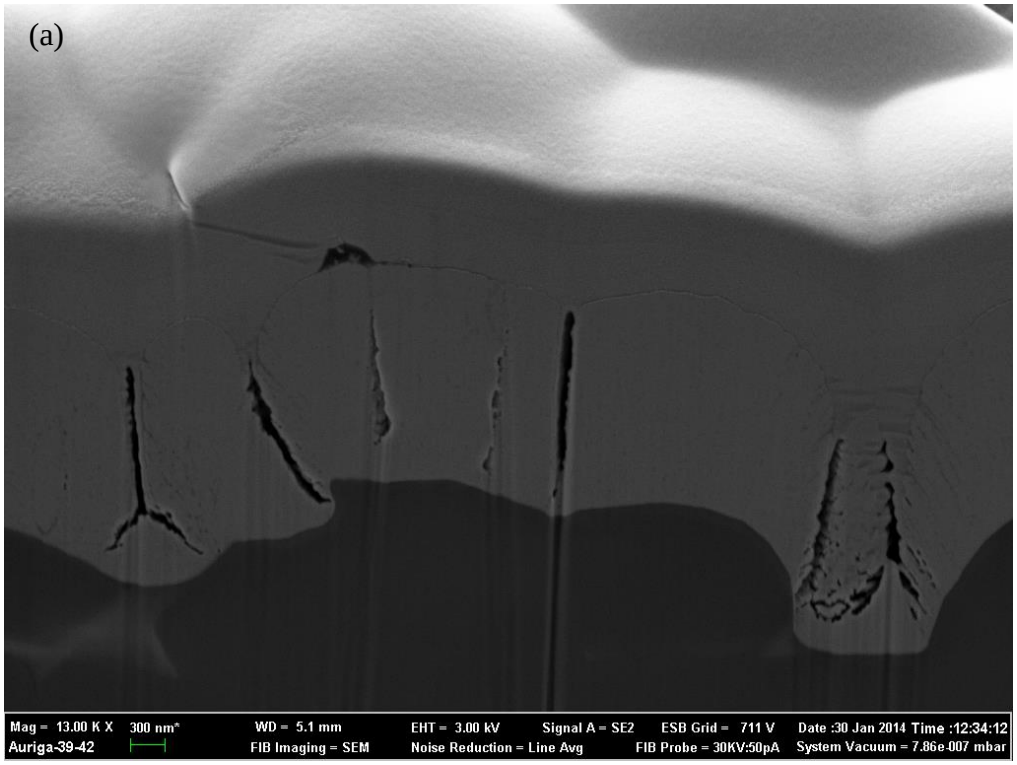

Figure G1.2. (a) A SEM micrograph taken at 13000 times magnification on the cross-section of the WO_3 film taken in the Secondary Electron Mode and showing the platinum topmost layer, cracked film layer and substrate, and (b) a SEM micrograph of a lamella of the film welded onto a copper grid with platinum to be used in TEM.

© University of Pretoria

G2. TEM

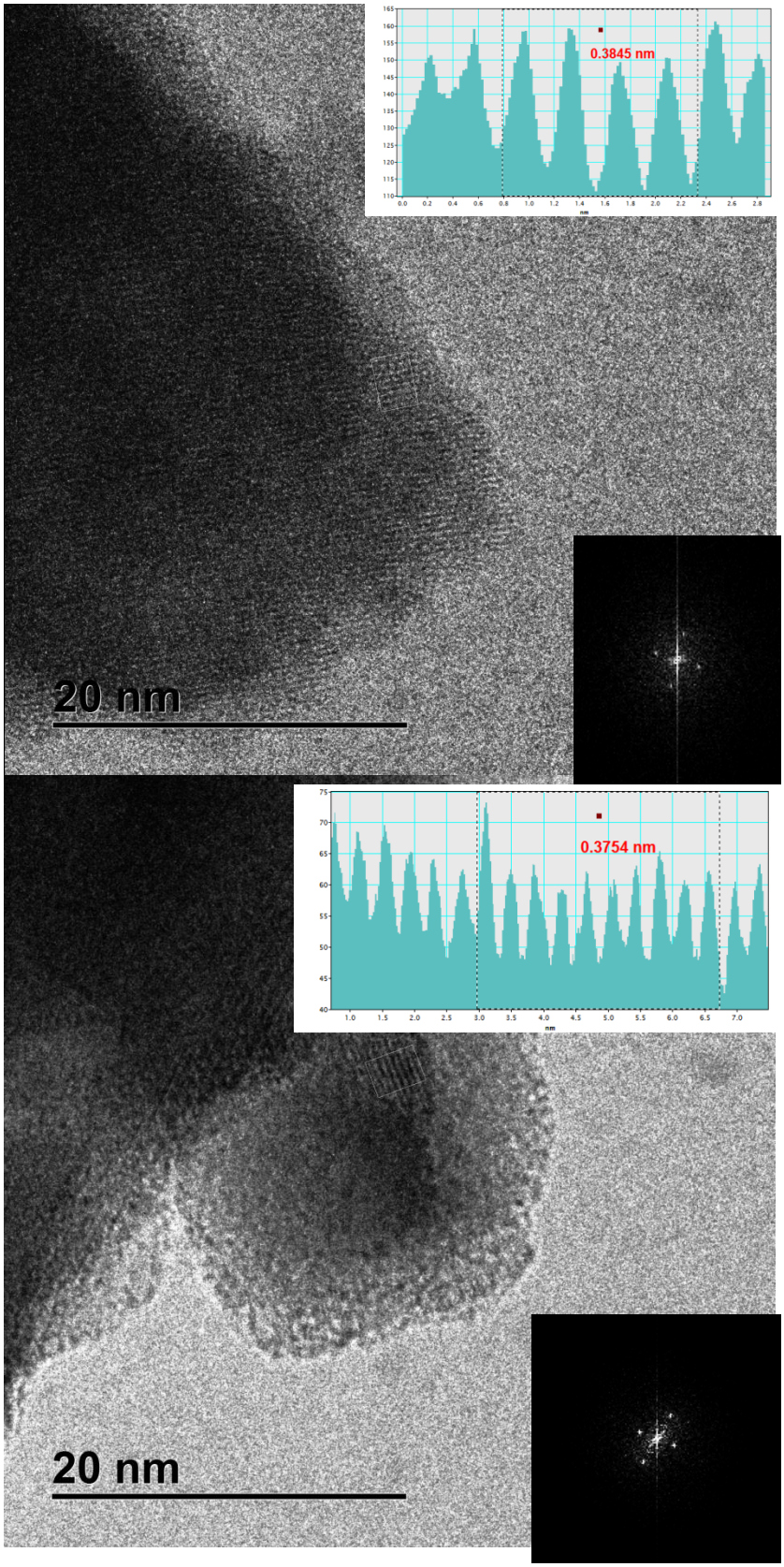

Figure G.2. An HRTEM micrograph taken at 200000 times magnification on the lamella of the WO_3 film to measure the interplanar-spacing. The inset shows the average interplanar-spacing and selected area electron diffraction pattern of single lattice.

© University of Pretoria

G3. XPS

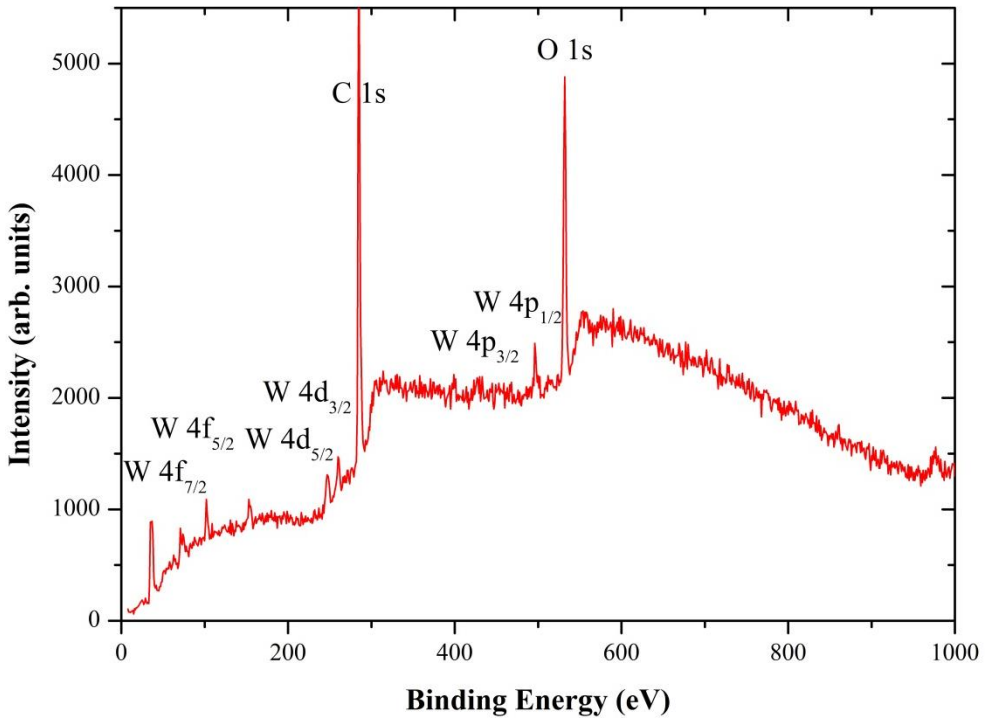

Figure G3.1. The XPS spectrum of the WO_3 film showing the binding energies of the bonds in WO_3. There is also a large carbon contamination on the surface whose origin is unknown.

G4. Raman Spectroscopy

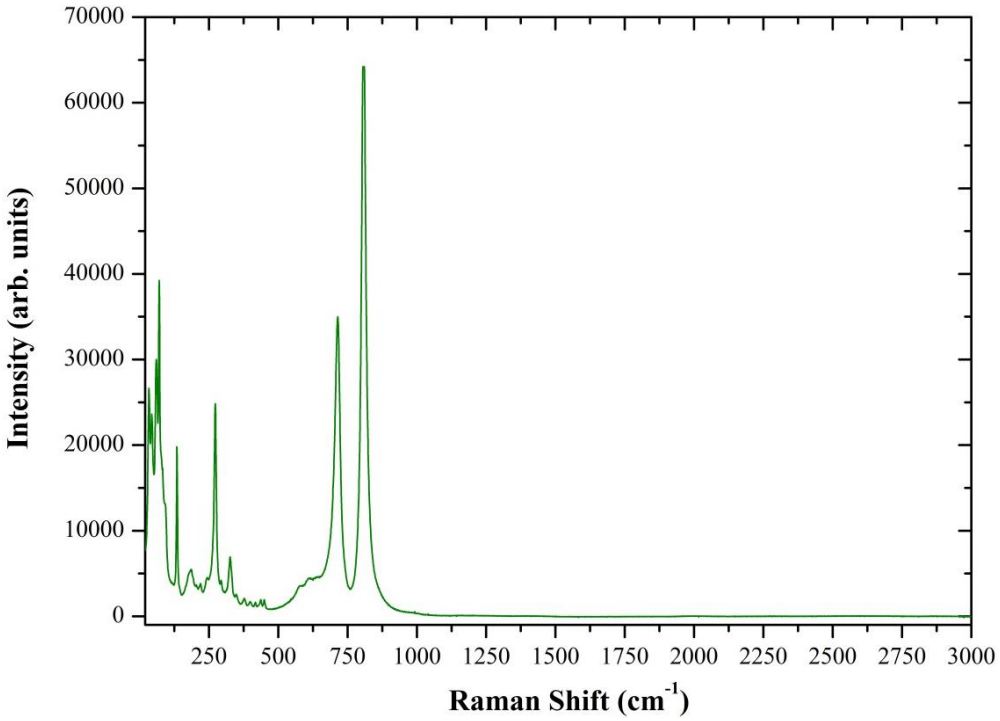

Figure G4.1. The Raman spectrum of the annealed WO_3 film taken in the extended range showing the absence of higher-order scattering processes.

© University of Pretoria

G5. PL Spectroscopy

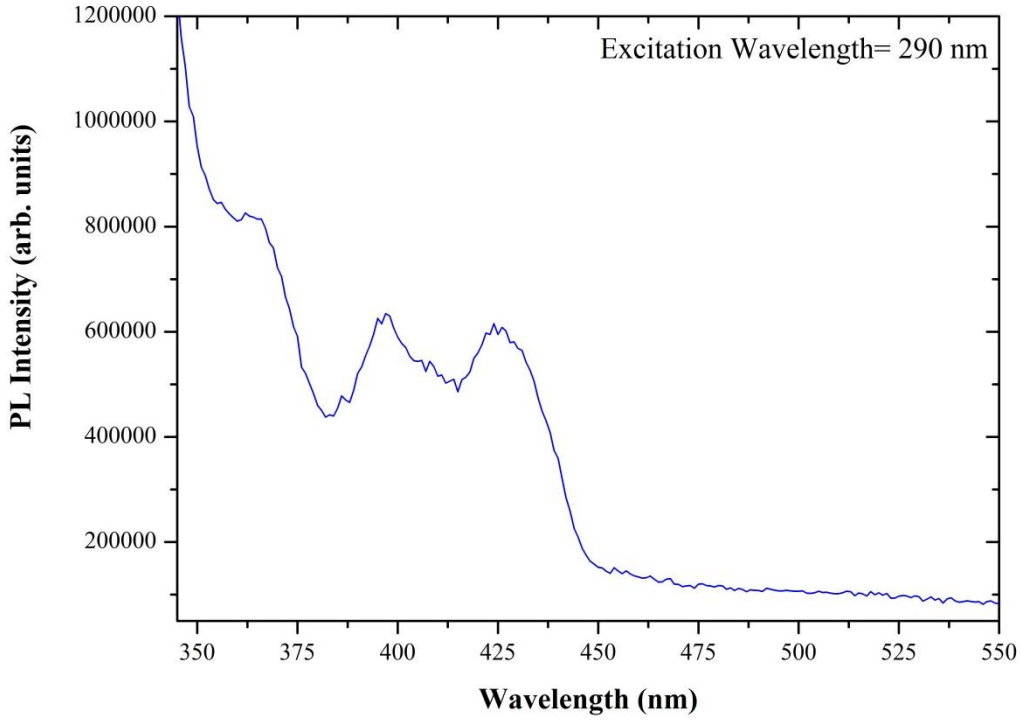

Figure G5.1. The PL spectrum of the WO_3 film taken with an excitation wavelength of 290 nm showing three distinct peaks and phonon replicas.

G6. R vs T

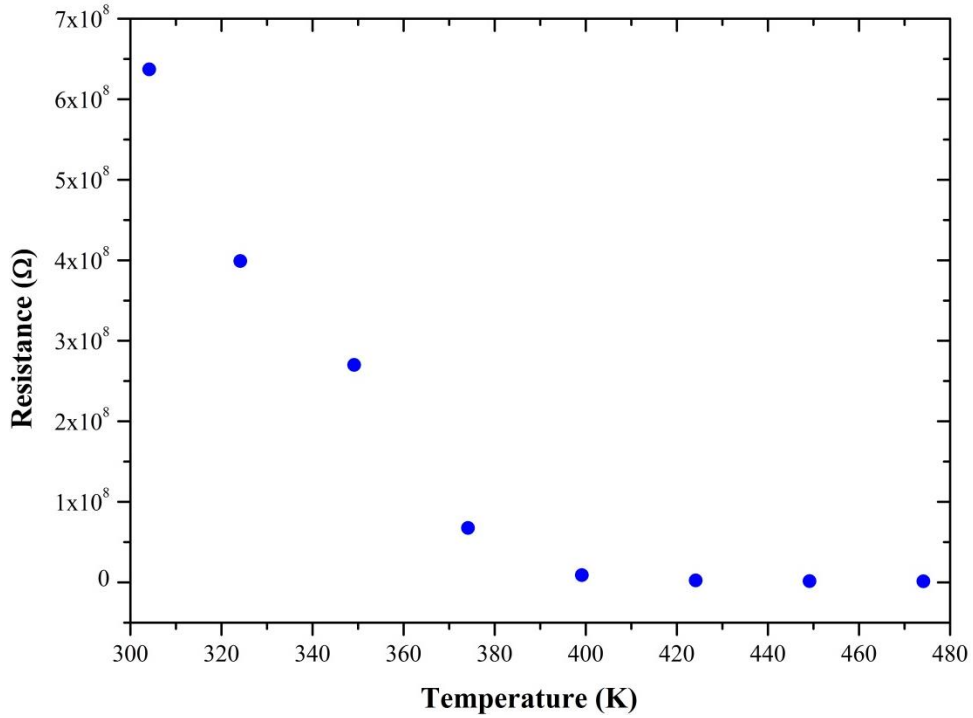

Figure G6.1. The change of resistance of the WO_3 film with temperature shows the typical exponential decrease for a metal oxide semiconductor according to the relation $R = R_0 e^{\kappa/T}$.

© University of Pretoria

G7. Gas Setup

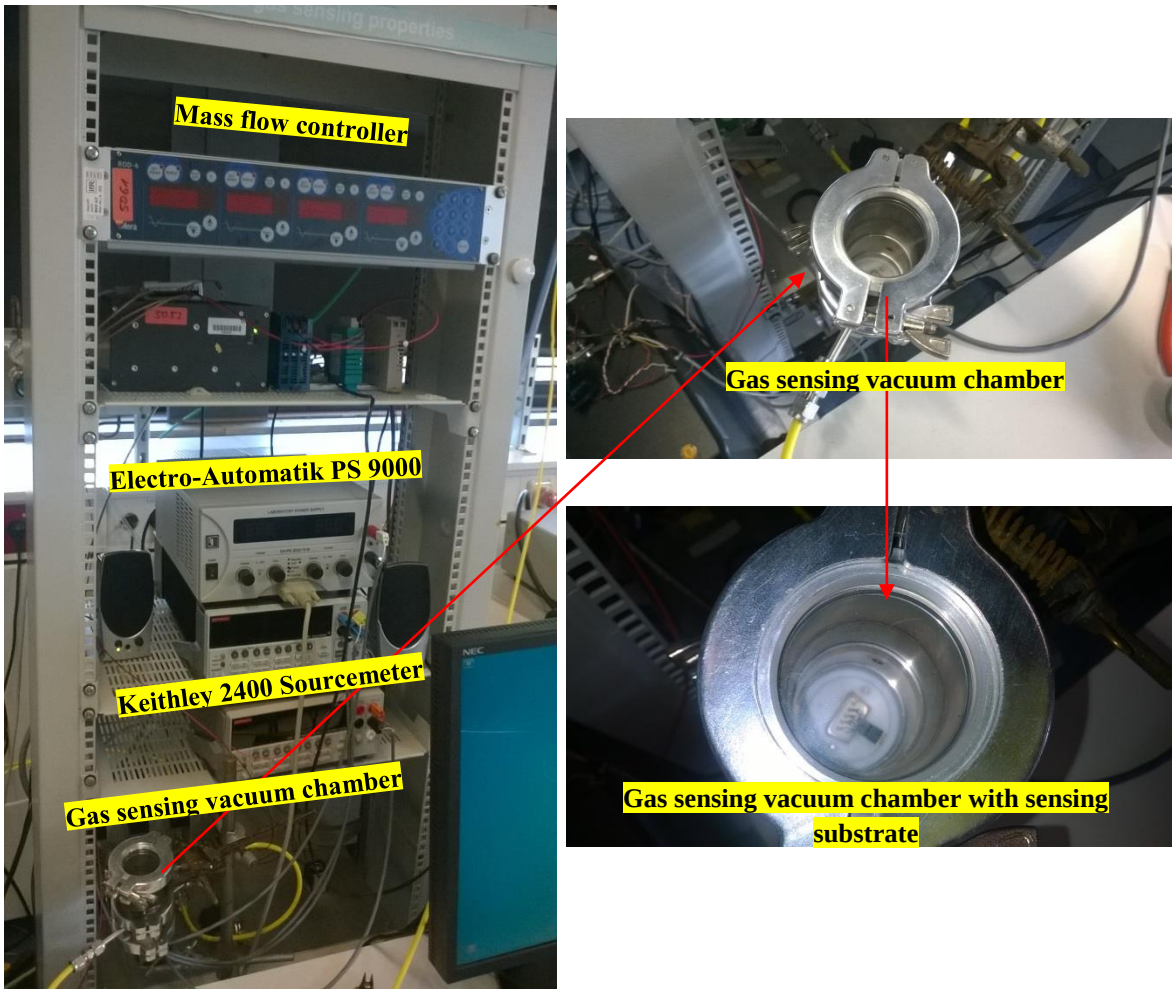

Figure G7.1. The picture shows the gas sensing setup used in this work with all its respective components.

© University of Pretoria

UNIVERSITEIT VAN PRETORIA
UNIVERSITY OF PRETORIA
YUNIBESITHI YA PRETORIA

Phys. Status Solidi C **9**, No. 10–11, 1978–1980 (2012) / **DOI** 10.1002/pssc.201200097

physica status solidi c
www.pss-c.com
current topics in solid state physics

Clebsch-Gordan coefficients for scattering processes in Si and Ge

H. W. Kunert[1], A. G. J. Machatine[*,1], P. Niyongabo[1], M. Govender[1,2], and B. W. Mwakikunga[2]

[1] Department of Physics, University of Pretoria, Pretoria 0002, South Africa
[2] CSIR National Centre for Nano-Structured Materials, P.O.Box 395, Pretoria 0001, South Africa

Received 29 April 2012, revised 30 May 2012, accepted 7 June 2012
Published online 30 July 2012

Keywords symmetrized Kronecker product, scattering processes, Si,Ge, Clebsch-Gordan coefficients, spin-orbit interaction

[*] Corresponding author: e-mail augusto.machatine@up.ac.za, Phone: +27-12-4202652, Fax: +27-362-5288

Scattering matrix for two phonon processes at $\mathbf{k} = 0$ in Si and Ge of O_h^7 symmetry is given. Also diagonalization of spin-orbit interaction Hamiltonian has been computed by means of Clebsh-Gordan coefficients.

© 2012 WILEY-VCH Verlag GmbH & Co. KGaA, Weinheim

1 Introduction The Raman active modes (RAM's) with $\mathbf{k} = 0$ in two-phonon processes are determined by irreducible representations (irreps) contained in symmetrized Kronecker product (SKP) of single valued (SV) vector representation (VR). For Si and Ge the VR is Γ_{4-} [1] with the basis $xf(r)$, $yf(r)$ and $z(fr)$ and we have $[\Gamma_{4-} \otimes \Gamma_{4-}]$. The irreps contained in the SKP determine the RAM's symmetry allowed. The Clebsch-Gordan coefficients (CGC's) matrix which diagonalizes the Kronecker product (KP), yields correct linear combinations of allowed phonon basis wave functions.
The spin-orbit (SO) interaction represented by KP, $\Gamma_{4-} \otimes D_{\frac{1}{2}}$, involves double valued (DV) spinor irreps. Here we diagonalize the SO matrix by means of suitable CGC's matrix.

2 The simplified coupling coefficients theory The KP of two irreps l and l' is equivalent to the sum of l'' irreps contained in the product

$$D^l \otimes D^{l'} \cong \sum_R (ll' \mid l'') D^{l''} \tag{1}$$

and the basis of l'' are of the form :

$$\psi_\alpha^{l''} = \sum U_{\alpha\beta}^{ll'} \psi_\alpha^l \psi_\beta^{l'} \tag{2}$$

The matrix elements of U are determined by

$$U_{aa',a''}^{ll',l''} U_{\bar{a}\bar{a}'\bar{a}''}^{ll',l''*} = \frac{l''}{g} \sum_R D^l(R)_{a\bar{a}} D^{l'}(R)_{a'\bar{a}'} D^{l''*}(R)_{a''\bar{a}''} \tag{3}$$

and putting $a = \bar{a} = a_0, a' = \bar{a}' = \bar{a}'_0, a'' = \bar{a}'' = \bar{a}''_0$

we calculate non-zero coefficients of $U_{a_0,a'_0a''_0} . U^*_{a_0,a'_0a''_0} = |U_{a_0,a'_0a''_0}|^2$.

Then all other matrix elements of $U_{a_0a'_0a''_0}$ are obtained from

$$U_{a_0a'_0a''_0} = \frac{1}{U^*_{a_0a'_0a''_0}} . \frac{l''}{g} \sum_R D^l(R)_{aa_0} D^{l'}(R)_{a'a'_0} D^{l''*}(R)_{a''a''_0} \tag{4}$$

3 Diagonalization of SKP for Raman active modes In this section we want to diagonalize the KP $[\Gamma_{4-} \otimes \Gamma_{4-}] \cong \Gamma_{1+} + \Gamma_{3+} + \Gamma_{5+}$.
The CGC's U matrix brings the above KP to the block diagonal form:
$U^{-1}[\Gamma_{4-} \otimes \Gamma_{4-}]U = \Gamma_{1+} \oplus \Gamma_{3+} \oplus \Gamma_{5+}$.

For SKP of identical irreps, $l = l' = \Gamma_{4-}$ we reformu-

© 2012 WILEY-VCH Verlag GmbH & Co. KGaA, Weinheim

© University of Pretoria

UNIVERSITEIT VAN PRETORIA
UNIVERSITY OF PRETORIA
YUNIBESITHI YA PRETORIA

Contributed Article

late the standard Eq. (3) in the following manner:

$$U^{\Gamma_{4-}\Gamma_{4-},l''}_{aa',a''} U^{\Gamma_{4-}\Gamma_{4-},l''*}_{\bar{a}\bar{a}'\bar{a}''} = \frac{dim(l'')}{2g} \sum_R [(\Gamma_{4-})_{aa'}(\Gamma_{4-})_{\bar{a}\bar{a}'} + (\Gamma_{4-})_{\bar{a}a'}(\Gamma_{4-})_{a\bar{a}'}] .\Gamma^{l''*}_{a''\bar{a}''} \quad (5)$$

where the irreps l'' are $\Gamma_{1+}, \Gamma_{2+}, \Gamma_{5+}$.

The diagonal elements of SKP $[\Gamma_{4-} \otimes \Gamma_{4-}]^s_{a\bar{a},a'\bar{a}'}$ are obtained using the index relation: $a\bar{a}, a'\bar{a}' \longrightarrow (aa'\bar{a}\bar{a}' + \bar{a}a'a\bar{a}')$ and
$U_s^{-1}[\Gamma_{4-} \otimes \Gamma_{4-}]_2 U_s = \Gamma_{1+} \oplus \Gamma_{3+} \oplus \Gamma_{5+}$

For calculation of non-zero diagonal elements we have: $a = \bar{a} = a_0, a' = \bar{a}' = a'_0, a'' = \bar{a}'' = a''_0$

$$U_{aa'a''} U^*_{a_0 a'_0 a''} = \frac{dim(l'')}{2g} \sum_R [(\Gamma_{4-}(R))_{a\bar{a}_0}(\Gamma_{4-}(R))_{a'\bar{a}'_0} + (\Gamma_{4-}(R))_{a''\bar{a}''_0}(\Gamma_{4-}(R))_{a''\bar{a}''_0}] .\Gamma^{l''*}_{a''\bar{a}''_0}(R) \quad (6)$$

Having the non-zero diagonal matrix elements, we calculate the remaining matrix elements of U as follows.

$$U_{aa'a''} = \frac{dim(l'')}{2g} \frac{1}{U^*_{a_0 a'_0 a''_0}} \sum_R [(\Gamma_{4-})_{a\bar{a}_0}(\Gamma_{4-})_{a'\bar{a}_0'} + (\Gamma_{4-})_{a''\bar{a}_0''}(\Gamma_{4-})_{a''\bar{a}_0''}] .D^{l''*}_{a''\bar{a}_0''} \quad (7)$$

The obtained U matrix is:

$$U = \begin{bmatrix} \pm b & \pm b & \pm b & 0 & 0 & 0 \\ 0 & 0 & 0 & 0 & 0 & \pm a \\ 0 & 0 & & 0 & \pm a & 0 \\ 0 & 0 & 0 & 0 & 0 & \pm a \\ \pm b & \pm w^\star b & \pm wb & 0 & 0 & 0 \\ 0 & 0 & 0 & \pm a & 0 & 0 \\ 0 & 0 & 0 & 0 & \pm a & 0 \\ 0 & 0 & 0 & \pm a & 0 & 0 \\ \pm b & \pm wb & \pm w^\star b & 0 & 0 & 0 \end{bmatrix} \quad (8)$$

where: $a = \frac{1}{\sqrt{2}}, b = \frac{1}{\sqrt{3}}$, and $w = -\frac{1}{2} + i\frac{\sqrt{3}}{2}$.
The matrix U diagonalizes the SKP

$$U^{-1}[\Gamma_{4-} \otimes \Gamma_{4-}] U = \Gamma_{1+} \oplus \Gamma_{3+} \oplus \Gamma_{5+} \quad (9)$$

The coefficients of the first column give an appropriate combination of phonon Γ_{1+} wave function: $\varphi^{\Gamma_{1+}}_{ph} = \pm bf(r)(x^2 + y^2 + z^2)$. Similarly the $\varphi^{\Gamma_{3+}}_{ph}$ and $\varphi^{\Gamma_{5+}}_{ph}$ can be constructed.

4 Diagonalization of spin-orbit interaction In this section we give second example of diagonalization of SO effective Hamiltonian frequently needed for band structure calculation in semiconductor. Particularly the $\bar{k}.\hat{p}$ perturbation method is very useful in the determination of $E(\bar{k})$. In the $\bar{\mathbf{k}}.\hat{\mathbf{p}}$ expansion to second degree in $\bar{k}$ the inclusion of SO interaction leads to 6×6 matrix: $\Gamma_{4-} \otimes D_{\frac{1}{2}}$ where $D_{\frac{1}{2}}(\alpha, \beta, \gamma)$ for full rotational group O_h^7 space group operators becomes Γ_{6+}[1] and therefore again we deal with KP; $\Gamma_{4-} \otimes \Gamma_{6+}$ which decomposed takes a form $\Gamma_{4-} \otimes \Gamma_{6+} \cong \Gamma_{8-} \oplus \Gamma_{6-}$. It means the top of three fold degenerate valence band of Γ_{4-} in Si and Ge splits onto Γ_{8-}(four fold degenerate hole states) and Γ_{6-}(two fold degenerate). The energy distance between Γ_{8-} and Γ_{6-} is the energy of SO interaction. The SO matrix elements can be straight forward computed using general formula:

$$\mathbf{H}_{so} = \frac{\hbar}{4m_0^2 c^2} (\nabla U \times \hat{\mathbf{p}}) \hat{\sigma} \quad (10)$$

The $\sigma_x, \sigma_y, \sigma_z$ are Pauli matrices. Choosing the basis:

$$\varphi_1 = yzf(r) \begin{pmatrix} 1 \\ 0 \end{pmatrix}, \varphi_2 = zxf(r) \begin{pmatrix} 1 \\ 0 \end{pmatrix}$$
$$\varphi_3 = xyf(r) \begin{pmatrix} 1 \\ 0 \end{pmatrix}, \varphi_4 = yzf(r) \begin{pmatrix} 0 \\ 1 \end{pmatrix}$$
$$\varphi_5 = zxf(r) \begin{pmatrix} 0 \\ 1 \end{pmatrix}, \varphi_6 = xyf(r) \begin{pmatrix} 0 \\ 1 \end{pmatrix}$$

one obtains:

$$H_{so} = -\frac{\Delta}{3} \begin{bmatrix} 0 & i & 0 & 0 & 0 & -1 \\ -i & 0 & 0 & 0 & 0 & i \\ 0 & 0 & 0 & 1 & -i & 0 \\ 0 & 0 & 1 & 0 & -i & 0 \\ 0 & 0 & i & i & 0 & 0 \\ -1 & -i & 0 & 0 & 0 & 0 \end{bmatrix} \quad (11)$$

where Δ is the SO energy distance between $P_{\frac{3}{2}}$ and $P_{\frac{1}{2}}$ hole states. In the Kane's Jm_s base [3] the matrix is diagonalized

$$H_{11} = H_{22} = H_{44} = H_{55} = \frac{\Delta}{3},$$
$$H_{33} = H_{66} = \frac{-2\Delta}{3}$$

where the new basis functions are given in terms of the old φ_i (i = 1 - 6) by CGC's matrix [3].

$$\varphi_j = \sum_{j=1}^{6} U_{ji} \varphi_i \quad (12)$$

The matrix U in Eq. (11) is the CGC's matrix that must be calculated by rigid group theoretical method using Eqs.

© 2012 WILEY-VCH Verlag GmbH & Co. KGaA, Weinheim

© University of Pretoria

(3), (4), (9) in our paper.
The SO Hamiltonian transforms according to the KP: $\Gamma_{4-} \otimes \Gamma_{6+}$ which contains the symmetry of heavy holes Γ_{8-} and the symmetry of light holes Γ_{6-}.

$$U^{-1}(\Gamma_{4-} \otimes \Gamma_{6+})U = \Gamma_{8-} \oplus \Gamma_{6-} \tag{13}$$

In order to perform calculations we have computed the 96 matrices of following irreps $\Gamma_{4-}, \Gamma_{6+}, \Gamma_{8-}$ and Γ_{6-} using augmenters from [1]. The resulting U matrix is:

$$U = \frac{1}{2}\begin{bmatrix} -1 & i & 0 & 0 & 0 & -1 \\ -i & -1 & 0 & 0 & 0 & i \\ 0 & 0 & -1 & 1 & -i & 0 \\ 0 & 0 & 1 & -1 & -i & 0 \\ 0 & 0 & i & i & -1 & 0 \\ -1 & -i & 0 & 0 & 0 & -1 \end{bmatrix} \tag{14}$$

Clearly our group theoretical diagonalization method by means of Eqs. (3), (4) is the most rigid and correct way.

5 Discussion Our diagonalization of SKP regarded to two-phonon processes can be used in analysis of Raman spectra [2]. From the Eqs. (5), (6) the correct linear combinations of RAM's wave functions follow. To our best knowledge, it is the first time that SKP is used for computing symmetrized Raman scattering tensors.
Concerning SO matrix the energy parameter Δ can not be calculated theoretically. It is measured by several experimental methods. Queisser and Panish were the first who measured Δ by photoluminescence (PL) spectroscopy from heavily doped by Zn- holes in GaAs [4]. They observed second PL band originating from transition between the lowest conduction band and split-off light hole valence band Γ_6 in GaAs with T_d^2 space group.
For Ge, $\Delta = 0.26$ meV and Si, $\Delta = 0.044$ meV have been measured by Ghosh [5].

6 Conclusion We have used group theoretical method for diagonalization of two-phonon using symmetrized Kronecker product. We also have diagonalized SO matrices. Our method can be extended to three-phonon processes as well as to other interactions like spin-spin, inter- and intravalley scattering. Our results are valid for all compounds with O_h^7 symmetry.

References

[1] A. P. Cracknell, B. L. Davies, S. C.Miller, and W. F. Love, Kronecker Product Tables, Vol. 1-4 (New York, 1979).
[2] J. L Birman, Theory of Crystal Space Groups and Lattice Dynamics (New York, 1984).
[3] A. O. Kane, Energy Band Structure in p-type Germanium and Silicon (New York, 1956), p. 82.
[4] H. J Queisser and M. B. Panish, J. Phys. Chem. Solids **28**, 1177 (1967).
[5] A. K Ghosh, Phys. Rev. **165**, 888 (1968).

© 2012 WILEY-VCH Verlag GmbH & Co. KGaA, Weinheim

© University of Pretoria

UNIVERSITEIT VAN PRETORIA
UNIVERSITY OF PRETORIA
YUNIBESITHI YA PRETORIA

Phys. Status Solidi C **9**, No. 10–11, 1974–1977 (2012) / **DOI** 10.1002/pssc.201200068

physica status solidi c
www.pss-c.com
current topics in solid state physics

Scattering tensors and optical transitions in Si and Ge

H. W. Kunert[**,1], **A. G. J. Machatine**[*,1], **P. Niyongabo**[1], **M. Govender**[1,2], **and B. W. Mwakikunga**[2]

[1] Department of Physics, University of Pretoria, Pretoria 0002, South Africa
[2] CSIR National Centre for Nano-Structured Materials, P. O. Box 395, Pretoria 0001, South Africa

Received 24 April 2012, revised 24 May 2012, accepted 27 May 2012
Published online 24 August 2012

Keywords scattering tensors, selection rules, Clebsch-Gordan coefficients, Si, Ge

[*] Corresponding author: e-mail augusto.machatine@up.ac.za, Phone: +27 124202652, Fax: +27 865466898
[**] e-mail herbert.kunert@up.ac.za, Phone: +27 12 420 3536, Fax: +27 865466898

The selection rules (SR's) for the Kronecker product (KP) of Si and Ge irreducible representations (irreps) are required to determine the intervalley scattering processes. The SR's for transitions between the lowest conduction band minima at Γ, X and L high symmetry points and the highest maximum of the valence band (VB) in the Brillouin zone of O_h^7 space group symmetry are determined. The symmetry of phonons due to electron-phonon (El-Ph) interaction follows from the KP's: $L_1 \otimes \Gamma_{12}(\Gamma_{2-})$, $\Delta_1 \otimes \Gamma_{12}(\Gamma_{2-})$, $L_1(L_{1+}) \otimes \Delta_1$ for Ge and $L_1 \otimes \Gamma_{15}(\Gamma_{4-})$, $\Delta_1 \otimes \Gamma_{15}(\Gamma_{4-})$, $L_1(L_{1+}) \otimes \Delta_1$ for Si. The elements of El-Ph scattering tensors are linear combinations of the Clebsch-Gordon coefficients (CGC's). Here we have computed the coupling coefficients relevant to scattering tensors. Our theoretical results confirm the available experimental data.

© 2012 WILEY-VCH Verlag GmbH & Co. KGaA, Weinheim

1 Introduction The scattering tensors (Sc.T's) are of great interest to experimentalists. Historically many authors have used polarized measurements to interpret and assign vibrational modes of Raman spectra and most recently this technique have become powerful research tool in many areas due to availability of lasers [1-3]. The CGC's can also be used to obtain the polarization SR's for dipole and quadrupole resonant Raman and Brillouin scattering, as well as in morphic effects. They are useful in interpretation of infrared absorption spectra in optical transitions in higher order optical processes. They also play a major role in determination of effective Hamiltonians. Birman showed [4] that the matrix elements of any Hamiltonian is prescribed as a sum of symmetry adapted components of symmetrised base times CGC's. The utility of CGC's can also be extended to second order phase transition phenomena where the so-called active representations (AR's) are needed. The antisymmetrized square and symmetrised cube of AR's involve CGC's. In this work we focus on intravalleys (Intra.V) and intervalleys (Inter.V) scattering of quasiparticles by phonons in Si and Ge, those were discussed by Lax et al. [5] and Birman et al. [6].

In order to establish the SR's associated with scattering processes the Wave Vector Selection Rules (WVSR's) have to be determined. The WVSR's are a primary step in finding the appropriate scattering tensors. The El-Ph interaction in Si and Ge is represented by the KP of the following irreps:

Ge: $\Gamma_{2-} \otimes L_1$, $\Gamma_{2-} \otimes \Delta_1$, $L_1 \otimes \Delta_1$

Si: $\Gamma_{4-} \otimes L_1$, $\Gamma_{4-} \otimes \Delta_1$, $L_1 \otimes \Delta_1$.

In general, the KP is reducible to the irreps of phonons $D^{*\mathbf{k}''l''}$, according to

$$D^{*\mathbf{k}l} \otimes D^{*\mathbf{k}'l'} \cong \sum c_{ll'l''}(j) D^{*\mathbf{k}''l''}. \quad (1)$$

The CGC's matrix diagonalises the El-Ph perturbation determined by the KP of irreps in a given Hamiltonian $\boldsymbol{H}$, and following from Eq. (1):

$$U^{-1}\left[D^{*\mathbf{k}l} \otimes D^{*\mathbf{k}'l'}\right]U = \sum c_{ll'l''}(j) D^{*\mathbf{k}''l''}. \quad (2)$$

In Eq. (2), the matrices of irreps l'' have diagonal block form. For calculations of U matrices we use the Birman

© 2012 WILEY-VCH Verlag GmbH & Co. KGaA, Weinheim

© University of Pretoria

UNIVERSITEIT VAN PRETORIA
UNIVERSITY OF PRETORIA
YUNIBESITHI YA PRETORIA

Contributed Article

method [7] and the CDML reps labelling [8]. It is the aim of this paper to obtain the U matrices for several scattering processes in Si and Ge.

2 The wave vector selection rules In this section we discuss the WVSR's for Inter.V and Intra.V scattering processes. In Ge there are four equivalent minima at the L point which are obtained from the star of the first wave vector denoted by $\mathbf{k}_L = \frac{\pi}{a}(1,1,1)$ of the little group $G^{\mathbf{k}_L}$. The star $\mathbf{k}_L$ is $\{^*\mathbf{k}_L\} = \{E\mathbf{k}_L, C_{2x}\mathbf{k}_L, C_{2y}\mathbf{k}_L, C_{2z}\mathbf{k}_L\}$ with $C_{2x}\mathbf{k}_L = \frac{\pi}{a}(-1,0,0)$, $C_{2y}\mathbf{k}_L = \frac{\pi}{a}(0,-1,0)$ and $C_{2z}\mathbf{k}_L = \frac{\pi}{a}(0,0,-1)$, where the symmetry operators transforms the $\mathbf{k}_L = \frac{\pi}{a}(1,1,1)$ into the remaining valleys. The WVSR for these scattering processes are listed in Tables 1 and 2 and the symmetry operators $E(1)$, $C_{2x}(2)$, $C_{2y}(3)$, $C_{2z}(4)$ and $C_{31}^{-}(5)$, $C_{31}^{+}(9)$ are labelled in CDML notation [8].

In Ge for Intra.V and Inter.V scattering processes within the four *L*-valleys and three *X*-valleys, the WVSR's and the CGC's are presented in Tables 1 and 2.

In Silicon the Inter.V scattering between the one Γ-valley and six Δ-valleys are governed by SR's listed in Table 3 $(\mathbf{k}_\Delta + \mathbf{k}_\Gamma = \mathbf{k}_\Delta)$ together with appropriate CGC's for these scattering processes. Empty places in the tables mean zero matrix elements.

Table 1 Clebsch-Gordan coeffiecients for scattering within valleys of the same symmetry type: $a = \frac{1}{2}$.

$L_{1+} \otimes L_{1+} =$	$\Gamma_{1+} \oplus$		Γ_{5+}	
WVSR's	1	1	2	3
$1\mathbf{k}_L + 1\mathbf{k}_L = \mathbf{k}_\Gamma$	*a*	*a*	*a*	*a*
$2\mathbf{k}_L + 2\mathbf{k}_L = \mathbf{k}_\Gamma$	*a*	*-a*	*a*	*-a*
$3\mathbf{k}_L + 3\mathbf{k}_L = \mathbf{k}_\Gamma$	*a*	*-a*	*-a*	*a*
$4\mathbf{k}_L + 4\mathbf{k}_L = \mathbf{k}_\Gamma$	*a*	*a*	*-a*	*a*

Table 2 Clebsch-Gordan coefficients for scattering between different valleys of the same symmetry type: $b = \frac{\sqrt{2}}{2}i$ and $c = \frac{\sqrt{2}}{2}$.

$[L_{1+} \otimes L_{1+}]_2$	X_1					
	1	2	3	4	5	6
$1\mathbf{k}_L + 3\mathbf{k}_L = \mathbf{k}_X$	*c*	*-b*				
$2\mathbf{k}_L + 4\mathbf{k}_L = \mathbf{k}_X$	*c*	*b*				
$1\mathbf{k}_L + 2\mathbf{k}_L = 5\mathbf{k}_X$			*c*	*b*		
$4\mathbf{k}_L + 3\mathbf{k}_L = 5\mathbf{k}_X$			*c*	*-b*		
$1\mathbf{k}_L + 4\mathbf{k}_L = 9\mathbf{k}_X$					*c*	*b*
$2\mathbf{k}_L + 3\mathbf{k}_L = 9\mathbf{k}_X$					*c*	*b*

Table 3 Clebsch-Gordon coefficients for scattering processes between different valleys Γ and Δ.

$\Gamma_{4-} \otimes \Delta_1 =$	Δ_1						$\oplus$				Δ_5							
	1	2	3	4	5	6	1	2	3	4	5	6	7	8	9	10	11	12
$\mathbf{k}_\Gamma + \mathbf{k}_\Delta = \mathbf{k}_\Delta$	0						1	0										
	0						0	*i*										
	i						0	0										
$\mathbf{k}_\Gamma + 2\mathbf{k}_\Delta = 2\mathbf{k}_\Delta$		0							-1	0								
		0							0	*i*								
		-i							0	0								
$\mathbf{k}_\Gamma + 3\mathbf{k}_\Delta = 3\mathbf{k}_\Delta$			*i*								1	0						
			0								0	*- i*						
			0								0	0						
$\mathbf{k}_\Gamma + 4\mathbf{k}_\Delta = 4\mathbf{k}_\Delta$				*- i*									0	0				
				0									1	0				
				0									0	*i*				
$\mathbf{k}_\Gamma + 5\mathbf{k}_\Delta = 5\mathbf{k}_\Delta$					*- i*										0	0		
					0										-1	0		
					0										0	*- i*		
$\mathbf{k}_\Gamma + 6\mathbf{k}_\Delta = 6\mathbf{k}_\Delta$						*i*											0	0
						0											-1	0
						0											0	*- i*

© 2012 WILEY-VCH Verlag GmbH & Co. KGaA, Weinheim

© University of Pretoria

Table 4 Generating matrices for induced representations.

O_h^7	4	2	9	26	37
L_{1+}	0 0 0 1 0 0 1 0 0 1 0 0 1 0 0 0	0 1 0 0 1 0 0 0 0 0 0 1 0 0 1 0	1 0 0 0 0 0 0 1 0 1 0 0 0 0 1 0	0 -1 0 0 1 0 0 0 0 0 0 -1 0 0 1 0	1 0 0 0 0 0 1 0 0 1 0 0 0 0 0 1
L_{2-}	0 0 0 1 0 0 1 0 0 1 0 0 1 0 0 0	0 1 0 0 1 0 0 0 0 0 1 1 0 0 0 0	1 0 0 0 0 0 0 1 0 1 0 0 0 0 1 0	0 1 0 0 -1 0 0 0 0 0 0 1 0 0 -1 0	1 0 0 0 0 0 1 0 0 1 0 0 0 0 0 1

Generators=2.2, 4.1, 9, 26.2 and 37 and generating relations. 4.1x4.1=1, 11.3x5=3.3, 2,2x5=6.2, 5x4.1=7.3, 5x2.2=8.1, 9x4.1=10.2, 9x2.2=11.3, 4.1x9=12.1, 37x25=13, 2.2x13=14.2, 3.3x13=15.3, 4.1x13=16.1, 13x9=17, 2.2x17=19.2, 4.1x17=20.1, 13x5=21, 2.2x21=22.2, 3.3x21=23.3, 4.1x21=24.1, 2.2x26.2=25, 3.3x25=27.3, 4.1x25=28.1, 6.2x25=30.2, 7.3x25=31.3, 8.1x25=32.1, 10.2x25=34.2, 11.3x25=35.3, 12.1x25=36.1, 14.2x25=38.2, 15.3x25=39, 16.1x25=40.1, 17x25=41, 18.2x25=42.2, 19.3x25=43.3, 20,1x25=44.1, 21x25=45, 21.4x25=45.4, 22.2x25=46.2, 23.3x25=25=47.3 and 24.1x25=48.1.

3 Scattering processes in Ge and Si For scattering processes between different valleys belonging to the same star, the following symmetric KP's have to be considered:

- Ge: $[\Gamma_{2'}]_{(2)}$; $[L_{1'}]_{(2)}$; $[\Delta_1]_{(2)}$
  Si: $[\Gamma_{15}]_{(2)}$; $[L_1]_{(2)}$; $[\Delta_1]_{(2)}$ in Lax et al. [2]

- Ge: $[\Gamma_{2-}]_{(2)}$; $[L_{1+}]_{(2)}$; $[\Delta_1]_{(2)}$
  Si: $[\Gamma_4]_{(2)}$; $[L_{1+}]_{(2)}$; $[\Delta_1]_{(2)}$ in CDML [5]

For scattering between one valley Γ_{2-} and four L-valleys $\mathbf{k}_L$, $2\mathbf{k}_L$, $3\mathbf{k}_L$ and $4\mathbf{k}_L$, the phonon symmetry is L_{2-} (LA) and the CGC's of U are obtained from:

$$U^{-1}\left(\Gamma_{2-}\otimes\uparrow L_{1+}\right)U=\uparrow L_{2-}. \tag{3}$$

- The $\uparrow L_{2-}$ is the full induced 4×4-dimensional rep where U is given by:

$$U=\begin{pmatrix}\pm i & 0 & 0 & 0\\ 0 & \pm i & 0 & 0\\ 0 & 0 & \pm i & 0\\ 0 & 0 & 0 & \pm i\end{pmatrix}. \tag{4}$$

In order to prove the correctness of the U matrix, we have computed the matrix U by Sakata method [9], using:

$$F=\sum_{r\in H}D'(r)\,AD^{\dagger}(r). \tag{5}$$

where all quantities have their usual meaning. In this method one uses the full induced reps. We have computed the generators of L_{2-} full induced phonon representation. It is clear that the generating matrices are not diagonal, and so the matrix U diagonalizes the KP of Eq. (3) and the rep $\uparrow L_{2-}$ on the right-hand side has a block diagonal 4×4-form. The matrix calculated by Sakata method is identical to our U matrix.

4 Discussion In Table 1, we list the WVSR's for L-Inter.V and the corresponding CGC's. The scattering processes in all valleys are the same and the symmetry of the participating phonons is $\Gamma(\mathbf{k}\approx 0)$.

In Table 2 we present the WVSR and CGC's for $[L_1\otimes L_1]_2=X_1\oplus\ldots$ Inter.V scattering between four different L-valleys. It follows that the symmetry of phonons belongs to X-valley $(\mathbf{k}_X,5\mathbf{k}_X,9\mathbf{k}_X)$. We can estimate the energy lost by an electron in emitting an acoustic phonon. In our tables we list momentum conservation principles for scattering processes. The energy of these particles must also be conserved. For $\mathbf{k}'=\mathbf{k}_L$, $\mathbf{k}'=3\mathbf{k}_L$ and $\mathbf{k}'=9\mathbf{k}_L$, we read:

$$E_{\mathbf{k}'_L}-E_{\mathbf{k}_L}=E_{Ph}(\mathbf{k}_X);\ \hbar\mathbf{k}_L-\hbar 3\mathbf{k}_L=\hbar\mathbf{q}(\mathbf{k}_X) \tag{6}$$

where $\mathbf{k}$, $\mathbf{k}'$ and $\mathbf{q}$ runs through $\mathbf{k}_L$, $2\mathbf{k}_L$, $3\mathbf{k}_L$, $4\mathbf{k}_L$, $\mathbf{k}_X$, $5\mathbf{k}_X$ and $9\mathbf{k}_X$. An electron with initial energy $E_{\mathbf{k}}$ and wave vector $\mathbf{k}$ is scattered to another energy state with $E'_{\mathbf{k}}$ and wave vector $\mathbf{k}'$. Assuming that we deal with parabolic bands and where the effective mass is given, for example, $(m_e^*)_{\perp}=1.6m_0$ in Ge [10]. Obviously our $\mathbf{q}$ lies between minimum and $5\mathbf{k}_X$. For the backscattering we have:

$$E_{\mathbf{k}'_L}-E_{\mathbf{k}_L}=h\nu_s\mathbf{q}_{\max}=2\hbar\nu_s\left(k-2m\upsilon_s^2\right), \tag{7}$$

where $\upsilon_s\cong 10^6\ m/s$ is the phonon velocity.

For $k_L\approx 4\times10^6\,\mathrm{cm}^{-1}$, $k'_L\approx 4.2\times10^6\,\mathrm{cm}^{-1}$, $E_{\mathbf{k}_L}=(\hbar\mathbf{k})^2/2m_e^*\approx 47\,\mathrm{meV}$ and $k_q\approx 8.2\times10^{-6}\,\mathrm{cm}^{-1}$, we obtain 8 meV. In emitting a phonon with the same vector $(\mathbf{k}_X,5\mathbf{k}_X,9\mathbf{k}_X)$, the electron reverses its direction and energy changes by 10% [10].

5 Conclusion In this work, we focused on utilisation of group theory with regard to matrix elements of scattering tensors which are a linear combination of Clebsch-

© 2012 WILEY-VCH Verlag GmbH & Co. KGaA, Weinheim

© University of Pretoria

UNIVERSITEIT VAN PRETORIA
UNIVERSITY OF PRETORIA
YUNIBESITHI YA PRETORIA

Gordon coefficients. The required phonon symmetries are determined by irreps contained in KP. We have calculated the U matrix for the LA phonon which diagonalizes the intervalley scattering between the Γ_{2-} valley and the four L-valleys of the same star symmetry. We also have estimated an electron energy loss to X-valley acoustic phonon emission due to L-valleys electron scattering in a quasi-elastic process in agreement with available experimental data.

References

[1] A. Jorio, M. Dresselhaus, R. Siato, and G. Dresselhaus, Raman Spectroscopy in Graphene and Related Materials (Springer, 2011); ISBN 978-3-527-40811-5.
[2] S.-L. Zhang, Raman Spectroscopy and Its Applications in Nanostructures (Wiley, 2012); ISBN 978-0-470-68610-2.
[3] M. Govender, L. Shikwambana, B.W. Mwakikunga, E. Sideras-Haddad, R.M. Erasmus, and A. Forbes, Nanoscale Res. Lett. **6**, 166 (2011).
[4] J. L Birman and T. K. Lee, Phys. Rev. B **14**, 318 (1976).
[5] M. Lax and J. J. Hopfield, Phys. Rev. **124**, 115 (1961).
[6] J. L. Birman, M. Lax, and R. Loudon, Phys. Rev. **145**, 620 (1965).
[7] J. L. Birman, Theory of Space Groups and Lattice Dynamics (Springer, 1974); ISBN 3-540-13395-X.
[8] A. P. Cracknell, B. L. Davies, S. C. Miller, and W. F. Love, Kronecker Product Tables (Plenum, New York, Washington, 1979).
[9] I. Sakata, J. Math. Phys. **15**, 1702 (1974).
[10] P. Y. Yu and M. Cardona, Fundamentals of Semiconductors (Springer, 2010).

© 2012 WILEY-VCH Verlag GmbH & Co. KGaA, Weinheim

© University of Pretoria

UNIVERSITEIT VAN PRETORIA
UNIVERSITY OF PRETORIA
YUNIBESITHI YA PRETORIA

Operating Temperature Effect in WO_3 Films for Gas Sensing

M. Govender, D. E. Motaung,*
B. W. Mwakikunga[+] IEEE Member
DST/CSIR National Centre for Nano-Structured Materials
Council for Scientific and Industrial Research
P. O. Box 395, Pretoria, 0001, South Africa
*MGovender2@csir.co.za
[+]BMwakikunga@csir.co.za

S. Umapathy, S. Sil
Department of Inorganic and Physical Chemistry,
Indian Institute of Science,
Bangalore, 560012, India

A. K. Prasad
Surface and Nanoscience Division
Indira Gandhi Centre for Atomic Research,
Kalpakkam, 603102, India

A. G. J. Machatine, H. W. Kunert
School of Physics
University of Pretoria
Pretoria, 0002, South Africa

***Abstract*— WO_3 film sputtered on Al_2O_3 was used to sense ppm concentrations of NO_2 and NH_3 gas. The optimum working temperature of the amorphous film was found to be 200°C for both the gases, in accordance with literature. However, thermo-gravimetric analysis of the films predicts a different mechanism from that in literature which speculates that there is loss of water molecules from WO_3 at 200°C and therefore better sensing response. Thermo-gravimetric analysis shows that there is an increase in weight percentage in air at 200°C, which we speculate to be due to optimum surface oxygen content which leads to better sensing response. Raman spectroscopy at 200°C supports our speculation by showing no structural change in the WO_3 compound and no shifting of the ~700 cm^{-1} peak which is indicative of water loss. Furthermore, there was a marked change in the heating-cooling hysteresis at 200°C, which could result from the optimum surface oxygen content changing the electron transport properties The 200°C may also be regarded as a new transition temperature in WO_3 although the transition is not structural (electron-phonon coupling) but is electronic in nature (electron-electron correlation) and this transition temperature could be linked to the optimum sensing temperature of WO_3.**

***Index Terms*— Gas sensing, operating temperature, thermo-gravimetric analysis, tungsten trioxide**

Manuscript received August 13, 2013. This work was supported in part by Council for Scientific and Industrial Research (CSIR), South Africa (Project No. HGER27S) and the India – Brazil – South Africa (IBSA) trilateral programme (Project No: HGER24X).

M. Govender is a PhD student registered at the University of Pretoria but conducting his research at the Council for Scientific and Industrial Research (CSIR) in Pretoria, South Africa. (Corresponding author email: MGovender2@csir.co.za, Tel: +27128413137 Fax:+27128412229

D. E. Motaung is a Senior Researcher at the DST/CSIR National Centre for Nano-Structured Materials, Pretoria, South Africa

B. W. Mwakikunga is a Principal Research Scientist at the DST/CSIR National Centre for Nano-Structured Materials in Pretoria, South Africa. (Corresponding author email: BMwakikunga@csir.co.za, Tel: +27128414771 Fax:+27128412229

A. K Prasad is a Senior Scientist in the Indira Gandhi Centre for Atomic Research in India.

S. Umapathy is a Professor of Inorganic Chemistry at the Indian Institute for Science, Bangalore, India.

Sachita Sil is a PhD student in Inorganic Chemistry at the Indian Institute for Science, Bangalore, India.

A.G.J Machatine is a Senior Lecturer in the Department of Physics of the University of Pretoria in South Africa.

H. W. Kunert is an Emeritus Professor of Physics at the Department of Physics, University of Pretoria, Pretoria, South Africa.

I. Introduction

IT is well known that tungsten trioxide (WO_3) undergoes temperature-dependent phase evolution with the stable crystalline phases being triclinic, monoclinic, orthorhombic and tetragonal [1]. The structural information of the respective phases is summarized in Table I. The symmetry of WO_3 is lowered from tetragonal α phase to triclinic δ phase as the temperature decreases, and this is accompanied by a change in the physical properties [2]. Undoped WO_3 is typically an *n*-type semiconductor at room temperature with an indirect band gap ranging from 2.6 eV to 3.3 eV for highly crystalline and amorphous WO_3, respectively.

In 1991, γ-WO_3 thin/thick films were found to have excellent sensitivity to NO_x at 300°C [3], and this metal oxide is currently still being studied for NO_x detection. WO_3 can also sense other gases such as O_3 [4], H_2S [5] and NH_3 [6] but with lower sensitivity than to that of NO_x. The selective sensing properties can be modified with dopants such as Cu [7], Cr [8] and noble metals [9] which substantially increases sensitivity.

Like other metal oxides, the sensing mechanism of WO_3 involves gas molecule adsorption, reaction with ionosorbed oxygen species and electron extraction processes [10]. It was also found that the dipole moment of the sensed gas molecules on the surface of WO_3 affects the sensitivity. As a

978-1-4673-4642-9/13/$31.00 ©2013 IEEE

© University of Pretoria

consequence, it was found that ε-WO_3 favors polar molecules as opposed to γ-WO_3 [11].

TABLE I
STRUCTURAL INFORMATION OF WO_3 PHASES [12]

Structure	Symbol	Curie Temperature (°C)	Space group
Tetragonal	α	720-900	P4/nmm
Orthorhombic	β	320~720	Pmnb
Monoclinic	γ	17-320	$P2_1/n$
Triclinic	δ	-40~17	$P\bar{1}$
Monoclinic	ε	<-40	Pc

II. EXPERIMENTAL METHODS

A. Synthesis Procedure

WO_3 films were deposited on ultrasonically cleaned Al_2O_3 substrates at room temperature (RT) by reactive dc magnetron sputtering (AJA International, Inc). A circular WO_3 target of 100 mm in diameter with a purity of 99.99% (AJA International Inc.) was used. For homogeneous deposition, the substrates were allowed to rotate during the deposition time. The discharge gas was argon flowing at 15 sccm. The chamber was first evacuated to 4×10^{-4} Pa and was then kept at 20 Pa during film deposition by filling the discharge gas. The total film thickness was found to be approximately 1139 nm.

B. Characterization

Cross-sectioning and imaging of the film was carried out using a Focused Ion Beam (FIB) system with a Crossbeam® FIB Workstation with Gemini® FESEM Column and worked in tandem with the Carl Zeiss SMT Auriga™ Scanning Electron Microscopy (SEM) microscope. The Raman spectroscopy was carried out using a Horiba Jobin-Yvon HR800UV Raman Spectrograph with at a wavelength of 514.5 nm from an argon ion laser set at a laser power of ~1 mW at the sample which was heated on a Linkam THMS hot stage (Linkam Scientific Instruments). Thermo-gravimetric analysis was carried out using a TGA Q500 (TA Instruments). Film resistance measurements were taken using a two-point probe system connected to a Keithley 4200 Semiconducting Characterization System and the sample was heated on a hot-plate with temperature control.

III. RESULTS AND DISCUSSION

A cross-section micrograph of the as-prepared film is shown in Figure 1 depicting a double-layer WO_3 with the respective thicknesses. The top layer was found to be 351.7 nm and the bottom later was found to be 748.1 nm. Note the 178.6 nm layer on the uppermost part of the film is platinum which is used to keep the film intact upon milling with FIB.

Raman analysis was carried out on the film at room temperature and 200°C, and the spectrum is shown in Figure 2. The spectrum showed the characteristic peaks of γ-WO_3 phase according to literature [13, 14] and apart for the decrease in intensity of the Raman peaks at 200°C, there was no appearance of new shifts which indicates that there was no structural changes or dehydration of the compound.

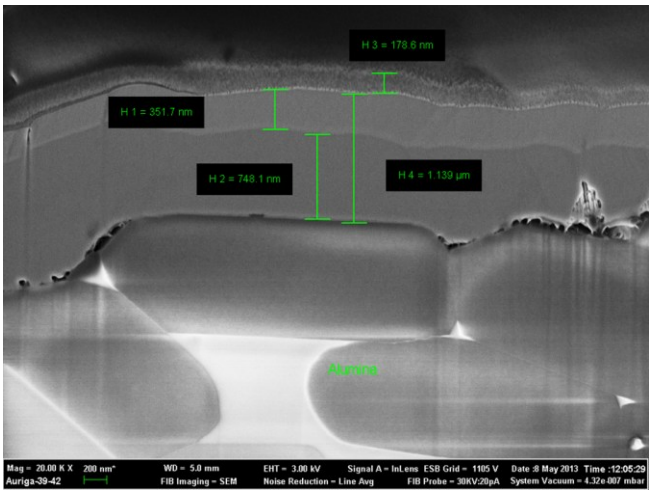

Figure 1. A cross-section micrograph of the as-prepared WO_3 film showing a double-layer with the approximate layer thicknesses.

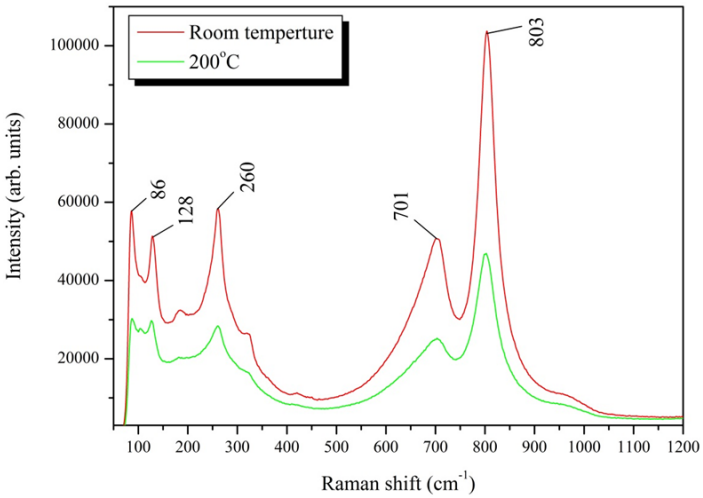

Figure 2. The Raman spectra of the as-prepared WO_3 film taken at room temperature and 200°C.

TGA was carried out in air on scrapings of the WO_3 film to check the reduction profile of the sample. This change in sample weight with temperature is shown in Figure 3. It is evident that there is a gradual loss of mass from 200˚C to about 300˚C which is probably due to evaporation of surface water and moisture or the possible formation of WO_2 or WO_{3-x}. There are two distinct weight losses at about 590-630°C and 860˚C, which may be associated with a reduction to WO_{3-x} and to W, respectively [13]. Alternatively, the distinct irregularities in the TGA spectrum correlate well with the expected phase change temperature regions of WO_3, and so we have reason to believe that TGA showed evidence of phase evolution at the higher temperatures.

© University of Pretoria

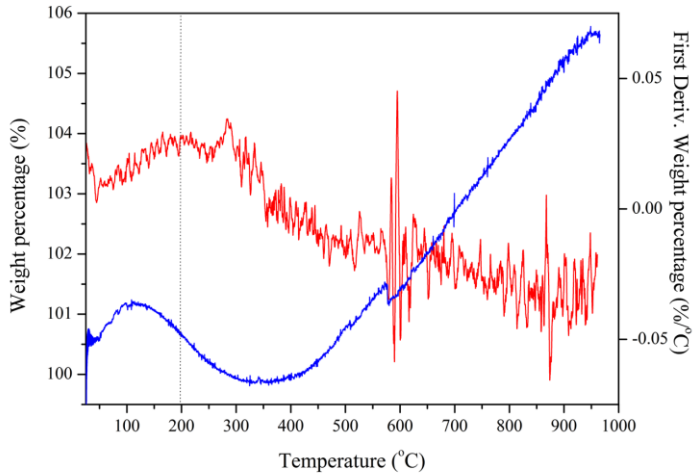

Figure 3. TGA traces of weight loss and first derivative of weight loss as a function of temperature for as-prepared WO_3.

The heating cooling hysteresis of the WO_3 resistance measurements are shown in Figure 4. We have found no evidence of structural change around 200°C, and neither can the resistance change be attributed to electron-phonon interaction model [15-17], but fits rather well to the electron-electron correlation models [16-18]. In the latter mechanism, electronic structural changes due to thermal variations results in order-of-magnitude change in conductivity of the material.

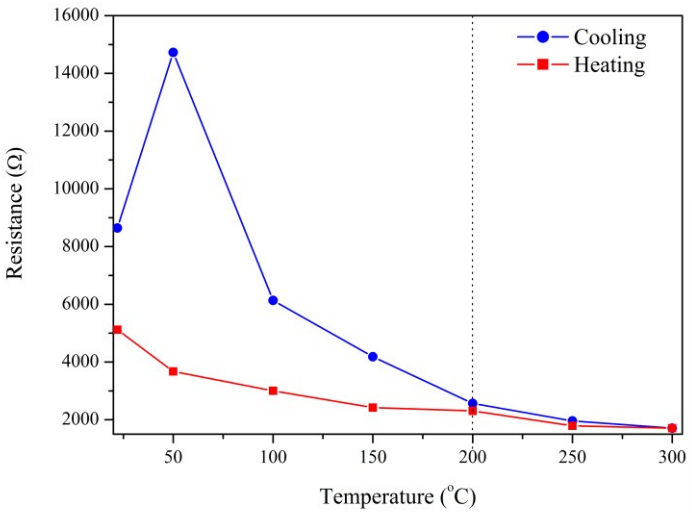

Figure 4. The heating-cooling hysteresis of resistance of the WO_3 film.

Figure 5 shows the dynamic response of the WO_3 films exposed to 50 ppm concentration of respective gas at different operating temperatures. As it can be seen from the graph, the response is obtained for as low as 100°C for both NO_2 (oxidation gas) and NH_3 (reducing gas). As the operating temperature is raised the response increases gradually and reaches a maximum at 200°C for both gases, and then decreases. At higher temperatures, increased electronic disturbance on the surface hinders the sensor activity hence the response drops. Hence 200°C is the optimum temperature for sensing.

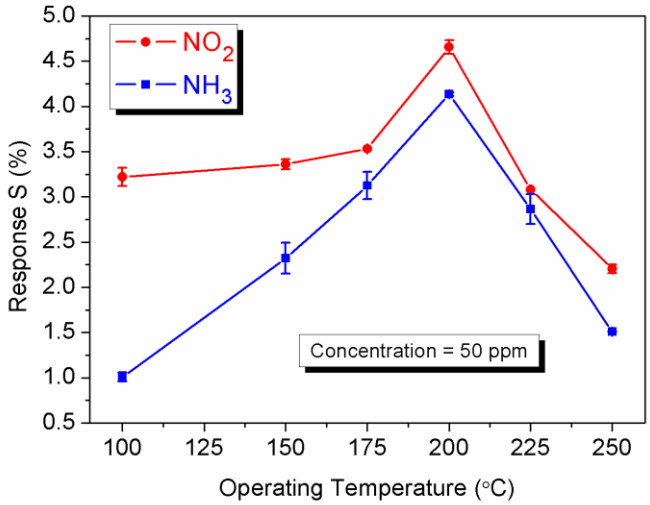

Figure 5. The WO_3 film shows optimum sensitivity response at 200°C.

Figure 6 shows the systematic response transient at the optimum sensing temperature for different concentrations of NO_2 and NH_3. Since WO_3 is an *n*-type semiconductor, the sensor resistance decreases in the presence of reducing species and increases in the presence of oxidizing species. This anomalous behavior towards NO_2 which is an oxidizing gas can be explained by the oxygen partial pressure present in the chamber. The decrease in resistance when exposed to NO_2 can hence be attributed to the interaction of the NO_2 gas molecules with the WO_3 surface at elevated temperatures. In the temperature range from 150 to 300 °C, the most stable oxygen species is O^- species [19]. The simple sensing mechanism comprises the dissociative chemisorption of the target molecules and the formation of transitory concentrations of chemisorbed atoms on the WO_3 film surface [20].

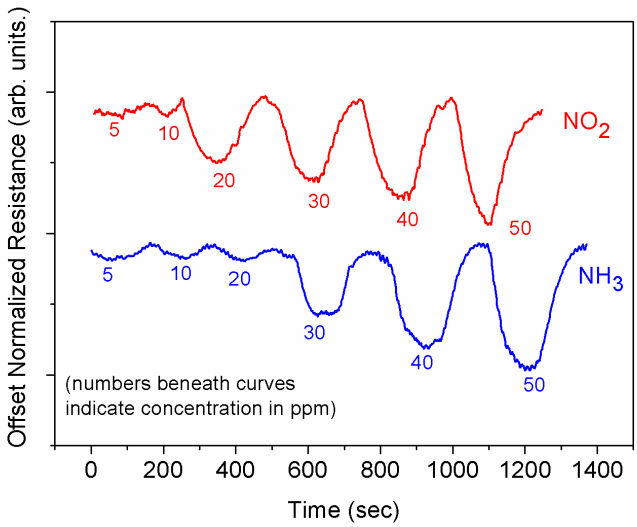

Figure 6. The WO_3 film response to different ppm-concentrations of NO_2 and NH_3 gas at 200°C.

© University of Pretoria

The interaction of the NO_2 gas species with the film can be either

$$NO_{2(gas)} + e^- \xrightarrow{200^oC} NO^-_{2(ads)}, \quad (1)$$

or

$$NO_{2(gas)} + O^-_{(ads)} \xrightarrow{200^oC} NO_{(gas)} + e^-. \quad (2)$$

At higher operating temperatures above 150°C, the amount of O^- ions available on the WO_3 surface increases considerably. Hence, in this case, the adsorbing NO_2 molecules interact directly with the adsorption sites at the oxide surface.

A similar reaction was also observed by Min [21], when NO_2 molecules interacted with the ZnO surface and occupied the active adsorption sites; the NO_2 got reduced, dissociated and released electrons. This reaction is very much dependent on the O^- states available at any particular temperature. The partial pressure of oxygen in the chamber at that temperature determines whether NO_2 reacts with the metal oxide surface directly increasing its resistance by extracting electrons, or the O^- species decreasing the resistance by releasing electrons into the material. Figure 7 shows the plot between response versus concentration for both NO_2 as well as NH_3. The degree of the greater response at 200°C for NO_2 to that of NH_3 is observed.

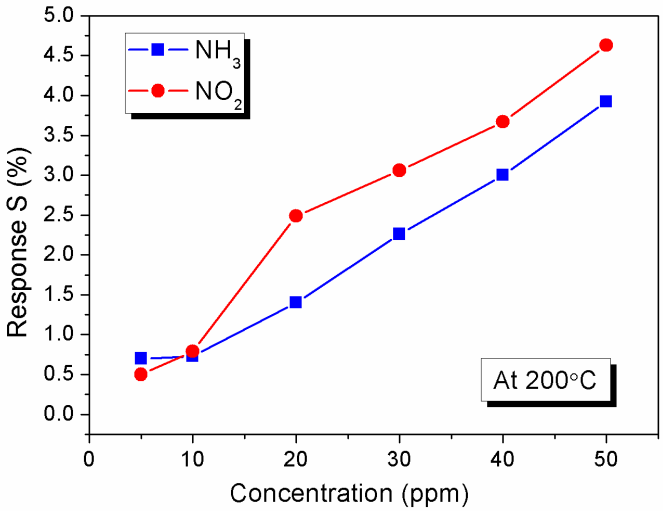

Figure 7. The plot between response versus concentration for both NO_2 as well as NH_3. It is observed that the response at 200°C for NO_2 is higher than that of NH_3.

IV. Conclusions

We have shown that WO_3 thin film has a non-structural transition temperature at 200°C, and this happens to be the optimum sensitivity response temperature to both NO_2 and NH_3. The sensing mechanism is attributed to adsorbed oxygen which is corroborated by thermo-gravimetric analytical experimental data. The sensing data shows that WO_3 is more reactive to NO_2 than NH_3 at all concentrations.

References

[1] R. Chatten, A. V. Chadwick, A. Rougier, P. J. D. Lindan, "The oxygen vacancy in crystal phases of WO_3", J. Phys. Chem. B, 2005, pp. 70-76.

[2] E. Salje, K. Viswanathan, "Physical properties and phase-transitions in WO_3", Acta Crystallogr. Sect. A, 1975, pp. 356-359.

[3] M. Akiyama, J. Tamaki, N. Miura, N. Yamazoe, "Tungsten oxide-based semiconductor sensor highly sensitive to NO and NO_2", Chem. Lett. 1991, pp. 1611-1614.

[4] M. Gillet, K. Aguir, M. Bendahan, P. Mennini, "Grain size effect in sputtered tungsten trioxide thin films on the sensitivity to ozone", Thin Solid Films, 2005, pp. 358-363.

[5] A. Ponzoni, E. Comini, G. Sberveglieri, J. Zhou, S. Z. Deng, N. S. Xu, Y. Ding, Z. L. Wang, "Ultrasensitive and highly selective gas sensors using three-dimensional tungsten oxide nanowire networks", Appl. Phys. Lett., 2006, pp. 203101 .

[6] E. Llobet, G. Molas, P. Molinas, J. Calderer, X. Vilanova, J. Brezmes, J. E. Sueris, X. Correig, "Fabrication of highly selective tungsten oxide ammonia sensors", J. Electrochem. Soc., 2000, pp. 776-779.

[7] E. Rossinyol, A. Prim, E. Pellicer, J. Rodriguez, F. Peiro, A. Cornet, J. R. Morante, B. Z. Tian, T. Bo, D. Y. Zhao, "Mesostructured pure and copper-catalyzed tungsten oxide for NO_2 detection", Sens. Actuators B Chem., 2007, pp. 18-23.

[8] E. Rossinyol, A. Prim, E. Pellicer, J. Arbiol, F. Hernandez-Ramirez, F. Peiro, A. Cornet, J. R. Morante, L. A. Solovyov, B.Z. Tian, T. Bo, D. Y. Zhao, "Synthesis and characterization of chromium-doped mesoporous tungsten oxide for gas-sensing applications", Adv. Funct. Mater., 2007, pp. 1801-1806.

[9] M. Penza, C. Martucci, G. Cassano, "NO_x gas sensing characteristics of WO_3 thin films activated by noble metals (Pd, Pt, Au) layers", Sens. Actuators B Chem., 1998, pp. 52-59.

[10] R. S. Khadayate, V. Sali, P. P. Patil, "Acetone vapor sensing properties of screen printed WO_3 thick films", Talanta, 2007, pp. 1077-1081.

[11] K. Garrity, A. M. Kolpak, S. Ismail-Beigi, E. I. Altman, "Chemistry of ferroelectric surfaces", Adv. Mater., 2010, pp. 2969-2973.

[12] P. M. Woodward, A. W. Sleight, T. Vogt, "Ferroelectric tungsten trioxide", J. Solid. State Chem., 1997, pp. 9-17.

[13] A. Baserga, V. Russo, F. Di Fonzo, A. Bailini, D. Cattaneo, C.S. Casari, A. Li Bassi, C.E. Bottani, "Nanostructured tungsten oxide with controlled properties: Synthesis and Raman characterization, Thin Solid Films, 2007, pp. 6465-6469.

[14] .Y. Lu, J. Chen, S. Z. Deng, N. S. Xu, W. H. Zhang, "The most powerful tool for the structural analysis of tungsten suboxide nanowires: Raman spectroscopy", J. Mater. Res., 2008, pp. 402-408.

[15] C. J. Arendse, G. F. Malgas, T. F. G. Muller, D. Knoesen, C. J. Oliphant, D. E. Motaung, B. W. Mwakikunga, "Thermally Induced Nano-Structural and Optical Changes of nc-Si:H Deposited by Hot-Wire CVD", Nanoscale Research Letters, 2009, pp. 307-312.

[16] B. W. Mwakikunga, M. Maaza, K. T. Hillie, C. J. Arendse, T. Malwela, E. Sideras-Haddad, "From phonon confinement to phonon splitting in flat single nanostructures: A case of VO_2@V_2O_5 core-shell nano-ribbons", Vibrational Spectroscopy, 2012, pp. 105-111.

[17] L. M. Sikhwivhilu, S. Mpelane, B. W. Mwakikunga, S. S. Ray, "Photoluminescence and Hydrogen Gas-Sensing Properties of Titanium Dioxide Nanostructures Synthesized by Hydrothermal Treatments", ACS Applied Materials & Interfaces, 2012, pp. 1656-1665.

[18] B. W. Mwakikunga, S. Motshekga, L. Sikhwivhilu, M. Moodley, G. Malgas, M. Scriba, S. S. Ray, "A classification and ranking system on the H_2 gas sensing capabilities of nanomaterials based on proposed coefficients of sensor performance and sensor efficiency equations", Sens. Actuators B Chem., 2013, pp. 170-178.

[19] K. Wetchakun, T. Samerjai, N. Tamaekong, C. Liewhiran, C. Siriwong, V. Kruefu, A. Wisitsoraat, A. Tuantranont, S. Phanichphant, "Semiconducting metal oxides as sensors for environmentally hazardous gases", Sens. Actuators B Chem., 2011, pp. 580-591.

[20] B. T. Marquis, J. F. Vetelino, "A semiconducting metal oxide array for the detection of NO_x and NH_3", Sens. Actuators B, 2001, pp. 100-110.

[21] Y. Min, "Properties and Sensing Performance of Zinc Oxide Thin Films", PhD Dissertation, 2003, MIT Cambridge, USA.

© University of Pretoria

ISSN 1610-1642
Phys. Status Solidi C
11 · No. 2 February
181–354 (2014)

physica status solidi pss c

www.pss-c.com

current topics in solid state physics

2
2014

Electrical and optical properties of mixed phase tungsten trioxide films grown by laser pyrolysis

M. Govender, B. W. Mwakikunga, A. G. J. Machatine, and H. W. Kunert

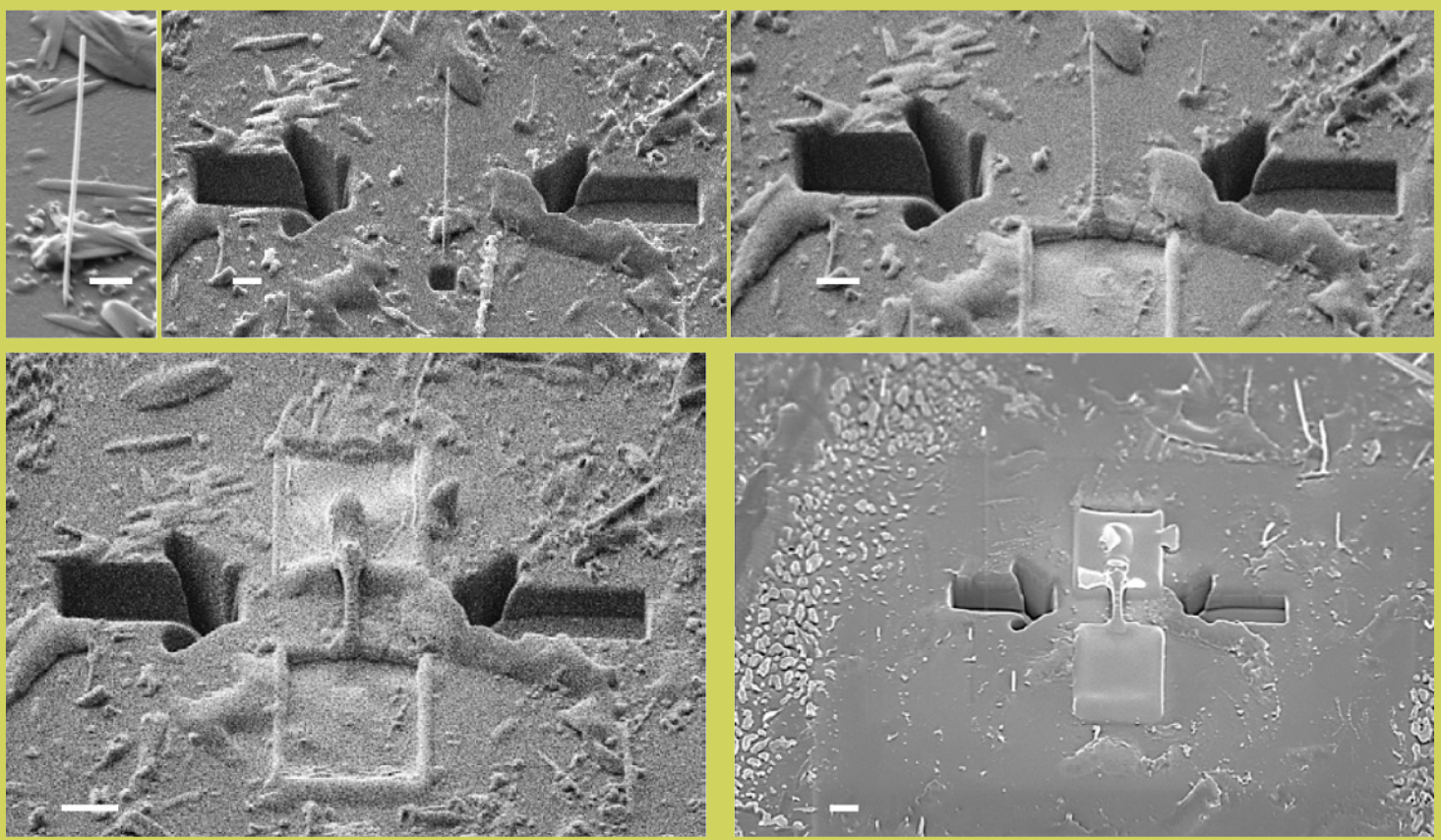

WILEY-VCH

© University of Pretoria

UNIVERSITEIT VAN PRETORIA
UNIVERSITY OF PRETORIA
YUNIBESITHI YA PRETORIA

Phys. Status Solidi C **11**, No. 2, 349–354 (2014) / **DOI** 10.1002/pssc.201300212

physica status solidi c
www.pss-c.com
current topics in solid state physics

Electrical and optical properties of mixed phase tungsten trioxide films grown by laser pyrolysis

M. Govender[*,1,2], B. W. Mwakikunga[1], A. G. J. Machatine[2], and H. W. Kunert[2]

[1] National Centre for Nanostructured Materials, CSIR, P. O. Box 395, Pretoria 0001, South Africa
[2] School of Physics, University of Pretoria, Pretoria 0002, South Africa

Received 14 June 2013, revised 19 October 2013, accepted 20 December 2013
Published online 3 February 2014

Keywords laser pyrolysis, tungsten trioxide, nanorods, FIB-SEM, gas sensors

[*] Corresponding author: e-mail mgovender2@csir.co.za

Laser pyrolysis was chosen to synthesize tungsten trioxide starting with tungsten ethoxide precursor. The film was found to have a thickness that varied from 205 nm to 1 µm. X-ray diffraction and Raman spectroscopy confirmed the presence of a mixture of hexagonal and tetragonal phase WO_3 in the synthesized film, as well as tungsten bronzes. It was evident that annealing greatly influenced the phases and types of structures formed, and EDXS was carried out in an attempt to quantify the tungstate bronzes to tungsten oxide. I-V curves of the films showed n-type semiconducting behaviour, but the mixed phase appeared to cause a similar behaviour of dopants in a semiconductor. The refractive index decreased with increasing wavelength and gave values of up to 21 at low wavelengths. The average optical band gap was found to be 3.6 eV from UV/Vis spectroscopy. Scanning Electron Microscopy (SEM) showed a mixture of nano- and microstructures after annealing. Nanorod structures were isolated and Pt-contacted using FIB for possible applications such as an active sensing medium in gas sensors.

© 2014 WILEY-VCH Verlag GmbH & Co. KGaA, Weinheim

1 Introduction Tungsten trioxide (WO_3) is an n-type semiconducting metal oxide with a wide band gap that exhibit superior electronic and optical properties [1-7]. At room temperature, WO_3 usually exists as a mixture of monoclinic (γ) and triclinic (δ) crystal phase structure, and undergoes phase changes to higher symmetries upon heating [8-12]. WO_3 has commonly been studied for its electro-chromic, gaso-chromic and photo-chromic properties. In recent years, it has been studied for its sensing properties, making it about the fifth most researched metal oxide for this purpose [13].

More focus is put into single crystalline one-dimensional nanostructures of WO_3 such as nanowires because the properties were found to be well tailored for applications such as gas-sensing [14]. The unique properties have been speculated to arise from the anisotropic geometry, large surface-to-volume ratio, and carrier photon/phonon confinement in two dimensions (1-D system) [15]. The synthesis of good quality nanostructures thus becomes imperative and much attention is directed towards controlled synthesis and characterization of nanostructures. It is still challenging to rationally fabricate nanostructures with precisely controlled and tuneable chemical composition, size, structure, morphology and with dopants. Therefore, much opportunity exists to try different synthesis techniques depending on the application of the product materials. Here we concern with laser pyrolysis to synthesize WO_3 nanostructures because this technique does not allow the reactants to make contact with any side-walls, and so the products are of high purity and quality [16-18]. It is also shown here how individual nanostructures are isolated for possible sensing applications.

2 Experimental The laser pyrolysis experimental setup was discussed in detail in [16, 18, 19], and only an overview will be presented here. The laser pyrolysis method is carried out inside a stainless steel chamber (see Fig. 1(a)) at atmospheric pressure. A wavelength tunable continuous wave (CW) CO_2 laser was used in the experiments (Edinburgh Instruments, PL6) and the beam was focused into the reaction chamber. The chosen laser wavelength was 10.16 µm and the measured power density was found to be 51.2 W/cm^2.

© 2014 WILEY-VCH Verlag GmbH & Co. KGaA, Weinheim

© University of Pretoria

The synthesis of tungsten trioxide commenced by mixing 0.1 g of greyish-blue anhydrous tungsten hexachloride WCl_6 (Aldrich 99.9%) powder in 100 mL of absolute ethanol C_2H_5OH (Aldrich 99.9%) to give a tungsten ethoxide $W(OC_2H_5)_6$ starting precursor. The liquid precursor was decanted into an aerosol generator (Micro Mist, model EN) which was attached to the laser pyrolysis system via a multiflow nozzle that allows argon gas to pass through it and carry a stream of very fine precursor droplets (~5 μm droplet diameter according to the manufacturer) into the laser beam. Acetylene (C_2H_2) sensitizer gas and argon encasing gas flowed adjacent to the precursor, guiding it towards a glass substrate as depicted in Fig. 1(b). The gas flow rates are chosen such that the ablated precursor collects on the substrate after interacting with the laser. The temperature of the interaction zone of the laser and precursor were considered elsewhere [20] and found to be approximately 127 °C. The sample was annealed for 17 hours at 500 °C under argon atmosphere [21]. It is noted here that reproducibility still remains a problem of this technique, and more attempts are being made to achieve controllability.

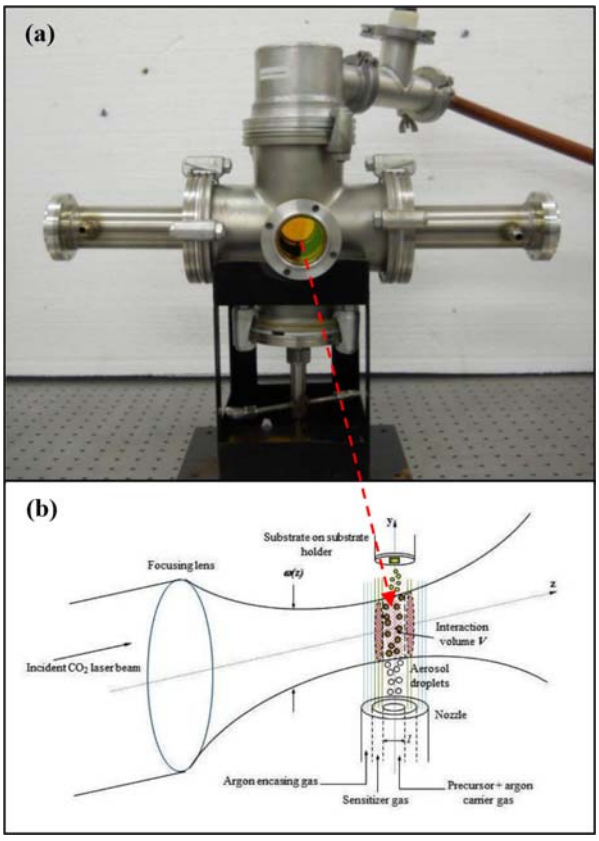

Figure 1 (a) The laser pyrolysis chamber and (b) a schematic of the inside of the chamber during synthesis.

Morphology studies were carried out using a Carl Zeiss SMT Auriga™ Scanning Electron Microscopy (SEM) microscope. The Focused Ion Beam (FIB) system used was a Crossbeam® FIB Workstation with Gemini® FESEM Column and worked in tandem with the SEM system. Raman spectroscopy was carried out using a Horiba Jobin-Yvon HR800UV Raman Spectrograph with a wavelength of 514.5 nm from an argon ion laser set at a laser power of ~1 mW at the sample. X-ray diffraction (XRD) was carried out using a Philips Xpert powder diffractometer at a wavelength of 154.184 pm. UV/Vis spectroscopy was carried out using a PerkinElmer Lamda 750S spectrometer in the wavelength range 190-2500 nm, and ellipsometry was carried out on the film using a J. A. Woollam Co. Inc. XLS-100 ellipsometer. I-V curves were taken using a two-point probe (1 mm spacing between probes) system connected to a Keithley 4200 Semiconducting Characterization System.

3 Results and discussion

3.1 Vibrational and structural analysis Raman and XRD analysis of tungsten trioxide have been reported numerous times [22-26], and despite the simple stoichiometry, the structure is very complex [27-29]. Raman spectroscopy was done on two areas of the sample as denoted by spot 1 and spot 2 of the Raman image shown in the inset of Fig. 2. The spectra from either spot had different Raman shifts, indicating the possibility of mixed phases. This could be due to the Gaussian intensity profile of the laser used in the synthesis [18]. There is also a mixture of several shaped nano- and microstructures as seen in the SEM micrographs of Fig. 9.

The most intense peak in the Raman spectrum shown in Fig. 2 of spot 2 had a shoulder. This peak was deconvoluted into peaks centred at 775 cm^{-1} and 816 cm^{-1}. ElBatal [25] observed Raman shifts at 333 cm^{-1}, 775 cm^{-1} and 945 cm^{-1} from 10% WO_3 melted together with glass at 1100 °C. This combination of peaks is similar to that found in spot 2 of Fig. 2 of our synthesized and annealed sample and these peaks arise from a combination of WO_6 groups and the glass. Daniel et al. [22] and Breedon et al. [26] reported on Raman shifts at 150 cm^{-1}, 165 cm^{-1}, 695 cm^{-1} and 816 cm^{-1} after annealing their samples on glass above 500 °C. These peaks were assigned to hexagonal phase WO_3, and according to Gerand et al. [30] hexagonal phase WO_3 can be easily obtained by annealing $WO_3.1/3\,H_2O$. According to the peaks at 150 cm^{-1} and 332 cm^{-1}, this strongly suggests the presence of hydrated WO_3 which could have led to the formation of the hexagonal phase WO_3 [31-35]. Analysing spot 1, the peaks at 110 cm^{-1} and 152 cm^{-1} suggest a WO_3 hydrate [22]. The combination of peaks at 704 cm^{-1} and 798 cm^{-1} are indicative of tetragonal phase WO_3 [36]. Therefore, spot 1 which appears brighter in contrast and almost luminescent-like under the Raman microscope when imaged is assigned to tetragonal phase WO_3 and spot 2 which appears has the duller contrasting material is assigned to hexagonal phase WO_3 probably stemming from clusters of nanoparticels. Both spots also contain hydrated phases of WO_3.

© 2014 WILEY-VCH Verlag GmbH & Co. KGaA, Weinheim

© University of Pretoria

UNIVERSITEIT VAN PRETORIA
UNIVERSITY OF PRETORIA
YUNIBESITHI YA PRETORIA

The XRD diffractogram in Fig. 3 was compared to [26, 37-39] and indicates peaks of hydrated, hexagonal phase WO_3, tetragonal phase WO_3 and sodium tungstate also known as tungsten bronze. The intense peak at $2\theta=12^o$ is attributed to the tungstate bronze (Na_xWO_3). The peaks at $2\theta=22\text{-}24^o$ are indicative of WO_3 with stronger peaks for hexagonal phase than tetragonal. It is noted here that to get an idea of the crystallite size in our sample to correlate with SEM micrographs, Scherrer's formula [40, 41] was applied to the peaks in our diffractogram. It was found that the crystallite size varied between 0.47 nm-0.76 nm. Our XRD diffractogram was also compared against the ICCD database and was found to match best with sodium tungstate compound (PDF number 01-080-2471). The sodium tungstate (tungstate bronze) phase was confirmed by the weak Raman shift at 915 cm^{-1} [26] for spot 2 in Fig. 2.

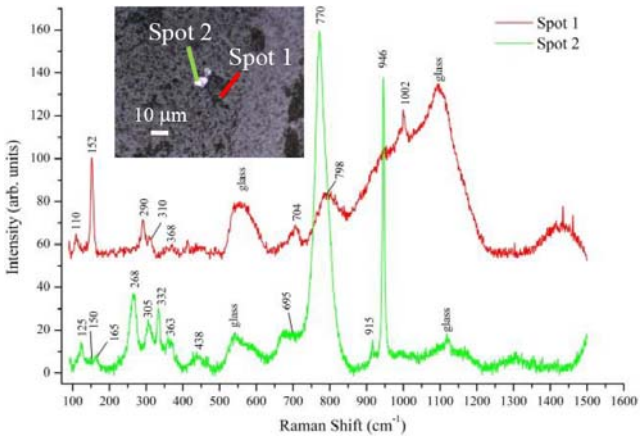

Figure 2 The Raman spectrum showing two spots of different phases and the optical image in the inset shows the variation in the appearance of the material.

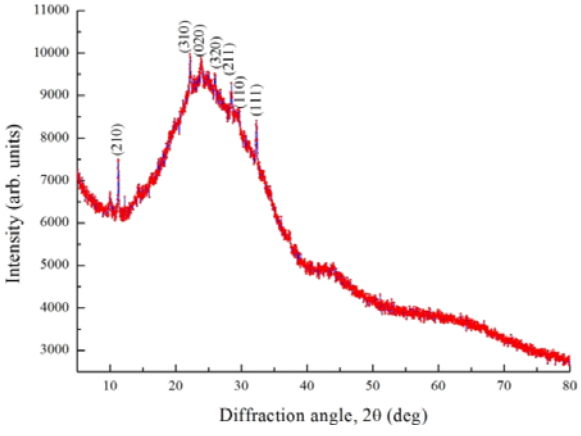

Figure 3 The XRD diffractogram of laser pyrolysis grown film on glass that shows characteristic peaks of sodium tungstate, as well as hexagonal and tetragonal phase WO_3.

To get a better idea of the quantity of tungstate bronze to that of tungsten oxide, X-ray dispersive spectroscopy (EDX) was carried out on the sample. The spectrum is shown in Fig. 4. From the spectrum, it is estimated from the weight% that approx. 22% of the sample is sodium tungstate bronze.

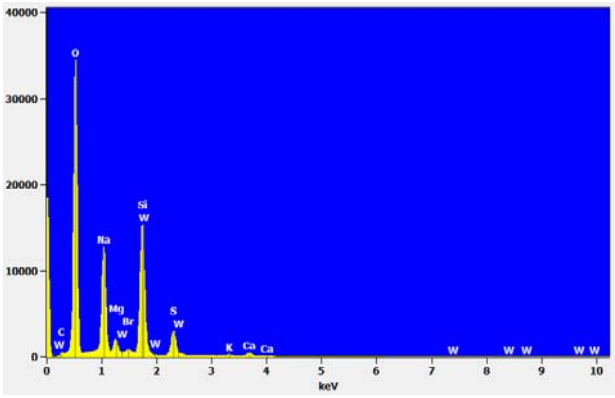

Figure 4 The EDX spectrum showing the presence of sodium, tungsten and oxygen from the sample. The glass impurities of Ca and K are also seen.

It is speculated that the aerosol precursor encounters varying intensities upon entering the laser beam used in laser pyrolysis, which causes different phases, shapes and stoichiometries of WO_3 to form. Furthermore, the influence of glass with its impurities and annealing above 400 ^oC [42, 43] appear to significantly influence the vibrational modes of WO_3 as evidenced in the literature.

3.2 Optical properties The refractive index of the film depends primarily on the deposition and annealing temperature. The thickness of the laser pyrolysis grown film and the effective refractive index was calculated using ellipsometry using the Cauchy model. It should be noted that laser pyrolysis did not give a uniform film, but instead a thin film at the centre surrounded by a thicker ring of film. Therefore, the thickness given by the ellipsometer is mainly from the centre and thinnest part of the film, which was found to be 205±10 nm with a large MSE value of 27. The raw experimental data with the theoretical fit is shown in Fig. 5. The refractive index is very high for smaller wavelengths and decreases gradually to very low refractive index for longer wavelengths as shown in Fig. 6. This large refractive index is not usually seen for samples annealed at 500 ^oC [44]. Refractive indices of transparent materials such as glass are on average about 1.5. However refractive indices of non-transparent materials such silicon can be as high as more than 10. Also light of short wavelengths get more refracted than that of long wavelengths. For instance red light from a white source almost goes through unrefracted whereas blue light bends with very big angle of refraction. Therefore one should expect large refractive indices as the wavelength gets shorter and shorter.

© 2014 WILEY-VCH Verlag GmbH & Co. KGaA, Weinheim

© University of Pretoria

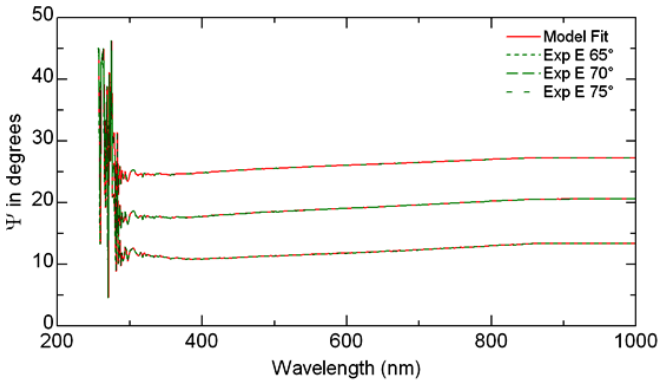

Figure 5 Spectral ellipsometric Ψ data at 65°, 70° and 75° angle of incidence of the laser pyrolysis synthesized mixed phase WO_3 film.

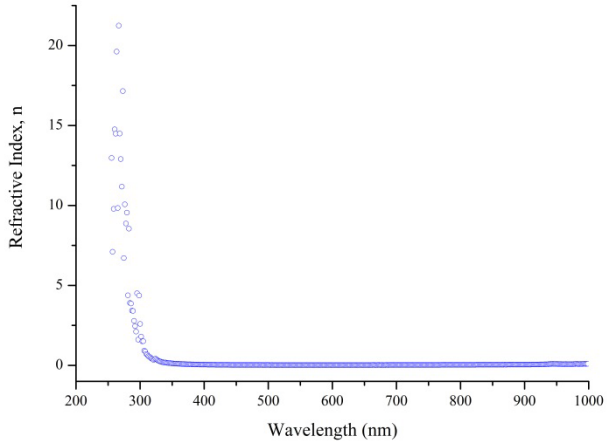

Figure 6 Effective refractive index vs. light wavelength for the laser pyrolysis synthesized mixed phase WO_3 film.

Optical transmittance (%T) was carried out on the film and shows a very high transparency in the spectral region and transmits less light below the spectral region. Below this spectral region, the logarithm of the absorption coefficient α vs. photon energy hv shows a linear dependence. Plotting the dependence $(\alpha hv)^{1/2}$ vs. hv, the optical band gap is determined by extrapolating to zero absorption [44]. Since our sample did not have uniform thickness, we took the thickness given from ellipsometry as 205.02±10 nm and 1000±25 nm from cross-sectioning the sample. Cross-sectioning was done using FIB to cut into the film and the thickness was measured with SEM. According to Fig. 7, the optical band gap was found to be 3.74±0.05 eV for a 1000 nm thick film and 3.69±0.03 eV for a 205 nm thick film. The average band gap is much higher than the 3.25 eV quoted in literature for WO_3 annealed at 500 °C [45]. The sodium tungstate usually has a small bandgap energy of ~0.6 eV, which is about 16% of the total optical bandgap found. This amount of sodium tungstate that contributes here is close to the 22% of sodium tungstate found in EDX. It should also be noted that there is also two phases of tungsten oxide contributing to the bandgap estimation.

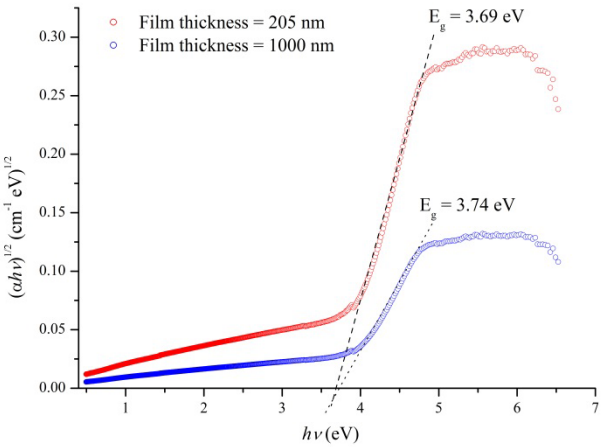

Figure 7 $(\alpha hv)^{1/2}$ vs. hv plots for the laser pyrolysis synthesized mixed phase WO_3 film for the thinnest and thickest part of the film. Linear fits of the absorption data indicate the indirect band gap of WO_3.

3.3 Electrical properties Using a two-probe setup, a sweeping voltage between -5 V and 5 V was passed through the film while the other probe measured current. The sample was measured at liquid nitrogen temperature by pouring liquid nitrogen on the film. The sample was also measured at 300 °C by placing the film on a hot-plate. From Fig. 8 of the I-V curve, the film exhibits n-type semiconducting behavior by decreasing in resistance with increasing temperature [46].

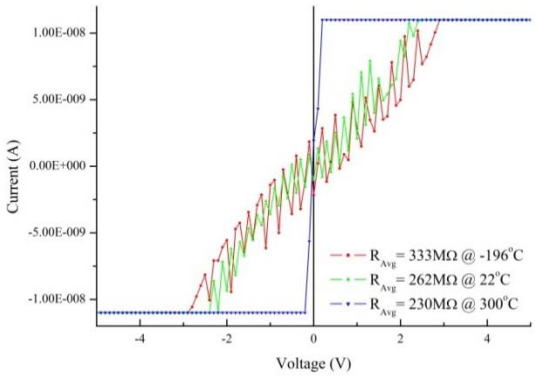

Figure 8 I-V curves of the film taken at liquid nitrogen temperature, room temperature and 300 °C.

The film reaches threshold current at 2.8 V at liquid nitrogen temperature, and 2.4 V at room temperature. The film exhibits metallic behavior at higher temperatures by reaching threshold voltage at 0.2 V as the gap between the conduction and valence band almost overlap. The shape of the curves at room and liquid nitrogen temperature are similar to that of doped metal oxide semiconductors [47]. It is probable that the mixed phases influences the electron carrier properties in a way similar to how dopants influence the carrier properties in a metal oxide. Deposition on alumina substrate shows different properties due to the absence of impurities and nanostructures.

© 2014 WILEY-VCH Verlag GmbH & Co. KGaA, Weinheim

© University of Pretoria

UNIVERSITEIT VAN PRETORIA
UNIVERSITY OF PRETORIA
YUNIBESITHI YA PRETORIA

Contributed Article

4 Applications Using focused ion beam-scanning electron microscopy (FIB-SEM), platinum (Pt) contacts can be made on either side of the nanorod so that an electric circuit is produced. The nanorod can now be used as an active sensing-medium for example, making it possible to perform gas sensing. The electronic properties can be measured through the wire via the Pt contacts when a gas is adsorbed on the nanorod surface. The surface around the nanorod is cleaned with FIB to make it discontinuous with the rest of the film. Figures 9(a-e) show the progression from identifying a nanorod on the sample surface with SEM to making Pt-contacts with FIB. The next step will be to connect the Pt contacts to a microcircuit and do I-V curve measurements from the single nanostructure and compare it to the bulk [48]. The area around the nanorod will be removed and wires bonded to the Pt-contacts to obtain the electrical properties of the isolated nanorod only.

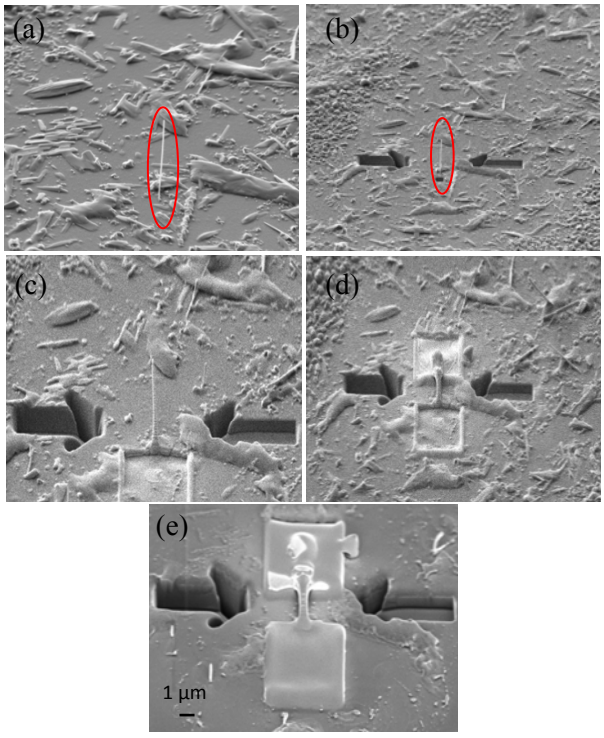

Figure 9 (a-e) Progression of making Pt-contacts on a WO_3 nanorod with FIB and SEM imaging.

Acknowledgements The CSIR National Laser Centre and the University of the Witwatersrand for the equipment used in this study.

References

[1] J. L. Solis, S. Saukko, L. B. Kish, C. G. Granqvist, and V. Lantto, Sens. Actuators B **77**, 316-321 (2001).
[2] S. C. Moulzolf, S.-a. Ding, and R. J. Lad, Sens. Actuators B **77**, 375-382 (2001).
[3] K. Aguir, C. Lemire, and D. B. B. Lollman, Sens. Actuators B **84**, 1-5 (2002).
[4] Y. B. Li, Y. Bando, D. Goldberg, and K. Kurashima, Chem. Phys. Lett. **367**, 214-218 (2003).
[5] L. G. Teoh, Y. M. Hon, J. Shieh, W. H. Lai, and M. H. Hon, Sens. Actuators B **96**, 219-225 (2003).
[6] X.-L. Li, T.-J. Lou, X.-M. Sun, and Y.-D. Li, Inorg. Chem. **43**, 5442-5449 (2004).
[7] K. J. Lethy, S. Potdar, V. P. M. Pillai, and V. Ganesan, J. Phys. D**42**, 095412 (2009).
[8] E. Salje, Acta Cryst. A **31**, 360 (1975).
[9] E. Salje, and K. Viswanathan, Acta Cryst. A **31**, 356 (1975).
[10] K. R. Locherer, I. P. Swainson, and E. K. H. Salje, J. Phys.: Condens. Matter **11**, 6737-6756 (1999).
[11] M. Boulova, N. Rosman, P. Bouvier, and G. Lucazeau, J. Phys.: Condens. Matter **14**, 5849-5863 (2002).
[12] Y. Fujioka, J. Frantti, and V. Lantto, Integr. Ferroelectr. **123**, 81-86 (2011).
[13] K. J. Choi, and H. W. Jang, Sensors **10**, 4083-4099 (2010).
[14] M. M. Arafat, B. Dinan, S. A. Akbar, and A. S. M. A. Haseeb, Sensors **12**, 7207-7258 (2012).
[15] B. W. Mwakikunga, E. Sideras-Haddad, A. Forbes, and C. Arendse, Phys. Status Solidi A **205**, 150-154 (2008).
[16] B. W. Mwakikunga, A. Forbes, E. Sideras-Haddad, and C. Arendse, Nanoscale Res. Lett. **3**, 372 (2008).
[17] L. Shikwambana, M. Govender, B. W. Mwakikunga, E. Sideras-Haddad, and A. Forbes, Adv. Mater. Res. **227**, 80-83 (2011).
[18] M. Govender, L. Shikwambana, B. W. Mwakikunga, E. Sideras-Haddad, R. M. Erasmus, and A. Forbes, Nanoscale Res. Lett. **6**, 166 (2011).
[19] B. W. Mwakikunga, A. Forbes, E. Sideras-Haddad, R M Erasmus, G. Katumba, and B. Masina, Int. J. Nanoparticles **1**, 3 (2008).
[20] B. W. Mwakikunga, A. E. Mudau, N. Brink, and C.J. Willers, Appl. Phys B **105**, 451-462 (2011).
[21] B. W. Mwakikunga, E. Sideras-Haddad, M. Witcomb, C. Arendse, and A. Forbes, J. Nanosci. Nanotechnol **9**, 3286 (2008).
[22] M. F. Daniel, B. Desbat, J. C. Lassegues, B. Gerand, and M. Figlarz, J. Solid State Chem. **67**, 235-247 (1987).
[23] K. Nonaka, A. Takase, and K. Miyakawa, J. Mater. Sci. Lett. **12**, 274-277 (1993).
[24] D. Y. Lu, J. Chen, H. J. Chen, L. Gong, S. Z. Deng, N. S. Xu, and Y. L. Liu, Appl. Phys. Lett. **90**, 041919 (2007).
[25] F. H. ElBatal, Ind. J. Pure Appl. Phys. **47**, 471-480 (2009).
[26] M. Breedon, P. Spizzirri, M. Taylor, J. du Plessis, D. McCulloch, J. Zu, L. Yu, Z. Hu, C. Rix, W. Wlodarski, and K. Kalamtar-zadeh, Cryst. Growth Design **10**, 430-439 (2010).
[27] P. M. Woodward, A. W. Sleight, and T. Vogt, J. Phys. Chem. Solids **56**, 1305-1315 (1995).
[28] M. Boulova, G. Lucazeau, T. Pagnier, and A. Gaskov, J. Phys. IV France **11,** 1057-1062 (2001),
[29] C. J. Howard, V. Luca, and K. S. Knight, J. Phys.: Condens. Matter **14**, 377-387 (2002),
[30] B. Gerand, G. Nowogrocki, J. Guenot, and M. Figlarz, J. Solid State Chem. **29**, 429-434 (1979).
[31] A. Cremonesi, D. Bersani, P. P. Lottici, Y. Djaoued, and P. V. Ashrit, J. Non-Cryst. Solids **345-346**, 500-504 (2004).
[32] C. Santato, M. Odziemkowski, M. Ulmann, and J. Augustynski, J. Am. Chem. Soc. **123**, 10639-10649 (2001).
[33] C. Balázsi, L. Wang, E. O. Zayim, I. M. Szilágyi, K. Sedlacková, J. Pfeifer, A. L. Tóth, and P. -I. Gouma, J. Eur. Ceram. Soc. **28**, 913-917 (2008).

© 2014 WILEY-VCH Verlag GmbH & Co. KGaA, Weinheim

© University of Pretoria

[34] T. Peng, D. Ke, J. Xiao, L. Wang, J. Hu, and L. Zan, J. Solid State Chem. **194**, 250-256 (2012).
[35] H.-F. Pang, X. Xiang, Z.-J. Li, Y.-Q. Fu, and X.-T. Zu, Phys. Status Solidi A **209**, 537-544 (2012).
[36] L. Van Ngoc, T. C. Vinh, L. Q. Toai, N. D. Thinh, H. T. Dat, T. Tuan, and D. A. Phuong, VNU J. Sci., Math., Phys. **25**, 47-55 (2009).
[37] C. Cantalini, H. T. Sun, M. Faccio, M. Pelino, S. Santucci, L. Lozzi, and M. Passacantando, Sens. Actuators B **31**, 81-87 (1996).
[38] I. Jiménez, J. Arbiol, A. Cornet, and J. R. Morante, IEEE Sens. J. **2**, 329-336 (2002).
[39] Z. Liu, M. Miyauchi, T. Yamazaki, and Y. Shen, Sens. Ac tuators B **140**, 514-219 (2009).
[40] S.-H. Wang, T.-C. Chou, and C.-C. Liu, Sens. Actuators B **94**, 343-351 (2003).
[41] G. Singla, K. Singh, and O. P. Panday, Powder Technology **237**, 9-13 (2013).
[42] R. E. Tanner, A. Szekeres, D. Gogova, and K. Gesheva, Appl. Surf. Sci. **218**, 162-168 (2003).
[43] Y. Djaoued, p. V. Ashrit, S. Badilescu, and R. Brünning, J. Sol-Gel Sci. Technol. **28**, 235-244 (2003).
[44] D. Gogova, K. Gesheva, A. Szekeres, and M. Sendova-Vassileva, Phys. Status Solidi A **176**, 969 (1999).
[45] S. K. Gullapalli, R. S. Vemuri, and C. V. Ramana, Appl. Phys. Lett. **96**, 171903 (2003).
[46] H. Zheng, J. Z. Ou, M. S. Strano, R. B. Kaner, A. Mitchell, and K. Kalantar-zadeh, Adv. Funct. Mater. **21**, 2175-2196 (2011).
[47] T. Zhai, X. Fang, M. Liao, X. Xu, H. Zeng, B. Yoshio, and D. Golberg, Sensors **9**, 6504-6529 (2009).
[48] M. Gillet, R. Delamare, and E. Gillet, Eur. Phys. J. D **34**, 291-294 (2005).

© 2014 WILEY-VCH Verlag GmbH & Co. KGaA, Weinheim

© University of Pretoria

UNIVERSITEIT VAN PRETORIA
UNIVERSITY OF PRETORIA
YUNIBESITHI YA PRETORIA

Phys. Status Solidi A **211,** No. 2, 435–439 (2014) / **DOI** 10.1002/pssa.201300187

physica status solidi a
www.pss-a.com
applications and materials science

Optical selection rules and scattering processes in rocksalt wide band gap ZnO

H. W. Kunert*[,1], M. Govender[1,2], A. G. J. Machatine[1], B. W. Mwakikunga[2], and P. Niyongabo[1]

[1] Department of Physics, University of Pretoria, Pretoria 0002, South Africa
[2] DST/CSIR National Centre for Nano-Structured Materials, CSIR, P. O. Box 395, Pretoria, 0001, South Africa

Received 6 June 2013, revised 15 January 2014, accepted 16 January 2014
Published online 12 February 2014

Keywords excitons, group theory, scattering processes, zinc oxide

* Corresponding author: e-mail herbert.kunert@up.ac.za, Phone: +27 12 4202636, Fax: +27 12 3625288

At sufficiently high pressures, wurtzite structure zinc oxide (*W*-ZnO) can be transformed to the cubic rocksalt (*R*-ZnO) structure. The *R*-ZnO exhibits semiconductor behavior with an indirect wide band gap of $E_g = 5.5$ eV. The maximum valence band is found far away from the center of the Brillouin zone (BZ) at high symmetry point *L* and line Σ, depending on the pressure. The unusual electronic band structure (EBS) of the *R*-ZnO leads to several direct and indirect optical transitions which find applications in ultraviolet optoelectronic devices. We have investigated radiative and non-radiative symmetry restricted selection rules, as well as inter- and intra-valley scattering processes.

© 2014 WILEY-VCH Verlag GmbH & Co. KGaA, Weinheim

1 Introduction The *R*-ZnO structure (*R*-O_h^5, $Fm3n$ space group) has recently attracted much attention due to an unconventional EBS that can be used in mechanical and optoelectronic applications [1–4]. Jaffe et al. [5] calculated the EBS of *R*-ZnO by the all-electron local-orbits Hartree–Fock method along some major symmetry lines and points, shown in Fig. 1a. Some symmetry assignments are contrary to that commonly accepted, for example, the band structure of R-ZnO in [5], which is presented in Fig. 1b, where one of the VB maximum has W_1 symmetry instead of W_5 symmetry, and the *K* point seems to be incorrectly assigned. Reference to group theoretical assignments has not yet been provided.

Segura et al. [6] reported on pressure dependence of the optical absorption edge in *R*-ZnO up to 20 GPa measured at room temperature. The low-energy tail of the absorption has been assigned to an indirect transition. Figure 2 shows the EBS of *R*-ZnO along some high symmetry directions of the BZ at several pressures. The minimum of the lowest conduction band (CB) remains at the center of the BZ (point Γ), while the highest maximum of the valence band (VB) occurs on the Σ-line and at the *L* point. No group theoretical assignments of electron and hole states have been discussed, and therefore no optical selection rules (OPSRs) have been considered. Based on pressure absorption dependence, the optical absorption leads to indirect transitions: *L*–Γ, Σ–Γ as well as direct transitions at *X*, *L*, and high symmetry points have been assigned by us using a group theoretical approach. In this paper, we provide rigidly calculated OPSRs for all transitions, as well as selection rules for possible inter- and intra-valley scattering processes.

In Section 2 of this paper, we discuss assignments of electrons and holes in CBs and VBs needed for determination of OPSRs. In Section 3, we deal with the general quantum mechanical rules needed for matrix element transitions. In Section 4, we discuss the wave vector selections rules (WVSRs) which follow from the momentum conservation principle. The direct radiative transition selection rules (DrTrSRs) and the symmetry of excitons are discussed in Section 5. The indirect transitions (InDrTrs) involving vibrational modes are considered in Section 6. In the last section we discuss our results and predictions regarding the splitting of *L* excitons.

2 Symmetry assignments of electron and hole states in the conduction and valence bands in *R*-ZnO The states of electrons and holes in a crystal are characterized by the wave vector $\boldsymbol{k}$ and the irreducible representations (irrps) of a space group $G(\boldsymbol{k})$. When the spin of a particle or quai-particle is disregarded, the states are classified according to the so-called single-valued irrps (SVirrps). The inclusion of spin leads to double-valued irrps (DVirrps) known as spinors. The EBS can be determined by several experimental techniques such as absorption, Raman, photoluminescence and reflectivity spectroscopies.

© 2014 WILEY-VCH Verlag GmbH & Co. KGaA, Weinheim
© University of Pretoria

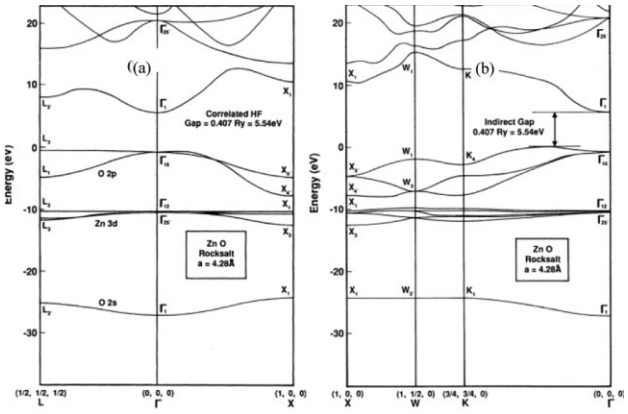

Figure 1 (a) Correlation-corrected Hartree–Fock band structure of ZnO in the rocksalt structure and (b) correlation-corrected Hartree–Fock band structure of ZnO in the rocksalt structure for some additional directions in reciprocal space. Diagrams adopted from Ref. [5].

Segura et al. [6] did not take into account SRs for their high symmetry points, so based on group theoretical techniques, we have determined the major high symmetry line and points of the respective BZ according to the irrps of O_h^5 space group using Cracknell, Davies, Miller and Love Tables (CDML) labeling [7]. In Table 1, we list the respective states of electron and holes in terms of CDML labeling of irrps in CBs and VBs. In Table 2, we show a correspondence of irrps labeling between Bouckaert, Smoluchowski and Wigner (BSW) [8] Jaffet and Koster (JK) [9], and CDML tables.

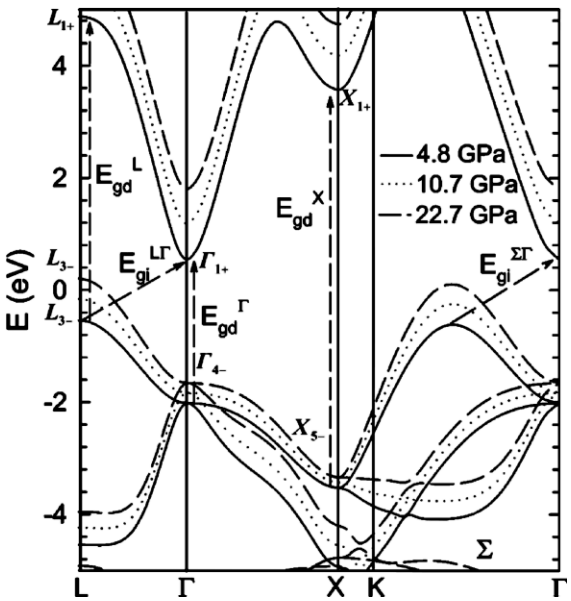

Figure 2 Electronic band structure of rocksalt ZnO along high-symmetry directions of the BZ at several pressures, as calculated through *ab initio* DFT-LDA pseudopotential method. Diagram adopted from Ref. [6].

Table 1 Symmetry assignment of high symmetry points in cubic *R*-ZnO.[a]

single-valued representations–spin excluded			
conduction bands	L_{1+}	Γ_{1+} (lowest)	X_{1+}
valence bands	L_{3-} (highest)	Γ_{4-}	X_{5-}
double-valued representations–spin included			
conduction bands	L_{6+}	Γ_{6+}	X_{6+}
valence bands[b]	L_{4-}, L_{5-}, L_{6-}	Γ_{8-}, Γ_{6-}	X_{7-}, X_{6-}

[a]The assignment is in terms of CDML irreducible representations. The double-valued representations have been obtained by multiplication of the single-valued representations by two-dimensional representations (spinor representation $D_{(1/2)}$ CDML [7], p. 9);
[b]Due to possible spin–orbit interactions, the valence band L_{3-} (two-dimensional, small representation) $\times D_{(1/2)}$ splits onto L_{4-} (one-dimensional), L_{5-} (one-dimensional) and L_{6-} (two-dimensional) representations. Similar effects happen for Γ_{6+} and X_{6+} representations.

Table 2 Labels of irreducible representations for the point Γ for O_h^5–*Fm3n* space group of *R*-ZnO.[a]

JK [8]	BSW [9]	CDML [7]
Γ_{1+}	Γ_1	Γ_{1+}
Γ_{2+}	Γ_2	Γ_{2+}
Γ_{3+}	Γ_{12}	Γ_{3+}
Γ_{4+}	$\Gamma_{15'}$	Γ_{4+}
Γ_{5+}	$\Gamma_{25'}$	Γ_{5+}
Γ_{1-}	$\Gamma_{1'}$	Γ_{1-}
Γ_{2-}	$\Gamma_{2'}$	Γ_{2-}
Γ_{3-}	Γ_{12+}	Γ_{3-}
Γ_{4-}	Γ_{15+}	Γ_{4-}
Γ_{5-}	Γ_{25}	Γ_{5-}

[a]For more details, see Ref. [10], p. 533.

3 Selection rules We first recall the basic theorems on SRs [9]. The study of an absorption or scattering cross section for a process involving the absorption or scattering of particles or quasi-particles with wave vector $\boldsymbol{k}$ in a crystal involves the calculation of transition probabilities, which in turn involves the calculation of quantum mechanical matrix elements. The matrix elements of a perturbation f between an initial and final state are of the form $V_{pq}^{\mu\nu} = \left\langle \psi_q^\mu | f | \psi_p^\nu \right\rangle$, where ψ_q^μ and ψ_p^ν are the wave functions (with respective basis functions for irrps D^μ and D^ν) of the particle or quasi-particles involved in the absorption or scattering processes.

Acting by symmetry operators of a given space group on the matrix elements (wave functions and perturbation operator f, we obtain the Kronecker product (KP) between three irrps $D^\mu \times D^f \times D^\nu$. When the KP contains the unit representation, normally denoted as Γ_1, Γ_{1+} or A_1, the transition between states due to perturbation f is allowed, otherwise it is forbidden. The square of any irrps always contains the identity representation. Therefore, it suffices to consider only single KPs between two irrps and check whether the third representation is in the decomposition. All

© 2014 WILEY-VCH Verlag GmbH & Co. KGaA, Weinheim

© University of Pretoria

UNIVERSITEIT VAN PRETORIA
UNIVERSITY OF PRETORIA
YUNIBESITHI YA PRETORIA

Original Paper

possible KPs for 230 space groups have been tabulated in CDML.

4 Momentum conservation principles: Wave vector selection rules An electron in a state $\boldsymbol{k}$ can be scattered into another state $\boldsymbol{k}'$ due to an interaction with a phonon at the $\boldsymbol{k}''$ state. The momentum conservation $\boldsymbol{k}+\boldsymbol{k}'=\boldsymbol{k}''$ determines the WVSRs. The WVSRs originate from appropriate combinations of arms of stars $*\boldsymbol{k}$, $*\boldsymbol{k}'$ and $*\boldsymbol{k}''$[11]. For face-centered cubic crystals with tetragonal and cubic symmetries (T_d^2, O_h^5, and others), the WVSRs have been tabulated in Table 2. In *R*-ZnO, there are three pronounced valleys at Γ, *L*, and *X* points. The star of the *L* valley is $*\boldsymbol{k}(L):\boldsymbol{kL}$, $2\boldsymbol{kL}$, $3\boldsymbol{kL}$, and $4\boldsymbol{kL}$, and the star of the *X* valley is $\boldsymbol{kX}$, $5\boldsymbol{kX}$, and $9\boldsymbol{kX}$. At the Γ point, we have only one wave vector $\boldsymbol{k}=0$. The numbers 1, 2, 3, 4, 5, and 9 denote the symmetry operators of O_h^5 group [7]. The first minima at each of these points are characterized by the first wave vectors $\boldsymbol{k}=0$, $\boldsymbol{kL}$, and $\boldsymbol{kX}$ in the fundamental domain of the BZ. It means that we deal with four non-equivalent *L* valleys, three *X* and one Γ valley. The inter- and intra-valley scattering processes are subjected to WVSRs and are discussed in Section 6.

5 Direct radiative transition selection rules in *R*-ZnO

5.1 Point Γ At point Γ, the momentum of the electron and hole are very small (almost zero). The respective KP of a radiative transition from the minimum CB of Γ_{1+} symmetry (spin of electron and hole excluded) to the maximum of the VB of Γ_{4-} symmetry (Table 1) due to the laser beam with electric field $\boldsymbol{E}=\boldsymbol{E}_0\exp(\boldsymbol{kr}-\omega t)$, (E_x,E_y,E_z) which transforms like an ordinary vector x,y,z. Therefore, according to Γ_{4-} representation (VR) is of the form: $\{(\Gamma_{1+})\times(\Gamma_{4-})\times(\Gamma_{4-})\}$. The KP contains the identity representation and therefore the direct transitions at Γ are in accordance with absorption measurements [6].

5.2 Points *L* and *X* The appropriate WVSR for direct transitions between the minimum of the *L*'s CB of L_{1+} symmetry and the maximum of VB of L_{3-} symmetry is $\boldsymbol{kL}+\boldsymbol{kL}=\boldsymbol{kG}$ in channel Γ and $\boldsymbol{kL}+3\boldsymbol{kL}=\boldsymbol{kX}$, $\boldsymbol{kL}+2\boldsymbol{kL}=5\boldsymbol{kX}$, and $\boldsymbol{kL}+4\boldsymbol{kL}=9\boldsymbol{kX}$ in the *X* channel. The SR is $\{L_{1+}(\mathrm{CB})\times L_{3-}(\mathrm{VB})\times\Gamma_{4-}\}=(\Gamma_{3-}+\Gamma_{4-}+\Gamma_{5-})\times(\Gamma_{4-})$ in the Γ channel and $(X_{1-}+X_{2-}+X_{3-}+X_{4-}+2X_{5-})$ in the *X* channel. Clearly the KP contains the identity representation Γ_{1+}. Consequently, the direct transitions at the *L* point are allowed in accordance with experimental data [6].

For point *X*, we have $\boldsymbol{kX}+\boldsymbol{kX}=\boldsymbol{kG}$ in the Γ channel and $\boldsymbol{kX}+5\boldsymbol{kX}=9\boldsymbol{kX}$ for the *X* channel, respectively. The respective KP is of the form $\{(X_{1+})\times(X_{5-})\times(\Gamma_{4-})\}=(\Gamma_{1-}+\Gamma_{5-})\times\Gamma_{4-}$, in the Γ channel and for the *X* channel $(X_{3-}+X_{4-}X_{5-})\times\Gamma_{4-}$. Again the transitions are allowed, as confirmed by Segura et al. [6].

5.3 Σ line Inspecting Fig. 2 [6], we note that the transition from Σ-VB to Σ-CB needs a very high energy laser beam. Therefore, we will not consider this transition. Nevertheless, the indirect transition Σ–Γ is of interest and we will discuss them here.

5.4 Spin inclusion and excitons in *R*-ZnO The EBS have been studied by several authors [5, 6]. They have not taken spin of electrons and holes into consideration. The hexagonal *W*-ZnO, from which the *R*-ZnO has been made, experiences strong magnetic properties evidenced by pronounced spin–orbit (S–O) interaction values. The strong magnetic properties and crystalline field split the VB into three sub-bands which contribute to the three A, B, and C excitons, and are seen by reflectance, photoluminescence and absorption techniques.

We believe that *R*-ZnO will also exhibit some magnetic properties that require an inclusion of spin. To our best knowledge, there are no magnetic experimental data on *R*-ZnO available. Nevertheless, we include the spin to our considerations in OPSRs in an attempt to predict some new features. When spin is included, the states of particles or quasi-particles are classified according to DVirrps. We have calculated the double-valued representation $D_{(1/2)}$ [11], reduced to the symmetry operations of O_h^5 group for points Γ, *L*, and *X* using Eq. (9.65) and Table 3.1 in Ref. [7]. With the help of the $D_{(1/2)}$ representation, we were able to determine the spinor representations for the *R*-ZnO at high symmetry points. The inclusion of electron spin in CBs results in the classification of states in terms of the spinor representations: $\Gamma_{6+}=\Gamma_{1+}\times D_{(1/2)}$, $L_{6+}=L_{1+}\times D_{(1/2)}$ and $X_{6+}=X_{1+}\times D_{(1/2)}$. All the representations are now doubly degenerate.

The holes in the VBs after an inclusion of spin are classified according to the following DVirrps: Γ_{8-} and Γ_{6-} contained in $\Gamma_{4-}\times D_{(1/2)}$; L_{4-}, L_{5-}, and L_{6-} contained in the KP: $L_{3-}\times D_{(1/2)}$ and X_{6+} in $X_{1+}\times D_{(1/2)}=X_{6+}$. It means that the state L_{3-} of the holes at the highest VB maximum at *L* point splits into three VBs (when spin is included) of L_{4-}, L_{5-}, and L_{6-} symmetries each of them two-fold degenerated. Similarly, holes at the Γ split onto fourfold degenerate (Γ_{8-}) heavy and two-fold degenerate (Γ_{6-}) light holes like states of holes in Si and Ge and GaAs.

Consequently, several direct and indirect excitons are expected to be observed experimentally. For direct *L* excitons we have three types of them as: $L_{6+}\times L_{4-}$ (let's call them L_1 excitons), $L_{6+}\times L_{5-}$ (L_2 excitons) and $L_{6+}\times L_{6+}$ (L_3 excitons). This is in analogy to *W*-ZnO's A, B, and C, Γ excitons [11]. We believe that the magneto-photoluminescence, reflectance and absorption will confirm our predictions. The *R*-ZnO structure (*R*-O_h^5, $Fm3n$ space group) has recently attracted much attention due to an unconventional EBS that can be used in mechanical and optoelectronic applications

6 Indirect electronic transitions and inter and intra-valley scattering processes in *R*-ZnO

6.1 Electronic indirect transitions in *R*-ZnO The vertical direct radiative transitions preserve the $\boldsymbol{k}$ vector and

© 2014 WILEY-VCH Verlag GmbH & Co. KGaA, Weinheim
© University of Pretoria

InDrTrs involve participation of phonons. We must distinguish between the two kinds of InDrTrs; those with inclusion of electron and hole spin dependent on the magnitude of S–O interactions and those without. When S–O, spin–spin (S–S), or spin–lattice (S–L) interactions are neglible, we deal with SVirrps which are the classification of electron and hole states. In such cases of the InDrTrs in *R*-ZnO, an electron in the CB can drop radiatively from L_{1+} to L_{3-} and then be scattered in the VB by a phonon from L_{3-} to the Γ_{4-} VB. In the process, the radiative transition from L_{1+} to L_{3-} is allowed as discussed in Section 5. The scattering processes in the VB requires KP: $L_{4-} \times \Gamma_{4-} = L_{1+} + L_{2+} + 2L_{3+}$. The decomposition of the KP clearly indicates the symmetry allowed phonons: L_{1+} (no phonon), L_{2+} (longitudinal acoustic LA phonon), and L_{3+} (transverse acoustic TA phonon). In the second scattering process, an electron can be scattered from the L_{1+} to the Γ_{1+} CB, described by KP $L_{1+} \times \Gamma_{1+} = L_{1+}$ (longitudinal optical LO phonon) and then drop radiatively from Γ_{1+} to Γ_{4-}, which is allowed.

6.2 Inter- and intra-valley scattering processes in R-ZnO Regarding the theory of inter-valley scattering (InterVSc) and intra-valley scattering (IntraVSc) processes, we refer to the work by Lax–Hopfield (LH), and Birman–Lax–Loudon (BLL) [12, 13]. More about the IntraVSc by acoustic and optical phonons and InterVSc in GaAs, Si, and Ge [14]. Recently, Kunert et al. [15] considered the scattering processes in hexagonal *W*-ZnO.

In this section, we determine the allowed symmetries of vibrational modes of an electron scattered from one valley to another. There are three different scattering processes involved. In *R*-ZnO [5, 6], the electronic bands resolve valleys at Γ, (Γ_{1+}), $K(K_1)$, $V(V_1)$, and possibly $L(L_{1+})$ points. Point X consists of three non-equivalent valleys with electrons at $\boldsymbol{k}X$, $5\boldsymbol{k}X$, and $9\boldsymbol{k}X$ states, while at point L we deal with four non-equivalent valleys with electrons of $\boldsymbol{k}L$, $2\boldsymbol{k}L$, $3\boldsymbol{k}L$, and $4\boldsymbol{k}L$ momentum. The IntraVSc means scattering of electrons within three valleys at X point or within four valleys at the L point, while InterVSc refers to scattering processes between three X valleys and four L valleys. Theses scattering processes involve KPs between SVirrps (no-spin). Here we consider the following KPs for InterVSc: $\Gamma \times X$, $\Gamma \times L$, $\Gamma \times V$ and for IntraVSc: $\Gamma \times X$, $X \times X$, and $L \times L$.

For InterVSc we have: $\Gamma_{1+} \times X_{1+} = X_{1+}$ (LO and LA phonons dependent on masses of ions), $\Gamma_{1+} \times L_{1+} = L_{1+}$ (LO and LA phonons), and $\Gamma_{1+} \times V_1 = V_1$ (unknown). Our predictions of phonon symmetries participating in scattering processes is based on group theoretical connectivity relations. To the best of our knowledge, there are no experimental data on phonon dispersion curves and phonon density of states in *R*-ZnO.

In an IntraVSc process, which means scattering within or between valleys belonging to the same star, two kinds of phonons are involved, phonons with large momentum like $h\boldsymbol{k}L$, $h\boldsymbol{k}W$, or $h\boldsymbol{k}X$ and with very low momentum $h\boldsymbol{k} = 0$. The IntraVSc requires a special symmetric KP [11], and for *R*-ZnO, take the form $[\Gamma_{1+} \times \Gamma_{1+}]_2 = \Gamma_{1+}$, $[X_{1+} \times X_{1+}]_2 = \Gamma_{1+} + \Gamma_{3+}$, and $[L_{1+} \times L_{1+}]_2 = \Gamma_{1+} + \Gamma_{5+}$ for low momentum of Γ phonons and $[X_{1+} \times X_{1+}]_2 = X_{1+}$ and $[L_{1+} \times L_{1+}]_2 = X_{1+} + X_{4+}$ for large phonon momentum. Consequently, phonons involved in IntraVSc in *R*-ZnO are of symmetries: Γ_{1+} (TA and LA), Γ_{3+}, Γ_{5+} (TO and LO), and X_{4+} (TO).

7 Discussion We have derived optical selection rules based on the assignments of electronic bands listed in Table 1. We believe that electron states in CBs with no spin (Γ_{1+}, L_{1+}, and X_{1+}) and with spin (Γ_{6+}, L_{6+}, and X_{6+}) are properly assigned. Experimentally, it has been shown that the VB maxima in *R*-ZnO are at L point and Σ line, but not at the center of the BZ (Γ point). In many compounds, the highest VB maximum is at the Γ point and holes states (p_x, p_y, p_z) which transform as the VR. Since the center of the BZ is of the highest symmetry, we assigned it as Γ_{4-} = VR (no spin). The highest VB maximum has been assigned by L_{3-} two-dimensional representations according to which holes (p_x, p_y) supposed to transform. Our OPSRs are based mainly on theoretical derivations and are in agreement with absorption data. There is a lack of experimental data on *R*-ZnO, such as Raman, photoluminescence, and reflectance spectra. There is also no phonon dispersion relation and density of phonon states measured by X-ray and neutron scattering techniques. The forthcoming experimental work will verify our selection rules.

8 Conclusions An attempt has been made on assignments of the EBS of *R*-ZnO. Some optical selection rules related to direct and indirect transitions were discussed. Splitting of the maximum VB at point L due to possible S–O interaction onto three sub-bands of L_{4-}, L_{5-}, and L_{6-} symmetries, may result in the three observed exciton bands. We hope that magneto-photoluminescence and reflectivity will prove our predictions. It is well known that in the *W*-ZnO at point Γ, three excitons A, B, and C contribute to the optoelectronic devices application. It would mean that by pressure, one can "shift" the A, B, and C parabolic excitons in *W*-ZnO to the $L_1(L_{4-})$, $L_2(L_{5-})$, $L_3(L_{6-})$, and non-parabolic ones in *R*-ZnO.

References

[1] C. W. Litton, D. C. Reynolds, and T. C. Collins, Zinc Oxide Materials for Electronic and Optoelectronic Device Applications, Technology and Engineering (John Wiley & Sons, New York, 2011).
[2] K. Li, C. Kang, and D. Xue, Mater. Res. Bull. **47**, 2902–2905 (2012).
[3] H. Y. Wu, X. L. Cheng, C. H. Hu, and P. Zhou, Physica B **405**, 606–612 (2010).
[4] M. J. S. Spencer, Progr. Mater. Sci. **57**, 437–486 (2012).
[5] J. E. Jaffe, R. Pandey, and A. B. Kunz, Phys. Rev. **43**, 14030 (1991).
[6] A. Segura, J. A. Sans, F. J. Manjon, A. Munoz, and H. Cabrera, Appl. Phys. Lett. **83**, 278 (2003).

© 2014 WILEY-VCH Verlag GmbH & Co. KGaA, Weinheim

© University of Pretoria

UNIVERSITEIT VAN PRETORIA
UNIVERSITY OF PRETORIA
YUNIBESITHI YA PRETORIA

[7] A. P. Cracknell, B. L. Davies, S. C. Miller, and W. F. Love, Kronecker Product Tables, Vols. 1–4 (IFI/Plenum, New York, Washington, London, 1979).
[8] L. P. Bouckaert, R. Smoluchowski, and E. Wigner, Phys. Rev. **50**, 266–280 (1936).
[9] M. Hamermesh, Group Theory and Its Application to Physical Problems (Addison-Wesley Publ. Co., Inc., Reading, Massachusetts, London, 1962).
[10] H. W. Kunert, J. Popenda, and M. Suffczynski, J. Physique **39**, 526 (1978).
[11] H. W. Kunert, Cryst. Eng. **4**, 233–240 (2001).
[12] M. Lax and J. J. Hopfield, Phys. Rev. **124**, 115 (1961).
[13] J. L. Birman, M. Lax, and R. Loudon, Phys. Rev. **145**, 620 (1966).
[14] Y. Yu and M. Cardona, Fundamentals of Semiconductors, Physical and Material Properties (Springer-Verlag, Berlin, Heidelberg, New York, 1966).
[15] H. W. Kunert, M. R. Wagner, A. G. J. Machatine, P. Niyongabo, J. B. Malherbe, A. Hoffmann, J. Barnas, and W. Florek, Phys. Status Solidi B **247**(7), 1802–1806 (2010).

© University of Pretoria

© 2014 WILEY-VCH Verlag GmbH & Co. KGaA, Weinheim

UNIVERSITEIT VAN PRETORIA
UNIVERSITY OF PRETORIA
YUNIBESITHI YA PRETORIA

Selective Room-Temperature Sensing of NO_2 by WO_3 Film/Graphene Layers

*M. Govender**,
B. W. Mwakikunga[+] IEEE Member
DST/CSIR National Centre for Nano-Structured Materials
Council for Scientific and Industrial Research
P. O. Box 395, Pretoria, 0001, South Africa
*MGovender2@csir.co.za
[+]BMwakikunga@csir.co.za

S. Mathur, T. Singh, A. Kaouk, Y. Gönüllü
Lehrstuhl für Anorganische und Materialchemie,
Universität zu Köln,
D-50939 Köln, Germany

A. G. J. Machatine, H. W. Kunert
Department of Physics
University of Pretoria
Pretoria, 0002, South Africa

***Abstract*— This is one of the first attempts of making WO_3 thick film selective at low operating temperature by placing graphene sheets directly on the film surface. The WO_3 film was prepared by DC magnetron reactive sputtering of a pure tungsten target and annealing in air. The thickness of the film averaged 507 nm from FIB cross-sectioning and STEM measurement. The film was characterized with XRD, XPS and Raman spectroscopy. Graphene was synthesized on copper foil using plasma enhanced chemical vapor deposition of methane gas, which was found to produce three monolayers of graphene sheets according to Raman spectroscopic analysis. The graphene was transferred onto the WO_3 film and annealed. It was found that the pure WO_3 sensed low concentrations of nitrogen dioxide at 30°C and 100°C operating temperature. The selectivity towards nitrogen dioxide over ammonia and carbon monoxide was achieved with graphene on the tungsten trioxide film at the compromise of sensitivity at both operating temperatures. The analysis of the graphene/WO_3 composite orientation may lead to improved sensor capabilities as well as better understanding of the sensing mechanism.**

Keywords*— *Gas sensing, nitrogen dioxide, graphene, tungsten trioxide

I. Introduction

It is well known that tungsten trioxide (WO_3), amongst other semiconducting metal oxides (SMOs), offers the best resistive-type sensing of highly toxic nitrogen dioxide (NO_2) gas [1, 2]. However, WO_3 also shows good sensing towards reducing gases such as H_2S, NH_3, acetone and ethanol, which negatively impacts selectivity [3]. In an attempt to make WO_3 selective towards NO_2 gas, it has been shown that doping the WO_3 with noble metals such as Pt, Pd and Au has been successful [4]. It has also been shown that 1-D WO_3 nanorods anchored on graphene showed better sensitivity and selectivity towards NO_2 than metal doped WO_3 [5]. Thus, graphene offers superior properties for gas sensing and is a cheaper alternative.

Monolayer graphene is a gapless semiconductor [6], but the band gap increases with the number of layers. It was found that above 10 layers of graphene, the properties become similar to that of bulk graphite [7]. If the work function and conduction band (CB) of graphene is close to that of an SMO, the transfer of electrons from graphene to the SMO is theoretically favorable [8]. This is expected to greatly improve the conductivity properties of the SMO which is advantageous in resistive-type gas sensing because the gas sensing principle is based on conductance variations [1]. The other advantage of using graphene in this type of sensor is its large surface area could improve gas adsorption [9]. In the case of sensing oxidative gases such as NO_2, graphene acts as an electron mediator which facilitates the transfer of electrons from the SMO to the gas [10]. It is for the same reason that selectivity is achieved by the graphene/WO_3 composite, because electron donation from reducing gas to WO_3 is less favorable than electron transfer from graphene to WO_3 [5]. In this paper we combine graphene on the surface of a WO_3 film and show its gas sensing properties towards NO_2 at low operating temperatures.

II. Experimental Methods

A. Synthesis Procedure

WO_3 films were deposited on cleaned alumina (Al_2O_3) sensor substrates that have four Pt-electrodes at ambient temperature by reactive dc magnetron sputtering (PORTA 900, Plasma Electronics) of a tungsten target. The power used to produce the plasma was 900 W and the Ar:O_2 ratio was 10:1 and flowed at 500 sccm. Deposition time was 6 hours. The as-deposited sample was annealed in air at 450°C for 2 hours.

The graphene was produced on 17 µm thick Alfa Aesar copper foil (area=1 cm×0.6 cm) by plasma enhanced chemical vapour deposition (Plasma Electronics). The

Manuscript received July 25, 2014. This work was supported in part by Council for Scientific and Industrial Research (CSIR), South Africa (Project No. HGER27S) and the Wirox European project FP7.

M. Govender is a PhD student registered at the University of Pretoria but conducting his research at the Council for Scientific and Industrial Research (CSIR) in Pretoria, South Africa. (Corresponding author email: MGovender2@csir.co.za, Tel: +27128412278 Fax: +27128412229

B. W. Mwakikunga is a Principal Research Scientist at the DST/CSIR National Centre for Nano-Structured Materials in Pretoria, South Africa.

S. Mathur is a Professor and Chair of Inorganic and Material Chemistry at the University of Cologne, Germany.

T. Singh is a Postdoctoral fellow at the University of Cologne, Germany.

A. Kaouk is a Doctoral candidate at the University of Cologne, Germany.

Y. Gönüllü is a Postdoctoral fellow at the University of Cologne, Germany.

A. G. J. Machatine is a Senior Lecturer in the Department of Physics at the University of Pretoria, South Africa.

H. W. Kunert is an Emeritus Professor of Physics at the Department of Physics, University of Pretoria, South Africa.

© University of Pretoria

substrate temperature was 700°C and the gas mixture used was Ar:CH_4 in a 40:1 ratio. The deposition time was 8 minutes. The graphene was then transferred using 10% poly [(3-mercaptopropyl)-methylsiloxane] PMMS in toluene as the transfer polymer, and iron (III) nitrate as the etching solution. The graphene (1 cm×0.6 cm) was transferred directly on top of the annealed WO_3 film and dried at 100°C for 2 hours. The polymer was then dissolved in acetone and the graphene/WO_3 composite was annealed at 450°C for 2 hours.

III. Results And Discussion

From the SEM micrograph shown in Figure 1 (a) of the graphene/WO_3 composite surface, there are loosely packed structures composed of micro-sized WO_3 grains resulting from the sputtering. The film is porous with a grain size between 1-5 µm and the spacing between the grains is ~230 nm. A lamella of the composite was cut using FIB-SEM and analyzed under STEM in the dark field as shown in Figure 1 (b). The micrograph shows a platinum layer deposited on top to keep the lamella intact, and the WO_3 film with a thickness of 405-608 nm. The alumina substrate is seen at the bottom. The graphene layer sits at the interface of the platinum deposition and the WO_3 film, but this is not clearly visible and so other techniques are used for verification.

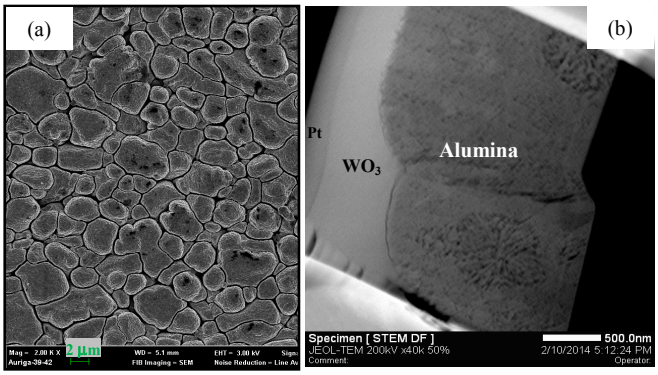

Figure 1. (a) A SEM micrograph of the topography of the graphene/WO_3 composite and (b) a STEM micrograph of a lamella of the composite sandwiched between platinum and the alumina substrate.

XRD and XPS were carried out on the graphene/WO_3 composite (not shown here). The XRD revealed that the graphene layer was alloyed to the WO_3 film and the spectrum was similar to that found by Qin et al. [11] for graphene-wrapped WO_3 nanoparticles. The XRD also confirmed that the crystalline phase of WO_3 was triclinic. The XPS confirmed that the WO_3 was indeed stoichiometric, and the carbon (C-C) 1 s binding energy peak of graphene was centered at 284.88 eV [11] and contributed to 78.6% atomic concentration of the surface stoichiometry. Raman analysis is a powerful technique used to characterize both WO_3 and graphene. Figure 2 shows the Raman spectrum of WO_3, graphene and the graphene/WO_3 composite. Only the higher wavenumber range of the graphene/WO_3 composite was shown because the intensity signal from WO_3 is orders of magnitude greater than that of graphene. The Raman peaks have been indexed [11, 12] and confirmed the XRD and XPS results of triclinic WO_3. The pure graphene showed the *D*-band, *G*-band and 2*D*-band. The ratio of intensities between the 2*D*- and *G*-band was found to be 0.86, and so it was concluded that there are three monolayers of graphene sheets [13]. Upon incorporation of the graphene with WO_3, it is seen that the graphene peaks are shifted to higher wavenumbers. It is also seen that the graphene spectrum becomes less resolved due to the strong signal from WO_3 film. The shifting probably results from the interface between the graphene and WO_3 which alters the vibrational modes accordingly since this was not observed for the nanocomposites [12]. It is assumed that the three monolayers of graphene sheets stayed intact during the transfer process based on XRD and XPS.

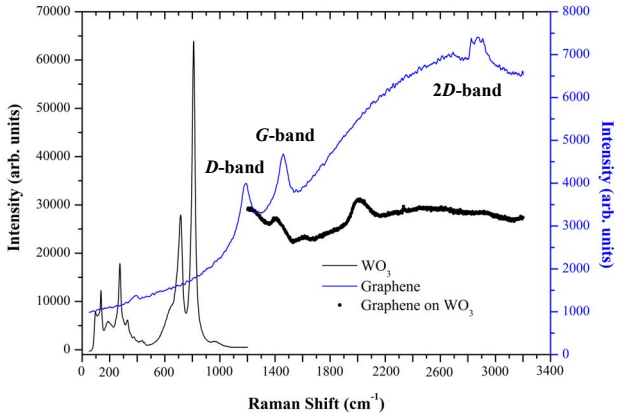

Figure 2. The Raman spectra of triclinic-phase WO_3 film, 3-monolayer graphene and graphene/WO_3 composite.

The resistance as a function of temperature of the WO_3 film and graphene/WO_3 composite are shown in Figure 3. It was not possible to get the electrical measurements of graphene only, due to the experimental configuration. It is evident that graphene causes a major drop in resistance of the *n*-type WO_3 as was expected [5, 14]. Although the estimated optical band gap of the thick triclinic-WO_3 film was found to be 3.17 eV, and the work function of graphene is believed to be 4.66 eV [5], the measured drop in resistance of the composite implies that the electron transfer is still favorable despite the overlap difference in CB.

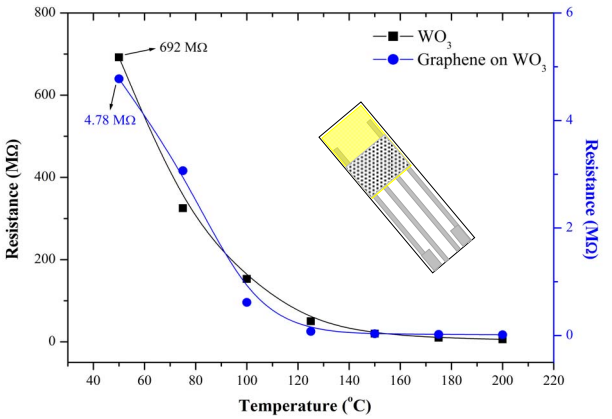

Figure 3. Resistance as a function of temperature for WO_3 and graphene/WO_3 composite shows a large drop in resistance due to electron transfer from graphene to WO_3. The inset shows a schematic (*not to scale*) of the sensor substrate with four Pt-electrodes where the yellow represents WO_3 film and the patterned-patch on the film represents graphene.

© University of Pretoria

The sensing response and comparison of the WO_3 film and graphene/WO_3 composite at operating temperatures of 30°C and 100°C towards NO_2, NH_3 and CO was tested. There was no detectable response found for CO gas under both temperatures and configurations as is expected for WO_3. The sensing response (which is the ratio of the resistivity of the sensor when exposed to the target gas minus the resistivity of the sensor in air all divided by the resistivity in air) is plotted below for NO_2 and NH_3 target gas.

Figure 4 compares the response of NO_2 to 25 times more concentrated NH_3 at an operating temperature of 30°C for the pure WO_3. It is clear that despite the more concentrated ammonia, WO_3 is much more sensitive to NO_2. At 30°C, it is believed that the predominant oxygen species on the WO_3 surface that can react with target gas is O_2^- [1]. NO_2 can either react with O_2^- or chemisorb directly on the WO_3 surface, and being an oxidizing gas, remove electrons from the film CB. This is measured as a consequent increase in resistivity. It should be noted here that there was an initial drop in resistance upon first exposure of NO_2 before the resistance started to decrease. This could imply that O_2^- is weakly bound to the surface due to low temperatures and is easily swept off the WO_3 surface causing a drop in resistance, followed by chemisorption of NO_2 on the surface. At this low temperature, there is not enough activation energy to cause a quick response and recovery time. The non-linearity in response results from the incomplete recovery of the films before the next concentration of gas is flowed in. In the case of NH_3, the low temperature is inefficient for adsorption and the reaction with O_2^- species is very slow. The transfer of electrons from the reducing gas into the film is thus unfavorable. It is proposed here that the general preference of WO_3 towards NO_2 gas could be owed to the well-known catalytic properties of this SMO.

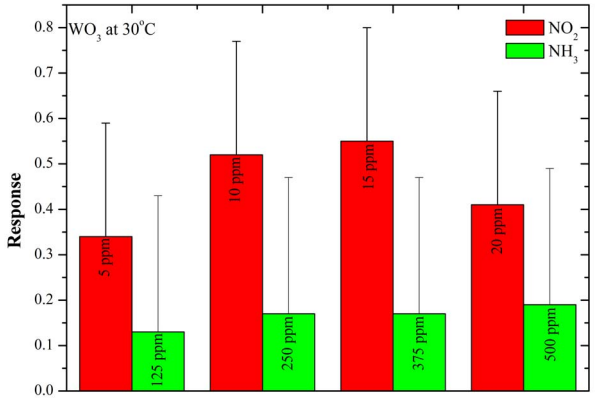

Figure 4. Response of WO_3 film towards NO_2 and NH_3 gas at 30°C.

Figure 5 shows the corresponding sensor response of graphene/WO_3 composite at 30°C. There is a 31% drop in response for NO_2 when graphene is placed on the WO_3 surface. The graphene covers 38% of the WO_3 surface which diminishes the number of adsorption sites for the target gas. It was expected that the high surface area of graphene would aid in adsorption and electron transfer, but the results suggest that WO_3 is solely responsible for sensing. Even though the graphene provides more electrons in the WO_3 CB which can be transferred to the oxidizing gas, it is still the number of adsorption sites that are significant. It is also noticed that there is no initial drop in resistance as was seen for pure WO_3. This could mean that the incorporation of graphene inhibits the adsorption of oxygen and subsequent formation of the O_2^- species. This is also supported by the increased recovery time. The response for NH_3 drops by 72%, which apart from the decreased adsorption area, could result from graphene's electron saturation of the WO_3 CB. Thus, the electron donating NH_3 is not favored and in this way, selectivity is achieved.

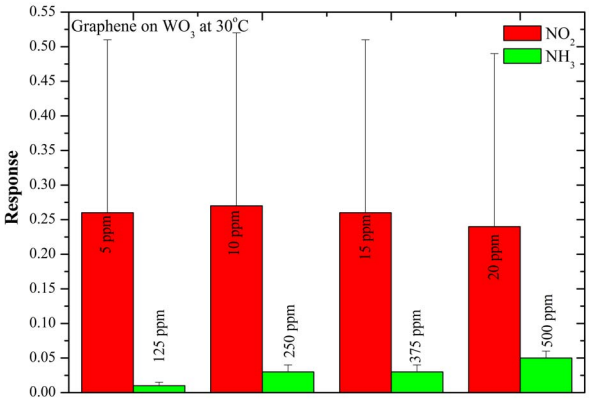

Figure 5. Response of graphene/WO_3 composite towards NO_2 and NH_3 gas at 30°C.

Figure 6 shows the sensor response of WO_3 at an operating temperature of 100°C. The response towards NO_2 increases by more than 80% at the increased temperature. It is believed that the predominant oxygen species on the WO_3 surface at 100°C is the more reactive O^- [1]. This should drastically increase the response along with other factors such as an increase in activation energy and adsorption efficiency, as well as an increase in the number of electrons in the CB. The response and recovery time almost doubles when compared to the response at the 30°C operating temperature. The response towards NH_3 also increases by 80%, which suggests that the main factor influencing sensing is the more reactive O^- surface specie and possibly the increased activation energy.

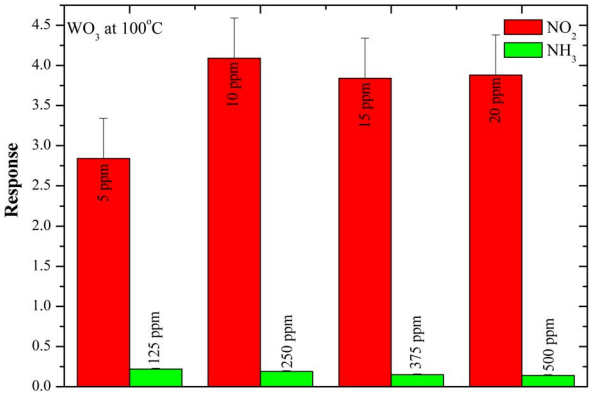

Figure 6. Response of WO_3 film towards NO_2 and NH_3 gas at 100°C.

© University of Pretoria

Figure 7 shows the corresponding sensor response of graphene/WO_3 composite at 100°C. There is a 49% drop in response for NO_2 when graphene is placed on the WO_3 surface at the 100°C temperature. The drop is more significant at this temperature because the general response is more significant at elevated temperature. The response towards NH_3 becomes almost negligible at 100°C with graphene. Besides the decreased surface area, the contribution of electrons from graphene and the WO_3 valence band into the WO_3 CB is much greater. This implies that NH_3 is almost blocked from donating electrons to WO_3 and therefore the response drops drastically. Thus, the selectivity becomes even more pronounced at this temperature.

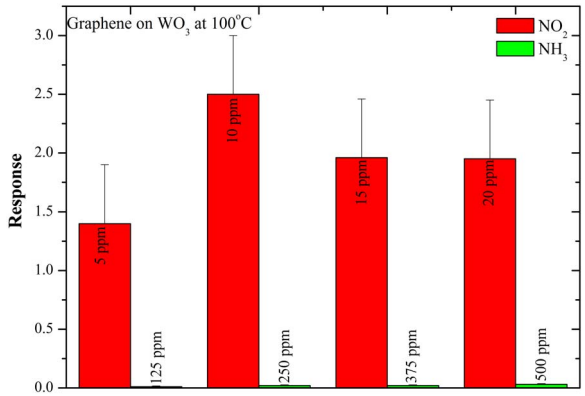

Figure 7. Response of graphene/WO_3 composite towards NO_2 and NH_3 gas at 100°C.

IV. CONCLUSION

We have incorporated graphene sheets directly on the surface of WO_3 film and tested the gas sensing response of the composite. Raman analysis was used to identify the *G*-, *D*- and 2*D*-bands of graphene, and the number of monolayers was estimated to be three. It was found from resistance measurements, that there was a 99.3% drop in resistance of the WO_3 film when graphene was alloyed to the film. The response and sensitivity of pure WO_3 increased with operating temperature towards both the NO_2 and NH_3 target gas. However, the use of graphene directly on the WO_3 surface decreased the overall response due to the decrease in adsorption surface area. The large adsorption area of graphene plays no part in sensing. The response towards NH_3, which is 25 times more concentrated than NO_2, dropped much more than that of NO_2, which in a way results in the composite being more selective towards NO_2. The results also speculate about the nature and role of the oxygen adsorbed species at the chosen operating temperatures.

REFERENCES

[1] K. Wetchakun, T. Samerjai, N. Tamaekong, C. Liewwhiran, C. Siriwong, V. Kruefu, A. Wisitsoraat, A. Tuantranont, S. Phanichphant, "Semiconducting metal oxides as sensors for environmentally hazardous gases", Sensors and Actuators B:Chemical **160**, 2011, pp. 580-591.

[2] M. Govender, D. E. Motaung, B. W. Mwakikunga, S. Umapathy, S. Sil, A. K. Prasad, A. G. J. Machatine, and H. W. Kunert, "Operating Temperature Effect in WO_3 Films for Gas Sensing", Sensors **2013** IEEE, 2013, pp. 1-4.

[3] G. Korotcenkov, "Metal oxides for solid-state gas sensors: What determines our choice?", Materials Science and Engineering B **139**, 2007, pp. 1-23.

[4] M. Penza, C. Martucci, G. Cassano, "NO_x gas sensing characteristics of WO_3 thin films activated by noble metals (Pd, Pt, Au) layers", Sensors and Actuators B:Chemical **50**, 1998, pp. 52-59.

[5] X. An, J. C. Yu, Y. Wang, Y. Hu, X. Yu, G. Zhang, "WO_3 nanorods/grapheme nanocomposites for high-efficiency visible-light-driven photocatalysis and NO_2 gas sensing", Journal of Materials Chemistry **22**, 2012, pp.8525-8531.

[6] K. S. Novoselov, A. K. Geim, S. V. Morozov, D. Jiang, M. I. Katsnelson, I. V. Grigorieva, S. V. Dubonos, A. A. Firsov, "Two-dimensional gas of massless Dirac fermions in graphene", Nature **438**, 2005, pp. 197-200.

[7] K. S. Novoselov, A. K. Geim, S. V. Morozov, D. Jiang, Y. Zhang, S. V. Dubonos, I. V. Grigorieva, A. A. Firsov, "Electric field effect in atomically thin carbon films", Science **306**, 2004, pp. 666-669.

[8] L. Weinhardt, M. Blum, M. Ba1r, C. Heske, "Electronic Surface Level Positions of WO_3 Thin Films for Photoelectrochemical Hydrogen Production", Journal of Physical Chemistry C **112**, 2008, pp. 3078-3082.

[9] M. Zhou, Y. Lu, Y. Cai, C. Zhang, Y. Feng, "Adsorption of gas molecules on transition metal embedded graphene: a search for high-performance graphene-based catalysts and gas sensors", Nanotechnology **22**, 2011, pp. 385502 (1-8).

[10] G. Singh, A. Choudhary, D. Haranath, A. Joshi, N. Singh, S. Singh, R. Pasricha, "ZnO decorated luminescent graphene as a potential gas sensor at room temperature", Carbon **50**, 2012, , pp. 385-394.

[11] J. Qin, M. Cao, N. Li, C. Hu, "Graphene-wrapped WO_3 nanoparticles with improved performances in electrical conductivity and gas sensing properties", Journal of Materials Chemistry **21**, 2011, pp. 17167-17174.

[12] S. Thangavel, M. Elayaperumal, G. Venugopal, "Synthesis and Properties of Tungsten Oxide and Reduced Graphene Oxide Nanocomposites", Materials Express **2**, 2012, pp. 327-334.

[13] J. S. Park, A. Reina, R. Saito, J. Kong, G. Dresselhaus, M. S. Dresselhaus, "G′ band Raman spectra of single, double and triple layer graphene", Carbon **47**, 2009, pp. 1303-1310.

[14] M. Govender, B. W. Mwakikunga, A. G. J. Machatine, and H. W. Kunert, "Electrical and optical properties of mixed phase tungsten trioxide films grown by laser pyrolysis", Physica Status Solidi (c) **11**, 2014, pp. 349-354.

© University of Pretoria

References

[1] I. O. Osunmakinde, International Journal of Distributed Sensor Networks **2013**, 159273 (2013).
[2] M. Kreuzer, L. Walsh, M. Schnelzer, A. Tschense, and B. Grosche, British Journal of Cancer **99** (11), 1946–1953 (2008).
[3] T. R. Yager, United States Geological Survey-Minerals Yearbook South Africa, 37 (2007).
[4] M. C. Betournary, Interstate Technical Group on Abandoned Underground Mines Fourth Biennial Abandoned Underground Mine Workshop, Report MMSL, 02-021 (2010).
[5] C. Lagny, Environ Earth Sci **71**(2), 923-929 (2014).
[6] W. Matuszewski, and M. E. Meyerhoff, Analytica Chimica Acta **248**, 379-389 (1991).
[7] R. Muda, E. Lewis, S. O'Keeffe, G. Dooly. and J. Clifford, Journal of Physics: Conference Series **178**, 1-6 (2009).
[8] F. W. Noble, K. Abel, and P. W. Cook, Anal. Chem. **36**(8), 1421-1427 (1964).
[9] E. Vitz, and H. Chan, J. Chem. Educ., **72**(10), 920-925 (1995).
[10] E. Roduner, Chem. Soc. Rev. **35**(7), 583-592 (2006).
[11] K. Balasubramanian, and M. Burghard, Small **1**(2), 180-192 (2005).
[12] N. Barsan, D. Koziej, and U. Weimar, Sensors and Actuators B **121**, 18-35 (2007).
[13] G. Eranna, B. C. Joshi, D. P. Runthala, and R. P. Gupta, Critical Review in Solid State and Materials Science **29**, 111-188 (2004).
[14] K. J. Choi, and H. W. Jang, Sensors **10**, 4083-4099 (2010).
[15] G. Korotcenkov, Materials Science and Engineering B **139**, 1-23 (2007).
[16] O. V. Krilov, and V. F. Kisilev, Chemistry, Moscow (1981).
[17] G. V. Samsonov, The Oxide Handbook, IFI/Plenum, New York (1973).
[18] M. J. Gordon, S. Gaur, S. Kelkar, and R. W. Baldwin, Catal. Today **28**, 305–317 (1996).
[19] C. Sol, and J. D. Tilley, Mater. Chem. **11**, 815–820 (2001).
[20] E. Salje, and K. Viswanathan, Acta. Crystallogr. A **31**, 356-359 (1975).
[21] S. Gulati, N. Mehan, D. P. Goyal, and A. Mansingh, Sens Actuators B **87**, 309-320 (2002).
[22] M. Govender, L. Shikwambana, B. W. Mwakikunga, E. Sideras-Haddad, R. M. Erasmus, and A. Forbes, Nanoscale Research Letters **6**, 166 (2011).
[23] M. Govender, B. W. Mwakikunga, A. G. J. Machatine, and H. W. Kunert, Phys. Stat. Sol. (c) **11**, 349-354 (2014).
[24] B. W. Mwakikunga, E. Sideras-Haddad, A. Forbes, and C. Arendse, Phys. Stat. Sol. (a) **205**, 150-154 (2008).
[25] J. Solis, S. S. Saukko, L. Kish, C. G. Granqvist, and V. Lantto, Thin Solid Films **391**, 255-260 (2001).
[26] B. S. Thabethe, G. F. Malgas, D. E. Motaung, T. Malwela, and C. J. Arendse, Journal of Nanomaterials **2013**, 712361 (2013).
[27] M. Govender, D. E. Motaung, B. W. Mwakikunga, S. Umapathy, S. Sil, A. K. Prasad, A. G. J. Machatine, and H. W. Kunert, Sensors **2013** IEEE, 1-4 (2013).
[28] M. Seman, and C. A. Wolden, Solar Energy Materials and Solar Cells **82**, 517-530 (2004).

© University of Pretoria

[29] I. M. Szilágyi, S. Saukko, J. Mizsei, A. L. Tóth, J. Madarász, G. Pokol, Solid State Sciences **12**, 1857-1860 (2010).
[30] A. Boudiba, C. Zhang, C. Bittencourt, P. Umek, M.-G. Olivier, R. Snyders, and M. Debliquy, Procedia Engineering **47**, 1033-1036 (2012).
[31] M. Di Giulio, D. Manno, G. Micocci, A. Serra, and A. Tepore, J. Phys. D: Appl. Phys. **30**, 3211–3215 (1997).
[32] A. P. Cracknell, B. L. Davies, S. C. Miller, and W. F. Love, "Kronecker Product Tables", Plenum, New York, Washington, (1979).
[33] E. Comini, Analytica Chimica Acta **568**, 28-40 (2006).
[34] Y.-F. Sun, S.-B. Liu, F.-L. Meng, J.-Y. Liu, Z. Jin, L.-T. Kong, and J.-H. Liu, Sensors **12**, 2610-2631 (2012).
[35] I.-D. Kim, A. Rothschild, and H. L. Tuller, Acta Materialia **61**, 974-1000 (2013).
[36] P.T. Moseley, Meas. Sci. Technol. **8**, 223–237 (1997).
[37] S. Capone, P. Siciliano, F. Quaranta, R. Rella, M. Epifani, and L. Vasanelli, Sensors and Actuators B **77**, 503-511 (2001).
[38] B. W. Mwakikunga, S. Motshekga, L. Sikhwivhilu, M. Moodley, M. Scriba, G. Malgas, A. Simo, B. Sone, M. Maaza, S. S. Ray, Sensors and Actuators B **184**, 170-178 (2013).
[39] M. E. Franke, T. J. Koplin, U. Simon, Small **2**(1), 36-50 (2006).
[40] N. Barsan, Sens Actuat B **17**(3), 241-246 (2006).
[41] M. Pardo, and G. Sberveglieri, MRS Bull **29**(19), 703-708 (2004).
[42] G. F. Fine, L. M. Cavanagh, A. Afonja, and R. Binions, Sensors **10**, 5469-5502 (2010).
[43] S. Samson, and C. G. Fonstad, J Appl Phys **44**(10), 4618-4621 (1973).
[44] Z. M. Jarzebski, and J. M. Marton, J Electrochem Soc **123**, 299C-310C (1976).
[45] P. B. Weisz, J Chem Phys **21**, 1531-1538 (1953).
[46] P. Å. Öberg, T. Togawa, and F. A. Spelman, Sensors in medicine and health care, In: J. Hesse, J. Gardner, and W. Göpel (eds), Sensors Application Vol. **3**, Wiley-VCH, Weinheim (2004).
[47] K. D. Schierbaum, U. Weimar, W. Göpel, and R. Kowalowski, Sens Actuat B **3**, 205-214 (1991).
[48] M. I. Barton, L. Merhari, H. Ferkerl, J. F. Catagnet, Mater Sci Eng C **19**, 315-321 (2002).
[49] J. Madou, and S. R. Marison, Chemical sensing with solid state devices, Academic Press, New York (1989).
[50] P. J. Barth, B. Muller, U. Wagner, and A. Bittinger, Eur. Resp. J. **8**, 1115-1121 (1998).
[51] M. Wegmann, A. Fehrenbach, S. Heimann, H. Fehrenbach, H. Renz, H. Garn, and U. Herz, Expt. Tox. Path. **56**, 341-350 (2005).
[52] M. Akiyama, J. Tamaki, N. Miura, and N. Yamazoe, Chem. Lett. **20**, 1611-1614 (1991).
[53] Z. Zhou, H. Gao, R. Liu, and B. Du, Theochem **545**, 179-186 (2001).
[54] M. Sulka, M. Pitonak, P. Neogrady, and M. Urban, Int J Quantum Chem **108**, 2159-2171 (2008).
[55] E. Leblanc, L. Perier-Camby, G. Thomas, G. Giber, R. M. Primet, and P. Gerlin, Sens Act B **62**, 67-72 (2000).
[56] Ammonia, in Ullmann's Encyclopedia of Industrial Chemistry, Appl M Ed, Wiley-VCH:Weinheim, Germany (2006).

© University of Pretoria

[57] C. S. Rout, M. Hedge, C. N. R. Rao, Nanostechnology **18**, 205504 (2007).
[58] M. Hamermesh, "Group Theory and Its Application to Physical Problems", (Addison-Wesley Publ. Co., Inc., Reading, Massachusetts, USA, London, England), (1962).
[59] L. D. Landau, and E. M. Lifshitz, "Statistical Physics" Vol. 5 of Theoretical Physics, Pergamon Press (1969).
[60] www.helsinki.fi/~serimaa/soft-luento/soft-2-phase.html, acquired on (14-04-2014)
[61] T. Vogt, P. M. Woodward and B. A. Hunter, Journal of Solid State Chemistry **144**, 209-215 (1999).
[62] M. Kawaminami, and T. Hirose, Journal of the Society of Japan **46**(3), 864-870 (1979).
[63] F. Corà, A. Patel, N. M. Harrison, R. Dovesi, and C. R. A. Catlow, J. Am. Chem. Soc. **118**, 12174-12182 (1996).
[64] M. G. Stachiotti, F. Corà, C. R. A. Catlow, and C. O. Rodriguez, Physical Review B **55**(12), 7508-7514 (1997).
[65] F. Corà, M. G. Stachiotti, and C. R. A. Catlow, J. Phys. Chem. B **101**, 3945-3952 (1997).
[66] R. Diehl, G. Brandt, and E. Salje, Acta Cryst. B **34**, 1105-1111 (1977).
[67] C. J. Howard, V. Luca, and K. S. Knight, J. Phys.: Condens. Matter **14**, 377-387 (2002).
[68] P. M. Woodward, A. W. Sleight, and T. Vogt, J. Phys. Chem. Solids **56**(10), 1305-1315 (1995).
[69] E. Salje, Acta Cryst. A **31**, 360 (1975).
[70] K. R. Locherer, I. P. Swanson, and and E. K. H. Salje, J. Phys.: Condes. Matter **11**, 6737-6756 (1999).
[71] K. R. Locherer, I. P. Swainson, and E. K. H. Salje, J. Phys.: Condes. Matter **11**, 4143-4156 (1999).
[72] A. G. Souza-Filho, V. N. Freire, O. Pilla, A. P. Ayala, J. M. Filho, F. E. A. Melo, V. N. Freire, and V. Lemos, Phys. Rev. B **62**, 3699-3703 (2000).
[73] E. Salje, Acta Cryst. B **33**, 574-577 (1975).
[74] M. Boulova, N. Rosman, P. Bouvier, and G. Lucazeau, J. Phys.: Condens. Matter **14**, 5849-5863 (2002).
[75] K. R. Locherer, J. Chrosch, and E. K. H. Salje, Phase Transitions **67**, 51-63 (1998).
[76] G. Ya. Lyubarskii, "The Application of Group Theory in Physics", Translated by S. Dedijer, Pergamon Press (1960).
[77] J. L. Birman, M. Lax, and R. Loudon, Phys. Rev. **145**, 620 (1965).
[78] J. L Birman, and R. Berenson, Phys. Rev. B **9**(10), 4512-4517 (1974).
[79] M. Boulova, G. Lucazeau, T. Pagnier, and A. Gaskov, J. Phys. IV France **11**, 1057-1062 (2001).
[80] C. Cantalini, H. T. Sun, M. Faccio, M. Pelino, S. Santucci, L. Lozzi, and M. Passacantando, Sensors and Actuators B **31**, 81-87 (2007).
[81] S.-H. Wang, T.-C Chou, and C.-C. Liu, Sensors and Actuators B **94**, 343-351 (2003).
[82] D. Gogova, K. Gesheva, A. Szerkeres, and M. Sendova-Vassileva, Phys. Stat. Sol. (a) **176**, 969 (1999).
[83] I. Jiménez, J. Arbiol, A. Cornet, and J. R. Morante, IEEE Sensors **2**(4) 329-335 (2002).
[84] E. Gillet, K. Mašek, D. Lollman, and M. Gillet, Vacuum **82**, 261-265 (2008).

© University of Pretoria

[85] D. Chen, X. Hou, H.Wen, Y.Wang, H. Wang, X. Li, R. Zhang, H. Lu, H. Xu, S. Guan, J. Sun, and L. Gao, Nanotechnology **21**, 1-12 (2010).
[86] D. Demiz, D. J. Frankel, and R. J. Lad, Thin Solid Films **518**, 4095 (2010); W. J. Li, and Z. W. Fu, Appl. Surf. Sci. **256**, 2447 (2010).
[87] C.-J. Jin, T. Yamazaki, Y. Shirai, T. Yoshizawa, T. Kikuta, N. Nakatani, and H. Takeda, Thin Solid Films **474**, 255-260 (2005).
[88] F. Wang, C. Di Valentin, and G. Pacchioni, J. Phys. Chem. C **115**, 8345-8353 (2011).
[89] H. Y. Wong, C. W. Ong, R. W. M. Kwok, K. W. Wong, S. P. Wong, and W. Y. Cheung, Thin Solid Films **376**, 131 (2000).
[90] J. Gabreusenoks, A. Veispals, A. von Czarnowski, and K.-H. Meiwes-Broer, Electrochim. Acta **46**, 2229, (2001).
[91] E. Cazzanelli, C. Vinegoni, G. Mariotto, A. Kuzman, and J. Purans, J. Solid, State Chem. **143**, 24 (1999).
[92] D. Y. Lu, J. Chen, S.Z. Deng, N.S. Xu, and W.H. Zhang, J. Mater. Res. **23** (2), 402-408 (2008).
[93] J. Bardeen, F. J. Slatt, and L. Hall, Photoconductivity Conference, Wiley, New York, 146 (1965).
[94] D. G. Barton, M. Shtein, R. D. Wilson, S. L. Soled, and E. Iglesia, J. Phys. Chem. B **103**, 630-640 (1999).
[95] M. G. Hutchins, O. Abu-Alkhair, M. M. El-Nahaas, and K. Abdel-Hady, J. Phys.: Condens. Matter **18**, 9987-9997 (2006).
[96] A. Subrahmanyam, and A. Karuppasamy, Sol. Energy Mater. Sol. Cells **91**, 266 (2007).
[97] M. B. Johansson, G. Baldissera, I. Valyukh, C. Persson, H. Arwin, G. A. Niklasson, and L. Osterlund, J. Phys.:Condens. Matter **25**, 1-11 (2013).
[98] H.-F. Pang, X. Xiang, Z.-J. Li, Y.-Q. Fu, and X.T. Zu, Phys. Status Solidi A **209**(3), 237-544 (2012).
[99] M. Feng, A. L. Pan, H. R. Zhang, Z. A. Li, F. Liu, H. W. Lu, D. X. Shi, B. S. Zou, and H. J. Gao, Applied Physics Letters **86**, 1-3 (2005).
[100] S. Park, H. Kim, C. Jin, and C. Lee, Nanoscale Research Letters **6**(451), 1-6 (2011).
[101] K. Aguir, C. Lemire and D. B. B. Lollman, Sensors and Actuators B **84**(1), 1-5 (2002).
[102] G. Eranna, B. C. Joshi, D. P. Runthala, and R. P. Gupta, Crit Sol State Mater Sci **29**, 111-188 (2004).
[103] C. Hui-Qing, H. Ming, Z. Jing, and W. Wei-Dan, Chin. Phys. B. **21**(5), 058201 (2012).

© University of Pretoria